

**Photodynamic Therapy: Biophysical Mechanisms
and Molecular Responses**

by

Soumya Mitra

**Submitted in Partial Fulfillment
of the
Requirements for the Degree
Doctor of Philosophy**

Supervised by

Professor Thomas H. Foster

**Department of Biochemistry and Biophysics
School of Medicine & Dentistry**

**University of Rochester
Rochester, New York**

2004

*To my parents,
grandparents
and Sathi*

Curriculum Vitae

Soumya Mitra was born in New Delhi, India on October 13th, 1972. In 1990, he graduated from Ramjas School, a private high secondary school in R.K. Puram, New Delhi. After graduating from high school, he enrolled at the S.G.T.B Khalsa College, University of Delhi, India. Soumya graduated from college in the spring of 1993 with a Bachelor of Science degree in Physics. He then attended the Department of Physics and Astronomy at the University of Delhi from 1993 to 1995 and graduated with a Master of Science degree in Physics.

In the fall of 1996, Soumya came to the United States to pursue higher studies and joined the doctoral program in Physics at the University of Wisconsin at Milwaukee, Wisconsin. Before the end of the second semester at Wisconsin, he developed a keen interest in the field of Biophysics. In the summer of 1997, he left Wisconsin and entered the graduate program in Biophysics at the University of Rochester. He began his thesis research in the field of photodynamic therapy under the direction of Professor Thomas H. Foster and earned his Master of Science degree in Biophysics in 2000. He became a doctoral candidate that year and completed his doctoral thesis work in 2004.

PUBLICATIONS

S. Mitra and T. H. Foster (2000) Photochemical oxygen consumption sensitized by a porphyrin phosphorescent probe in two model systems. *Biophys. J.* **78**: 2597-2605.

S. Coutier, S. Mitra, L. N. Bezdetnaya, R. M. Parache I. Georgakoudi, T. H. Foster, and F. Guillemin (2001) Effects of fluence rate on cell survival and photobleaching in meta-tetra-(hydroxyphenyl) chlorin-photosensitized Colo 26 multicell tumor spheroids. *Photochem. Photobiol.* **73**: 297-303.

S. Mitra, J. C. Finlay, D. McNeill, D. L. Conover, and T. H. Foster (2001) Photochemical oxygen consumption, oxygen evolution and spectral changes during UVA irradiation of EMT6 spheroids. *Photochem. Photobiol.* **73**: 703-708.

C. E. Bigelow, S. Mitra, R. Knuechel, and T. H. Foster (2001) ALA- and ALA-hexylester-induced protoporphyrin IX fluorescence and distribution in multicell tumor spheroids. *Br. J. Cancer* **85**: 727-734.

C. E. Bigelow, C. J. Harkrider, D. L. Conover, T. H. Foster, I. Georgakoudi, S. Mitra, M. G. Nichols, and M. Rajadhyaksha (2001) Retrofitted confocal laser scanner for a commercial inverted fluorescence microscope. *Rev. Sci. Inst.* **72**: 3407-3410.

J. C. Finlay, S. Mitra, and T. H. Foster (2002) In vivo mTHPC photobleaching in normal rat skin exhibits unique irradiance-dependent features. *Photochem. Photobiol.* **75**: 282-288.

S. Mitra, E. M. Goren, J. G. Frelinger, and T. H. Foster (2003) Activation of heat shock protein 70 promoter with meso-tetrahydroxyphenyl chlorin photodynamic therapy reported by green fluorescent protein in vitro and in vivo. *Photochem. Photobiol.* **78**: 615-622.

S. Mitra and T. H. Foster (2004) Carbogen breathing significantly enhances the penetration of red light in murine tumors in vivo. *Phys. Med. Biol.* In press.

Acknowledgements

The thesis document is the product of the research that I pursued for several years, none of which would have been accomplished without the help and guidance from several individuals to whom I am gratefully indebted.

First and foremost, I wish to express my deepest gratitude to Professor Thomas Foster to have given me the opportunity to be a graduate student in his research group. It has been a privilege to have him as my mentor. I am very appreciative of the time and effort that he devoted to guide me in a wide variety of subjects ranging from research problems to career direction. He has been instrumental in training me in the process of scientific writing and his patience and careful proofreading has been invaluable in the development of this document. The research conducted under Prof. Foster was supported by funds from the USPHS grant CA68409.

As a member in Prof. Foster's group, I had the pleasure of interacting with fellow graduate students Jarod Finlay, Chad Bigelow, Irene Georgakoudi, Edward Hull, William Cottrell and Jeremy Wilson. Irene was instrumental in teaching me the fundamentals of spheroid culture and the oxygen microelectrode experiments. My research work benefited greatly from help from both Jarod and Chad. I had the opportunity to work closely with Jarod on studying the *in vivo* photobleaching kinetics of mTHPC and Photofrin. He also helped me

significantly with the preparation of tissue-simulating erythrocyte phantoms. Chad was instrumental in setting up the confocal imaging and spectroscopy system which is used extensively in the studies described in chapters 3 and 4. It's my pleasure to thank Jarod and Chad for their wonderful friendship and for being more than just scientific colleagues. William and Jeremy are relatively new graduate students in our group and have been very helpful to me in the past few months. I sincerely appreciate the help from two undergraduate students, Evan Goren and David Niles, who diligently maintained the cell and spheroid culture over the last three years. Evan also performed a lot of the cell monolayer imaging analysis described in chapter 6.

I wish to acknowledge the significant contribution of David Conover, a research associate in the Department of Radiology. Numerous times, his technical expertise, valuable assistance and insights have helped me to improve experimental methods and are greatly appreciated.

During these years, I also had the opportunity to work with several other investigators in the Medical Center. Professor Frelinger and Ms. Andrea Brooks were extremely helpful with matters related to the plasmid transfection, clone selection and other related molecular biology aspects of the experiments described in chapter 6. Mr. Scott Gibson, a member in the lab of Professor Russell Hilf, has helped me several times with various matters related to the biology of my experiments.

I would like to acknowledge the inspiration from my Physics teacher, the late Mr. N. B. Roy, during my high school years towards motivating me to pursue higher studies in physical sciences. I also gratefully acknowledge the influence of my uncle, Professor Dipak Basu, whose encouragement in inquisitiveness was valuable in helping me develop a scientific inclination.

The love and company of friends during my stay in Rochester have been invaluable. In particular, I would like to thank Shubhadeep Purakayastha, Mishkatul Bhattacharya, Subhranil De and Subhadip Raychaudhuri for their genuine and sincere friendship. The many inspiring and joyous moments and enlightening conversations I had with them will remain in my mind as fond memories.

The constant support that I received from my aunt, Mrs. Sumita Basu, since my very first day in the United States is priceless. I hereby express to her my sincerest gratitude.

I gratefully acknowledge the encouragement and influence of my loving parents and grandparents. Whatever I have learned from them, since my childhood, has been crucial in shaping my character and mindset. Finally, I am deeply thankful to my wife Sathi for her emotional support, and whose love and boundless patience has made the completion of this work possible.

Abstract

In photodynamic therapy (PDT), photochemical reactions induced by optical activation of sensitizer molecules cause destruction of the target tissue. In this thesis we present results of several related studies, which investigated the influence of photophysical properties and photobleaching mechanisms of sensitizers and oxygen-dependent tissue optical properties on PDT treatment efficacy.

The bleaching mechanism of the sensitizer meso-tetra hydroxyphenyl chlorin (mTHPC) is examined indirectly using measurements of photochemical oxygen consumption during PDT irradiation of multicell tumor spheroids. Analysis of the results with a theoretical model of oxygen diffusion that incorporates the effects of sensitizer photobleaching shows that mTHPC is degraded *via* a singlet-oxygen ($^1\text{O}_2$)-mediated bleaching process. The analysis allows us to extract photophysical parameters of mTHPC which are used to account for its enhanced clinical photodynamic potency in comparison to that of Photofrin.

Evaluation of the spatially-resolved fluorescence in confocal optical sections of intact spheroids during PDT irradiation allows for the direct experimental verification of mTHPC's $^1\text{O}_2$ -mediated bleaching mechanism. The technique is also used to investigate the complex bleaching kinetics of Photofrin.

The results allow us to successfully reconcile apparently contradictory experimental observations and to confirm the predictions of a new theoretical model in which both $^1\text{O}_2$ and excited triplet sensitizer molecules are allowed to contribute to photobleaching.

Based on studies performed in tissue-simulating erythrocyte phantoms and in a murine tumor model *in vivo*, we present clinically relevant results which indicate that a shift toward increased hemoglobin-oxygen saturation due to improved tissue oxygenation reduces PDT treatment beam attenuation and may allow for more effective treatment of deeper lesions.

Finally, we investigate the induction of the stress protein, heat shock protein 70 (HSP70), in response to mTHPC-PDT. The studies are performed using a murine tumor cell line transfected with a plasmid containing the gene for Green Fluorescent Protein (GFP) under the control of an hsp70 promoter. We obtain increased levels of GFP fluorescence at a cellular level and *in vivo* in response to sub-lethal doses of mTHPC-PDT. These results demonstrate the potential of using fluorescent reporter proteins as biomarkers of PDT-induced oxidative stress.

Table of Contents

<i>Curriculum Vitae</i>	<i>iii</i>
<i>Acknowledgements</i>	<i>v</i>
<i>Abstract</i>	<i>viii</i>
<i>Table of contents</i>	<i>x</i>
<i>List of tables</i>	<i>xv</i>
<i>List of figures</i>	<i>xvii</i>
CHAPTER 1: INTRODUCTION AND OVERVIEW	1
1.1 A HISTORICAL PERSPECTIVE ON PHOTODYNAMIC THERAPY	1
1.2 THE PHOTOPHYSICS OF PHOTODYNAMIC THERAPY	6
1.3 PHOTOCHEMICAL ³ O ₂ CONSUMPTION AND SENSITIZER PHOTBLEACHING DURING PDT	9
1.4 FLUORESCENCE AND CONFOCAL FLUORESCENCE MICROSCOPY AS TOOLS FOR DIRECT INVESTIGATION OF SENSITIZER PHOTBLEACHING MECHANISM	16
1.5 TISSUE OXYGENATION: AN IMPORTANT KEY IN IMPROVING THERAPEUTIC EFFICACY OF PDT	19
1.6 FLUORESCENT MOLECULAR MARKERS OF PDT-INDUCED DAMAGE	21
REFERENCES	23

CHAPTER 2: AN INVESTIGATION INTO THE PHOTODYNAMIC EFFICACY OF MESO-TETRA HYDROXYPHENYL CHLORIN (mTHPC).....	29
2.1 INTRODUCTION.....	29
2.2 EXPERIMENTAL METHODS AND RESULTS	32
2.2.1 <i>Theory for analysis of 3O_2 concentration measurements</i>	32
2.2.2 <i>Nonuniform initial sensitizer distribution and its effect on the maximum rate of photodynamic 3O_2 consumption</i>	36
2.2.3 <i>3O_2 concentration measurements during PDT and indirect investigation of sensitizer bleaching mechanisms</i>	41
2.2.4 <i>Effects of irradiance on mTHPC-photosensitized cell survival</i>	49
2.2.5 <i>Estimation of photodynamic dose and 1O_2 threshold</i>	50
2.2.6 <i>Comparison of treatment efficacy for mTHPC vs. Photofrin based on their respective photophysical characteristics</i>	55
2.3 DISCUSSION.....	61
REFERENCES	68
CHAPTER 3: EXPERIMENTAL VERIFICATION OF mTHPC PHOTOBLEACHING MECHANISM.....	73
3.1 INTRODUCTION.....	73
3.2 EXPERIMENTAL METHODS AND RESULTS	76
3.2.1 <i>Studies examining loss of mTHPC fluorescence in PDT-treated spheroids and comparison with simulated results based on 3O_2 concentration measurements</i>	76

3.2.2	<i>Test of mTHPC's bleaching mechanism using confocal optical sectioning in intact spheroids</i>	81
3.2.2.1	<i>Confocal fluorescence imaging and spectroscopy in spheroids during PDT</i>	81
3.2.2.2	<i>Image analysis</i>	86
3.3	DISCUSSION.....	93
	REFERENCES.....	98
 CHAPTER 4: INVESTIGATION INTO PHOTOFRIN BLEACHING KINETICS: DIRECT TEST OF A NEW MODEL OF PHOTBLEACHING.....100		
4.1	INTRODUCTION.....	100
4.2	THE FORMULATION OF A SIMULTANEOUS MULTIPLE BLEACHING MECHANISM (SSTB) MODEL.....	106
4.3	EXPERIMENTAL METHODS.....	114
4.3.1	<i>Spheroid preparation</i>	114
4.3.2	<i>Confocal fluorescence spectroscopy of Photofrin-PDT treated spheroids</i> ..	115
4.3.3	<i>Spectral analysis to quantify Photofrin and photoproduct fluorescence</i>	119
4.4	RESULTS.....	122
4.4.1	<i>Predictions of the SSTB model</i>	122
4.4.2	<i>Fluorescence photobleaching and photoproduct formation in multicell tumor spheroids</i>	129
4.5	DISCUSSION.....	139
	REFERENCES.....	146

CHAPTER 5: INCREASED OXYGENATION IMPROVES LIGHT PENETRATION AT 630 AND 650 NM IN MURINE TUMORS <i>IN VIVO</i>.....	150
5.1 INTRODUCTION.....	150
5.2 MATERIALS AND EXPERIMENTAL METHODS.....	154
5.2.1 <i>Erythrocyte phantom preparation</i>	154
5.2.2 <i>Hemoglobin-oxygen dissociation curve: The Hill curve</i>	156
5.2.3 <i>Measurements in tissue-simulating erythrocyte phantoms</i>	157
5.2.4 <i>Measurements in vivo</i>	159
5.2.5 <i>Efficacy comparison between mTHPC- and Photofrin-PDT</i>	160
5.3 RESULTS AND ANALYSIS	161
5.3.1 <i>Erythrocyte phantom experiments</i>	161
5.3.2 <i>In vivo experiments</i>	165
5.3.3 <i>Potency of mTHPC vs. Photofrin: Influence of tissue optical properties</i>	171
5.4 DISCUSSION AND CONCLUSIONS.....	176
5.4.1 <i>Influence of improved oxygenation on PDT treatment fluence rate</i>	176
5.4.2 <i>Effects of hemoglobin absorption on photodynamic efficacy of mTHPC vs. Photofrin</i>	184
REFERENCES	188
CHAPTER 6: FLUORESCENT REPORTER PROTEINS AS BIOMOLECULAR MARKERS IN PDT.....	192
6.1 INTRODUCTION.....	192
6.2 EXPERIMENTAL METHODS	197

Table of contents	xiv
6.2.1 Chemicals.....	197
6.2.2 Establishing a transfected cell line	197
6.2.3 Cell monolayer imaging.....	198
6.2.4 Image analysis.....	201
6.2.5 In vivo treatment and microscopy of HSP70-GFP/EMT6 tumors	204
6.3 RESULTS AND ANALYSIS	205
6.3.1 Cell monolayer experiments.....	205
6.3.2 In vivo experiments	217
6.4 DISCUSSION.....	220
6.5 FUTURE DIRECTION	227
REFERENCES	231
APPENDIX I: SPHEROID CULTURE	234
APPENDIX II: PREPARATION OF SPHEROID FROZEN SECTIONS.....	236
APPENDIX III: A PROCEDURE FOR DETERMINING SENSITIZER CONCENTRATION IN SPHEROIDS	238

List of tables

4.1	Definitions and units of variables used in the kinetic analysis of simultaneous sensitizer triplet and $^1\text{O}_2$ -mediated bleaching	108
4.2	Numerical values assigned to variables describing the Photofrin photobleaching kinetics of the SSTB model	113
4.3	Photofrin concentrations corresponding to the high, intermediate and low regimes at which experimentally observed bleaching patterns are in agreement with the general predictions of the SSTB model	143
5.1	Average normalized fluence rate at 630 and 650 nm measured at three depths of 0, 0.5 and 1 cm inside an erythrocyte phantom for a range of hemoglobin-oxygen saturations from 1.0 to 0.1	172
5.2	$^1\text{O}_2$ doses for Photofrin and mTHPC calculated at three depths using irradiances which incorporated the effects of light attenuation based on 630 and 650 nm fluence rate measurements in erythrocyte phantoms consisting of fully-saturated hemoglobin <i>i.e.</i> $\text{SO}_2 = 1.0$	174
5.3	$^1\text{O}_2$ doses computed from simulated dose plots for Photofrin- and mTHPC-PDT performed at a depth of 1 cm in a tissue volume for a range of SO_2 from 1.0 to 0.1	177
6.1	The percentage of GFP-positive pixels with intensities greater than	

100 are evaluated from imaged fields exposed to the indicated treatment conditions	215
---	-----

List of figures

1.1	Energy level diagram for photosensitized formation of $^1\text{O}_2$ during PDT ..8	8
1.2	Similarities between an <i>in vivo</i> tumor and a multicell spheroid	13
2.1	Absorption spectra of mTHPC and Photofrin	33
2.2	Nonuniform distribution of mTHPC measured in frozen section of a spheroid	38
2.3	Nonuniform distribution of Photofrin measured in frozen section of a spheroid	40
2.4	Experimental setup for the microelectrode experiment	42
2.5	Initial transients of $^3\text{O}_2$ concentration changes measured in mTHPC- sensitized spheroid	44
2.6	Time-dependent $^3\text{O}_2$ concentration changes measured in mTHPC- sensitized spheroids are consistent with a $^1\text{O}_2$ -mediated bleaching process and not with a fluence-dependent simple exponential decay	46
2.7	Clonogenic cell survival measured from mTHPC-sensitized Colo26 spheroids subjected to PDT at three different irradiances	51
2.8	Radial distributions of net photochemical $^3\text{O}_2$ consumption in PDT treated mTHPC-sensitized spheroids	54
2.9	Estimation of $^1\text{O}_2$ threshold dose for mTHPC-PDT	56
2.10	Simulated $^1\text{O}_2$ dose plots for efficacy comparison between mTHPC-	

	and Photofrin-PDT	58
3.1	Experimentally measured fluorescence loss in PDT treated mTHPC-sensitized spheroids compared to mathematical predictions based on $^1\text{O}_2$ -mediated photobleaching mechanism	78
3.2	Confocal fluorescence microscope setup for imaging and spectroscopy on spheroid optical sections during PDT	82
3.3	Normalized fluorescence edge response of the confocal microscope for a 10X, 0.5 NA objective	83
3.4	Confocal fluorescence spectra and image obtained from an mTHPC- sensitized spheroid	87
3.5	Representative plots of initial and post-PDT radial mTHPC fluorescence distribution in a PDT-treated spheroid	89
3.6	Radially-resolved average mTHPC fluorescence distribution in spheroids post-PDT at irradiances of 25, 50 and 200 mW cm^{-2}	91
3.7	Mean mTHPC fluorescence amplitude as a function of fluence for 650 nm irradiation at 10, 50 and 200 mW cm^{-2}	92
4.1	<i>In vivo</i> measurements of Photofrin fluorescence loss and accumulation of photoproduct amplitude during PDT of normal rodent skin	104
4.2	Plot of Photofrin fluorescence counts as a function of incubation concentration	116
4.3	Confocal image of a Photofrin-sensitized spheroid with ROI	

	boxes superimposed on the interior and peripheral regions where fluorescence spectra are acquired.....	118
4.4	Basis spectra used for singular value decomposition fitting.....	121
4.5	Simulated plots of changes in ground state sensitizer and photoproduct concentrations predicted on the basis of mixed- mechanism bleaching for a Photofrin concentration of 34 μM	124
4.6	Simulated plots of changes in ground state sensitizer and photoproduct concentrations predicted on the basis of mixed- mechanism bleaching for a Photofrin concentration of 17 μM	127
4.7	Simulated plots of changes in ground state sensitizer and photoproduct concentrations predicted on the basis of mixed- mechanism bleaching for a Photofrin concentration of 170 μM	128
4.8	Representative series of fluorescence emission spectra obtained from the peripheral region of a spheroid sensitized with 30 $\mu\text{g mL}^{-1}$ Photofrin during irradiation with 514 nm	130
4.9	SVD analysis of typical pre- and post-irradiation fluorescence spectra obtained from spheroids.....	131
4.10	Mean normalized Photofrin and photoproduct amplitudes as a function of fluence obtained from interior and peripheral regions of spheroids sensitized with 30 $\mu\text{g mL}^{-1}$ Photofrin.....	133
4.11	Mean normalized Photofrin and photoproduct amplitudes as a	

	function of fluence obtained from interior and peripheral regions of spheroids sensitized with $10 \mu\text{g mL}^{-1}$ Photofrin.....	134
4.12	Mean normalized Photofrin and photoproduct amplitudes as a function of fluence obtained from interior and peripheral regions of spheroids sensitized with $2.5 \mu\text{g mL}^{-1}$ Photofrin	135
4.13	Time-dependent $^3\text{O}_2$ concentration changes measured in Photofrin-sensitized spheroids are consistent with a $^1\text{O}_2$ -mediated and a sensitizer triplet-mediated reaction process	138
5.1	Absorption spectra of oxy- and deoxyhemoglobin	152
5.2	630 and 650 nm fluence rate changes with depth in a well-oxygenated and completely deoxygenated homogeneous tissue-simulating liquid phantom.....	162
5.3	Hemoglobin-oxygen saturation and 650 nm fluence rate measured in a homogeneous erythrocyte-containing phantom as function of oxygen partial pressure.....	164
5.4	630 nm fluence rate changes measured in erythrocyte-containing tissue-simulating phantoms as a function of oxygen partial pressure and hemoglobin-oxygen saturation	166
5.5	650 nm fluence rate changes measured in erythrocyte-containing tissue-simulating phantoms as a function of oxygen partial pressure and hemoglobin-oxygen saturation	167

5.6	630 nm fluence rate changes recorded continuously at the base of a 1-cm-thick subcutaneous EMT6 tumor while the mouse was subjected to a variety of breathing conditions.....	169
5.7	Average changes in 630 and 650 nm fluence rate measured at the base of 1-cm-thick EMT6 tumors <i>in vivo</i> under different breathing conditions	170
5.8	Plot of the ratio of mTHPC vs. Photofrin efficacy at depths of 0, 0.5 and 1 cm, taking into account absorption effects of oxyhemoglobin.....	175
5.9	Ratio of PDT efficacy for mTHPC vs. Photofrin, assuming PDT treatment at a depth of 1 cm inside a tissue volume for a range of SO ₂ from 1.0 to 0.1	178
5.10	Ratio of normalized fluence rates at 650 vs. 630 nm measured in erythrocyte phantoms at a depth of 1 cm for a range of SO ₂ from 1.0 to 0.1	187
6.1	A model of heat shock factor regulation	194
6.2	Expression of heat shock proteins under different stress and non-stress conditions	196
6.3	GFP fluorescence images of a selected clone under control and heat-treated conditions	199
6.4	Absorption and emission spectra of EGFP	202
6.5	Bright field and GFP fluorescence images of HSP70-GFP/EMT6	

	cells incubated with various concentrations of mTHPC	206
6.6	Mean GFP fluorescence intensity and fraction of cells expressing GFP for a range of mTHPC incubation concentrations	208
6.7	Mean GFP fluorescence intensity and fraction of cells expressing GFP as a function PDT treatment fluence.....	210
6.8	Histograms of GFP fluorescence intensity in HSP70-GFP/EMT6 cells subjected to different drug incubation concentrations and PDT treatment fluences	211
6.9	Histograms of intracellular GFP intensity in cells treated with $0.5 \mu\text{g mL}^{-1}$ mTHPC and a fluence of 0.1 J cm^{-2}	213
6.10	Bright field and the corresponding GFP fluorescence images of HSP70-GFP/EMT6 cells assayed for viability with trypan blue	216
6.11	Cell viability as a function of mTHPC drug concentration and PDT fluence quantified from trypan blue assays.....	218
6.12	GFP fluorescence images of control and PDT-treated HSP70-GFP/EMT6 tumors grown subcutaneously in BALB/c mice and imaged through the skin <i>in vivo</i>	219
6.13	Confocal microscope setup for simultaneous two-color imaging of GFP and mTHPC fluorescence in spheroids.....	229

Chapter 1: Introduction and Overview

1.1 A Historical Perspective on Photodynamic therapy

Photodynamic therapy (PDT) is a relatively new and promising modality for the treatment of cancerous and other non-malignant conditions using a combination of visible or near-infrared light and a light-activated drug. The light-activated drug is often referred to as a photosensitizer. The light or the photosensitizers used in PDT induce little or no toxic effects by themselves. It is only the activation of the photosensitizer by light that results in the production of cytotoxic species which lead to the destruction of the targeted tissue.

The concept of cell death being induced by the interaction of light and chemicals has been recognized for over 100 years and was first reported in 1900

by Oscar Raab, a medical student of Professor Herman von Tappeiner in Munich. Oscar Raab observed that acridine orange was lethal to paramecia in the presence of light (1). Three years later, Von Tappeiner in collaboration with a dermatologist named Jesionek used this discovery to treat skin cancers with a combination of eosin and white light (2) and noted a beneficial effect with this therapy. He also went on to demonstrate the requirement of oxygen in photosensitization reactions and in 1907 introduced the term “photodynamic action” to describe the phenomenon.

Following this early work by Von Tappeiner and Jesionek little research on the clinical therapeutic applications of PDT was performed until nearly 60 years later. In 1960, researchers at the Mayo Clinic observed that injection of hematoporphyrin led to preferential fluorescence of neoplastic lesions. Following this discovery, new photosensitizers were developed which were designed to target cancerous tissue. Among these, a porphyrin derivative called “hematoporphyrin derivative” (HPD) was found to have superior localizing and photosensitizing properties compared to the parent hematoporphyrin or other porphyrins (3, 4). Systematic studies in tumor-bearing animals started only in the mid-1970’s following a landmark paper in 1972 in the *Lancet* by Diamond *et al.* (5), where the authors studied the effect of light activation of hematoporphyrin in an experimental rat glioma both *in vitro* and *in vivo*. In both cases they found significant treatment effects with 100% cell killing *in vitro* and

tumor necrosis and growth suppression *in vivo*. Based on these results the authors concluded that PDT offered a new approach to the treatment of brain tumors. Since then much pioneering research has been performed to develop PDT as an evolving clinical tool. Notable among these efforts are the first successful complete tumor cure in animals reported by Dougherty and co-workers at the Roswell Park Cancer Institute in 1975 using a combination of HPD and red light (6) and the work of Kelly, a urologist at St. Mary's Hospital in London, U.K., who demonstrated nearly 100% destruction of human bladder tumors implanted in mice with HPD-PDT (7). Since then several large scale clinical studies of PDT in humans were performed using different photosensitizers, including HPD, to treat skin, bladder, oral cavity, bronchial, esophageal, head and neck, brain and rectal cancer (8, 9).

Almost a century after Raab's original observations, great strides have been made in realizing the clinical potential of PDT. In 1993, Photofrin[®] (porfimer sodium), a refined and purified form of HPD, was approved for PDT of recurrent superficial papillary bladder cancer by the Canadian Health Agency. This was the first official approval of PDT in the world and a milestone in PDT history. The next major breakthrough was achieved when Photofrin[®] was accepted by the US Food and Drug Administration (FDA) in 1998 for treatment of esophageal and lung cancer. Photofrin is currently approved in several countries worldwide for the treatment of bronchial, esophageal, lung, cervical

and bladder cancer (www.scandipharm.com, 10, 11). In 2003, Photofrin received approval from FDA for the ablation of high-grade dysplasia in Barrett's esophagus, a condition that can lead to esophageal adenocarcinoma. This approval is of significant importance as it marks the first instance of PDT being considered as the primary treatment option for an early stage neoplastic condition.

Currently, several new photosensitizers are undergoing clinical trials. These sensitizers are designed to overcome the major limitations of HPD and Photofrin. Both HPD and its purified successor Photofrin causes prolonged skin photosensitivity, have weak absorption peaks at wavelengths which are short of the optimal transmission of tissue, and are composed of mixtures of different porphyrins. In contrast, the second-generation photosensitizers such as meso-tetra hydroxyphenyl chlorin (mTHPC, Foscan[®]), Lutetium Texaphyrin (Lutex, Lutrin[®]), benzoporphyrin derivative monoacid ring A (BPD-MA, Verteporfin[®]) and mono-N-aspartyl chlorin e6 (NPe6, Taloporfin[®]) are pure compounds that have absorption bands shifted to longer wavelengths where light penetrates tissue more easily. mTHPC is one of the most potent photosensitizers and is involved in clinical trials for treatment of skin, oral, mesothelioma and prostate cancers (12-15). In 2001, mTHPC received approval in the European Union for the treatment of advanced head and neck cancer (www.biolitecpharma.com). Lutex is currently being investigated in clinical trials for the treatment of prostate,

cervical and recurrent breast cancer (www.pharmacyclics.com). BPD-MA is currently in phase III clinical trials at 15 sites in the U.S. and Canada for the treatment of multiple basal cell carcinoma (www.qltinc.com). NPe6 is in clinical trials in Japan and the U.S. for the treatment of several types of solid tumors in the head and neck, rectum, prostate and lung (www.lightsciences.com).

Another PDT agent which has exhibited promise in treating a number of malignant and non-malignant conditions is δ -aminolevulinic acid (ALA). It is unique and different from the other sensitizers mentioned earlier in the sense that ALA itself is not a photosensitizer, but it causes endogenous photosensitization by inducing formation of the sensitizer protoporphyrin IX (PpIX) in cells using the heme biosynthetic pathway. Levulan[®], a topical formulation of ALA, was approved by the U.S.-FDA in 2000 for the treatment of the precancerous skin condition actinic keratoses. Clinical trials have demonstrated that ALA-PDT can successfully treat skin conditions such as psoriasis, acne and viral warts with little or no side effects (16). A second-generation of ALA-based drugs use esterified forms of ALA, which penetrate and sensitize target tissues more effectively. Metvix[®], a formulation of ALA methylester, is now approved in 16 European countries in addition to New Zealand and Australia for PDT of both actinic keratoses and basal cell carcinoma. Hexvix[®], a formulation of ALA hexylester, is currently undergoing clinical trials for both photodetection and photodynamic treatment of bladder cancers (www.photocure.com).

Furthermore, the property of some photosensitizers to localize in blood vessels selectively has been used to treat non-cancerous vascular diseases. Prominent among them is the worldwide approval in over 70 countries, including the U.S., for BPD-MA (Visudyne[®])-based PDT for the treatment of patients with predominantly classic neovascularization due to age-related macular degeneration (AMD), pathologic myopia and ocular histoplasmosis (www.novartis.com). AMD, a condition resulting from overproliferation of blood vessels behind the retina, is the leading cause of blindness in elderly people. Based on preclinical findings that Lutex is selective for atherosclerotic plaques and targets macrophages, which are inflammatory cells known to accumulate in these plaques, Lutex-PDT is now undergoing clinical trials for treatment of atherosclerosis and the prevention of restenosis following conventional angioplasty (17). Finally, PDT is going back to its origins in microbiology and is offering an alternative treatment for destroying microorganisms (16).

1.2 The photophysics of photodynamic therapy

The basis of PDT is the initiation of toxic photochemistry in the target tissue volume. This involves a combination of two steps, the first being the injection of a photosensitizer subsequently followed by light illumination of the sensitized

target tissue at a specific wavelength that is appropriate for absorption by the sensitizer. Although the exact biological mechanisms underlying PDT may vary with the nature of the sensitizer, its distribution in the tissue, the intracellular localization sites and other parameters, the primary photochemistry involved in PDT-induced damage is similar for all photosensitizers.

Singlet oxygen ($^1\text{O}_2$), an excited state of molecular oxygen, is considered to be the main cytotoxic species generated during PDT (18). The photochemical and photophysical processes that lead to $^1\text{O}_2$ formation are illustrated in the energy level diagram in Figure 1.1. The sensitizer molecule in its ground state is a spectroscopic singlet, denoted S_0 . The ground state molecule is excited to its singlet excited state, S_1 , upon absorption of a photon. PDT sensitizers are designed to have high intersystem crossing rates, and thus a large fraction of the singlet excited state molecules evolve to their triplet state, T_1 . Unlike most molecules, molecular oxygen has a ground state that is a spectroscopic triplet, denoted $^3\text{O}_2$, and a lowest-lying spectroscopic singlet excited state that is $^1\text{O}_2$. Direct excitation of oxygen from its triplet to the singlet is forbidden by molecular selection rules but is a possible outcome of collision between a ground state oxygen molecule and a triplet excited state sensitizer molecule due to an energy transfer reaction. This pathway, resulting in the formation of $^1\text{O}_2$, is referred to as the type-II mechanism. $^1\text{O}_2$ is a strong oxidizing agent and thus highly reactive, with a lifetime of less than 0.01 - 0.05 μs in a biological

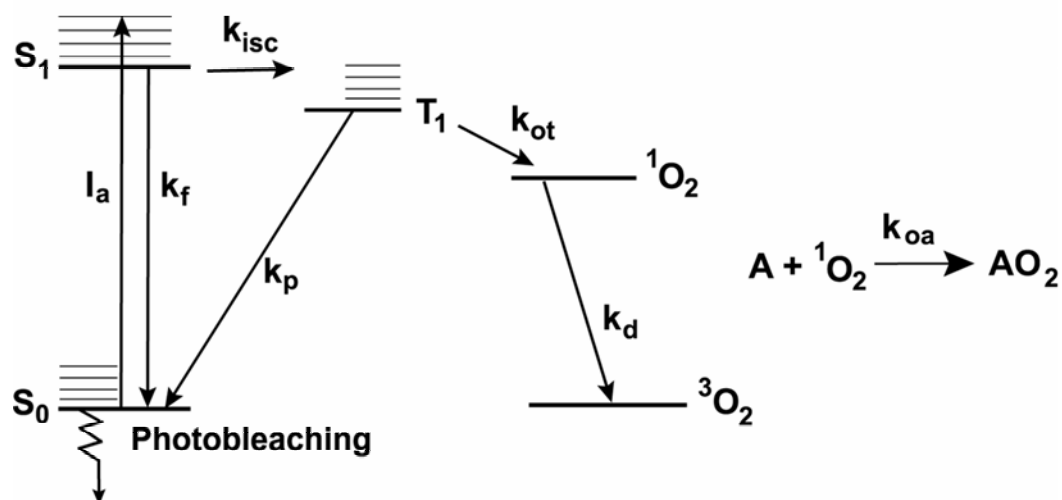


Figure 1.1. Jablonski diagram for type II photooxidation reactions resulting in the formation of singlet oxygen (1O_2). Upon absorption of light, a sensitizer molecule in its ground state, S_0 , is excited to its first excited state, S_1 . I_a refers to the rate of photon absorption in this process. The sensitizer in its S_1 state can either decay back to its ground state *via* radiative or non-radiative processes at a rate k_f , or it can undergo an intersystem crossing to an excited triplet state, T_1 , at a rate k_{isc} . The emission from the radiative decay from S_1 to S_0 is known as fluorescence. T_1 can also either decay to the ground state at a rate k_p or it can be quenched *via* a collision reaction with a ground state molecular oxygen molecule (3O_2). This quenching process proceeds with a bimolecular reaction rate constant k_{ot} and results in the formation of 1O_2 and S_0 . 1O_2 can either decay to ground state 3O_2 at a rate k_d or it can contribute to photodynamic damage by reacting with cellular substrates, denoted here as A , at a bimolecular reaction rate k_{oa} .

environment (19). The reactions of $^1\text{O}_2$ with cellular targets lead to damage of organelles such as the plasma membrane, mitochondria, lysosomes, golgi, endoplasmic reticulum, etc., resulting in cell death through apoptosis or necrosis. It is to be noted that hypoxic tumor regions are protected from direct cell death during PDT, as $^1\text{O}_2$ formation is limited by $^3\text{O}_2$ availability.

1.3 Photochemical $^3\text{O}_2$ consumption and sensitizer photobleaching during PDT

Singlet oxygen reactions are generally irreversible, and because of this PDT is capable of inducing a transient type of hypoxia due to photodynamic $^3\text{O}_2$ consumption (20-23). The photochemical $^3\text{O}_2$ consumption rate is a direct function of the treatment irradiance (power per unit area). This process can severely diminish the diffusion-limited $^3\text{O}_2$ availability in tumor regions remote from capillaries when high irradiances are used. Therefore, we expect larger tumor fractions to be protected from cytotoxic effects of $^1\text{O}_2$, and consequently diminished tumor cure rates, at relatively higher vs. lower irradiances. Several studies using PDT protocols involving low irradiances and/or fractionated irradiations have shown improved tumor response using different sensitizers, including Photofrin, mTHPC and ALA-induced PpIX (24-29). Further, investigators have shown direct evidence that lower irradiances maintain higher

tumor oxygenation levels during PDT with Photofrin and mTHPC (23, 28). Because photodynamic $^3\text{O}_2$ consumption originates in $^1\text{O}_2$ reaction with biological targets, the net photochemical $^3\text{O}_2$ consumed during the irradiation period constitutes the photodynamic dose delivered during treatment.

In addition to causing PDT damage by reacting with cellular substrates, $^1\text{O}_2$ can also react with sensitizer molecules that are responsible for its formation. This causes irreversible sensitizer photobleaching and/or fluorescent photoproduct formation. Irreversible photobleaching reduces the concentration of sensitizer molecules and the rate of $^1\text{O}_2$ generation. Most PDT photosensitizers are fluorescent, therefore PDT-mediated sensitizer bleaching can be monitored *via* measurement of the loss of sensitizer fluorescence. Sensitizer bleaching plays an important role in modifying the effects of PDT-induced $^3\text{O}_2$ consumption, as irreversible destruction of sensitizer molecules decreases the rate of photon absorption and acts to diminish the severity of $^3\text{O}_2$ depletion. However, the relationship is potentially far richer. To the extent that the photochemical reactions responsible for bleaching and for deposition of photodynamic dose are related to each other in a definable way, the cytotoxic reactions may be monitored through noninvasive measurements of the sensitizer bleaching during therapy, using, for example, fluorescence or absorption spectroscopy. Indeed, the notion that the use of fluorescence measurements of photosensitizer bleaching could be used as a quantitative dosimeter has led to the

description of “implicit” PDT dosimetry (30). A mathematical dosimetry model proposed by Georgakoudi *et al.* (31) related the deposition of PDT dose to the sensitizer photodegradation, provided the photobleaching is mediated predominantly by $^1\text{O}_2$. The model has an $^3\text{O}_2$ dependence and predicts that increased sensitizer bleaching corresponds to increased PDT dose. Since then, investigators have measured photosensitizer bleaching during PDT and attempted to correlate it with treatment response (29, 32). These reports indicate that bleaching of the sensitizer proceeds more rapidly at reduced treatment irradiance and also generates enhanced biological response. However, it is to be noted that the relationship between sensitizer bleaching and PDT dose deposition expressed in this particular dosimetry model assumes that the photobleaching process is mediated predominantly by $^1\text{O}_2$ -reactions. The bleaching mechanism is sensitizer-specific, and therefore it is important to investigate the process through which a sensitizer photodegrades before it can be incorporated into any dosimetry model.

Previous work performed in our laboratory has extensively studied the importance of photochemical $^3\text{O}_2$ depletion in limiting the effectiveness of PDT performed at high treatment irradiances. As it is extremely difficult to quantitatively evaluate *in vivo* $^3\text{O}_2$ tensions, a simpler system of multicell tumor spheroids has been used for measuring $^3\text{O}_2$ concentration changes during PDT. Spheroids are avascular spherical cellular aggregates. As illustrated in

Figure 1.2, they have gradients in nutrients and oxygen as well as heterogeneity in cell populations similar to those encountered in the intercapillary regions of a tumor. Spheroids thus provide an excellent solid tumor model. Spheroids also provide easy accessibility to oxygen-sensitive probes and, due to their spherical geometry, they are useful for one-dimensional mathematical modeling to study certain aspects of $^3\text{O}_2$ diffusion and consumption during PDT. Based on $^3\text{O}_2$ measurements in spheroids and using a model of $^3\text{O}_2$ diffusion that incorporates the effects of sensitizer photobleaching, our laboratory has reported findings that the rate of photodynamic $^3\text{O}_2$ consumption in Photofrin- and ALA-sensitized spheroids decreases during irradiation in a manner that is consistent with a $^1\text{O}_2$ -mediated bleaching process (31, 33).

As mentioned earlier, the photosensitizer mTHPC is one of the most potent and efficient PDT drugs available. A clinical study performed in patients with diffuse malignant mesothelioma reported a 10-mm-deep tumor necrosis with a dose of 0.3 mg kg^{-1} mTHPC activated with 10 J cm^{-2} fluence (34). Similar successful tumor responses obtained in animal and human clinical studies have been reported by several investigators (34-38) using low fluences of $10 - 20 \text{ J cm}^{-2}$ and even lower mTHPC doses of $0.1 - 0.15 \text{ mg kg}^{-1}$. Comparable treatment responses with Photofrin-PDT require at least 2 mg kg^{-1} drug and 100 J cm^{-2} fluence (35, 36). However, in spite of these remarkable clinical

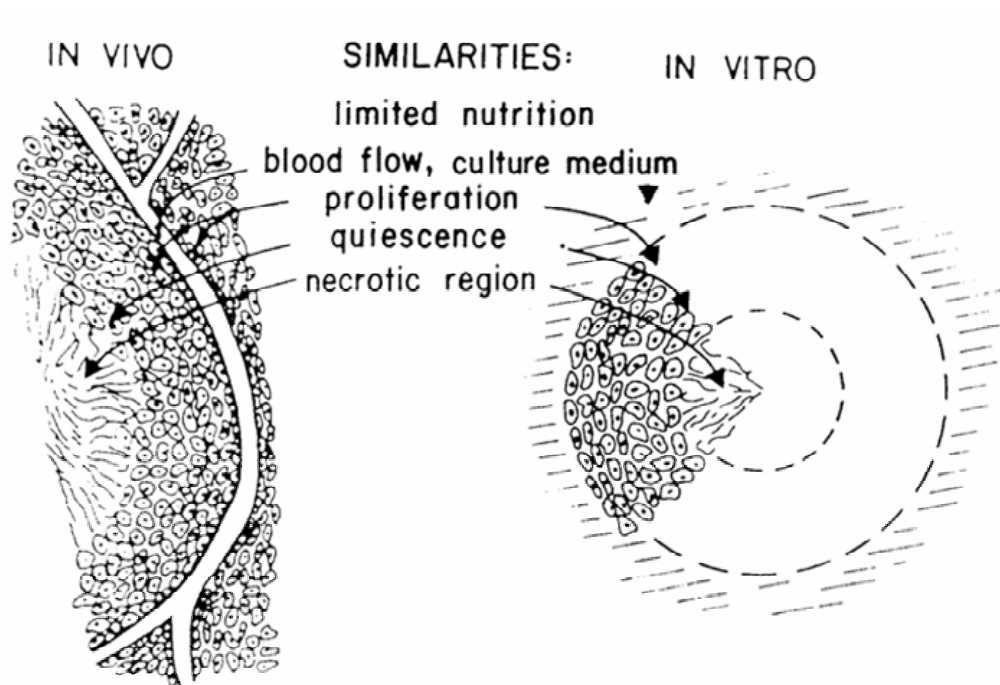


Figure 1.2. The similarities in cell population distributions and gradients in nutrients and oxygen between an *in vivo* tumor (left) and a spheroid (right) model *in vitro* are illustrated. The images are reproduced from Sutherland, R.M (*Cancer* **58**:1668-80, 1986).

observations with mTHPC, much still remains to be understood about this sensitizer, particularly the reason(s) behind its enhanced efficacy and its photobleaching mechanism.

An investigation into mTHPC's bleaching mechanism based on $^3\text{O}_2$ measurements performed at the edge of 500 μm diameter mTHPC-sensitized EMT6 spheroids during irradiation is presented in chapter 2. The $^3\text{O}_2$ concentration changes are analyzed using a model of oxygen diffusion with consumption that incorporates the effects of sensitizer photobleaching. We consider initially a $^1\text{O}_2$ -mediated sensitizer bleaching process and one that can be described in terms of fluence-dependent simple exponential decay kinetics. The basic equations of the oxygen diffusion with consumption model and the photobleaching expressions presented in this chapter were developed by Nichols and Foster (39) and Georgakoudi *et al.* (31). For analysis of the data from mTHPC-sensitized spheroids we account for the extremely nonuniform spatial drug distribution, as characterized by fluorescence measurements performed with 15- μm -thick frozen spheroid sections. We find that the $^3\text{O}_2$ concentration changes resulting from mTHPC photodegradation are consistent with the $^1\text{O}_2$ -mediated bleaching model.

The analysis allows us to generate PDT dose depositions for a range of treatment regimes, correlate them with clonogenic cell survival data obtained from mTHPC-PDT-treated spheroids, and extract estimates of the $^1\text{O}_2$ -threshold

dose, which is the minimum $^1\text{O}_2$ concentration required to kill cells. The cell survival data was obtained by our collaborators in Nancy, France and is already published (40). The clonogenic survival exhibited significant inverse irradiance dependence, with greater cell kill in response to low irradiance PDT, consistent with a sensitizer whose primary mechanism is oxygen-dependent.

In chapter 2 we also perform a re-analysis of previously reported $^3\text{O}_2$ concentration measurements at the edge of Photofrin-sensitized EMT6 spheroids during PDT (31). The reason for doing so was based on our recent finding that the spatial distribution of Photofrin in spheroids is not uniform, as was previously assumed. The re-analysis demonstrated that Photofrin bleaches *via* $^1\text{O}_2$ -reactions, a result consistent with the earlier findings (31).

Another important aim of the study reported in chapter 2 was to investigate the mechanisms responsible for the improved photodynamic efficacy of mTHPC compared to other photosensitizers, such as Photofrin. Using values of parameters extracted from the electrode measurement analysis, we compute the $^1\text{O}_2$ dose depositions for mTHPC- and Photofrin-PDT. Based on the analysis we conclude that the increased potency of mTHPC is a result of a combination of its ability to tightly sequester in cells (41) and its higher extinction coefficient at a red-shifted wavelength. mTHPC's long-wavelength absorption maximum at 650 nm has an extinction coefficient which is significantly higher than that of Photofrin's absorption maximum at 630 nm, and this property of mTHPC not

only causes more photochemical $^3\text{O}_2$ consumption, which defines $^1\text{O}_2$ dose, but also allows for improved penetration of PDT treatment beams into tissue due to reduced light attenuation at 650 vs. 630 nm.

1.4 Fluorescence and confocal fluorescence microscopy as tools for direct investigation of sensitizer photobleaching mechanism

The $^3\text{O}_2$ measurements performed on mTHPC-sensitized spheroids during PDT, reported in chapter 2, allow for only an indirect evaluation of sensitizer photobleaching. The next logical step was to study these processes directly. Towards the goal of establishing sensitizer fluorescence as a means for monitoring PDT dosimetry, it is of the highest importance to determine whether or not the volume-averaged and the spatially-resolved decays of sensitizer fluorescence in PDT-treated spheroids follow the predictions resulting from the analysis of electrode recordings. In chapter 3, we report published results from a collaborative investigation with a group in Nancy, France, in which we examined the irradiance-dependent photobleaching of mTHPC measured in cell suspensions from dissociated PDT-treated spheroids (40). As anticipated from a sensitizer whose primary bleaching mechanism is oxygen-dependent, the volume-averaged loss of mTHPC fluorescence in the spheroids showed an

inverse irradiance dependence, a trend qualitatively similar to that of the clonogenic survival reported in chapter 2. This suggests that mTHPC photobleaching and photodynamic damage during PDT share a similar oxygen dependence. The volume-averaged photobleaching results were consistent with predictions from a mathematical model which incorporated photophysical parameters obtained from the electrode data analysis reported in chapter 2, indicating that mTHPC photobleaching kinetics are consistent with self-sensitized $^1\text{O}_2$ -reactions.

A more powerful direct means of studying sensitizer photobleaching mechanisms is by performing confocal optical sectioning of intact spheroids. The main advantage of this method is that it allows monitoring of spatially-resolved sensitizer fluorescence in intact spheroids, with their gradients in initial sensitizer distribution and in oxygen. Optical sectioning enables the observation of different rates of photobleaching in different radial locations of the spheroid in response to PDT irradiation. Various candidate sensitizer photobleaching mechanisms give rise to specific predictions about how the sensitizer fluorescence should change as a function of radial position in the spheroid optical section during PDT (31, 33). We present results which show that during mTHPC-PDT the drug preferentially bleaches in the outermost regions of the spheroid where oxygen is most available, consistent with predictions of a $^1\text{O}_2$ -mediated sensitizer photobleaching mechanism.

In chapter 4, we present a study of the bleaching mechanism of Photofrin using our approach of confocal optical sectioning in spheroids. We attempt to reconcile the observations from *in vivo* Photofrin bleaching measurements and the predictions of a previously developed mathematical model. In a study performed with J.C. Finlay we examined the changes in Photofrin fluorescence during PDT of normal rodent skin *in vivo* (42). The results demonstrated an interesting pattern. Over a wide range of clinically-relevant incident irradiances, the bleaching of Photofrin was independent of irradiance. However, an irradiance dependence in the formation of a fluorescent photoproduct was observed, with enhanced photoproduct accumulation at lower irradiance. The bleaching result was not anticipated given previous results from our group (31) and those presented in chapter 2, which indicated that Photofrin bleaching is mediated predominantly by $^1\text{O}_2$ -reactions. Further, the *in vivo* observations appeared inconsistent with published reports showing that tumor response to Photofrin PDT *in vivo* is enhanced significantly at lower irradiance (25, 26). To interpret and reconcile these observations, Finlay developed a more sophisticated mathematical model of photosensitizer bleaching and photoproduct accumulation in which reactions between $^1\text{O}_2$ and the sensitizer as well as between triplet sensitizer molecules and biological targets are both allowed to contribute to bleaching.

The predictions of this model were then tested in experiments performed on EMT6 spheroids which were sensitized with a wide range of low to high Photofrin concentrations and subjected to PDT. The spatially-resolved Photofrin and photoproduct fluorescence in these PDT-treated spheroid optical sections were acquired using a confocal fluorescence spectroscopy setup (43, 44) and quantified using spectral analysis techniques developed previously in our laboratory (45, 46). Photofrin photodegradation and photoproduct formation were found to be in qualitative agreement with predictions of this new theoretical model, confirming that Photofrin bleaching kinetics involves two simultaneous bleaching mechanisms and reconciling the *in vivo* observations with the results of the electrode analysis.

1.5 Tissue oxygenation: an important key in improving therapeutic efficacy of PDT

The absorption spectrum of hemoglobin, the principal tissue chromophore at PDT treatment wavelengths, is strongly oxygen dependent. The oxygen dependence is such that a shift toward increased hemoglobin oxygen saturation is expected to reduce attenuation of the treatment beam and thus allow effective treatment of deeper lying tissues. In chapter 5, we present results from a study in which we evaluated the influence of oxygenation on the penetration of red light

in tissue, with particular emphasis on 630 and 650 nm, wavelengths that are used clinically with Photofrin- and mTHPC-PDT, respectively (47). Direct measurements were performed in tissue-simulating phantoms comprised of intact human erythrocytes suspended in a scattering emulsion and in murine tumor models *in vivo*. We found that the fluence rate measured in the phantoms at depths from 0.5 - 2 cm from the irradiated surface was significantly enhanced in a well-oxygenated *vs.* fully deoxygenated sample at both wavelengths. This observation was qualitatively consistent with the *in vivo* results, where we found that improved oxygenation, induced by carbogen inhalation administered to tumor-bearing mice, resulted in a 40 - 50% average increase in optical fluence rate measured through a 1-cm-thick tumor. These results indicate that improved tumor oxygenation is important in PDT not only for the maintenance of the oxygen-dependent photochemistry but, through the effects reported in this chapter, may also enable more efficient treatment of thicker lesions. These findings may have immediate clinical relevance to the design of better treatment protocols for tumor eradication using PDT. The results of this chapter have been accepted for publication in *Physics in Medicine and Biology* (47), and co-authorship with Thomas H. Foster is gratefully acknowledged.

1.6 Fluorescent molecular markers of PDT-induced damage

Among the cellular responses to oxidative stress generated by photodynamic therapy (PDT) is the activation of signaling pathways, including the induction of heat shock proteins (HSPs) (48-50). HSPs, commonly referred to as stress proteins, are inducible in response to variety of stressful conditions and play a major role in protecting cells by binding to denatured proteins and assisting in proper refolding (51). In chapter 6 we present a published study in which we examined mTHPC-PDT-mediated hsp70 activation in an EMT6 cell line stably transfected with a plasmid containing the gene for Green Fluorescent Protein (GFP) driven by an hsp70 promoter (52). The goal of the study was to investigate the range of mTHPC-PDT treatment conditions that would act as a molecular switch to activate a widely applicable fluorescent reporter gene. We observed that hsp70-driven GFP expression is induced at a cellular level by not only mTHPC-PDT but also by mTHPC incubation alone. For initial evaluation of hsp70 activation *in vivo*, transfected EMT6 cells were grown as tumors in mice. Increased GFP fluorescence levels were obtained in a tumor subjected to mTHPC-PDT. These cellular and *in vivo* findings demonstrated that sublethal doses of mTHPC-PDT stimulate GFP expression under the control of an hsp70 promoter and illustrated the potential of noninvasively monitoring reporter

protein fluorescence as a measure of molecular response to PDT. The results of this chapter have been published in *Photochemistry and Photobiology* (52), and co-authorship with Evan M. Goren, John G. Frelinger and Thomas H. Foster is gratefully acknowledged.

REFERENCES

1. Raab, O. (1900) Uber die wirkung fluoreszierender stoffe auf infusorien. *Z. Biol.* **39**: 524-546.
2. Von Tappeiner, H. and A. Jesionek (1903) Therapeutische versuche mit fluoreszeirenden stoffen. *Muench. Med. Wochenschr.* **47**: 2042-2044.
3. Lipson, R. L. and E. J. Baldes (1960) The photodynamic properties of a particular hematoporphyrin derivative. *Arch. Dermatol.* **82**: 508-516.
4. Lipson, R. L., E. J. Baldes, and A. M. Olsen (1961) The use of a derivative of hematoporphyrin in tumor detection. *J. Natl. Cancer Inst.* **26**: 1-11.
5. Diamond, I., S. G. Granelli, A. F. McDonagh, S. Nielsen, C. B. Wilson, and R. Jaenicke (1972) Photodynamic therapy of malignant tumours. *Lancet* **2**: 1175-1177.
6. Dougherty, T. J., G. B. Grindey, R. Fiel, K. R. Weishaupt, and D. G. Boyle (1975) Photoradiation therapy. II. Cure of animal tumors with hematoporphyrin and light. *J. Natl. Cancer Inst.* **55**: 115-121.
7. Kelly, J. F., M. E. Snell, and M. C. Berenbaum (1975) Photodynamic destruction of human bladder carcinoma. *Br. J. Cancer* **31**: 237-244.
8. Dougherty, T. J., C. J. Gomer, B. W. Henderson, G. Jori, D. Kessel, M. Korbelik, J. Moan, and Q. Peng (1998) Photodynamic therapy. *J. Natl. Cancer Inst.* **90**: 889-905.
9. Ackroyd, R., C. Kelty, N. Brown, and M. Reed (2001) The history of photodetection and photodynamic therapy. *Photochem. Photobiol.* **74**: 656-669.
10. Dolmans, D. E., D. Fukumura, and R. K. Jain (2003) Photodynamic therapy for cancer. *Nat. Rev. Cancer* **3**: 380-387.
11. Moan, J. and Q. Peng (2003) An outline of the hundred-year history of PDT. *Anticancer Res.* **23**: 3591-3600.

12. Baas, P., A. E. Saarnak, H. Oppelaar, H. Neering, and F. A. Stewart (2001) Photodynamic therapy with meta-tetrahydroxyphenylchlorin for basal cell carcinoma: a phase I/II study. *Br. J. Dermatol.* **145**: 75-78.
13. Kubler, A. C., J. de Carpentier, C. Hopper, A. G. Leonard, and G. Putnam (2001) Treatment of squamous cell carcinoma of the lip using Foscan-mediated photodynamic therapy. *Int. J. Oral Maxillofac. Surg.* **30**: 504-509
14. Friedberg, J. S., R. Mick, J. Stevenson, J. Metz, T. Zhu, J. Buyske, D. H. Serman, H. I. Pass, E. Glatstein, and S. M. Hahn (2003) A phase I study of Foscan-mediated photodynamic therapy and surgery in patients with mesothelioma. *Ann. Thorac. Surg.* **75**: 952-959.
15. Nathan, T. R., D. E. Whitelaw, S. C. Chang, W. R. Lees, P. M. Ripley, H. Payne, L. Jones, M. C. Parkinson, M. Emberton, A. R. Gillams, A. R. Mundy, and S. G. Bown (2002) Photodynamic therapy for prostate cancer recurrence after radiotherapy: a phase I study. *J. Urol.* **168**: 1427-1432.
16. Salva, K. A. (2002) Photodynamic therapy: unapproved uses, dosages, or indications. *Clin. Dermatol.* **20**: 571-581.
17. Krammer, B. (2001) Vascular effects of photodynamic therapy. *Anticancer Res.* **21**: 4271-4277.
18. Weishaupt, K. R., C. J. Gomer, and T. J. Dougherty (1976) Identification of singlet oxygen as the cytotoxic agent in photoinactivation of a murine tumor. *Cancer Res.* **36**: 2326-2329.
19. Moan, J. and K. Berg (1991) The photodegradation of porphyrins in cells can be used to estimate the lifetime of singlet oxygen. *Photochem. Photobiol.* **53**: 549-553.
20. Foster, T. H., R. S. Murant, R. G. Bryant, R. S. Knox, S. L. Gibson, and R. Hilf (1991) Oxygen consumption and diffusion effects in photodynamic therapy. *Radiat. Res.* **126**: 296-303.
21. Tromberg, B. J., A. Orenstein, S. Kimel, S. J. Barker, J. Hyatt, J. S. Nelson, and M. W. Berns (1990) In vivo tumor oxygen tension measurements for

- the evaluation of the efficiency of photodynamic therapy. *Photochem. Photobiol.* **52**: 375-385.
22. Sitnik, T. M., J. A. Hampton, and B. W. Henderson (1998) Reduction of tumour oxygenation during and after photodynamic therapy in vivo: effects of fluence rate. *Br. J. Cancer* **77**: 1386-1394.
 23. Henderson, B. W., T. M. Busch, L. A. Vaughan, N. P. Frawley, D. Babich, T. A. Sosa, J. D. Zollo, A. S. Dee, M. T. Cooper, D. A. Bellnier, W. R. Greco, and A. R. Oseroff (2000) Photofrin photodynamic therapy can significantly deplete or preserve oxygenation in human basal cell carcinomas during treatment, depending on fluence rate. *Cancer Res.* **60**: 525-529.
 24. Feins, R. H., R. Hilf, H. Ross, and S. L. Gibson (1990) Photodynamic therapy for human malignant mesothelioma in the nude mouse. *J. Surg. Res.* **49**: 311-314.
 25. Gibson, S. L., K. R. VanDerMeid, R. S. Murant, R. F. Raubertas, and R. Hilf (1990) Effects of various photoradiation regimens on the antitumor efficacy of photodynamic therapy for R3230AC mammary carcinomas. *Cancer Res.* **50**: 7236-7241.
 26. Sitnik, T. M. and B. W. Henderson (1998) The effect of fluence rate on tumor and normal tissue responses to photodynamic therapy. *Photochem. Photobiol.* **67**: 462-466.
 27. van Geel, I. P., H. Oppelaar, J. P. Marijnissen, and F. A. Stewart (1996) Influence of fractionation and fluence rate in photodynamic therapy with Photofrin or mTHPC. *Radiat. Res.* **145**: 602-609.
 28. Coutier, S., L. N. Bezdetnaya, T. H. Foster, R. M. Parache, and F. Guillemin (2002) Effect of irradiation fluence rate on the efficacy of photodynamic therapy and tumor oxygenation in meta-tetra (hydroxyphenyl) chlorin (mTHPC)-sensitized HT29 xenografts in nude mice. *Radiat. Res.* **158**: 339-345.

29. Robinson, D. J., H. S. de Bruijn, d. van, V, M. R. Stringer, S. B. Brown, and W. M. Star (1999) Protoporphyrin IX fluorescence photobleaching during ALA-mediated photodynamic therapy of UVB-induced tumors in hairless mouse skin. *Photochem. Photobiol.* **69**: 61-70.
30. Wilson, B. C., M. S. Patterson, and L. Lilge (1997) Implicit and explicit dosimetry in photodynamic therapy: a new paradigm. *Lasers Med. Sci.* **12**: 182-199.
31. Georgakoudi, I., M. G. Nichols, and T. H. Foster (1997) The mechanism of Photofrin photobleaching and its consequences for photodynamic dosimetry. *Photochem. Photobiol.* **65**: 135-144.
32. Robinson, D. J., H. S. de Bruijn, d. van, V, M. R. Stringer, S. B. Brown, and W. M. Star (1998) Fluorescence photobleaching of ALA-induced protoporphyrin IX during photodynamic therapy of normal hairless mouse skin: the effect of light dose and irradiance and the resulting biological effect. *Photochem. Photobiol.* **67**: 140-149.
33. Georgakoudi, I. and T. H. Foster (1998) Singlet oxygen- versus nonsinglet oxygen-mediated mechanisms of sensitizer photobleaching and their effects on photodynamic dosimetry. *Photochem. Photobiol.* **67**: 612-625.
34. Ris, H. B., H. J. Altermatt, R. Inderbitzi, R. Hess, B. Nachbur, J. C. Stewart, Q. Wang, C. K. Lim, R. Bonnett, M. C. Berenbaum, and . (1991) Photodynamic therapy with chlorins for diffuse malignant mesothelioma: initial clinical results. *Br. J. Cancer* **64**: 1116-1120.
35. van Geel, I. P., H. Oppelaar, Y. G. Oussoren, M. A. van der Valk, and F. A. Stewart (1995) Photosensitizing efficacy of MTHPC-PDT compared to photofrin-PDT in the RIF1 mouse tumour and normal skin. *Int. J. Cancer* **60**: 388-394.
36. Milkvy, P., H. Messmann, J. Regula, M. Conio, M. Pauer, C. E. Millson, A. J. MacRobert, and S. G. Bown (1998) Photodynamic therapy for gastrointestinal tumors using three photosensitizers--ALA induced PPIX, Photofrin and MTHPC. A pilot study. *Neoplasma* **45**: 157-161.

37. Savary, J. F., P. Grosjean, P. Monnier, C. Fontolliet, G. Wagnieres, D. Braichotte, and B. H. van den (1998) Photodynamic therapy of early squamous cell carcinomas of the esophagus: a review of 31 cases. *Endoscopy* **30**: 258-265.
38. Copper, M. P., I. B. Tan, H. Oppelaar, M. C. Ruevekamp, and F. A. Stewart (2003) Meta-tetra(hydroxyphenyl)chlorin photodynamic therapy in early-stage squamous cell carcinoma of the head and neck. *Arch. Otolaryngol. Head Neck Surg.* **129**: 709-711.
39. Nichols, M. G. and T. H. Foster (1994) Oxygen diffusion and reaction-kinetics in the photodynamic therapy of multicell tumor spheroids. *Phys. Med. Biol.* **39**: 2161-2181.
40. Coutier, S., S. Mitra, L. N. Bezdetsnaya, R. M. Parache, I. Georgakoudi, T. H. Foster, and F. Guillemin (2001) Effects of fluence rate on cell survival and photobleaching in meta-tetra-(hydroxyphenyl)chlorin-photosensitized Colo 26 multicell tumor spheroids. *Photochem. Photobiol.* **73**: 297-303.
41. Ball, D. J., D. I. Vernon, and S. B. Brown (1999) The high photoactivity of m-THPC in photodynamic therapy. Unusually strong retention of m-THPC by RIF-1 cells in culture. *Photochem. Photobiol.* **69**: 360-363.
42. Finlay, J. C. (2003) *Reflectance and fluorescence spectroscopies in photodynamic therapy*. Ph.D. Thesis. University of Rochester, Rochester, NY.
43. Bigelow, C. E., C. J. Harkrider, D. L. Conover, T. H. Foster, I. Georgakoudi, S. Mitra, M. G. Nichols, and M. Rajadhyaksha (2001) Retrofitted confocal laser scanner for a commercial inverted fluorescence microscope. *Rev. Sci. Inst.* **72**: 3407-3410.
44. Bigelow, C. E., D. L. Conover, and T. H. Foster (2003) Confocal fluorescence spectroscopy and anisotropy imaging system. *Opt. Lett.* **28**: 695-697.

45. Finlay, J. C., D. L. Conover, E. L. Hull, and T. H. Foster (2001) Porphyrin bleaching and PDT-induced spectral changes are irradiance dependent in ALA-sensitized normal rat skin in vivo. *Photochem. Photobiol.* **73**: 54-63.
46. Finlay, J. C., S. Mitra, and T. H. Foster (2002) In vivo mTHPC photobleaching in normal rat skin exhibits unique irradiance-dependent features. *Photochem. Photobiol.* **75**: 282-288.
47. Mitra, S. and T. H. Foster (2004) Carbogen breathing significantly enhances the penetration of red light in murine tumors in vivo. *Phys. Med. Biol.* In press.
48. Gomer, C. J., M. Luna, A. Ferrario, S. Wong, A. M. Fisher, and N. Rucker (1996) Cellular targets and molecular responses associated with photodynamic therapy. *J. Clin. Laser Med. Surg.* **14**: 315-321.
49. Oleinick, N. L. and H. H. Evans (1998) The photobiology of photodynamic therapy: cellular targets and mechanisms. *Radiat. Res.* **150**: S146-S156.
50. Moor, A. C. (2000) Signaling pathways in cell death and survival after photodynamic therapy. *J. Photochem. Photobiol. B* **57**: 1-13.
51. Morimoto, R. I. (1993) Cells in stress: transcriptional activation of heat shock genes. *Science* **259**: 1409-1410.
52. Mitra, S., E. M. Goren, J. G. Frelinger, and T. H. Foster (2003) Activation of heat shock protein 70 promoter with meso-tetrahydroxyphenyl chlorin photodynamic therapy reported by green fluorescent protein in vitro and in vivo. *Photochem. Photobiol.* **78**: 615-622.

Chapter 2: An investigation into the photodynamic efficacy of meso-tetra hydroxyphenyl chlorin (mTHPC)

2.1 Introduction

As mentioned in Chapter 1, mTHPC is turning out to be an extremely promising second-generation photosensitizer for PDT, and several investigators have reported it to be most potent of all the photosensitizers presently being studied (1-6). On the basis of clinical PDT results, mTHPC is estimated to be 100 – 200 times more potent than Photofrin (7). The important factors that govern the efficacy of a particular sensitizer are its intracellular localization sites, photophysical properties, photobleaching characteristics, $^1\text{O}_2$ threshold dose,

retention or binding in cells, and its extinction coefficient at the PDT treatment wavelength. While Hopkinson *et al.* (8) have suggested that mTHPC is taken up by tissues from the plasma in an aggregated form bound to an unidentified protein fraction and this unusual uptake may be a factor in explaining its photodynamic activity, other studies have suggested that the subcellular localization of mTHPC could be responsible for its higher efficacy (9-11). Among the photophysical characteristics of PDT sensitizers that contribute to their efficiency are their triplet and $^1\text{O}_2$ yields. The triplet and $^1\text{O}_2$ yields for Photofrin are 0.8 and 0.2-0.3, respectively (12). These values are not remarkably different than those of mTHPC, which has triplet and $^1\text{O}_2$ yields of 0.89 and 0.3-0.43, respectively (12, 13). Thus, despite these recent findings about mTHPC's photophysical properties, intracellular localization, and tissue uptake and retention, we still do not have a clear understanding of the mechanism(s) that contribute to the enhanced phototoxicity of this photosensitizer.

The focus of this chapter is to investigate in detail the factors influencing the potency of mTHPC *vs.* that of Photofrin, with emphasis on the aspects contributing to PDT dose deposition with the two sensitizers. Such a complete analysis requires knowledge of the mechanism by which a sensitizer photobleaches, as it informs the photodynamic dose estimates. Sensitizer photodegradation results in the irreversible reduction of the rate of photon absorption and hence reduces the depletion of $^3\text{O}_2$ during PDT. Therefore, it is

possible to study the sensitizer photobleaching process indirectly through its effect on the rate of $^3\text{O}_2$ consumption. Previous work in our laboratory has extensively analyzed the time-dependent $^3\text{O}_2$ consumption and diffusion in spheroids incorporating the effects of drug photobleaching (14-16). Using similar measurements and data analysis, we investigate the bleaching characteristics of mTHPC using a model that incorporates the effects of either $^1\text{O}_2$ -mediated bleaching or a description of photobleaching based on simple exponential decay kinetics (15). The analysis also takes into account the extremely nonuniform spatial distribution of mTHPC in the spheroids. An important parameter that is obtained from the analysis and that emerges in the $^1\text{O}_2$ mechanism is the ratio, $k_{\text{os}}/k_{\text{oa}}[A]$, where k_{os} and k_{oa} are the biomolecular rates for $^1\text{O}_2$ reaction with the sensitizer molecules and cellular substrates, A, respectively. With the knowledge of $k_{\text{os}}/k_{\text{oa}}[A]$, it is possible to establish a quantitative link between photodynamic $^3\text{O}_2$ consumption and the photodegradation of the sensitizer (15). Because the photochemical $^3\text{O}_2$ consumption during PDT originates in $^1\text{O}_2$ reaction with biological targets, this coefficient allows the effects of sensitizer bleaching to be incorporated in PDT dose estimates. Our measurements found mTHPC's bleaching mechanism to be consistent predominantly with a $^1\text{O}_2$ -reaction process. Using a theoretical model informed by photophysical properties extracted from microelectrode measurements, a quantitative interpretation of results of clonogenic survival

experiments in mTHPC-sensitized Colo26 spheroids was performed. These calculations allowed us to extract a $^1\text{O}_2$ threshold dose for mTHPC-PDT.

Clinical PDT irradiation is generally performed at a sensitizer's longest-wavelength absorption band to achieve the greatest tissue penetration. In this respect, mTHPC's absorption features are more favorable than those of Photofrin, because its molar extinction at 650 nm is much greater than that of Photofrin at 630 nm, as illustrated in Figure 2.1. It is thus expected that the stronger extinction at a longer absorption wavelength for mTHPC will allow for improved PDT-beam penetration and increased $^1\text{O}_2$ dose deposition under equivalent irradiation conditions. In this chapter we test this hypothesis and present results which unequivocally establish that a combination of mTHPC's remarkable tight binding properties and high affinity for cells, as reported by Ball *et al.* (7), and its higher extinction at its typical treatment wavelength can successfully account for its 100 – 200 fold enhanced PDT efficacy in comparison to Photofrin.

2.2 Experimental Methods and Results

2.2.1 Theory for analysis of $^3\text{O}_2$ concentration measurements

Details of the mathematical model used to analyze the spatial and temporal distribution of the $^3\text{O}_2$ concentration, $[^3\text{O}_2](r,t)$, within and in the proximity of a

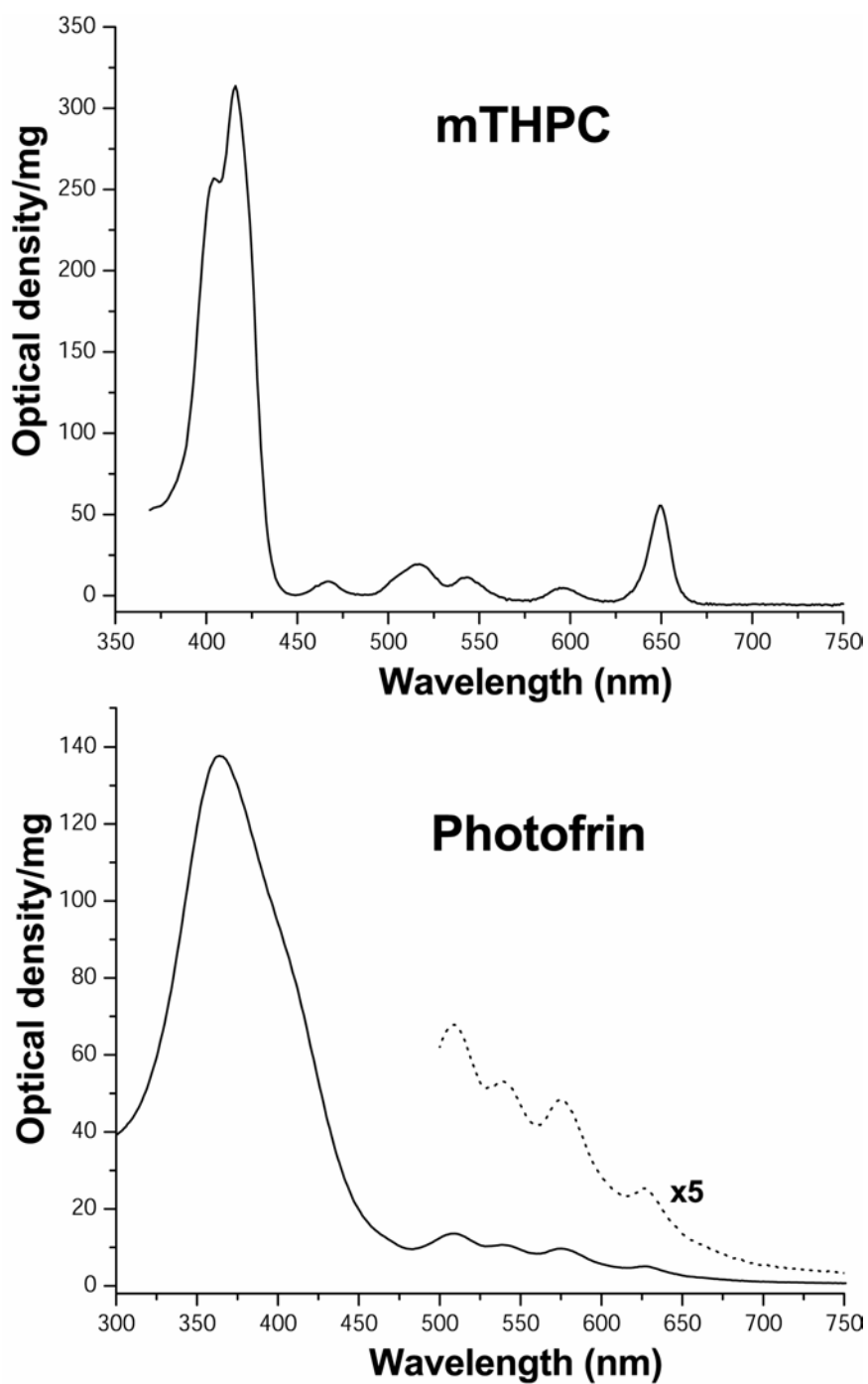


Figure 2.1. Absorption spectra of mTHPC (top) and Photofrin (bottom). mTHPC- and Photofrin-PDT are performed at 650 and 630 nm, respectively.

photosensitized multicell tumor spheroid during PDT have been reported previously (14). Briefly, the following pair of time-dependent diffusion equations are used to describe the kinetics of photochemical $^3\text{O}_2$ consumption:

$$\frac{\partial[{}^3\text{O}_2](r,t)}{\partial t} = D_d \nabla^2[{}^3\text{O}_2](r,t) \quad R_s \leq r \leq R_d \quad (1)$$

$$\frac{\partial[{}^3\text{O}_2](r,t)}{\partial t} = D_s \nabla^2[{}^3\text{O}_2](r,t) - \Gamma(r,t) \quad 0 \leq r \leq R_s \quad (2)$$

where D_d and D_s are the diffusion coefficients of $^3\text{O}_2$ in the medium and in the spheroid, respectively, R_s is the spheroid radius and R_d is the radius of the $^3\text{O}_2$ depletion zone, which is the region outside the spheroid where the $^3\text{O}_2$ concentration of the medium is affected by the presence of the spheroid. $\Gamma(r,t)$ is the sum of the metabolic, Γ_{met} , and photodynamic, Γ_{PDT} , rates of $^3\text{O}_2$ consumption. Γ_{met} can be determined from spatially resolved, steady-state measurements of the $^3\text{O}_2$ concentration inside and in the vicinity of a spheroid using a method introduced by Mueller-Klieser (17) and implemented experimentally by Nichols and Foster (14) and by Georgakoudi *et al.* (15).

Sensitizer photobleaching results in a decrease in the rate of photon absorption and consequently reduces $\Gamma_{\text{PDT}}(r,t)$. In the case of $^1\text{O}_2$ as the mediator of sensitizer photobleaching, $\Gamma_{\text{PDT}}(r,t)$, is given by the following expression,

$$\Gamma_{PDT}(r,t) = \Gamma_0 \left(\frac{[{}^3O_2](r,t)}{[{}^3O_2](r,t) + \frac{k_p}{k_{ot}}} \right) \exp \left(-\frac{k_{os}}{k_{oa}[A]} \int_0^t \Gamma_{PDT}(t') dt' \right), \quad (3)$$

where Γ_0 is the initial maximum 3O_2 consumption rate, k_{ot} is the bimolecular rate of triplet sensitizer quenching by oxygen, k_p is the rate of monomolecular decay of the triplet sensitizer state, and k_{os} and k_{oa} are the bimolecular rates of reaction of 1O_2 with ground state sensitizer and substrate, A, respectively. k_p/k_{ot} represents the 3O_2 concentration at which the sensitizer in its excited triplet state is as likely to be quenched by oxygen as it is to decay directly to its singlet ground state. The ratio $k_{os}/k_{oa}[A]$ is indicative of the probability of 1O_2 reaction with ground-state sensitizer. The derivation of this expression has been presented in detail elsewhere (15, 18). A second possible oxygen-independent mechanism of photobleaching gives rise to a reduction in the rate of photodynamic 3O_2 consumption according to a simple exponential bleaching term, $e^{-\alpha D}$, where D is the fluence ($J\ cm^{-2}$) and α is a bleaching coefficient. In this simple exponential decay model of sensitizer degradation, $\Gamma_{PDT}(r,t)$ is given by,

$$\Gamma_{PDT}(r,t) = \Gamma_0 \left(\frac{[{}^3O_2](r,t)}{[{}^3O_2](r,t) + \frac{k_p}{k_{ot}}} \right) \exp(-\alpha D). \quad (4)$$

It should be noted that the fluence rate or irradiance may be assumed to be uniform throughout a spheroid due to its small size (approximately 500- μm in

diameter) relative to the size of the irradiating laser beam, which is approximately 0.5 cm in diameter.

2.2.2 Nonuniform initial sensitizer distribution and its effect on the maximum rate of photodynamic $^3\text{O}_2$ consumption

In the presence of nonuniform sensitizer distribution, the initial maximum rate of photodynamic oxygen consumption, Γ_0 , becomes a function of the radial distance from the center of the spheroid. Thus, the expression of $\Gamma_0(r)$ used for analysis of mTHPC-sensitized spheroids has the form

$$\Gamma_0(r) = \Gamma_0 * F(r), \quad (5)$$

where $F(r)$ is a function describing the measured sensitizer distribution in a spheroid. Drug distribution was investigated by analyzing the spatial pattern of sensitizer fluorescence in 15- μm thick frozen sections of mTHPC- and Photofrin-sensitized EMT6 spheroids (500 μm diameter). The procedure for preparing spheroid frozen sections is described in Appendix II.

Imaging of mTHPC and Photofrin fluorescence in the spheroid sections was performed using a home-built laser scanning microscope system. The details of the microscope are described in Chapter 3. Fluorescence was excited with the 514 nm line of an argon-ion laser, and the emission was collected by a photomultiplier after it was filtered by a dichroic mirror (585dcsf, Chroma

Technology Corp., Brattleboro, VT) and a 550 nm longpass filter. Images were recorded with an in-plane resolution of 1 μm . Figure 2.2(a) shows a typical mTHPC fluorescence image of such a frozen section. As the image illustrates, the distribution of mTHPC is extremely nonuniform. We analyzed the fluorescence intensity of the spheroid sections, and Figure 2.2(b) shows a representative intensity profile from the spheroid edge to its center. The intensity of the mTHPC fluorescence falls off quickly with radial distance from the spheroid periphery with an e-folding distance of 20 - 25 μm . At 50 μm from the edge and persisting to the center, the mTHPC fluorescence assumes an approximately constant value, which is 5- to 10-fold less than that at the periphery but still significantly above the background fluorescence. The distribution of mTHPC fluorescence in Colo26 spheroids was found to be qualitatively similar (19). To quantify the sensitizer nonuniformity in the EMT6 spheroid sections, a monoexponential decay function given by

$$F(r) = \frac{\exp\left(-\frac{r}{\theta_1}\right) + \theta_2}{1 + \theta_2}, \quad (6)$$

where r , the radial distance from the spheroid edge, was fit to the fluorescence intensity cross-section. A representative fit is shown in Figure 2.2(b). The analysis yields θ_1 , a constant characteristic of the rate at which the intensity varies with distance, and θ_2 , the offset value that accounts for the almost constant

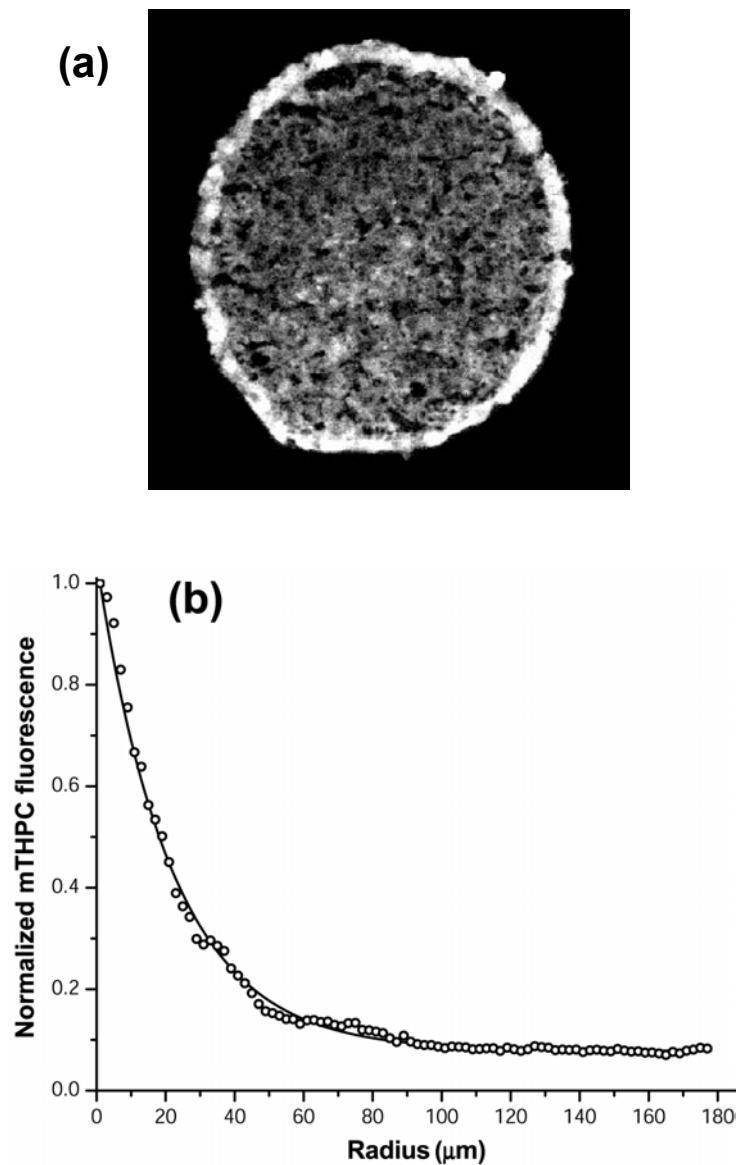


Figure 2.2. (a) Fluorescence image of a frozen section from an mTHPC-sensitized spheroid. (b) Representative plot shows the distribution of mTHPC fluorescence intensity from a spheroid edge (radius = 0) to its center. The fit of eqn. (6) to the distribution is given by the solid line.

fluorescence intensity after the initial decay. Analysis of a set of these frozen sections yielded mean values of 12.4 μm and 0.18 for θ_1 and θ_2 , respectively.

In order to perform a detailed investigation into the treatment efficacy of mTHPC in comparison to Photofrin, we also examined the drug distribution of Photofrin in spheroids. A previous study (18) had performed analysis in frozen sections of 10 $\mu\text{g mL}^{-1}$ Photofrin-sensitized EMT6 spheroids similar to the procedure described earlier and had concluded that the distribution was reasonably uniform. However, a more rigorous investigation revealed that the distribution of Photofrin is indeed nonuniform, albeit to a lesser extent than that of mTHPC. Figure 2.3a illustrates a fluorescence image of a frozen section from a Photofrin-sensitized spheroid, and Figure 2.3b shows the corresponding intensity profile from the edge to the spheroid center. At 25 μm from the spheroid edge, the Photofrin fluorescence intensity dropped to approximately 40% of its value at the periphery and then assumed a fairly constant value similar to the distribution pattern of mTHPC. The Photofrin intensity profile was then fitted using eqn. 6, from which θ_1 and θ_2 were obtained. Analysis of Photofrin distributions from a group of 6 spheroid sections yielded average values of 10.2 μm and 1.93 for θ_1 and θ_2 , respectively.

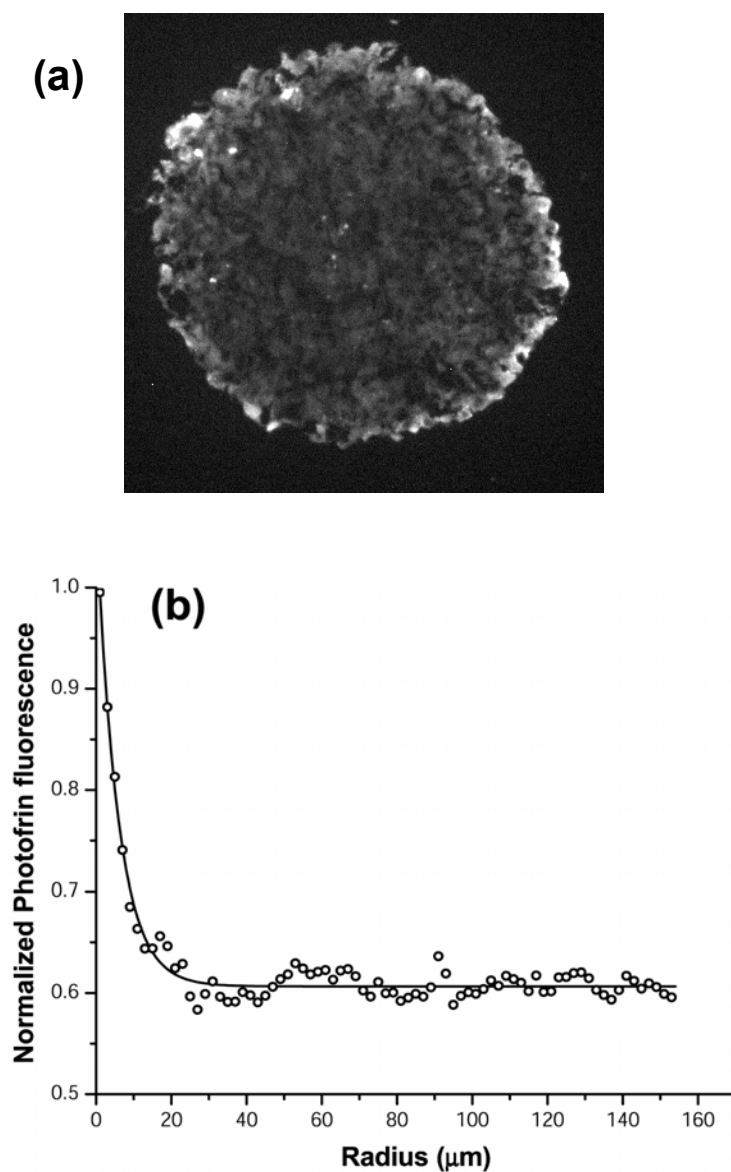


Figure 2.3. (a) Fluorescence image of a frozen section from a Photofrin-sensitized spheroid. (b) Representative plot shows the distribution of Photofrin fluorescence intensity from a spheroid edge (radius = 0) to its center. The fit of eqn. 6 to the distribution is given by the solid line.

2.2.3 $^3\text{O}_2$ concentration measurements during PDT and indirect investigation of sensitizer bleaching mechanisms

The experimental procedure for measuring the $^3\text{O}_2$ concentration changes at the edge of a multicell tumor spheroid has been described in detail previously (15). Briefly, 500- μm diameter spheroids were incubated with $0.3 \mu\text{g mL}^{-1}$ mTHPC. Following incubation, a single spheroid was selected and placed on top of a pedestal, which had an oxygen permeable membrane and was immersed in 20 mL of Hanks' Balanced Salt Solution (HBSS) (Figure 2.4). The spheroid was pinned down with a thin glass pipette, approximately 8 μm in tip diameter, and a Clark-style microelectrode (Diamond General, Ann Arbor, MI, USA) was placed at its edge. Two stereomicroscopes allow three dimensional control of the positioning of the pin and the microelectrode. The Clark-style microelectrode has a tip diameter of approximately 10 μm and a temporal response of less than 1 s. The oxygen-sensitive electrode recorded changes in $^3\text{O}_2$ concentration that occurred during PDT with irradiances of 5, 10 and 20 mW cm^{-2} of 650 nm light from an argon-ion laser pumped dye laser (Model 599, Coherent, Santa Clara, CA, USA). Consistently, the $^3\text{O}_2$ concentration decreased rapidly upon the onset of irradiation followed by a more gradual increase in $^3\text{O}_2$ levels as the sensitizer photobleaches and the photochemical $^3\text{O}_2$ consumption decreases. $\Gamma_0(r)$ and the ratio of photophysical rate constants, k_p/k_{ot} , were determined by fitting numerical

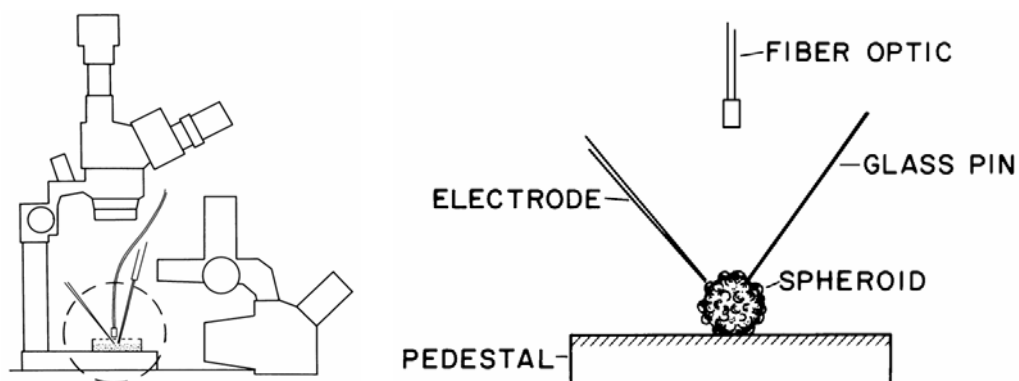


Figure 2.4. Experimental setup for measuring $^3\text{O}_2$ concentration changes in a photosensitized spheroid during PDT. The right panel shows a spheroid placed on a pedestal which has an oxygen-permeable membrane. The spheroid is pinned down by a glass pipette while the oxygen-sensitive microelectrode is placed to measure the $^3\text{O}_2$ concentrations as PDT is performed using light delivered by an optical fiber. The left panel shows a pair of stereomicroscopes positioned in such a way so that the user has a three-dimensional control on the placement of the pipette pin and the electrode. This setup allows recording of $^3\text{O}_2$ concentration changes with a spatial resolution of $12\ \mu\text{m}$ and a temporal resolution of $0.5\ \text{s}$. Reproduced from Georgakoudi (18).

solutions of eqns. (1) and (2) to the initial 20 - 25 s of electrode data using a Levenberg-Marquardt nonlinear least squares fitting algorithm (18, 20). The analysis was performed based on the assumption that negligible photobleaching occurs during these early times in $^3\text{O}_2$ depletion. Examples of the initial transients in the $^3\text{O}_2$ concentration recorded at the edge of mTHPC-sensitized spheroids for irradiances of 10 and 20 mW cm^{-2} are shown in Figure 2.5. The solid lines represent the best fits of numerical solutions of eqns. (1) and (2) to the data. From a total of nine experiments, the ratio k_p/k_{ot} extracted from fits was $8.7 \pm 2.9 \mu\text{M}$. The initial maximum $^3\text{O}_2$ consumption rate, $\Gamma_0(r)$, is a function of the incident irradiance, so we introduced another parameter, $\beta_{\text{PDT}}(r)$, which is the proportionality constant between $\Gamma_0(r)$ and the irradiance. As the microelectrode and consequently $\Gamma_0(r)$ have a spatial resolution of $\sim 12 \mu\text{m}$, so we calculated $\beta_{\text{PDT}}(r)$ in the middle of a $12 \mu\text{m}$ -thick radial shell located at the spheroid perimeter *i.e.* at $6 \mu\text{m}$ from the spheroid edge. The analysis yielded a value of $7.3 \pm 1.3 \mu\text{M s}^{-1} \text{mW}^{-1} \text{cm}^2$ for $\beta_{\text{PDT}}(r)$. After these two parameters were determined from the initial $^3\text{O}_2$ transients, the entire time-dependent data set, approximately 600 s of recordings, was analyzed to obtain either the constant photobleaching coefficient, α , or the ratio $k_{os}/k_{oa}[\text{A}]$. Details of the fitting procedure have been reported elsewhere (18). A typical complete time-dependent $^3\text{O}_2$ concentration observed at the edge of an mTHPC-sensitized

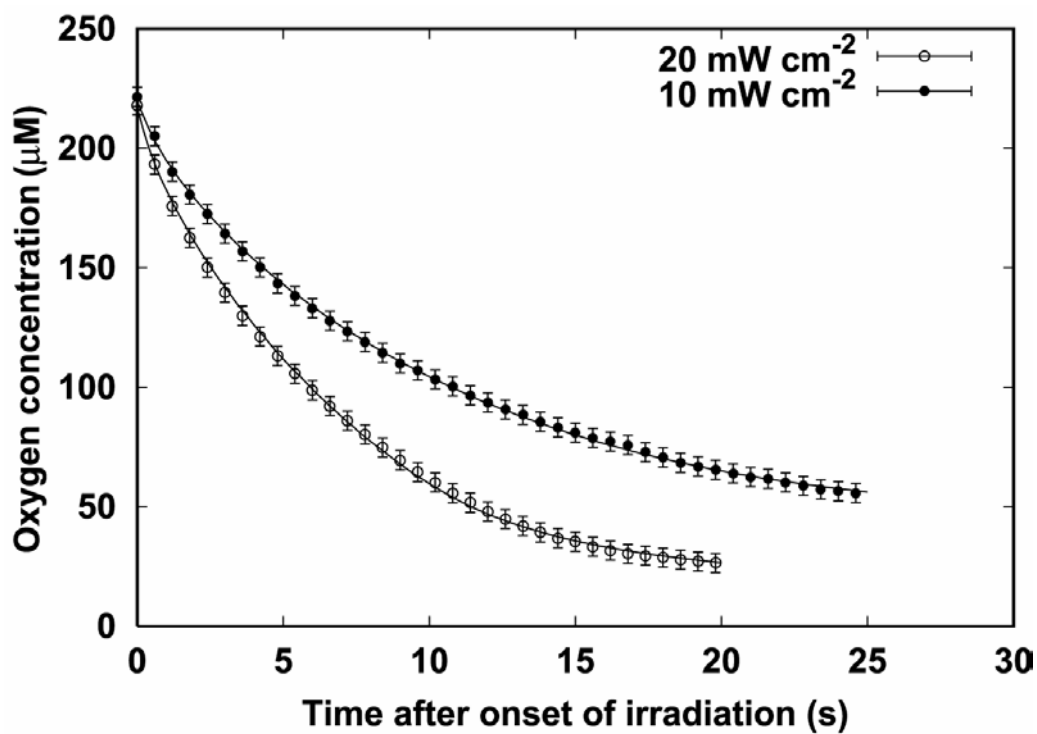


Figure 2.5. Microelectrode measurements of initial oxygen depletion versus time at the edge of an mTHPC-sensitized spheroid during 650 nm irradiation at two different irradiances of 10 and 20 mW cm^{-2} .

spheroid undergoing PDT at an irradiance of 20 mW cm^{-2} is shown in Figure 2.6a. The best fit to the $^3\text{O}_2$ distribution was obtained using solutions of eqns. (1) and (2) with Γ_{PDT} described by eqn. (3), *i.e.* assuming bleaching mechanism in which the sensitizer is degraded through self-sensitized $^1\text{O}_2$ reaction. This was compared to the best fit (Figure 2.6b) that could be achieved by considering a bleaching model based on a simple exponential decay in fluence with a constant photobleaching rate as described by eqn. (4). It was clear from the comparison that while the $^1\text{O}_2$ -mediated fit captured all the essential features of the $^3\text{O}_2$ distribution, the predictions from the simple exponential description of photobleaching were not in good agreement with the experimental data. Detailed analysis of 18 experiments using the three irradiances mentioned earlier showed a similar pattern, suggesting that mTHPC bleaching is consistent with a predominantly $^1\text{O}_2$ -mediated reaction process. The fits to the data also yielded the ratio $k_{\text{os}}/k_{\text{oa}}[\text{A}]$, which was found to be $29.7 \pm 4.6 \text{ M}^{-1}$ for mTHPC.

Nichols and Foster (14) and Georgakoudi *et al.* (15) reported results from similar microelectrode experiments performed on $10 \text{ } \mu\text{g mL}^{-1}$ Photofrin-sensitized EMT6 spheroids. However, the data analysis in these two studies had assumed a uniform distribution of Photofrin throughout a spheroid. Thus with the observation of Photofrin's nonuniform distribution, the microelectrode data were re-analyzed in order to extract $\Gamma_0(r)$, k_p/k_{ot} and $k_{\text{os}}/k_{\text{oa}}[\text{A}]$. Analysis of a set of seven experiments confirmed that Photofrin photodegradation was mediated

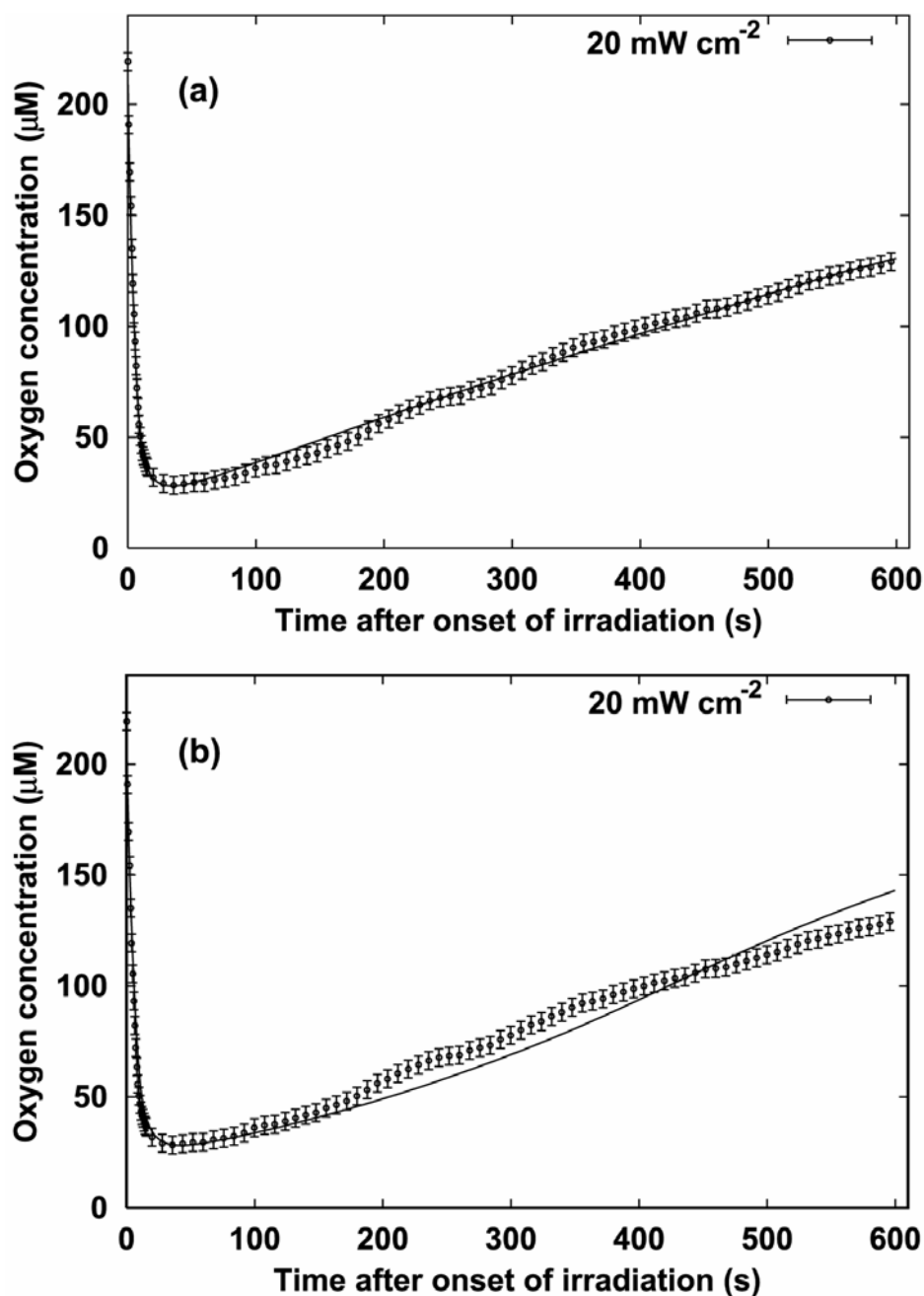


Figure 2.6. Time-dependent $^3\text{O}_2$ concentration changes recorded using a microelectrode placed at the edge of an mTHPC-sensitized spheroid during PDT with 650 nm light at an irradiance of 20 mW cm^{-2} . The solid line is the best fit to the data assuming (a) the $^1\text{O}_2$ bleaching model described by eqn. 3 or (b) a fluence dependent simple exponential decay given by eqn. 4. Error bars represent estimates of the uncertainty in the oxygen electrode measurements.

mainly *via* a $^1\text{O}_2$ mechanism, consistent with prior findings (15), and yielded a $\beta_{\text{PDT}}(r)$ value of $2.3 \pm 0.4 \mu\text{M s}^{-1} \text{mW}^{-1} \text{cm}^2$, at 6 μm from the spheroid edge, for PDT irradiation at 514 nm. This corresponds to a value of $0.77 \pm 0.1 \mu\text{M s}^{-1} \text{mW}^{-1} \text{cm}^2$ at 630 nm, which is the typical wavelength used for clinical Photofrin-PDT. This calculation was based on the fact that Photofrin extinction is approximately three times greater at 514 nm than it is at 630 nm (21, 22). Through the re-analysis of the data we also obtained new values of $12.1 \pm 3.4 \mu\text{M}$ and $56.5 \pm 8.6 \text{M}^{-1}$ for the parameters, k_p/k_{ot} and $k_{os}/k_{os}[A]$, respectively. These values were not remarkably different from $11.9 \mu\text{M}$ and 76M^{-1} for k_p/k_{ot} and $k_{os}/k_{os}[A]$, respectively, reported previously by Georgakoudi *et al.* (15), assuming uniform Photofrin distribution.

The above analysis indicates that the value of $\beta_{\text{PDT}}(r)$ for mTHPC at 650 nm is approximately 10 times greater than that of Photofrin at 630 nm. From the values of the extinction coefficients used for plotting Figure 2.1, we found that the O.D. mg^{-1} for mTHPC at 650 nm is 57.5, while that for Photofrin at 630 nm is 5.4. Thus, mTHPC's extinction is nearly 10.6-fold higher than that of Photofrin. This suggests that the concentrations of mTHPC and Photofrin to which the measurements of $\beta_{\text{PDT}}(r)$ are sensitive must be similar. Therefore, to make a quantitative comparison between the $\beta_{\text{PDT}}(r)$ values for mTHPC and

Photofrin, it was necessary to measure the sensitizer concentration in the spheroids.

Using a procedure described in Appendix III to estimate the sensitizer concentration in spheroids, we made measurements in spheroids incubated with $0.3 \mu\text{g mL}^{-1}$ mTHPC. The mTHPC concentration was estimated to be approximately $45 \mu\text{g mL}^{-1}$, which corresponds to a 150-fold higher mTHPC concentration than that of the incubation medium. Nichols and Foster (14) had previously measured the sensitizer concentration in $10 \mu\text{g mL}^{-1}$ Photofrin-sensitized spheroids and found it to be $102 \mu\text{g mL}^{-1}$, which corresponds to an ~ 10 -fold increase over the incubation medium concentration. These results demonstrate the remarkable retention properties of mTHPC *vs.* Photofrin.

The values of $\beta_{\text{PDT}}(r)$ for the two sensitizers were calculated from the measurements of their $\Gamma_0(r)$ which was determined at the spheroid periphery. $\Gamma_0(r)$ has a spatial resolution of $\sim 12 \mu\text{m}$, and we therefore wanted to quantify the amount of drug deposited in a $12 \mu\text{m}$ -thick spherical shell at the spheroid perimeter. This was done using the measured values of the total mTHPC and Photofrin concentrations and the exponential function in eqn. 6, which described the nonuniform distribution of the two sensitizers in spheroids based on their respective θ_1 and θ_2 values. The mTHPC and Photofrin concentrations in the radial shell were computed to be approximately $166 \mu\text{g mL}^{-1}$ and $132 \mu\text{g mL}^{-1}$,

respectively. Indeed, considering the experimental errors that may have occurred in estimating the total drug concentration in spheroids the values are reasonably comparable and suggest that the 10 times greater value of $\beta_{\text{PDT}(r)}$ for mTHPC in comparison to Photofrin at the spheroid periphery is largely accounted for on the basis of mTHPC's 10.6-fold higher extinction.

2.2.4 Effects of irradiance on mTHPC-photosensitized cell survival

These cell survival studies were performed in collaboration with a PDT research laboratory in Nancy, France led by Dr. Francois Guillemin and Dr. Lina Bezdetsnaya. Spheroids were grown from a nonmetastazing mouse Colo26 colorectal tumor cell line. The procedure for Colo26 spheroid culture was similar to that described in Appendix I for EMT6 spheroids. 500- μm diameter Colo26 spheroids were incubated with $5 \mu\text{g mL}^{-1}$ mTHPC for 24 hours before PDT irradiation. Control (photosensitizer, no light) and PDT-treated groups were composed of approximately 30 spheroids. After incubation with mTHPC, each group of 30 spheroids was transferred to one well of a 24-well cell culture plate containing 1 mL of cell culture medium. Spheroids in the PDT-treated groups were exposed to various fluences delivered at irradiances of 5, 30 and 90 mW cm^{-2} at 650 nm. Following irradiation, the spheroids were dissociated

and the fraction of cells that survived PDT was determined by a colony forming assay (19, 23).

The normalized cell survival derived from Colo26 spheroids that were dissociated after different irradiation protocols is reported in Figure 2.7. As is evident in the plot, the cytotoxicity after mTHPC-based PDT exhibited a strong irradiance dependence. As the irradiance was reduced from 90 to 5 mW cm⁻², the cell survival was markedly diminished at all fluences. Spheroids treated with a fluence of 10 J cm⁻², which is typically used in the clinical context, demonstrated cell survival of 76, 57 and 18% in response to irradiances of 90, 30 and 5 mW cm⁻², respectively. This trend was even more pronounced when spheroids were irradiated with increased fluences. Spheroid cell survival following a fluence of 45 J cm⁻² administered at the irradiances of 90, 30 and 5 mW cm⁻² was 60, 22 and 1.7%, respectively.

2.2.5 Estimation of photodynamic dose and ¹O₂ threshold

The calculation of the photodynamic dose throughout the spheroid was done as reported previously (14, 15) by integrating the value of Γ_{PDT} that corresponds to the irradiance used in a specific experimental protocol. Because the net photodynamic oxygen consumption originates in ¹O₂ reactions with biological targets, the integrated Γ_{PDT} obtained from a simulation provides an estimate of

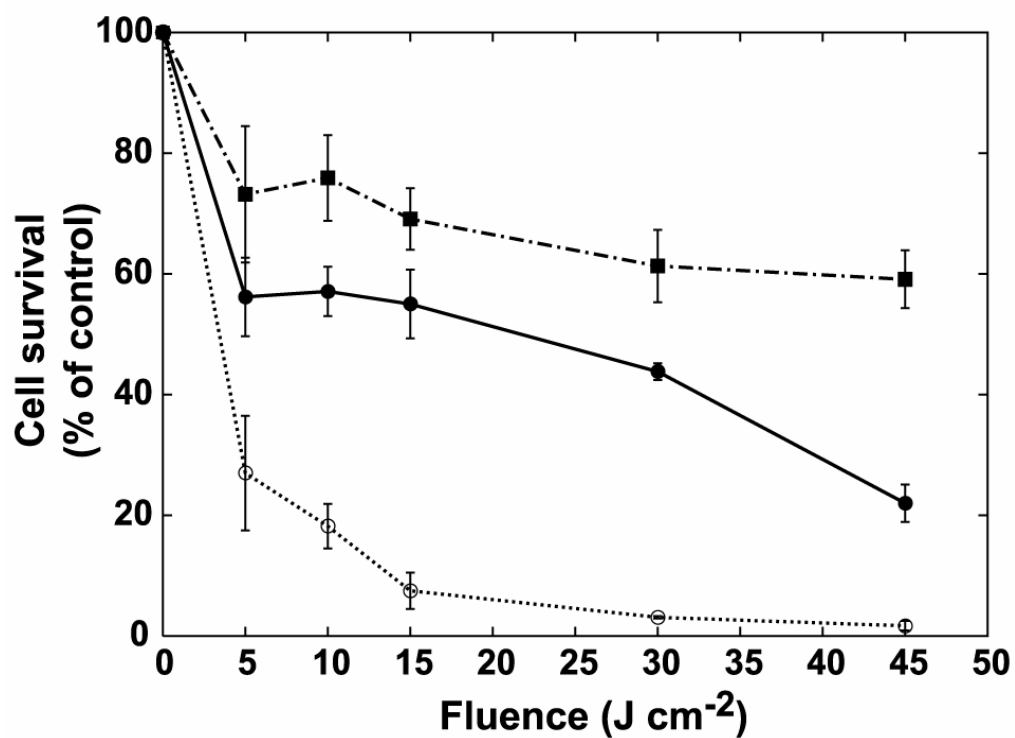


Figure 2.7. Surviving fractions (cell yield x plating efficiency) of cells dissociated from mTHPC-sensitized Colo26 spheroids treated with PDT delivered at irradiances of 5 (O), 30 (●), or 90 (■) mW cm⁻². Reproduced from Coutier *et al.* (19).

the total concentration of $^1\text{O}_2$ that has reacted as a function of radial location in the spheroid. Threshold dose estimates were computed to interpret the measured surviving fractions for various protocols with the assumption that the surviving cells originate within the anoxic central core of the spheroid where minimal $^1\text{O}_2$ dose is deposited.

Before the threshold dose for mTHPC-PDT could be computed, it was necessary to account for the fact that the conditions under which the mTHPC-sensitized spheroids were irradiated in the cell survival experiments performed in the French laboratory differed from those used in our microelectrode measurements, which are the source of the photophysical parameters used in the simulations. In particular, because 30 spheroids were irradiated simultaneously in 1 mL of medium in the cell survival experiments and just one spheroid was irradiated in 20 mL of fresh medium during the microelectrode experiments, we considered the possibility that nonnegligible $^3\text{O}_2$ depletion occurred during irradiation of the 30 spheroids. This depletion would influence the actual photodynamic doses, and therefore it was necessary to determine the magnitude of this effect and to incorporate it into the simulations so that meaningful comparisons could be made. To measure the $^3\text{O}_2$ depletion in the bulk medium, a Clark-style oxygen-sensitive electrode (Microelectrodes Inc., Londonderry, NH) was positioned inside a well of a 24-well plate containing 30 mTHPC-sensitized spheroids in 1 mL of medium. The sensitizer concentration and incubation

conditions were identical to those used for the Colo 26 spheroids. The spheroids were irradiated with 650 nm light at irradiances of 90, 30 and 5 mW cm⁻². Significant oxygen depletion in the bulk medium was observed for the two higher irradiances. These measured changes in the ³O₂ concentration of the bulk medium were incorporated into the simulations by allowing this concentration, a boundary condition in the model, to be adjusted at each time step.

Figure 2.8 shows the radial distribution of ¹O₂ reactions in an mTHPC-sensitized spheroid after a 30 J cm⁻² irradiation at 650 nm, taking into account the influence of bulk ³O₂ depletion. These plots demonstrate that the enhanced therapeutic effect observed in response to the lower irradiances was predominantly the result of extending a greater ¹O₂ dose into the central regions of the spheroid. By combining the calculated photodynamic dose plots of Figure 2.8 with the cell survival data shown in Figure 2.7, it was possible to estimate a threshold dose of reacting ¹O₂ for this system. The threshold dose was the concentration of ¹O₂ reactions at the border separating the volume occupied by the surviving fraction and the volume of cells that were killed under particular treatment conditions. This definition of the PDT threshold was adopted on the basis of the histologic observations reported by several investigators of a distinct boundary between tissue volumes that are and are not treated effectively by PDT *in vivo* (24). The volume of the surviving fraction is illustrated for the

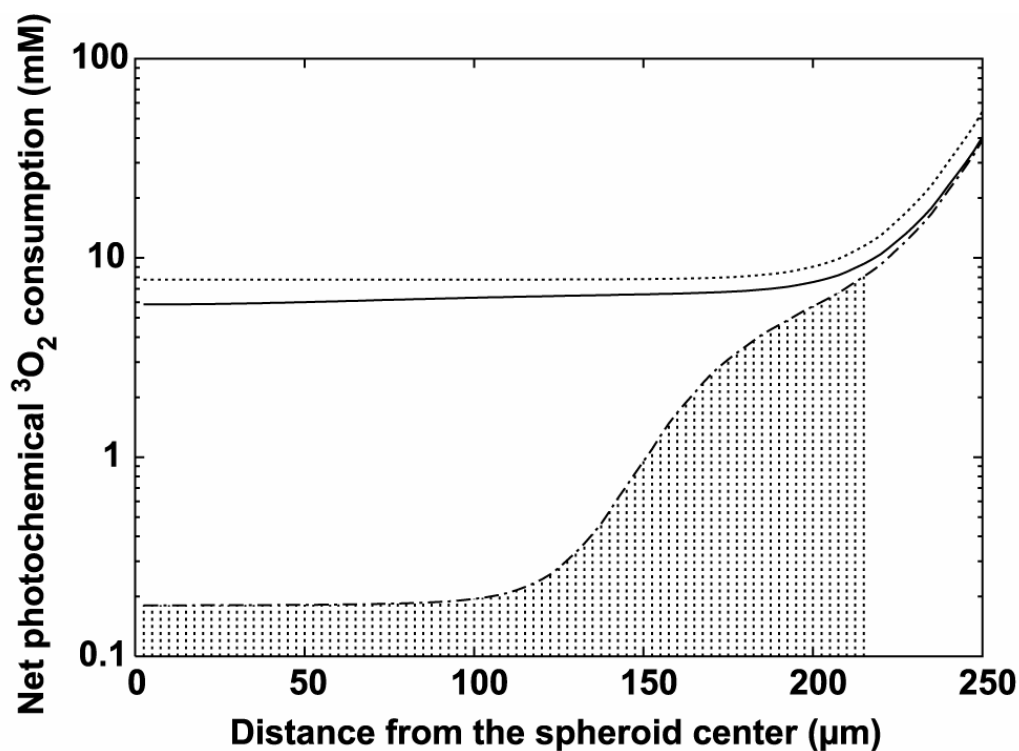


Figure 2.8. Calculated radial distributions of net photochemical $^3\text{O}_2$ consumption in mTHPC-sensitized spheroids subjected to a PDT treatment fluence of 30 J cm^{-2} delivered at three fluence rates of 5 (---); 30 (—); and 90 (- · -) mW cm^{-2} . The shaded region under the curve depicts the volume of the spheroid that corresponds to the surviving fraction in response to a treatment fluence of 30 J cm^{-2} delivered at 90 mW cm^{-2} .

90 mW cm⁻², 30 J cm⁻² case by the shaded region in Figure 2.8. The individual threshold determinations from 40 experiments performed at the three irradiances are summarized in Figure 2.9. The average of these estimates, represented by the solid horizontal line, was 7.9 ± 2.2 mM (mean \pm standard deviation).

Based on the new photophysical parameters for Photofrin extracted using an analysis incorporating the nonuniform drug distribution and combining it with the cell survival data reported by Nichols and Foster (14), the threshold ¹O₂ dose for Photofrin PDT was also re-calculated and found to be 11.9 ± 3.5 mM. The new threshold value was remarkably similar to the value of 12.1 ± 1.2 mM reported earlier by Georgakoudi *et al.* (15) using the same survival data, but computed assuming a uniform Photofrin distribution in spheroids.

2.2.6 Comparison of treatment efficacy for mTHPC vs. Photofrin based on their respective photophysical characteristics

We performed simulations of photodynamic dose depositions with mTHPC- and Photofrin-PDT at 650 and 630 nm, respectively. The irradiances used in the simulations for the two sensitizers were chosen so as to match their corresponding maximum initial rate of photochemical ³O₂ consumption, $\Gamma_0(r)$, at $54 \mu\text{M s}^{-1}$ in the middle of a 12 μm -thick spherical shell located at the perimeter

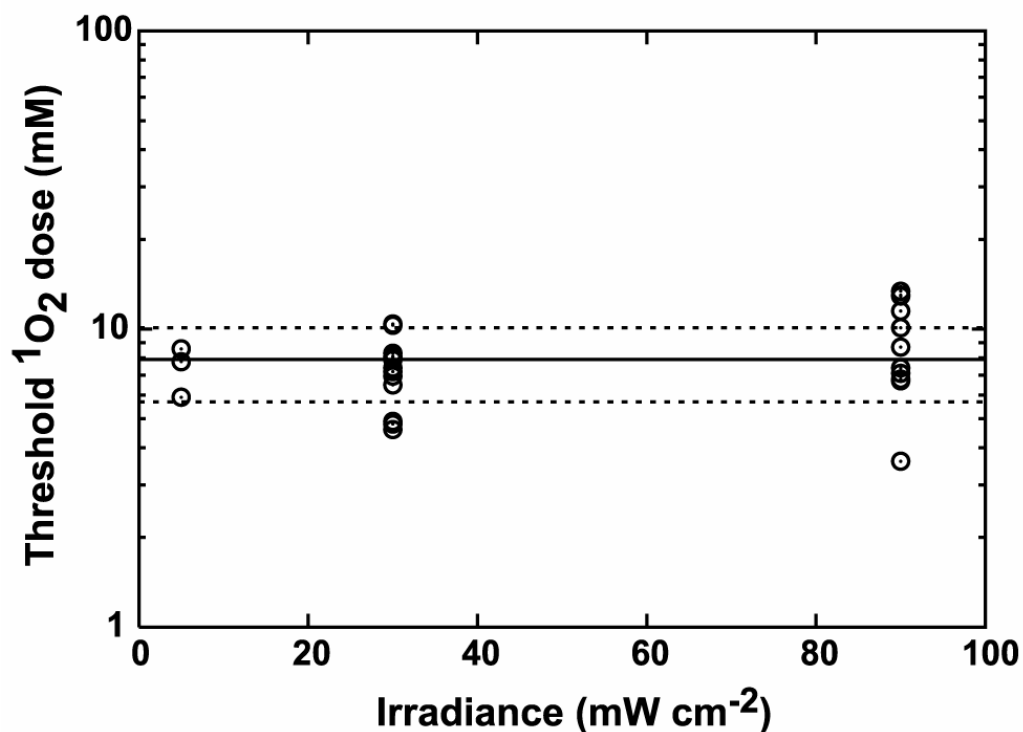


Figure 2.9. The threshold dose of reacting ¹O₂ (data points) estimated from 40 separate cell survival experiments performed at fluence rates of 5 (n = 10), 30 (n = 18) and 90 (n = 12) mW cm⁻². The estimates were computed using the results of the individual cell survival experiments that are summarized in Fig. 2.7 and the net photochemical ³O₂ consumption distributions plotted in Fig. 2.8. The mean threshold dose, represented by the solid line, is 7.9 ± 2.2 mM (mean \pm SD). The dashed lines depict 1 SD.

of a spheroid. The irradiances and the radial extent of the shell were carefully selected so as to avoid any effects of PDT-induced $^3\text{O}_2$ depletion that would limit dose deposition. By restricting the thickness of the shell to 12 μm we also reduce the influence of nonuniform drug distribution on dose deposition. Based on the experimentally determined values of $\beta_{\text{PDT}}(r)$ at this location, irradiances of 7.5 and 70 mW cm^{-2} were used for the mTHPC- and Photofrin- $^1\text{O}_2$ dose simulations, respectively. A higher irradiance for Photofrin-simulations was used because the extinction of Photofrin at 630 nm is significantly lower than that of mTHPC at 650 nm. Further, as the value of $\Gamma_0(r)$ for Photofrin was obtained from analysis of experiments conducted with 514 nm irradiation, the irradiance calculation took into account that Photofrin extinction is approximately 3 times greater at 514 nm than at 630 nm (21, 22). The treatment fluence was fixed at 10 J cm^{-2} for both sensitizers.

By summing the dose deposited in the 12 μm -shell, indicated by the shaded region in the dose plot of Figure 2.10a, we obtained a total $^1\text{O}_2$ dose of 129.6 mM with mTHPC-PDT. A similar computation yielded a $^1\text{O}_2$ dose of 24.5 mM with Photofrin-PDT (Fig. 2.10b). Thus, mTHPC deposited an approximately 5.3-fold higher PDT dose than Photofrin under conditions in which the initial rates of photochemical $^3\text{O}_2$ consumption were matched.

We then wanted to establish the contributions of mTHPC's lower $k_{\text{os}}/k_{\text{oa}}[\text{A}]$ value of 29.7 M^{-1} and its 10.6-fold higher extinction coefficient to the

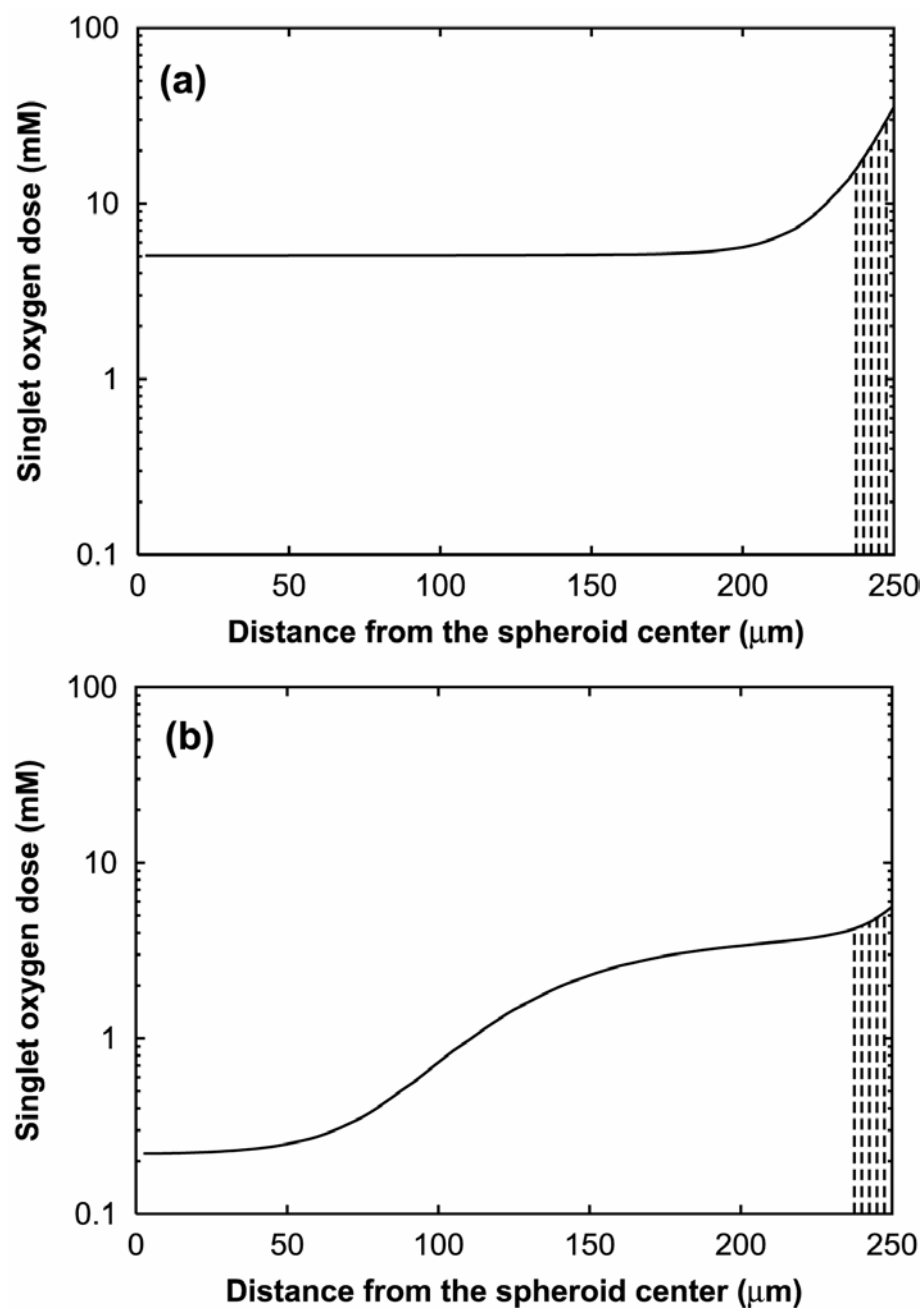


Figure 2.10. Simulated $^1\text{O}_2$ dose plots for (a) mTHPC-PDT at 650 nm with 7.5 mW cm^{-2} irradiance and (b) Photofrin-PDT at 630 nm with 70 mW cm^{-2} irradiance. Both simulations were generated for a total fluence of 10 J cm^{-2} . The shaded region (12 μm from the spheroid edge) corresponds to the spheroid volume from where the dose was computed.

5.3-fold enhanced PDT dose. In order to evaluate the effect of $k_{os}/k_{oa}[A]$, we performed an mTHPC-PDT dose simulation where we set the value of $k_{os}/k_{oa}[A]$ to that of Photofrin, *i.e.* 56.5 M^{-1} , keeping all other parameters unchanged. On performing this simulation and computing the dose deposited dose in the $12 \text{ }\mu\text{m}$ -radial shell, we obtained a $^1\text{O}_2$ dose of 96 mM. This indicates that mTHPC's lower $k_{os}/k_{oa}[A]$ value of 29.7 M^{-1} vs. 56.5 M^{-1} for Photofrin results in an approximately 35% increase in dose deposition.

The higher $^1\text{O}_2$ dose yield of 96 mM with mTHPC- vs. 24.5 mM with Photofrin-PDT under conditions of equivalent rates of photon absorption, and identical treatment fluence and $k_{os}/k_{oa}[A]$ is likely due to mTHPC's stronger extinction which causes a significant reduction in its PDT irradiance so as to avoid severe $^3\text{O}_2$ depletion. Consequently, in comparison to Photofrin the dose simulation with mTHPC runs for a longer irradiation period and deposits increased $^1\text{O}_2$ dose.

We therefore expected the remaining difference of ~ 3.9 -fold (96 mM / 24.5 mM) between mTHPC- and Photofrin-PDT doses to be accounted for on the basis of their different extinction coefficients. To evaluate the contribution from the extinction coefficients of the two sensitizers, we performed an mTHPC-PDT dose simulation with mTHPC's extinction coefficient at 650 nm matched to that of Photofrin's at 630 nm. In order to do that we reduced mTHPC's extinction by 10.6-fold and therefore increased the mTHPC-PDT irradiance from 7.5 mW cm^{-2}

to 79.5 mW cm^{-2} so as to maintain a constant value of Γ_0 of $54 \text{ } \mu\text{M s}^{-1}$. We also assigned a $k_{os}/k_{oa}[A]$ value of 56.5 M^{-1} instead of 29.7 M^{-1} , thus removing the influence of different bleaching rates. With the extinction coefficient, Γ_0 , and $k_{os}/k_{oa}[A]$ of mTHPC matched to that of Photofrin, we of course expected a $^1\text{O}_2$ dose of approximately 24.5 mM, which was the Photofrin-PDT dose obtained with a 10 J cm^{-2} fluence treatment. The computation yielded a comparable mTHPC-PDT dose of 20 mM from the $12 \text{ } \mu\text{m}$ -radial shell. We thus establish that the 10.6-fold higher extinction of mTHPC accounts for the remaining ~ 3.9 times increased $^1\text{O}_2$ dose obtained with mTHPC-PDT.

In summary, using PDT dose simulations we obtained approximately 5.3-fold enhanced $^1\text{O}_2$ dose with mTHPC- vs. Photofrin-PDT under conditions of equivalent rates of photon absorption and identical treatment fluence. We performed additional simulations to evaluate the contributions from different $k_{os}/k_{oa}[A]$ and extinction coefficients to the dose deposition with the two sensitizers, and our results suggest that these two parameters account for the ~ 5.3 -fold higher dose obtained with mTHPC-PDT.

The 100 – 200-fold increased efficacy of mTHPC in comparison to Photofrin is estimated on the basis of the typical clinical prescription of photodynamic dose, which is the product of the administered sensitizer concentration (mg kg^{-1}) and the incident fluence. Therefore, to invoke a similar potency comparison using the measurements in spheroids, we must account for

the incubation concentrations used for photosensitization with mTHPC and Photofrin. Incubation concentrations of $0.3 \mu\text{g mL}^{-1}$ mTHPC and $10 \mu\text{g mL}^{-1}$ Photofrin were used for the electrode measurements in the spheroids. Thus by computing the product of the 33.3-fold lower mTHPC incubation concentration and the 5.3-fold enhanced mTHPC-PDT dose calculated from the simulations that match the rates of photon absorption, we obtain an enhancement of nearly 175-fold in the efficacy of mTHPC compared to that of Photofrin.

2.3 Discussion

The photobleaching mechanism of mTHPC, the extraction of its photophysical parameters, the influence of treatment irradiances on photobleaching rates and cell survival, and finally a comparison of the photodynamic efficacy of mTHPC and Photofrin on the basis of their respective photophysical properties are the central issues of study in this chapter. The investigation of the sensitizer photodegradation process was performed using a mathematical model of photochemical $^3\text{O}_2$ consumption and photobleaching in spheroids that has been used previously in the analysis of other photosensitizers (14-16). In this study, we incorporated the effects of the measured nonuniform distribution of mTHPC inside of the spheroid. Analysis of the distribution of mTHPC fluorescence in spheroid sections demonstrated a pronounced, nonuniform sensitizer penetration

characterized by an intense mTHPC localization in the outermost rim of the spheroid and a considerably reduced mTHPC fluorescence at only 50 μm from the surface (Fig. 2.2). This high degree of nonuniformity may be related to the unusually high affinity of mTHPC for cells, as has been described by Ball *et al.* (7). Using the modified mathematical model, we demonstrated that electrode measurements of $^3\text{O}_2$ concentrations near an mTHPC-sensitized spheroid during PDT are consistent with a theory in which the photosensitizer concentration is diminished through photochemical reactions between $^1\text{O}_2$ and the sensitizer molecule. This result is consistent with previous findings based on investigations in solution, in cells *in vitro*, and *in vivo*, which have indicated $^1\text{O}_2$ as a major mediator of mTHPC photobleaching (25-27). The electrode analysis allowed us to obtain a value of 29.7 M^{-1} for the coefficient $k_{\text{os}}/k_{\text{oa}}[\text{A}]$, which describes the inverse of the sensitizer concentration at which a $^1\text{O}_2$ molecule is as likely to react with the sensitizer as it is to react with another target in the cell. This is about 2-fold lower than the $k_{\text{os}}/k_{\text{oa}}[\text{A}]$ value of 56.5 M^{-1} obtained for Photofrin. A lower value of this ratio implies that a $^1\text{O}_2$ molecule is relatively more likely to react with cell substrates, and it is thus a potentially important photophysical factor contributing to the higher photodynamic efficacy obtained with mTHPC-PDT in comparison to other sensitizers such as Photofrin or ALA-induced PpIX, whose $k_{\text{os}}/k_{\text{oa}}[\text{A}]$ is 90 M^{-1} (16).

Earlier published reports have indicated that the phototoxicity of mTHPC

is greatly inhibited in the absence of molecular oxygen or in the presence of a $^1\text{O}_2$ scavenger (1, 26, 28), thus suggesting $^1\text{O}_2$ as a major toxic agent in mTHPC photosensitization. Therefore, insufficient molecular oxygen can limit tumor cell destruction within tissue undergoing mTHPC-based PDT treatment. PDT itself causes changes in tumor oxygen tension as it consumes oxygen (29, 30) and alters blood flow processes (31-33). However, PDT-induced hypoxia may be circumvented by the use of low irradiances, since the reduced irradiance treatment protocols consume the available oxygen at a rate that is more likely to be balanced by oxygen transport throughout the course of treatment (29). A useful way to investigate the effects of irradiances on oxygen-dependent aspects of PDT is to make use of the multicell tumor spheroid model, as spheroids exhibit meaningful gradients in oxygen and sensitizer concentration in the absence of complex physiological and immunological factors.

In collaboration with a French laboratory, we examined the impact of irradiance on cell survival and mTHPC photobleaching in mTHPC-photosensitized multicell Colo 26 spheroids and examined the relationship of these two experimental endpoints in terms of a $^1\text{O}_2$ -mediated photobleaching mechanism. As illustrated in Fig. 2.7, the mTHPC therapeutic efficacy increased progressively when the irradiance was reduced over the range from 90 to 5 mW cm^{-2} . Previously, a strong dependence of the surviving fraction on the irradiance was observed for Photofrin-based PDT in EMT6 spheroids and for

ALA-PDT in human glioma spheroids, and was attributed to the decrease in the $^3\text{O}_2$ consumption rate at relatively low irradiances (23, 34). A clinically relevant observation was that lowering the irradiance reduced cell survival significantly even for the lowest fluences ($5.0 - 15 \text{ J cm}^{-2}$), as shown in Fig. 2.7. Another particularly interesting finding of the study was the significant decrease in mTHPC-sensitized spheroid cell survival when the irradiance was reduced from 30 to 5 mW cm^{-2} . The increased therapeutic effect achieved under this condition reflects the potential importance of photochemical $^3\text{O}_2$ depletion at what are typically considered rather modest irradiances, especially when sensitizers with high extinction at the irradiation wavelength are used. These findings are consistent with observations *in vivo*, where longer tumor regrowth time (35, 36) and increased tumor necrosis (37) were obtained with mTHPC-PDT at lower vs. higher treatment irradiances.

The enhanced therapeutic effect observed with lower irradiances was caused by the extension of the $^1\text{O}_2$ dose into the central regions of the spheroid, as is illustrated in the calculated plots of net photochemical $^3\text{O}_2$ consumption shown in Fig. 2.8. These plots of photodynamic dose were used to interpret the cell survival data of Fig. 2.7 and extract a value for the threshold of reacting $^1\text{O}_2$. To perform this calculation we took into account the bulk depletion of $^3\text{O}_2$ from the medium during irradiation of groups of mTHPC-sensitized Colo26 spheroids. The theoretical model used for the dose calculation assumes an air-saturated $^3\text{O}_2$

concentration far from the spheroids, which is not depleted during irradiation. However, direct measurements of the bulk $^3\text{O}_2$ concentration during sustained irradiation of 30 mTHPC-sensitized spheroids indicated that this assumption was not valid at the higher irradiances. Incorporation of this $^3\text{O}_2$ depletion in the bulk medium in addition to the inclusion of the inhomogeneous mTHPC distribution in spheroids had a significant effect on the model predictions of photodynamic dose. The value of the threshold dose of $^1\text{O}_2$ with mTHPC was determined to be 7.9 mM (Fig. 2.9), which is slightly lower than the 11.9 mM obtained for Photofrin-sensitized EMT6 spheroids. It is possible that this difference originates from the participation of radicals other than $^1\text{O}_2$ in the mTHPC-mediated photocytotoxicity or from the different subcellular localization of the two sensitizers. It should be noted, however, that the Photofrin threshold estimate was made without taking into account possible $^3\text{O}_2$ depletion during the irradiation of groups of spheroids in the original cell survival experiments (23). The effect of bulk $^3\text{O}_2$ depletion is to lower the dose of reacting $^1\text{O}_2$ in the spheroids. Thus, it may be that the Photofrin threshold estimate is somewhat high, thereby decreasing the apparent difference with mTHPC.

Nevertheless, it is quite unlikely that the approximately 34% lower value of $^1\text{O}_2$ -threshold dose with mTHPC-PDT could account for its 100 – 200-fold higher potency compared to Photofrin-PDT. As mentioned earlier, several investigators have attempted to unravel the possible reasons for this enhanced

efficacy. Although some unique properties of mTHPC, such as its ability to tightly sequester in cells, have been identified through these studies, they have not been able to successfully account for its improved efficacy. Bonnett *et al.* (13) examined the photophysical properties and biological activity of three photosensitizers including mTHPC and suggested that for constant light dose, PDT-induced tumor necrosis *in vivo* is a strong function of the molar extinction at the irradiation wavelength in the red region of the visible spectrum. In comparison to Photofrin, mTHPC's long-wavelength absorption maximum is red-shifted (650 nm for mTHPC vs. 630 nm for Photofrin), and its extinction coefficient in this wavelength range is higher by about an order of magnitude in solutions of equal mass concentration. This latter property of mTHPC clearly favors higher cytotoxic effect during therapy, as the photochemical $^3\text{O}_2$ consumption, which defines $^1\text{O}_2$ dose, will be considerably higher for mTHPC-PDT for equivalent irradiation protocols. Without invoking any effects of PDT treatment beam attenuation due to tissue absorbers such as hemoglobin, we found that the $^1\text{O}_2$ dose deposited with mTHPC-PDT was about 5.3 times higher than that obtained with Photofrin-PDT for equivalent rates of photon absorption. Using dose simulations and by varying the input photophysical parameters we establish that this enhanced $^1\text{O}_2$ dose with mTHPC can be accounted for on the basis of its higher extinction at the PDT treatment wavelength and a lower value of $k_{\text{os}}/k_{\text{oa}}[\text{A}]$. A lower $k_{\text{os}}/k_{\text{oa}}[\text{A}]$ value implies that, compared to Photofrin-PDT,

an mTHPC-PDT generated $^1\text{O}_2$ molecule has a greater probability of reacting with cellular substrates. This suggests that either mTHPC is inherently more photostable than Photofrin or that the substrates at the sites of mTHPC localization are more susceptible to $^1\text{O}_2$ -induced damage. The ~ 5.3 -fold enhanced $^1\text{O}_2$ dose with mTHPC-PDT, combined with the fact that the mTHPC incubation concentration was a factor of approximately 33 lower than Photofrin, resulted in an enhanced photodynamic efficacy with mTHPC of ~ 175 -fold.

We have thus shown results from detailed analysis which establishes that the higher potency of mTHPC compared to other prominent sensitizers such as Photofrin can be accounted for solely on the combined basis of its remarkable tight binding ability and improved photophysical properties, especially its lower $k_{\text{os}}/k_{\text{oa}}[A]$ value and higher extinction at a more red-shifted wavelength. The measurements and calculations presented in this chapter demonstrate an extensive and thorough method that can be used to evaluate the photodynamic efficacy of other PDT sensitizers of interest.

REFERENCES

1. Ma, L., J. Moan, and K. Berg (1994) Evaluation of a new photosensitizer, meso-tetra-hydroxyphenyl-chlorin, for use in photodynamic therapy: a comparison of its photobiological properties with those of two other photosensitizers. *Int. J. Cancer* **57**: 883-8881.
2. van Geel, I. P., H. Oppelaar, Y. G. Oussoren, M. A. van der Valk, and F. A. Stewart (1995) Photosensitizing efficacy of MTHPC-PDT compared to Photofrin-PDT in the RIF1 mouse tumour and normal skin. *Int. J. Cancer* **60**: 388-394.
3. Mlkvy, P., H. Messmann, J. Regula, M. Conio, M. Pauer, C. E. Millson, A. J. MacRobert, and S. G. Bown (1998) Photodynamic therapy for gastrointestinal tumors using three photosensitizers--ALA induced PPIX, Photofrin and MTHPC. A pilot study. *Neoplasma* **45**: 157-161.
4. Savary, J. F., P. Monnier, C. Fontolliet, J. Mizeret, G. Wagnieres, D. Braichotte, and B. H. van den (1997) Photodynamic therapy for early squamous cell carcinomas of the esophagus, bronchi, and mouth with m-tetra (hydroxyphenyl) chlorin. *Arch. Otolaryngol. Head Neck Surg.* **123**: 162-168.
5. Savary, J. F., P. Grosjean, P. Monnier, C. Fontolliet, G. Wagnieres, D. Braichotte, and B. H. van den (1998) Photodynamic therapy of early squamous cell carcinomas of the esophagus: a review of 31 cases. *Endoscopy* **30**: 258-265.
6. Reuther, T., A. C. Kubler, U. Zillmann, C. Flechtenmacher, and H. Sinn (2001) Comparison of the in vivo efficiency of Photofrin II-, mTHPC-, mTHPC-PEG- and mTHPCnPEG-mediated PDT in a human xenografted head and neck carcinoma. *Lasers Surg. Med.* **29**: 314-322.
7. Ball, D. J., D. I. Vernon, and S. B. Brown (1999) The high photoactivity of m-THPC in photodynamic therapy. Unusually strong retention of m-THPC by RIF-1 cells in culture. *Photochem. Photobiol.* **69**: 360-363.

8. Hopkinson, H. J., D. I. Vernon, and S. B. Brown (1999) Identification and partial characterization of an unusual distribution of the photosensitizer meta-tetrahydroxyphenyl chlorin (temoporfin) in human plasma. *Photochem. Photobiol.* **69**: 482-488.
9. Chen, J. Y., N. K. Mak, C. M. Yow, M. C. Fung, L. C. Chiu, W. N. Leung, and N. H. Cheung (2000) The binding characteristics and intracellular localization of temoporfin (mTHPC) in myeloid leukemia cells: phototoxicity and mitochondrial damage. *Photochem. Photobiol.* **72**: 541-547.
10. Leung, W. N., X. Sun, N. K. Mak, and C. M. Yow (2002) Photodynamic effects of mTHPC on human colon adenocarcinoma cells: photocytotoxicity, subcellular localization and apoptosis. *Photochem. Photobiol.* **75**: 406-411.
11. Teiten, M. H., L. Bezdetnaya, P. Morliere, R. Santus, and F. Guillemin (2003) Endoplasmic reticulum and Golgi apparatus are the preferential sites of Foscan localisation in cultured tumour cells. *Br. J. Cancer* **88**: 146-152.
12. Redmond, R. W. and J. N. Gamlin (1999) A compilation of singlet oxygen yields from biologically relevant molecules. *Photochem. Photobiol.* **70**: 391-475.
13. Bonnett, R., P. Charlesworth, B. D. Djelal, S. Foley, D. J. McGarvey, and T. G. Truscott (1999) Photophysical properties of 5,10,15,20-tetrakis (m-hydroxyphenyl)-porphyrin (m-THPP), 5,10,15,20-tetrakis (m-hydroxyphenyl)chlorin (m-THPC) and 5,10,15,20-tetrakis (m-hydroxyphenyl) bacterichlorin (m-THPBC): a comparative study. *J. Chem. Soc. Perkin Trans.* **2**: 325-328.
14. Nichols, M. G. and T. H. Foster (1994) Oxygen diffusion and reaction-kinetics in the photodynamic therapy of multicell tumor spheroids. *Phys. Med Biol.* **39**: 2161-2181.

15. Georgakoudi, I., M. G. Nichols, and T. H. Foster (1997) The mechanism of Photofrin photobleaching and its consequences for photodynamic dosimetry. *Photochem. Photobiol.* **65**: 135-144.
16. Georgakoudi, I. and T. H. Foster (1998) Singlet oxygen- versus nonsinglet oxygen-mediated mechanisms of sensitizer photobleaching and their effects on photodynamic dosimetry. *Photochem. Photobiol.* **67**: 612-625.
17. Mueller-Klieser, W. (1984) Method for the determination of oxygen consumption rates and diffusion coefficients in multicellular spheroids. *Biophys. J.* **46**: 343-348.
18. Georgakoudi, I. (1998) *Effects of photosensitizer bleaching and localization on photodynamic oxygen consumption and dosimetry*. Ph.D. Thesis. University of Rochester.
19. Coutier, S., S. Mitra, L. N. Bezdetnaya, R. M. Parache, I. Georgakoudi, T. H. Foster, and F. Guillemain (2001) Effects of fluence rate on cell survival and photobleaching in meta-tetra-(hydroxyphenyl)chlorin-photosensitized Colo 26 multicell tumor spheroids. *Photochem. Photobiol.* **73**: 297-303.
20. Nichols, M. G. (1996) *Transport of oxygen and light in model tumor systems*. Ph.D. Thesis. University of Rochester.
21. Bellnier, D. A., G. R. Prout, Jr., and C. W. Lin (1985) Effect of 514.5-nm argon ion laser radiation on hematoporphyrin derivative-treated bladder tumor cells in vitro and in vivo. *J. Natl. Cancer Inst.* **74**: 617-625.
22. Foster, T. H., S. L. Gibson, and R. F. Raubertas (1996) Response of Photofrin-sensitized mesothelioma xenografts to photodynamic therapy with 514 nm light. *Br. J. Cancer* **73**: 933-936.
23. Foster, T. H., D. F. Hartley, M. G. Nichols, and R. Hilf (1993) Fluence rate effects in photodynamic therapy of multicell tumor spheroids. *Cancer Res.* **53**: 1249-1254.
24. Patterson, M. S., B. C. Wilson, and R. Graff (1990) In vivo tests of the concept of photodynamic threshold dose in normal rat liver photosensitized

- by aluminum chlorosulphonated phthalocyanine. *Photochem. Photobiol.* **51**: 343-349.
25. Hadjur, C., N. Lange, J. Rebstein, P. Monnier, B. H. van den, and G. Wagnieres (1998) Spectroscopic studies of photobleaching and photoproduct formation of meta (tetrahydroxyphenyl) chlorin (m-THPC) used in photodynamic therapy. The production of singlet oxygen by m-THPC. *J. Photochem. Photobiol. B* **45**: 170-178.
 26. Dysart, J. S., M. S. Patterson, T. J. Farrell, and G. Singh (2002) Relationship between mTHPC fluorescence photobleaching and cell viability during in vitro photodynamic treatment of DP16 cells. *Photochem. Photobiol.* **75**: 289-295.
 27. Finlay, J. C., S. Mitra, and T. H. Foster (2002) In vivo mTHPC photobleaching in normal rat skin exhibits unique irradiance-dependent features. *Photochem. Photobiol.* **75**: 282-288.
 28. Melnikova, V. O., L. N. Bezdetnaya, A. Y. Potapenko, and F. Guillemin (1999) Photodynamic properties of meta-tetra(hydroxyphenyl)chlorin in human tumor cells. *Radiat. Res.* **152**: 428-435.
 29. Foster, T. H., R. S. Murant, R. G. Bryant, R. S. Knox, S. L. Gibson, and R. Hilf (1991) Oxygen consumption and diffusion effects in photodynamic therapy. *Radiat. Res.* **126**: 296-303.
 30. Sitnik, T. M., J. A. Hampton, and B. W. Henderson (1998) Reduction of tumour oxygenation during and after photodynamic therapy in vivo: effects of fluence rate. *Br. J. Cancer* **77**: 1386-1394.
 31. Star, W. M., H. P. Marijnissen, van den Berg-Blok AE, J. A. Versteeg, K. A. Franken, and H. S. Reinhold (1986) Destruction of rat mammary tumor and normal tissue microcirculation by hematoporphyrin derivative photoradiation observed in vivo in sandwich observation chambers. *Cancer Res.* **46**: 2532-2540.

32. Reed, M. W., F. N. Miller, T. J. Wieman, M. T. Tseng, and C. G. Pietsch (1988) The effect of photodynamic therapy on the microcirculation. *J. Surg. Res.* **45**: 452-459.
33. van Geel, I. P., H. Oppelaar, P. F. Rijken, H. J. Bernsen, N. E. Hagemeyer, A. J. van der Kogel, R. J. Hodgkiss, and F. A. Stewart (1996) Vascular perfusion and hypoxic areas in RIF-1 tumours after photodynamic therapy. *Br. J. Cancer* **73**: 288-293.
34. Madsen, S. J., C. H. Sun, B. J. Tromberg, V. P. Wallace, and H. Hirschberg (2000) Photodynamic therapy of human glioma spheroids using 5-aminolevulinic acid. *Photochem. Photobiol.* **72**: 128-134.
35. van Geel, I. P., H. Oppelaar, J. P. Marijnissen, and F. A. Stewart (1996) Influence of fractionation and fluence rate in photodynamic therapy with Photofrin or mTHPC. *Radiat. Res.* **145**: 602-609.
36. Coutier, S., L. N. Bezdetnaya, T. H. Foster, R. M. Parache, and F. Guillemin (2002) Effect of irradiation fluence rate on the efficacy of photodynamic therapy and tumor oxygenation in meta-tetra (hydroxyphenyl) chlorin (mTHPC)-sensitized HT29 xenografts in nude mice. *Radiat. Res.* **158**: 339-345.
37. Blant, S. A., A. Woodtli, G. Wagnieres, C. Fontolliet, B. H. van den, and P. Monnier (1996) In vivo fluence rate effect in photodynamic therapy of early cancers with tetra(m-hydroxyphenyl)chlorin. *Photochem. Photobiol.* **64**: 963-968.

Chapter 3: Experimental verification of mTHPC photobleaching mechanism

3.1 Introduction

The investigation into a photosensitizer's bleaching mechanism is extremely important towards establishing the sensitizer's fluorescence as a means of monitoring PDT dosimetry. Previous studies in our laboratory have examined sensitizer photobleaching by analyzing the changes in oxygen concentration measured in EMT6 tumor spheroids during PDT irradiation and have shown that while Photofrin and ALA-induced protoporphyrin IX are bleached predominantly *via* a self-sensitized $^1\text{O}_2$ -reaction mechanism (1, 2), Nile Blue sensitizer molecules are not (2). Results reported in chapter 2 from similar

measurements suggest that the photobleaching of the potent second generation photosensitizer, meso-tetra hydroxyphenyl chlorin (mTHPC), is also $^1\text{O}_2$ -mediated. However, these oxygen measurements allow us to investigate photobleaching mechanisms only in an indirect way. The purpose of the study presented in this chapter is to investigate the sensitizer bleaching processes in a more direct manner using two experimental techniques based on measurements of mTHPC fluorescence.

In the first method we examined the influence of treatment irradiance on sensitizer photodegradation in mTHPC-sensitized Colo26 spheroids (3). Using a steady-state fluorometer, experimental measurements of the volume-averaged loss of fluorescence were obtained from suspensions of cells dissociated from PDT-treated spheroids. The results were then compared with the predictions of a mathematical model of photobleaching based on $^1\text{O}_2$ -reactions with the sensitizer ground state. The model incorporates the photophysical parameters obtained from the analysis of electrode measurements in mTHPC-sensitized EMT6 spheroids, reported in chapter 2. We observed good agreement between the measured volume-averaged loss of fluorescence in these spheroids *vs.* the simulated loss of mTHPC fluorescence calculated from the theoretical model, thus indicating that mTHPC bleaching proceeds *via* a $^1\text{O}_2$ -mediated reaction process.

A second, more powerful technique allows direct examination of the

sensitizer photobleaching process in intact spheroids during PDT. During PDT, steep gradients in oxygen are quickly established in spheroids, with central regions becoming hypoxic. The severity of this therapy-induced hypoxia is irradiance-dependent. The existence of these PDT-induced oxygen gradients creates conditions for investigation of sensitizer photobleaching mechanisms in intact spheroids. In particular, by imaging the changes in sensitizer fluorescence intensity in confocal optical sections in intact spheroids, the oxygen dependence of these processes can be determined. Towards this end, we measure the fluorescence changes in approximately 90- μm -deep optical sections of PDT-treated spheroids using a laser scanning confocal fluorescence imaging and spectroscopy system of our own design and construction (4, 5). Optical sectioning enables the observation of different photobleaching rates in different radial locations of the intact spheroid in response to irradiation and allows the direct test of candidate photobleaching processes. The strategy employed is based on specific predictions of the patterns in which sensitizer fluorescence should change as a function of radial position in $\sim 10 \mu\text{m}$ -thick optical sections during irradiation. These predictions are derived from the three distinct photobleaching mechanisms described by Georgakoudi *et al.* (1) and Georgakoudi and Foster (2). If photobleaching is mediated predominantly by $^1\text{O}_2$, fluorescence will decay initially in the spheroid outer regions, where appreciable $^1\text{O}_2$ formation is confined during the initial treatment period, and will

then progress towards the center. If the bleaching is mediated predominantly by the sensitizer triplet reactions, then fluorescence will decay most rapidly in the spheroid center, where the oxygen concentration is lowest initially and hence the triplet state concentration will be highest. If however, the bleaching proceeds mainly through reactions involving the sensitizer singlet state, then the fluorescence will diminish uniformly throughout the spheroid section due to the lack of any oxygen dependence on the sensitizer singlet state concentration. Analysis of spatially-resolved changes in the fluorescence during PDT indicates that mTHPC bleaching has a radial dependence consistent with changes in PDT-induced oxygen gradients. We observe that following a modest initial loss of fluorescence throughout the optical section, subsequent irradiation preferentially bleaches mTHPC in the outermost regions of the spheroid where oxygen is most available.

3.2 Experimental Methods and Results

3.2.1 Studies examining loss of mTHPC fluorescence in PDT-treated spheroids and comparison with simulated results based on $^3\text{O}_2$ concentration measurements

Experiments were performed which investigated the influence of irradiance on mTHPC fluorescence loss during PDT of Colo26 spheroids (3). The

experimental protocol for spheroid culture, photosensitizer incubation and PDT irradiation were identical to the procedure described in section 2.2.4 of chapter 2. Briefly, 500- μm diameter spheroids were incubated with $5\ \mu\text{g mL}^{-1}$ mTHPC for 24 hours. Following incubation of control and PDT-treated groups, each consisting of approximately 30 spheroids, the groups were placed in single wells of a 24-well cell culture plate, each well containing 1 mL of culture medium. Spheroids in the PDT-treated groups were exposed to increasing fluences delivered at irradiances of 5, 30 or $90\ \text{mW cm}^{-2}$.

mTHPC fluorescence was measured in suspensions of cells from the spheroids that were dissociated immediately after irradiation. Steady-state emission spectra of the cells were recorded using a luminescence spectrometer (Perkin–Elmer LS50B). mTHPC fluorescence was excited with 422 nm and emission spectra were collected in the wavelength range between 600 and 760 nm. mTHPC photobleaching in response to the various irradiation protocols was analyzed as changes in the number of counts observed at the peak of the mTHPC fluorescence emission spectrum (650 nm) and normalized to the average protein content (3). The PDT-induced mTHPC fluorescence changes were expressed as a percentage of controls (mTHPC, no light). The resulting data are plotted in Figure 3.1. The rate of the irradiation-induced decay of mTHPC fluorescence intensity increased considerably with decreasing irradiance.

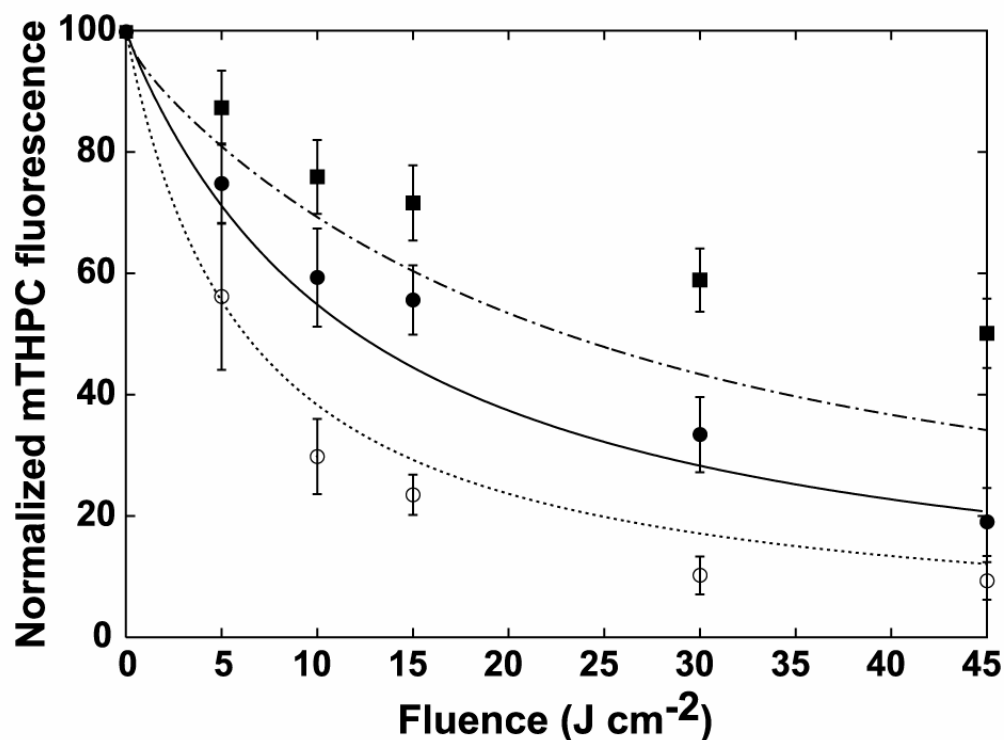


Figure 3.1. Fluorescence of mTHPC measured in Colo 26 cells after photodynamic treatment of intact spheroids performed at fluences from 5 to 45 J cm⁻² delivered at irradiances of 5 (O), 30 (●), or 90 (■) mW cm⁻². Data are normalized to the fluorescence of mTHPC-sensitized spheroids that were not irradiated. Experimental results are compared to mathematical predictions of the fluorescence based on a ¹O₂-mediated photobleaching mechanism. Simulations were performed for the three irradiances used in the experiments: 5 (---); 30 (—); and 90 (-·-) mW cm⁻².

Notably, with the lowest fluence of 5 J cm^{-2} delivered at 5 mW cm^{-2} approximately 50% of the mTHPC fluorescence remained, while with the same fluence delivered at 90 mW cm^{-2} , 85% of the fluorescence intensity remained. With the highest fluence of 45 J cm^{-2} , the loss of mTHPC fluorescence was 50, 80 and 90% in response to irradiances of 90, 30 and 5 mW cm^{-2} , respectively. These observations of an inverse irradiance dependence in mTHPC bleaching indicates that it photodegrades predominantly *via* an oxygen-dependent mechanism.

Computer simulations of the volume-averaged loss of mTHPC fluorescence in spheroids subjected to mTHPC-sensitized PDT were conducted using methods that have been described in detail previously (2). Values for the photophysical parameters of mTHPC needed for the simulations were determined experimentally from analysis of microelectrode measurements of the oxygen concentration at the edge of individual, mTHPC-sensitized EMT6 spheroids during irradiation as described in section 2.2.3.

Under conditions in which photobleaching takes place through $^1\text{O}_2$ reactions, the ground state sensitizer concentration in the spheroid, $[S_0](r, t)$, can be written as

$$[S_0](r, t) = [S_0](r, 0) \exp\left(-\frac{k_{os}}{k_{oa}[A]_0} \int_0^t \Gamma_{PDT}(t') dt'\right), \quad (1)$$

where $[S_0](r, 0)$ is the initial concentration of mTHPC in the spheroid prior to irradiation. Thus, in order to compare these experimental results with those of the simulations, eqn. (1) was integrated over the volume of the spheroid for a time corresponding to the particular irradiation protocol. As mentioned in chapter 2 (section 2.2.5), under the conditions of PDT treatment of Colo26 spheroids, oxygen depletion in the bulk medium is significant at irradiances of 90 and 30 mW cm^{-2} . Therefore, the changes in oxygen concentration of the bulk medium were incorporated as a boundary condition in the simulations, to be adjusted at each time step.

The results of these simulations are plotted with the experimental data in Fig. 3.1. We emphasize that the curves depict the results of a direct calculation of the normalized fluorescence averaged over the volume of the spheroid. They are neither a fit nor are they informed by the fluorescence measurements in any way. The calculated fluorescence for the three irradiances followed the trends that were evident in the experimental data, although the simulation appeared to underestimate systematically the measured fluorescence for the 90 mW cm^{-2} case, especially for the highest fluences. This result may reflect the fact that, for this highest irradiance, the extent of the oxygen consumption in the bulk medium was not reported accurately in our measurement and was therefore not incorporated entirely correctly in the simulation.

3.2.2 Test of mTHPC's bleaching mechanism using confocal optical sectioning in intact spheroids

3.2.2.1 *Confocal fluorescence imaging and spectroscopy in spheroids during PDT*

The instrumentation used for performing confocal fluorescence imaging of the intact multicell tumor spheroids has been described in detail previously (4-6). The setup (Figure 3.2) consists of a home-built laser scanning confocal imaging system attached to an inverted Nikon Diaphot microscope. Prior to imaging, the alignment of the confocal system is checked by performing an edge response measurement. Figure 3.3 shows the result of a typical fluorescence edge response measurement used to estimate the optical section thickness (axial resolution of the system). The plot is obtained by recording the fluorescence signal as the microscope objective is advanced axially toward a cover slip dish containing $0.7 \mu\text{g mL}^{-1}$ rhodamine 6G. The section thickness is obtained by measuring the objective translation distance necessary to increase the fluorescence from 20% to 80% of the maximum signal obtained with the focus inside the medium. Using this criterion, we find that the 10X, 0.5 NA objective in combination with a 75- μm diameter pinhole gives a 20% – 80% edge response of about 6 μm . Location of the focus in the axial direction is accomplished

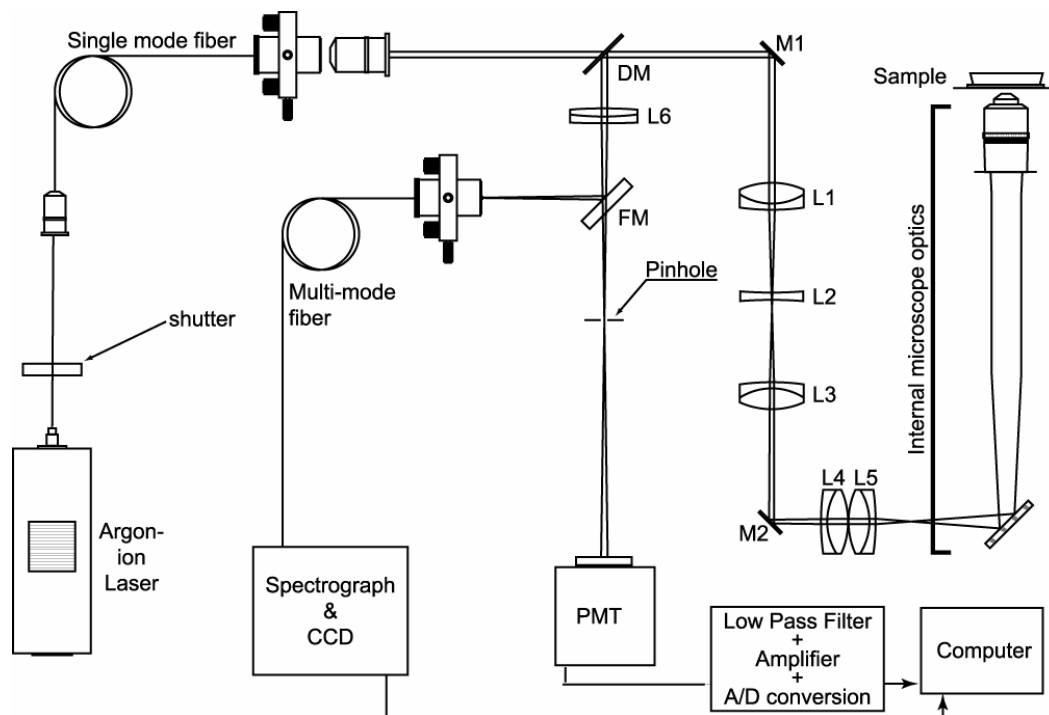


Figure 3.2. Confocal fluorescence microscope setup for imaging and spectroscopy during PDT. For the spheroid imaging, we use a 10X, 0.5 NA objective and 75- μm pinhole combination which gives an axial resolution (section thickness) of approximately 6 μm . Sensitizer fluorescence is excited with 514 nm light from the argon-ion laser. Incorporation of confocal fluorescence spectroscopy is accomplished through the use of a multimode optical fiber that plays the role of the pinhole aperture. PDT is performed on the spheroid on the microscope stage.

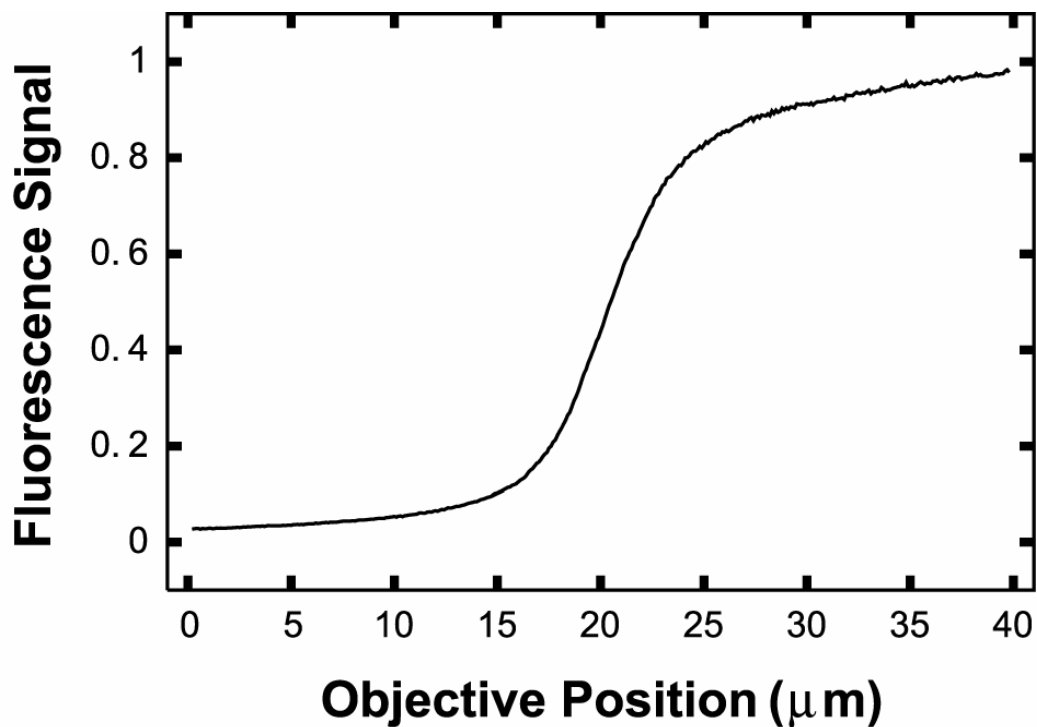


Figure 3.3. Normalized fluorescence edge response of the confocal microscope for a 10X, 0.5 NA objective. Data points were taken at 0.1 μm increments as the objective was advanced into a dish containing 0.7 μg mL⁻¹ Rhodamine 6G in DMSO. The 20% - 80% distance is 6.4 μm.

using an axial focus controller with 100 nm resolution (MAC 2000, Ludl Electronic Products, Hawthorne, NY). The axial resolution of $\sim 6 \mu\text{m}$ is adequate for the purpose of performing optical sectioning with subcellular resolution in the multicell spheroids.

Spheroids incubated with sensitizer are placed individually in a cover slip dish containing 1 mL of Hanks' Balanced Salt Solution (Gibco-BRL). The cover slip dish is then placed on the stage of the microscope. mTHPC fluorescence is excited with 514 nm light from an argon-ion laser (ILT5000, Ion Laser Technology, Salt Lake City, UT). Fluorescence collected for imaging is discriminated from excitation light using a 585 nm short pass dichroic mirror (DM) (585 dssp, Chroma Technology Corp., Brattleboro, VT) and transmitted through a long pass filter (KV 550; Schott, Duryea, PA). The fluorescence signal is then detected with a photomultiplier tube (HC-120-07 photosensor module, Hamamatsu, Bridgewater, NJ). Output from the photomultiplier is filtered, amplified and digitized at 16 bits. mTHPC fluorescence images are acquired using a $400 \mu\text{m} \times 400 \mu\text{m}$ field of view distributed over a 400×400 array of pixels resulting in an in-plane resolution of $1 \mu\text{m}/\text{pixel}$. We obtain confocal images from spheroid optical sections at a depth of 80-90 μm from the spheroids' bottom surface. The uncertainty in the exact location of the focus is due to lack of precise knowledge of the refractive index of the spheroids, as the exact depth of the optical section scales as the ratio of the sample index to the objective

immersion index (7). This depth range is chosen as it is sufficiently deep in terms of probing central regions of the spheroid while allowing for high-quality images. In particular this depth allows us to study changes in spatial distribution of the fluorescence due to oxygen gradients established during PDT.

For the purposes of acquiring fluorescence spectra during PDT, a second detection path with the ability to perform confocal spectroscopy with axial resolution and sensitivity comparable to that achieved with conventional confocal fluorescence imaging is required. This allows us to spectrally resolve the fluorescence emission from a region of a sample, such as a spheroid, rather than or in addition to recording the integrated fluorescence intensity in a particular spectral window, as is most often done in confocal imaging. Incorporation of confocal fluorescence spectroscopy is accomplished by flipping a mirror (FM) into the detection path downstream of the dichroic mirror (DM) (Figure 3.2) (5). Fluorescence is then reflected into the 50- μm core of a multimode optical fiber, which plays the role of the pinhole aperture. The output of this fiber is then lens coupled to the entrance of a grating spectrograph and dispersed onto a cooled CCD. The grating and detector area are such that approximately 340 nm of spectral coverage is available in a single acquisition. Spectral resolution is slightly better than 3 nm (FWHM) and is limited by the spectrograph's input slit width. The confocal spectroscopy system has an axial resolution of 4-5 μm (5). Typically, a confocal fluorescence image at 90- μm into a spheroid is acquired,

and regions of interest in the image are specified with a cursor. Mirror FM is then flipped up, and our custom acquisition software controlled by Labview (National Instruments) directs the excitation beam to the region of interest where a spectrum is obtained.

PDT irradiation is performed on mTHPC-sensitized spheroids on the microscope stage using 650 nm laser light from a dye laser (Model 599, Coherent, Santa Clara, CA) pumped with an argon ion laser (Innova 90, Coherent, Santa Clara, CA). The output of the dye laser is coupled into an optical fiber terminated by a gradient-index (GRIN) lens (Rawson Optics Inc., Brentwood, CA). EMT6 spheroids incubated with $5 \mu\text{g mL}^{-1}$ mTHPC for 24 hours are exposed to various fluences delivered at irradiances of 10, 25, 50 and 200 mW cm^{-2} . Irradiation is interrupted briefly at several intervals during PDT for fluorescence image acquisition (approx. 3 s per image). Diffusion of oxygen during this short interval is not a problem as the photobleaching due to PDT is irreversible.

3.2.2.2 *Image analysis*

As shown in the spectra illustrated in Figure 3.4a, in the case of mTHPC photobleaching there are no PDT-induced spectral changes such as fluorescent photoproduct formation. Therefore the bleaching pattern can be examined by just analyzing the spatially-resolved fluorescence distribution in the confocal

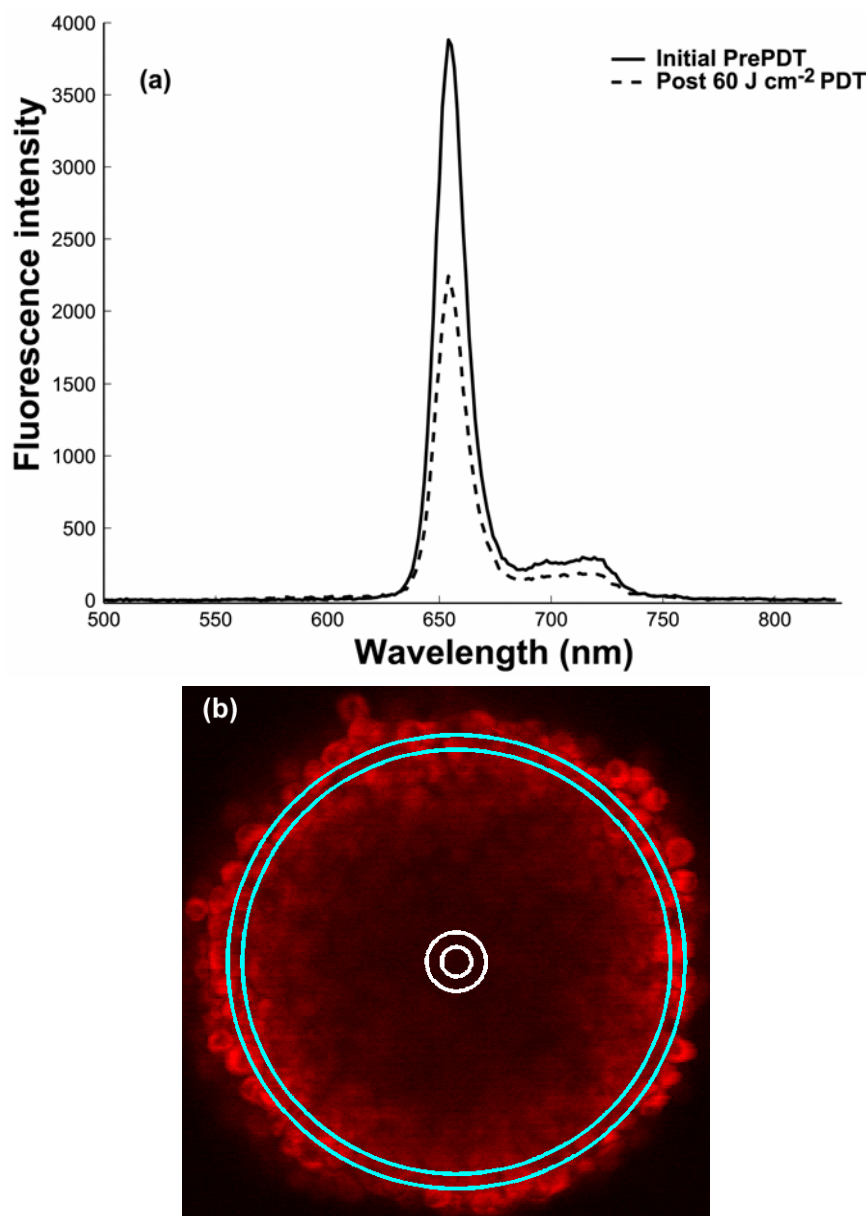


Figure 3.4. (a) Pre- and post-irradiation fluorescence spectra obtained from a region in the confocal optical section of an mTHPC-sensitized EMT6 spheroid. Except for loss in fluorescence intensity due to photobleaching, the spectral shape undergoes no observable change following PDT. (b) Optical section at 90- μm into an mTHPC-sensitized spheroid with two representative radial bins superimposed. The blue annular ring represents the outermost region and the white ring, the central region of the spheroid.

image slices. The mTHPC fluorescence distribution is quantified in the optical sections by resolving each image into a series of radial bins of equal thickness, and calculating the average fluorescence value for each bin by summing the signal from all the pixels in the bin and dividing it by the total number of pixels. Radial bins are delineated by superimposing concentric 10- μm -thick annular rings about the spheroid center onto the image (Figure 3.4b). Analysis was performed using Matlab (The Mathworks, Inc. Natick, MA).

Figure 3.5 illustrates the radially-resolved changes in mTHPC fluorescence induced by PDT. Figure 3.5a consists of representative plots of initial and post-PDT radial mTHPC distributions in a spheroid irradiated at 650 nm at 200 mW cm^{-2} . Radial bins 1 and 11 indicate the most central and the outermost regions of the spheroid, respectively. mTHPC bleaches appreciably in the outer regions of the spheroid, with negligible bleaching in radial bins 8 through 1. Figure 3.5b shows the mTHPC fluorescence distribution normalized to the initial pre-PDT distribution and shows the average of measurements from 5 spheroids. We clearly observe a distinct bleaching pattern, where following an initial loss of fluorescence throughout the optical slice, subsequent irradiation bleaches mTHPC in the spheroid periphery where oxygen is most available. Further, as the irradiation progresses from 10 to 60 J cm^{-2} we note that there is a gradual increase of mTHPC bleaching in the spheroid regions adjacent to the periphery.

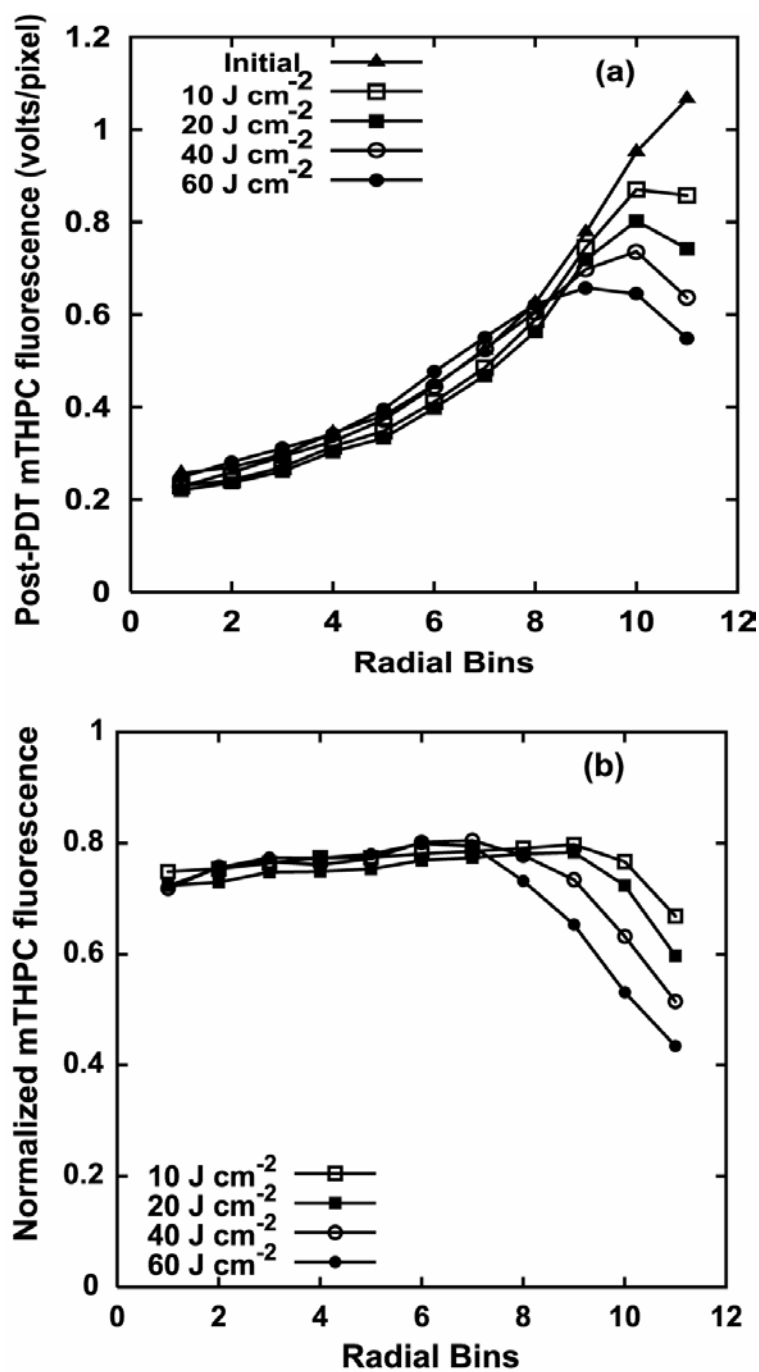


Figure 3.5. (a) Representative plots of initial and post-PDT radial mTHPC fluorescence distributions in a spheroid irradiated at 650 nm at 200 mW cm⁻². (b) Normalized fluorescence distribution, with each data point being an average of measurements from 5 spheroids. The most central region of the spheroid corresponds to radial bin 1, and the outermost region to radial bin 11.

Figure 3.6 exhibits the radially-resolved mTHPC fluorescence distributions in response to PDT performed at three irradiances of 25, 50 and 200 mW cm⁻² for the same fluence of 5 J cm⁻². We observe that with decreasing irradiance not only does mTHPC bleach more rapidly in the spheroid periphery but also the gradient in the spatially-resolved fluorescence diminishes. Both of these findings are consistent with a slower rate of PDT-induced photochemical oxygen consumption at lower irradiance and thus the availability of more oxygen throughout the spheroid. Almost no loss of fluorescence is evident in the most central region for even the lowest irradiance case, indicating that perhaps these regions are still hypoxic even under these treatment conditions.

We wanted to compare the spatially-resolved mTHPC bleaching results obtained from these optical sectioning experiments with those observed *in vivo* (8) and in dissociated Colo26 spheroids, where volume averaged fluorescence was quantified (Fig. 3.1). Towards that end, the signals in all of the radial bins in optical sections imaged at different fluences for a fixed PDT irradiance were summed. Figure 3.7 shows the total loss of mTHPC fluorescence measured from the optical section *vs.* fluence for three irradiances of 10, 50 and 200 mW cm⁻². Here again, we observe an oxygen-dependent photobleaching rate with more efficient bleaching at lower irradiances, consistent with a ¹O₂-mediated reaction process.

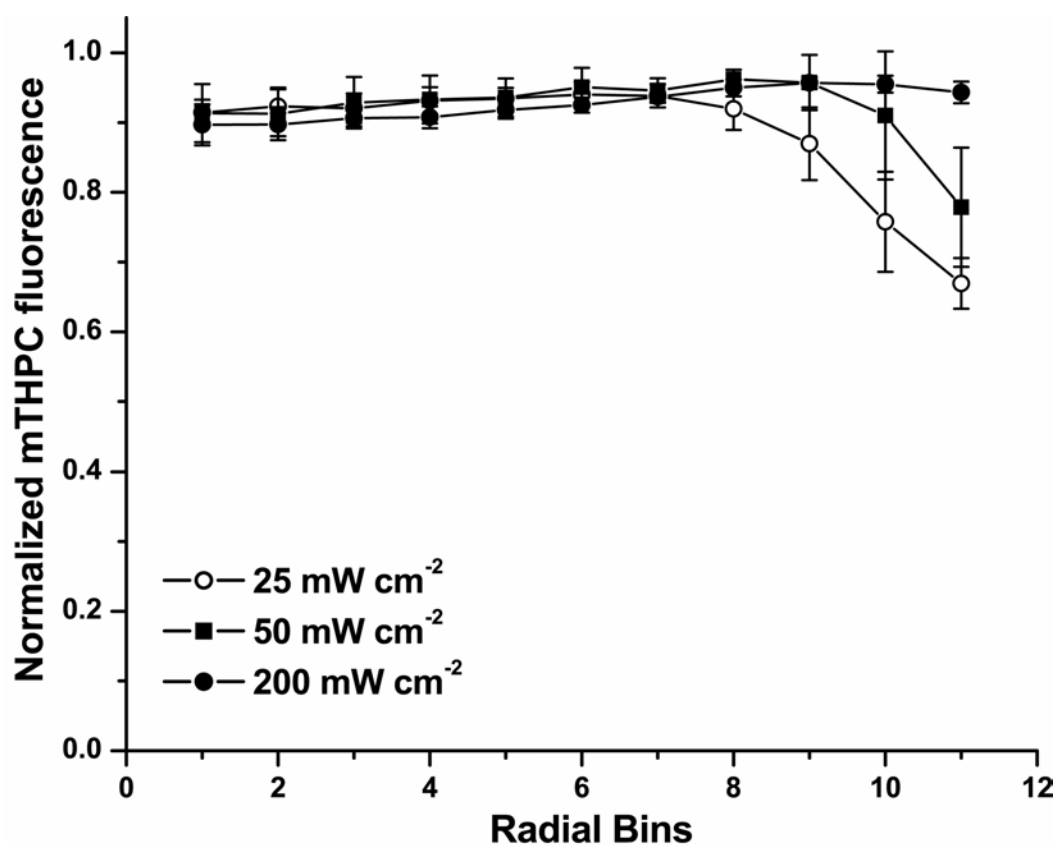


Figure 3.6. Radially-resolved fluorescence distribution in spheroids post-mTHPC-PDT at three irradiances of 25, 50 and 200 mW cm⁻² for a total fluence of 5 J cm⁻². The data points are normalized to the initial radially-resolved mTHPC fluorescence distribution.

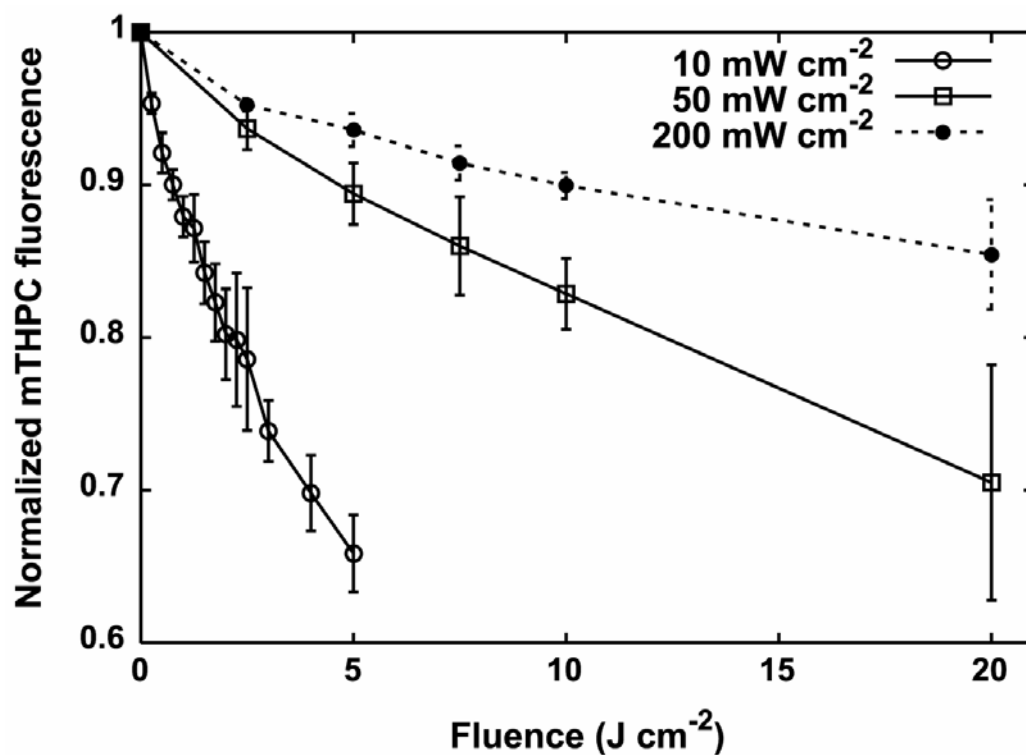


Figure 3.7. Mean mTHPC fluorescence amplitude as a function of fluence for 650 nm irradiation at 10, 50 and 200 mW cm^{-2} . Each data point represents the total mTHPC signal obtained by summing the signals over all of the radial bins of an optical section. The data points are normalized to the initial pre-PDT total mTHPC amplitude in an optical section.

3.3 Discussion

The direct investigation of the photobleaching mechanism of mTHPC using two different techniques applied to spheroid model systems is the central issue of study in this chapter. Photodegradation of mTHPC *in vivo* (8) and in solution (9) has been well documented, and the use of chemical traps indicated $^1\text{O}_2$ as a major mediator of mTHPC photobleaching in serum-enriched solution (9). Further, an approximate mathematical expression based on a $^1\text{O}_2$ -mediated photobleaching mechanism was found to be consistent with mTHPC fluorescence decay measurements observed in a clinical situation (10).

Our mTHPC photobleaching data, obtained from dissociated Colo26 spheroids following PDT treatment and illustrated in Figure 3.1, were also consistent with an oxygen-dependent mechanism with a faster rate of photobleaching at lower irradiances. Thus, with respect to their irradiance dependencies, the trends in the photobleaching kinetics and spheroid cell survival (Chapter 2, Figure 2.7) were qualitatively similar. These results were consistent with those reported by Dysart *et al.* (11) who performed PDT experiments on mTHPC-sensitized cell suspensions and observed a strong correlation between cell viability and mTHPC photobleaching. Thus, this relationship between sensitizer photodegradation and cell killing can be taken as an indication that the photobleaching of mTHPC is, using the terms introduced by Wilson *et al.* (12), coupled, *i.e.* rapid photobleaching of the photosensitizer implies an enhanced $^1\text{O}_2$

production and a concomitant biological effect.

As mentioned earlier, the fluorescence data obtained from the steady-state fluorometer experiments was analyzed using the expression for the sensitizer concentration described by eqn. (1). Its implementation was based on measured changes in the oxygen concentration at the edge of mTHPC-photosensitized EMT6 spheroids, the details of which were found to be consistent with a predominantly $^1\text{O}_2$ -mediated photobleaching mechanism, as demonstrated in chapter 2. In order to make this comparison between the experimental data and the theoretical predictions of mTHPC bleaching, we considered the bulk depletion of oxygen from the medium during irradiation of groups of mTHPC-sensitized Colo26 spheroids. Incorporation of this oxygen depletion in the bulk medium, especially at higher irradiances, had a significant effect on the simulated predictions of sensitizer photobleaching. The most direct comparison between the experimental measurements in Colo26 spheroids and the predictions of the model is shown in Fig. 3.1, where the simulated plots of the loss of mTHPC fluorescence during irradiation at three different irradiances were in reasonably good agreement with the experimental fluorescence data. The agreement for the 5 and 30 mW cm^{-2} cases was particularly good. However, the calculated fluorescence consistently underestimated the measured values for irradiation conducted at the highest irradiance of 90 mW cm^{-2} . In this case, the oxygen depletion of the bulk medium was most severe, setting up a significant gradient

in the oxygen concentration from the top to the bottom of the well during the irradiation. Because of this depth dependence, it is possible that our measurement of the oxygen concentration in the bulk medium underestimated the extent of the depletion in the vicinity of the spheroids. Incorporation of greater bulk depletion into the model would bring the theoretical estimate into better agreement with the measurements. Despite this detail, it is clear that the simulations derived from a model based on a $^1\text{O}_2$ -mediated photobleaching mechanism captured the essential features of the mTHPC fluorescence data over this range of irradiances.

Confocal optical sectioning enables a test of bleaching mechanisms in intact spheroids during PDT and allows us to verify whether the observed patterns of spatially-resolved sensitizer fluorescence loss follow the predictions based on the oxygen concentration measurements using microelectrodes. Results presented in Figure 3.5b show that as the treatment fluence increases from 10 to 60 J cm^{-2} , a greater number of sensitizer molecules are destroyed near the spheroid periphery. As the periphery is closest to the medium, and thus has the most oxygen available to it, these findings are in good agreement with the theory of $^1\text{O}_2$ -mediated mTHPC photobleaching. Bleaching of sensitizer molecules near the spheroid edge causes a reduction in the rate of photochemical oxygen consumption and allows oxygen diffusion to inner regions of the spheroid, thus resulting in a diminished gradient in the spatially-resolved mTHPC fluorescence

distribution, as is observed with increasing PDT fluences. A similar mTHPC bleaching pattern is observed in Figure 3.6, where spheroids were treated with three different irradiances of 200, 50 and 25 mW cm⁻² for the same fluence. Among the three irradiances, 25 mW cm⁻² has the lowest rate of photochemical oxygen consumption and therefore creates conditions which maintain the best oxygen tension in the spheroid. We observe that 25 mW cm⁻² causes the most efficient bleaching as well. This clearly confirms the hypothesis that mTHPC bleaches *via* an oxygen dependent mechanism.

Besides reiterating the previous finding that mTHPC photobleaching is more efficient at lower irradiances, the results illustrated in Figure 3.7 allow us to draw a comparison with our group's published report on *in vivo* mTHPC photobleaching kinetics (8). We investigated the bleaching kinetics of mTHPC during PDT performed on normal rodent skin *in vivo* with 650 nm light at irradiances of 5, 20 and 50 mW cm⁻² and reported an interesting biphasic bleaching pattern. We found that the PDT-induced loss of mTHPC fluorescence *vs.* fluence was independent of irradiance during an initial treatment period. Following this period, a pronounced discontinuity in the mTHPC bleaching rate was observed, after which the fluorescence loss proceeded in an irradiance-dependent manner consistent with a ¹O₂-mediated process. The discontinuity in the bleaching rate was evident at 20 mW cm⁻², but was most apparent for the lowest irradiance of 5 mW cm⁻². The authors also noted that the *in vivo*

fluorescence measurements had to be performed at finely spaced fluence intervals to successfully observe the biphasic phenomenon. For this very reason the results presented in Figure 3.1 are possibly inadequate to test the phenomenon in spheroids, as the fluorescence data from Colo26 spheroids were sampled only at fluences of 5, 10, 15 and 30 J cm⁻². The results presented in Figure 3.7 were obtained from experiments better informed by the *in vivo* results. Spheroids were treated with a low irradiance of 10 mW cm⁻², and fluorescence data was acquired at intervals of 0.25 J cm⁻² fluence. However, the results showed no features analogous to the two-phase bleaching observed *in vivo*. The discrepancy between the spheroid and the *in vivo* bleaching pattern may be due to processes unique to the *in vivo* environment, for example, therapy-induced physiological responses such as changes in blood flow.

REFERENCES

1. Georgakoudi, I., M. G. Nichols, and T. H. Foster (1997) The mechanism of Photofrin photobleaching and its consequences for photodynamic dosimetry. *Photochem. Photobiol.* **65**: 135-144.
2. Georgakoudi, I. and T. H. Foster (1998) Singlet oxygen- versus nonsinglet oxygen-mediated mechanisms of sensitizer photobleaching and their effects on photodynamic dosimetry. *Photochem. Photobiol.* **67**: 612-625.
3. Coutier, S., S. Mitra, L. N. Bezdetnaya, R. M. Parache, I. Georgakoudi, T. H. Foster, and F. Guillemain (2001) Effects of fluence rate on cell survival and photobleaching in meta-tetra-(hydroxyphenyl)chlorin-photosensitized Colo 26 multicell tumor spheroids. *Photochem. Photobiol.* **73**: 297-303.
4. Bigelow, C. E., C. J. Harkrider, D. L. Conover, T. H. Foster, I. Georgakoudi, S. Mitra, M. G. Nichols, and M. Rajadhyaksha (2001) Retrofitted confocal laser scanner for a commercial inverted fluorescence microscope. *Rev. Sci. Inst.* **72**: 3407-3410.
5. Bigelow, C. E., D. L. Conover, and T. H. Foster (2003) Confocal fluorescence spectroscopy and anisotropy imaging system. *Opt. Lett.* **28**: 695-697.
6. Bigelow, C. E., S. Mitra, R. Knuechel, and T. H. Foster (2001) ALA- and ALA-hexylester-induced protoporphyrin IX fluorescence and distribution in multicell tumour spheroids. *Br. J. Cancer* **85**: 727-734.
7. Visser, T. D., J. L. Oud, and G. J. Brakenhoff (1992) Refractive index and axial distance measurements in 3-D microscopy. *Optik* **90**: 17-19.
8. Finlay, J. C., S. Mitra, and T. H. Foster (2002) In vivo mTHPC photobleaching in normal rat skin exhibits unique irradiance-dependent features. *Photochem. Photobiol.* **75**: 282-288.
9. Hadjur, C., N. Lange, J. Rebstein, P. Monnier, B. H. van den, and G. Wagnieres (1998) Spectroscopic studies of photobleaching and

photoproduct formation of meta (tetrahydroxyphenyl) chlorin (m-THPC) used in photodynamic therapy. The production of singlet oxygen by mTHPC. *J. Photochem. Photobiol. B* **45**: 170-178.

10. Forrer, M., T. Glanzmann, D. Braichotte, G. Wagnieres, B. H. van den, J. F. Savary, and P. Monnier (1995) In vivo measurement of fluorescence bleaching of meso-tetra hydroxy phenyl chlorin (mTHPC) in the esophagus and the oral cavity. *Proc. SPIE* **2627**: 33-39.
11. Dysart, J. S., M. S. Patterson, T. J. Farrell, and G. Singh (2002) Relationship between mTHPC fluorescence photobleaching and cell viability during in vitro photodynamic treatment of DP16 cells. *Photochem. Photobiol.* **75**: 289-295.
12. Wilson, B. C., M. S. Patterson, and L. Lilge (1997) Implicit and explicit dosimetry in photodynamic therapy: a new paradigm. *Lasers Med. Sci.* **12**: 182-199.

Chapter 4: Investigation into Photofrin bleaching kinetics: Direct test of a new model of photobleaching

4.1 Introduction

This chapter presents an investigation of the photobleaching kinetics of Photofrin using confocal spectroscopy measurements on optical sections of intact spheroids. The study attempts to reconcile the bleaching predictions from a previously developed mathematical model and the observations of Photofrin bleaching patterns *in vivo*. As mentioned in chapter 1, Photofrin was the first photosensitizing drug to gain health agency approval for use in patients and is currently the most widely used clinically (1), however the details of its *in vivo*

dose deposition and photobleaching behavior are still not completely understood. Using the R3230AC tumor model in rats, Gibson *et al.* (2) observed significantly enhanced tumor response to Photofrin-PDT when the irradiation was divided into two fractions separated by a dark interval or when the treatment irradiance was reduced from 200 to 50 mW cm⁻². Subsequent studies using this tumor model (3, 4) and xenografts of human mesothelioma in nude mice (4, 5) confirmed this irradiance dependence and observed an even greater enhancement when the treatment was performed at 100 mW cm⁻² delivered in 30 s fractions separated by 30 s dark intervals. Later, a similar irradiance dependence was reproduced by Sitnik and Henderson (6) in mice bearing radiation-induced fibrosarcoma (RIF) tumors. Foster *et al.* (3) argued on the basis of a simple oxygen diffusion model that these effects could be explained by the photochemical consumption of oxygen, which is more significant during higher irradiance treatment. Direct measurements of tissue oxygenation during Photofrin-PDT have confirmed a significant reduction of local oxygen concentration (7, 8). In one such set of experiments, Sitnik and Henderson (9) demonstrated that the depletion of oxygen in murine RIF tumors is irradiance dependent. The quantitative predictions of the oxygen diffusion model in spherical geometry were tested by Foster *et al.* (10), who irradiated Photofrin-sensitized multicell tumor spheroids with various irradiances of 630 nm light. In that study, it was shown that decreasing the treatment irradiance decreased the fraction of cells that survived PDT, as

measured by a colony forming assay. This decrease was consistent with a model in which a central portion of the spheroid was rendered hypoxic by photochemical and metabolic oxygen consumption and hence protected from photodynamic damage. In a subsequent study, Nichols and Foster (11) made direct measurements of the oxygen consumption at the edge of spheroids during irradiation and used the oxygen diffusion-with-consumption model to estimate the reacted dose of $^1\text{O}_2$ as a function of radial position in the spheroid. These results and those of the previous animal studies are consistent with oxygen consumption and cell killing resulting from the reaction of $^1\text{O}_2$ with cellular targets. Georgakoudi *et al.* (12) extended the oxygen diffusion-with-consumption model to include the effects of photobleaching of the sensitizer. The authors used this improved model to demonstrate that the Photofrin-PDT induced oxygen concentration changes measured in spheroids are consistent with a photobleaching mechanism of Photofrin predominantly mediated by $^1\text{O}_2$.

Photobleaching of Photofrin has long been recognized as a factor in PDT. Early observations of photobleaching (13, 14) led to the development of a definition of photodynamic dose which included the effects of photobleaching (15) and to the suggestion that photobleaching could be exploited to reduce unwanted Photofrin-induced skin photosensitivity (16). A study by Spikes (17) in fluid solutions using a variety of reaction conditions examined the kinetics of photobleaching of several porphyrins, including Photofrin, and his results

suggested complex mechanisms of photobleaching of porphyrin sensitizers in cells and tissues. However, none of these studies addressed the question of whether the photobleaching of Photofrin was irradiance dependent. Based on the prior observations by Georgakoudi *et al.* (12) in Photofrin-PDT treated spheroids, it is reasonable to expect the *in vivo* photobleaching of Photofrin to be mediated by $^1\text{O}_2$ and hence dependent on the tissue oxygen concentration. It is therefore expected that low irradiance PDT will lead to an increase in the rate of photobleaching commensurate with the observed enhancement in biological response.

In a recent study performed with a fellow graduate student, J. C. Finlay, we investigated the irradiance dependence of the Photofrin bleaching kinetics during PDT of normal rat skin *in vivo*. The details of these *in vivo* experiments and analysis are described by Finlay in his Ph.D. thesis (18). Briefly, female Fischer rats were sensitized with 10 mg kg^{-1} Photofrin and irradiated 24 hours later with 514 nm light at 5 or 100 mW cm^{-2} . Fluorescence emission spectra were collected throughout treatment, and the bleaching of the sensitizer and the formation of a fluorescent photoproduct were quantified. As illustrated in Figure 4.1(a), the irradiance dependent photobleaching that is the hallmark of $^1\text{O}_2$ -mediated bleaching was not observed. Interestingly though, the accumulation of photoproduct was significantly greater at lower irradiance (Figure 4.1b). This

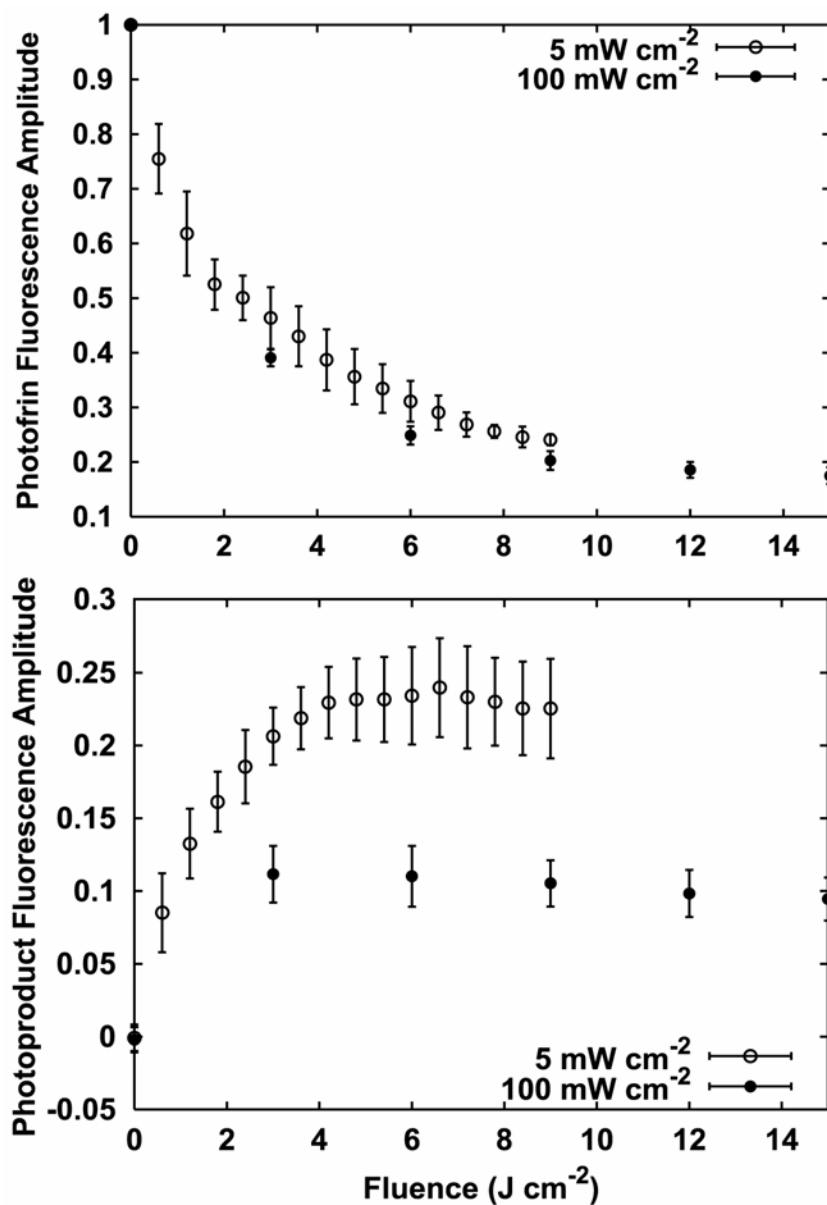


Figure 4.1. (a) Normalized Photofrin amplitude measured *in vivo* as a function of fluence for 514 nm irradiation of normal rodent skin at 5 and 100 mW cm^{-2} . (b) Normalized photoproduct amplitude as a function of fluence under the same irradiation conditions. Reproduced from Finlay (18).

trend is expected when the photoproduct is produced by the reaction of $^1\text{O}_2$ with the primary sensitizer. Indeed, experiments reported by König *et al.* (19) on the photobleaching of the Photofrin-like mixture hematoporphyrin derivative (HPD) in aqueous solution showed that photoproduct formation was inhibited by $^1\text{O}_2$ scavengers, indicating direct involvement of $^1\text{O}_2$ in photoproduct production.

In order to understand this observed discrepancy between the kinetics of Photofrin photobleaching *in vivo* and that predicted previously by Georgakoudi's analysis of oxygen measurements in spheroids (12), Finlay developed a simultaneous $^1\text{O}_2$ - and sensitizer triplet-mediated bleaching (SSTB) model (18). This theory extends the $^1\text{O}_2$ -mediated bleaching model developed by Georgakoudi *et al.* (12) to include bleaching by reactions between the triplet state sensitizer and cellular substrates. Georgakoudi *et al.* (20) had considered bleaching by reaction mechanisms other than $^1\text{O}_2$, but had not considered simultaneous $^1\text{O}_2$ and triplet sensitizer reactions as a possibility. This new extended model predicts that the relative importance of $^1\text{O}_2$ - and sensitizer triplet-mediated bleaching mechanisms is dependent on the initial concentration of the sensitizer. Specifically, when the initial sensitizer concentration is high, the photobleaching proceeds primarily through reactions involving $^1\text{O}_2$. As the initial sensitizer concentration is decreased, sensitizer triplet reactions play an increasingly important role.

To test these predictions, we measure the fluorescence bleaching during PDT in intact tumor spheroids incubated with varying concentrations of Photofrin. The existence of PDT-induced oxygen gradients in the spheroids creates conditions which allow for the testing of a sensitizer's photobleaching mechanism. The strategy is based on the specific predictions of candidate bleaching mechanisms, described in chapter 3, for the ways in which sensitizer fluorescence should change as a function of radial position in response to PDT irradiation. We demonstrate in this chapter that the direct photobleaching measurements in Photofrin-PDT treated intact spheroids can reconcile our *in vivo* observations, the SSTB model predictions, and the previously published indirect analysis of the Photofrin photobleaching mechanism through electrode measurements in spheroids.

4.2 The formulation of a simultaneous multiple bleaching mechanism (SSTB) model

The details of the SSTB model formulation have been described in J. C. Finlay's Ph.D. thesis (18). In this model, sensitizer molecules in the singlet excited state (S_1) and triplet excited state (T_1) are allowed to react with cellular targets (A). 1O_2 may react with A or with sensitizer molecules. The S_1 , T_1 and 1O_2 reactions with A deposit photodynamic dose, however in the case of S_1 and T_1 they also

result in irreversible photobleaching. In the $^1\text{O}_2$ case, bleaching and dose-deposition proceed separately. Adopting the nomenclature of the Jablonski diagram in Figure 1.1, the concentrations of ground-state and excited-states of the photosensitizer, singlet oxygen and ground-state oxygen are described by the following differential equations,

$$\frac{d[S_0]}{dt} = -I_a + k_f[S_1] + k_p[T_1] + k_{ot}[T_1][^3\text{O}_2] - k_{os}[S_0][^1\text{O}_2] \quad (1)$$

$$\frac{d[S_1]}{dt} = I_a - k_f[S_1] - k_{isc}[S_1] - k_{sa}[A][S_1] \quad (2)$$

$$\frac{d[T_1]}{dt} = k_{isc}[S_1] - k_p[T_1] - k_{ot}[T_1][^3\text{O}_2] - k_{ta}[A][T_1] \quad (3)$$

$$\frac{d[^3\text{O}_2]}{dt} = -S_\Delta k_{ot}[T_1][^3\text{O}_2] + k_d[^1\text{O}_2] \quad (4)$$

$$\frac{d[^1\text{O}_2]}{dt} = S_\Delta k_{ot}[T_1][^3\text{O}_2] - k_d[^1\text{O}_2] - k_{oa}[A][^1\text{O}_2] - k_{os}[S_0][^1\text{O}_2]. \quad (5)$$

The definitions of all the variables in the equations are listed in table 4.1. For most sensitizers, molecules in the S_1 state make the transition to T_1 or decay back to S_0 very quickly; typical S_1 lifetimes are on the order of 10 ns. Because each molecule spends only a small fraction of its time in the S_1 state, reactions between S_1 molecules and substrates are unlikely. The $k_{sa}[A][S_1]$ term in equation 2 can therefore be neglected. Because the excitation, intersystem crossing and de-excitation events are very rapid compared to bulk changes in either sensitizer or oxygen concentration, $[S_1]$, $[T_1]$, and $[^1\text{O}_2]$ rapidly come to

Table 4.1

Symbol	Definition	Units
I_a	Rate of photon absorption	$M s^{-1}$
ϕ_t	Sensitizer triplet yield	
S_Δ	Fraction of T_1 - 3O_2 reactions which produce 1O_2	
S_p	Fraction of S_0 - 1O_2 reactions which produce photoproduct	
σ_{S_0}	Absorption cross section of S_0	cm^2
Φ_i	Irradiance of incident light	$mW cm^{-2}$
$[S_0]$	Sensitizer ground state	M
$[S_1]$	Sensitizer singlet excited state	M
$[T_1]$	Sensitizer triplet excited state	M
$[P]$	Fluorescent photoproducts	M
$[^3O_2]$	Triplet ground-state oxygen	M
$[^1O_2]$	Singlet excited-state oxygen	M
$[A]$	Cellular targets	M
k_f	$S_1 \rightarrow S_0$	s^{-1}
k_p	$T_1 \rightarrow S_0$	s^{-1}
k_{isc}	$S_1 \rightarrow T_1$ (Intersystem crossing)	s^{-1}
k_d	$^1O_2 \rightarrow ^3O_2$	s^{-1}
k_{ot}	Bimolecular rate constant for reaction of 3O_2 with T_1	$M^{-1}s^{-1}$
k_{os}	Bimolecular rate constant for reaction of 1O_2 with S_0	$M^{-1}s^{-1}$
k_{oa}	Bimolecular rate constant for reaction of 1O_2 with A	$M^{-1}s^{-1}$
k_{sa}	Bimolecular rate constant for reaction of S_1 with A	$M^{-1}s^{-1}$
k_{ta}	Bimolecular rate constant for reaction of T_1 with A	$M^{-1}s^{-1}$

Table 4.1. Definitions and units of variables used in the kinetic analysis of simultaneous sensitizer triplet- and 1O_2 -mediated bleaching.

equilibrium with the concentrations of their respective ground states. Under conditions of steady-state irradiation the instantaneous equilibrium concentrations of these species can be obtained by setting their time derivatives to zero. This gives

$$[S_1] = \frac{I_a}{k_f + k_{isc}} \quad (6)$$

$$[T_1] = \frac{k_{isc}[S_1]}{k_p + k_{ot}[{}^3O_2] + k_{ta}[A]} \quad (7)$$

$$[{}^1O_2] = \frac{S_\Delta k_{ot}[T_1][{}^3O_2]}{k_d + k_{oa}[A] + k_{os}[S_0]} \quad (8)$$

Considering that the sensitizer concentration, $[S_0]$, in tissue is much lower than the effective intracellular concentration of targets for 1O_2 , we have $k_{os}[S_0] \ll k_{oa}[A]$, and therefore the term $k_{os}[S_0]$ can be dropped from the denominator of equation 8. Combining equations 6 and 7 and substituting into equation 1 gives

$$\frac{d[S_0]}{dt} = -k_{ta}[A][T_1] - k_{os}[S_0][{}^1O_2], \quad (9)$$

consistent with the interpretation that only reactions between 1O_2 and S_0 or between T_1 and cellular substrates result in irreversible loss of sensitizer concentration. Combining equations 7, 8 and 9 and noting that the triplet yield is defined, $\phi_t = k_{isc}/(k_{isc} + k_f)$, we obtain

$$[{}^1O_2] = S_\Delta \phi_t I_a \left(\frac{k_{ot}[{}^3O_2]}{k_p + k_{ot}[{}^3O_2] + k_{ta}[A]} \right) \left(\frac{1}{k_d + k_{oa}[A]} \right), \quad (10)$$

which differs from the corresponding expression for $^1\text{O}_2$ -mediated bleaching (12, Eqn. 9) only by the addition of the triplet-mediated bleaching term $k_{ta}[A]$.

It is important to consider that the rate of photon absorption, I_a , that appears in these expressions depends on the sensitizer concentration. Specifically, I_a can be expressed as

$$I_a = [S_0] \frac{\sigma_{S_0} \Phi_i}{h\nu}, \quad (11)$$

where Φ_i and $h\nu$ are the fluence rate and energy per photon of the irradiating light, respectively, and σ_{S_0} is the sensitizer's ground state absorption cross section. Finally, combining equations 6, 7, 10 and 11, we obtain the instantaneous rate of photobleaching due to simultaneous $^1\text{O}_2$ - and T_1 -mediated bleaching in terms of the concentrations of the ground state sensitizer and oxygen,

$$\begin{aligned} \frac{d[S_0]}{dt} &= -k_{ta}[A][T_1] - k_{os}[S_0][^1\text{O}_2] \\ &= - \left(\frac{(\frac{\sigma_{S_0} \Phi_i}{h\nu}) [S_0] \phi_i}{k_p + k_{ot}[^3\text{O}_2] + k_{ta}[A]} \right) \times \left(k_{ta}[A] + \frac{k_{os}[S_0] S_\Delta k_{ot}[^3\text{O}_2]}{k_d + k_{oa}[A]} \right). \end{aligned} \quad (12)$$

A complete solution of equation 12 must account for the fact that $[^3\text{O}_2]$ will be modified by treatment. This solution requires the use of numerical integration methods and the incorporation of oxygen diffusion into the model. However, the

implications of the SSTB model can be illustrated by a simplified analysis in which the local oxygen concentration is held constant. With the substitutions

$$C_1 = \frac{\left(\frac{\sigma_{S_0}\Phi_i}{h\nu}\right)\phi_i k_{ta}[A]}{k_p + k_{ot}[{}^3O_2] + k_{ta}[A]} \quad (13)$$

and

$$C_2 = \frac{k_{os}S_\Delta k_{ot}[{}^3O_2]}{k_{ta}[A](k_d + k_{oa}[A])}, \quad (14)$$

the equilibrium concentrations of 1O_2 (eqn. 10) and of T_1 (eqn. 7) can be written

$$[{}^1O_2] = \frac{C_1 C_2}{k_{os}} [S_0] \quad (15)$$

and

$$[T_1] = \frac{C_1}{k_{ta}[A]} [S_0], \quad (16)$$

respectively, reducing equation 12 to the form

$$\frac{d[S_0]}{dt} = -C_1[S_0] - C_1 C_2 [S_0]^2, \quad (17)$$

which can be solved using standard techniques to give the time-dependent sensitizer concentration as

$$[S_0]_t = \left[\left(\frac{1}{[S_0]_0} + C_2 \right) \exp(C_1 t) - C_2 \right]^{-1}, \quad (18)$$

where $[S_0]_0$ is the initial concentration of the sensitizer.

The reactions that cause irreversible photobleaching may lead to the formation of fluorescent photoproducts. Under the assumption that photoproducts are formed only as a result of reactions between S_0 and 1O_2 , the photoproduct concentration $[P]$ as a function of time is given by

$$[P]_t = \int_0^t S_p k_{os} [^1O_2]_{(t')} [S_0]_{(t')} dt' = C_1 C_2 S_p \int_0^t [S_0]_{(t')}^2 dt', \quad (19)$$

where S_p is the fraction of 1O_2 - S_0 reactions which produce photoproduct.

Many of the variables needed to calculate C_1 and C_2 have not been measured individually, although ratios among them often are available in the literature. In terms of these measurable ratios, C_1 and C_2 can be expressed as

$$C_1 = \frac{(\sigma_{S_0} \phi_t / h\nu) (k_{ta} [A] / k_{ot}) \Phi_i}{(k_p / k_{ot}) + [^3O_2] + (k_{ta} [A] / k_{ot})} \quad (20)$$

and

$$C_2 = \frac{(k_{os} / k_{oa} [A]) (\beta_{PDT} / [S_0]) [^3O_2]}{(k_{ta} [A] / k_{ot}) (\sigma_{S_0} \phi_t / h\nu)}. \quad (21)$$

β_{PDT} is the ratio of the PDT-induced oxygen consumption rate to the irradiance (12), given by

$$\beta_{PDT} = \frac{S_{\Delta} \phi_t I_{a(t=0)}}{\Phi_i} \left(\frac{k_{oa} [A]}{k_d + k_{oa} [A]} \right). \quad (22)$$

Measured values of the terms in parentheses in equations 20 and 21 for the sensitizer Photofrin are listed in table 4.2. The calculation of the quantity

Table 4.2

Variable	Value	Reference
$k_{os} / k_{oa}[A]$	76 M^{-1}	Georgakoudi <i>et al.</i> (12)
k_p / k_{ot}	$1.19 \times 10^{-5} \text{ M}$	Georgakoudi <i>et al.</i> (12)
$k_{ia}[A] / k_{ot}$	$6 \times 10^{-9} \text{ M}$	
β_{PDT}	$1.87 \times 10^{-3} \text{ M cm}^2 \text{ J}^{-1}$	Georgakoudi <i>et al.</i> (12)
$[S_0]_0$	$1.70 \times 10^{-4} \text{ M}$	Nichols and Foster (11)
$\beta_{PDT} / [S_0]$	$11 \text{ cm}^2 \text{ J}^{-1}$	Nichols and Foster (11), Georgakoudi <i>et al.</i> (12)
σ_{S_0}	$1.8 \times 10^{-17} \text{ cm}^2$	Measured in clear solution
ϕ_t	0.63	Foster <i>et al.</i> (1991)
$(\sigma_{S_0} \phi_t / h\nu)$	$29 \text{ cm}^2 \text{ J}^{-1}$	
S_p	1	

Table 4.2. Numerical values assigned to variables describing the Photofrin photobleaching kinetics of the SSTB model. The values used for the generation of figures 6, 7 and 8 are listed with the rationale for their adoption or published sources from which they were taken. S_p is set to 1 for convenience, and $(k_{ia}[A]/k_{ot})$ was chosen to illustrate the effects of triplet-mediated bleaching at various values of $[S_0]_0$. Parameters taken from Georgakoudi *et al.* (12) were measured with the sensitizer Photofrin. The values of β_{PDT} and $[S_0]_0$ are dependent on the initial Photofrin concentration in the spheroids in which they were measured.

($\beta_{\text{PDT}}/[\text{S}_0]$) requires knowledge of the sensitizer concentration in the spheroids in which β_{PDT} was measured. As described later in the text, the molar concentration of Photofrin for the microelectrode experiments performed by Georgakoudi *et al.* (12) is estimated to be 170 μM .

4.3 Experimental methods

4.3.1 Spheroid preparation

Spheroids were grown from the EMT6 mouse mammary tumor cell line. The details of spheroid culture are described in Appendix I. Once the spheroids reached a diameter of approximately 250 μm they were transferred individually to a petri dish containing BME with FCS and incubated with 2.5, 10 or 30 $\mu\text{g mL}^{-1}$ Photofrin for 24 hours. In a previous study in our laboratory, Nichols and Foster (11) used a scintillation counting assay to observe the spheroids' uptake of [^{14}C]polyhaematoporphyrin, a radioactively labelled analogue of Photofrin. In that study, it was determined that the Photofrin concentration in spheroids incubated at a concentration of 10 $\mu\text{g mL}^{-1}$ was 102 $\mu\text{g mL}^{-1}$. Photofrin is a mixture of porphyrins rather than a pure compound, and does not have a defined molecular weight. However, its molecular weight has been estimated to be approximately 600 (21). Therefore, the molar concentration of

Photofrin corresponding to $102 \mu\text{g mL}^{-1}$ is $170 \mu\text{M}$. As shown in Figure 4.2, using fluorescence measurements in optical sections of Photofrin-sensitized spheroids we observed that fluorescence counts increased linearly with drug concentration, thus verifying that drug uptake is proportional to incubation concentration within the range of incubation concentrations used in this study. The three incubation conditions therefore correspond approximately to initial sensitizer concentrations of 42.5, 170 and $510 \mu\text{M}$. After the incubation period the spheroids were placed in a coverlip dish containing HBSS for the imaging and spectroscopy measurements.

4.3.2 Confocal fluorescence spectroscopy of Photofrin-PDT treated spheroids

The formation of a fluorescent photoproduct at around 660 nm during Photofrin-PDT (22) does not allow the use of a purely imaging technique, which integrates fluorescence within a spectral window, to correctly quantify Photofrin fluorescence amplitude in the spheroid optical sections. A confocal fluorescence spectroscopy setup which allows acquisition of spectrally-resolved data is therefore used. The instrumentation has been described in detail in chapter 3 and in previously published papers (23, 24). Briefly, EMT6 spheroids ($\sim 250\text{-}\mu\text{m}$ diameter) are sensitized with Photofrin for 24 h. After the incubation period a

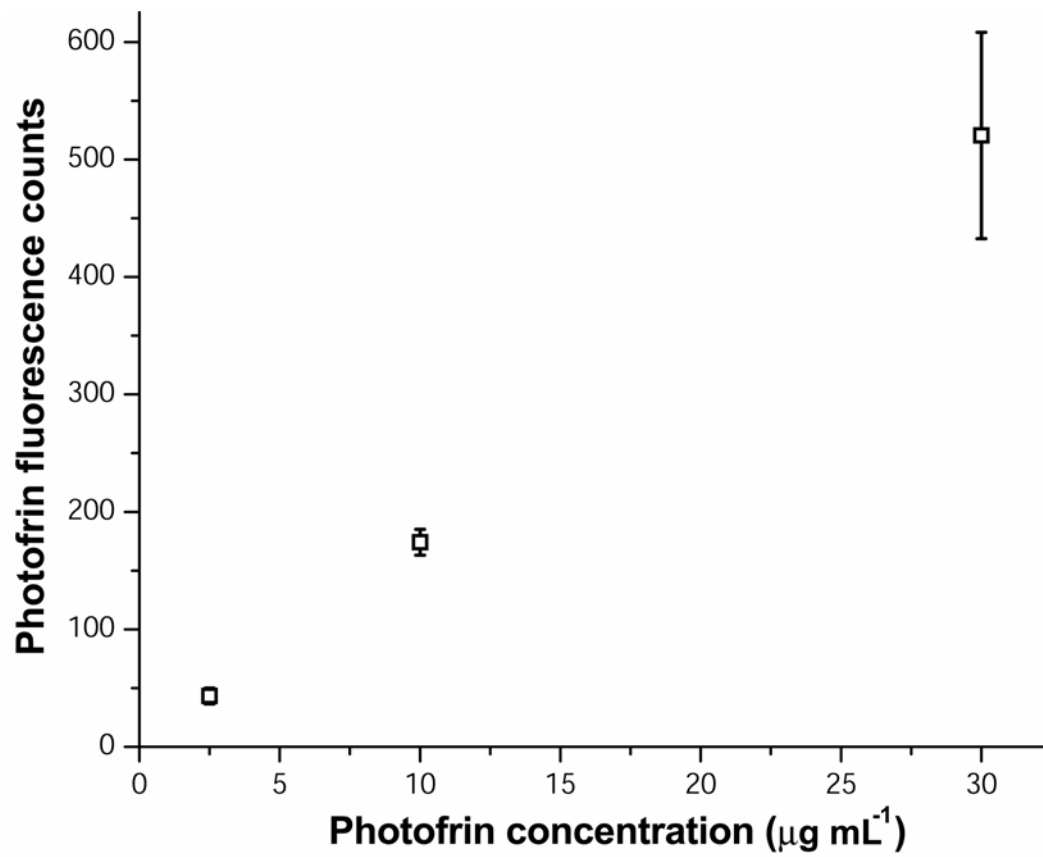


Figure 4.2. Photofrin fluorescence counts as a function of incubation concentration. The fluorescence counts were obtained from 225 µm² regions in spheroid optical sections for the three incubation concentrations of 2.5, 10 and 30 µg mL⁻¹.

single spheroid is placed in a coverslip dish filled with Hanks Balanced Salt solution (HBSS) for imaging or spectroscopy measurements. Sensitizer fluorescence is excited with 514 nm light from an argon-ion laser (ILT 5000, Ion Laser Technology, Salt Lake City, UT). An initial pre-irradiation confocal image of Photofrin fluorescence within the spheroid is acquired at a depth of 90 μm . Regions of interest (ROI) are then selected on the spheroid interior and periphery where pre- and post-irradiation fluorescence spectra are acquired (Figure 4.3). The ROI are square boxes with an area of 225 μm^2 . The typical acquisition time for each spectrum is 0.3 s. The combination of the acquisition period and the size of the ROI allows for minimal bleaching due to the fluorescence excitation beam. Confocal fluorescence spectroscopy is accomplished through the use of a multimode optical fiber that plays the role of the pinhole aperture. PDT irradiation of the spheroid is performed on the microscope stage with 514 nm light from an argon-ion laser (Innova 90, Coherent, Santa Clara, CA). Similar to the image acquisition process in chapter 3, once the initial fluorescence spectra from the ROI are collected, the confocal laser shutter is closed, and the PDT laser shutter is opened. The PDT shutter is closed and the treatment interrupted at specified time points to acquire fluorescence spectra at the corresponding fluence.

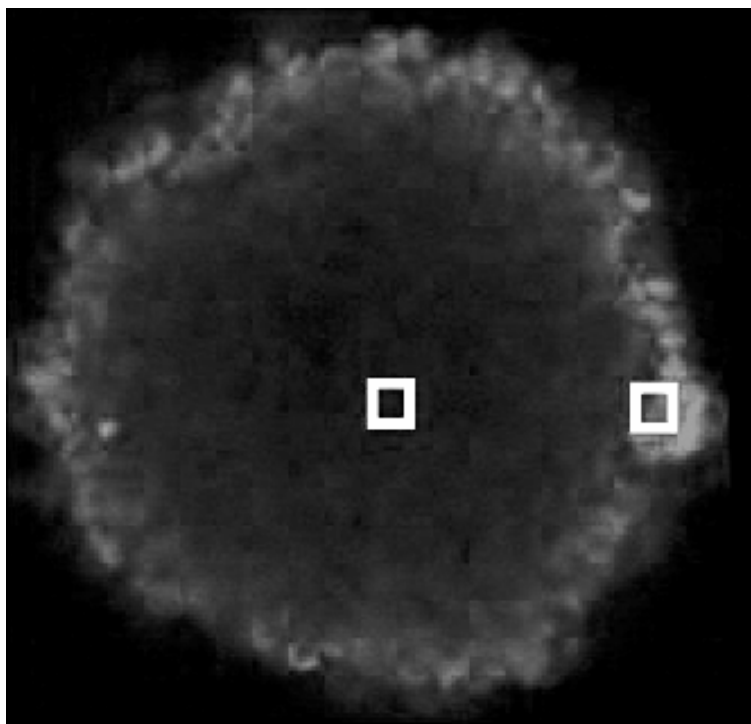


Figure 4.3. Confocal fluorescence image of a Photofrin-sensitized EMT6 spheroid with ROI boxes superimposed on the interior and periphery of the image. Fluorescence spectra are acquired from these ROI boxes.

4.3.3 Spectral analysis to quantify Photofrin and photoproduct fluorescence

The relative contributions of spheroid autofluorescence, Photofrin, and the fluorescent photoproduct to each measured spectrum are determined by a singular value decomposition (SVD) fitting algorithm based on that of Press *et al.* (25) implemented in MATLAB (The Mathworks, Inc., Natick, MA) (26). This fitting algorithm requires knowledge of the fluorescence emission spectra of these species, known as basis spectra.

The basis spectrum for spheroid autofluorescence is the average of the spectra obtained from five non-sensitized, untreated spheroids. The basis spectrum for Photofrin was constructed by averaging the emission spectra obtained from five spheroids sensitized with $10 \mu\text{g mL}^{-1}$ Photofrin. Because these spectra were acquired from spheroids, they contain a small contribution due to autofluorescence. This component was identified using the SVD fitting algorithm and subtracted prior to averaging, so that the final Photofrin basis spectrum includes only emission due to Photofrin. The use of spheroids to construct basis spectra is important because the emission spectrum of Photofrin is dependent on the local microenvironment.

In order to generate a basis spectrum for the photoproduct, six Photofrin-sensitized spheroids were treated with sufficient PDT to produce the

accumulation of significant photoproduct fluorescence with a peak at around 663 nm in the emission spectrum. In order to construct the photoproduct basis spectrum, SVD was used to identify and subtract the autofluorescence and Photofrin components from the individual spectrum from each of the spheroids. The remaining spectral data containing emission only from the fluorescent product exhibited a single, asymmetric emission peak. On averaging the photoproduct emission from the six spheroids we obtained an asymmetric peak which was fit accurately by a split Lorentzian line shape. Each basis spectrum is normalized to a peak value of 1.0 prior to fitting. The normalized basis vectors used to fit our spheroid spectra, autofluorescence (dashed line), Photofrin (solid line), and the fluorescent photoproduct (dotted line), are illustrated in Figure 4.4. While the spectral overlap among the basis spectra is significant enough to make single-wavelength measurements unreliable, the differences between spectra are sufficient that they can easily be distinguished by full spectral fitting methods such as SVD.

Each spectrum measured from the tumor spheroids during PDT is fit as a linear combination of the three basis spectra. An exponentially-weighted Fourier series is also added to the fit to account for the presence of unknown spectral components and for possible PDT-induced changes in autofluorescence, as described previously (26, 27). To summarize, the three basis spectra and the Fourier series are fit to the fluorescence data, f_{Total} , using the following equation,

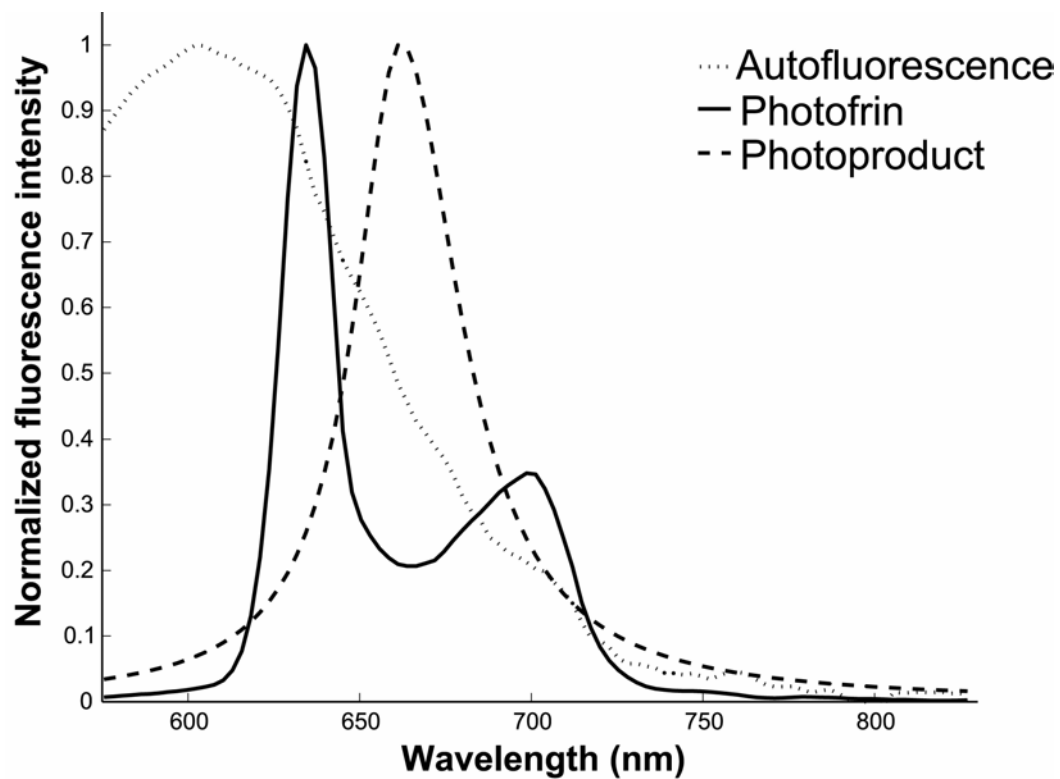


Figure 4.4. Basis spectra used for singular value decomposition fitting of fluorescence from Photofrin-PDT-treated spheroids. All spectra are based directly on spheroid measurements, as described in the text.

$$f_{\text{Total}} = A(100)f_{\text{Photofrin}} + B(100)f_{\text{Auto}} + C(100)f_{\text{Product}} + (2.0)D_0 + \sum_{k=1}^{30} (2.0e^{-k/20}) \times \left[E_k \sin\left(\frac{\pi k(\lambda - \lambda_i)}{\lambda_f - \lambda_i}\right) + F_k \cos\left(\frac{\pi k(\lambda - \lambda_i)}{\lambda_f - \lambda_i}\right) \right], \quad (23)$$

where the numbers in the small parentheses denote the weights used in the SVD fitting, as described above. The value of 20 in the exponentially decaying weights was determined empirically. The spectral amplitudes A through F_{30} are returned by the SVD algorithm. 30 is the number of cosine and sine terms included in the expansion, D_0 , E_k and F_k are the expansion coefficients and λ_f and λ_i are the final and initial wavelengths in the data set.

4.4 Results

4.4.1 Predictions of the SSTB model

Despite the previous observation of $^1\text{O}_2$ -mediated bleaching in spheroids (12), we had observed no irradiance dependence in the photobleaching of Photofrin *in vivo* (18). It is possible that these apparently conflicting results can be reconciled by a model in which the bleaching of Photofrin can proceed either *via* $^1\text{O}_2$ reactions or through reactions between the sensitizer triplet state and cellular targets, but in which only $^1\text{O}_2$ -mediated bleaching reactions lead to photoproduct formation. The kinetic equations describing such a simultaneous $^1\text{O}_2$ - and sensitizer triplet-mediated bleaching (SSTB) mechanism indicate that for a given set of physical parameters, the relative importance of the $^1\text{O}_2$ - and triplet-

mediated mechanisms is determined by the rate constants for the possible reactions of the sensitizer and oxygen and by the concentration of the sensitizer. For the purposes of the arguments outlined below, we adopted the values of rate constants and photophysical parameters listed in table 4.2.

Our *in vivo* experiments were conducted on the normal skin of rats 24 hours after *i.v.* injection of 10 mg kg⁻¹ Photofrin (18). We did not measure the concentration of Photofrin in the skin under these conditions, however it can be estimated based on values from the literature. Windahl *et al.* (28) found Photofrin concentrations in the lungs and hearts of female Wistar rats injected 1 hour previously with 10 mg kg⁻¹ Photofrin to be approximately 25 and 15 μg g⁻¹, respectively, and reported that these concentrations changed little over the 48 hours following injection. The uptake of Photofrin in mouse skin 24 hours after *i.p.* injection is similar to that in the lung and heart, as measured by Gibson *et al.* (4). Based on these studies, we estimate that the concentration of Photofrin in the skin of our rats is approximately 20 μg g⁻¹. Assuming a tissue density of 1 g cm⁻³, this corresponds to a concentration of 34 μM.

The photobleaching of Photofrin and accumulation of photoproduct predicted by the SSTB model for this initial sensitizer concentration are plotted in Figure 4.5. Both the sensitizer and photoproduct concentrations are plotted as

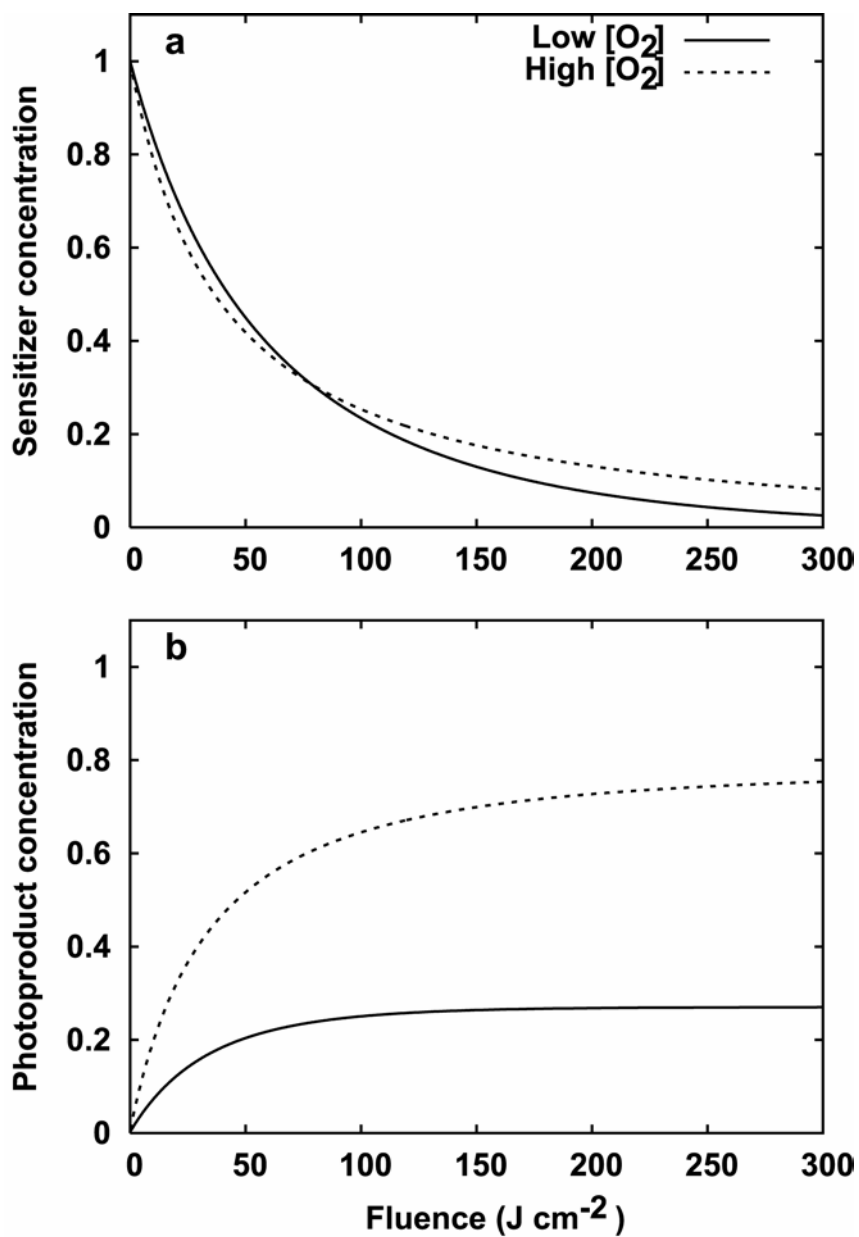


Figure 4.5. Concentrations of (a) ground state sensitizer and (b) photoproduct predicted by kinetic equations for mixed-mechanism bleaching in the case of constant oxygen for well (- - -) and poorly (—) oxygenated tissue based on a sensitizer concentration of 34 μM . Reproduced from Finlay (18).

fractions of the initial sensitizer concentration. The concentration of oxygen which is considered normal for well-oxygenated tissues is approximately $67 \mu\text{M}$ (29). The two curves shown in each panel of Figure 4.5 represent conditions of normal ($67 \mu\text{M}$) and reduced ($5 \mu\text{M}$) tissue oxygenation, corresponding to low and high irradiance irradiation, respectively. The oxygen dependence in the photobleaching profile is slight enough to be masked by experimental error, while the photoproduct accumulation is significantly greater when oxygen is abundant. The qualitative similarity between these curves and the corresponding measured *in vivo* data (Figure 4.1) is clear, although the irradiance at which a given fraction of bleaching occurs differs. In highly scattering media such as tissue illuminated by plane-wave irradiation, the irradiance within the superficial 2 mm may be higher than that of the incident beam by a factor of 3 to 4, depending on tissue optical properties and the refractive index mismatch between the tissue and the surrounding air (30, 31). Taking into account this irradiance enhancement, the bleaching and photoproduct accumulation observed *in vivo* require approximately 2.5 times less total fluence than the SSTB model predicts. Given the uncertainty in the bleaching parameters measured in spheroids, the simplification of treating living tissue as a uniformly oxygenated homogeneous medium, and the neglect of oxygen consumption and diffusion effects, this discrepancy is a minor one. For simplicity, we have assumed that S_p is equal to 1, so the concentration of photoproduct shown in Figure 4.5b is equal to the

fraction of sensitizer molecules bleached by reactions with $^1\text{O}_2$. While the bleaching profiles in the high and low oxygen cases are similar, the fraction of the bleaching mediated by $^1\text{O}_2$ and hence the accumulation of photoproduct are much greater when oxygen is abundant.

To illustrate the effect of changes in the initial sensitizer concentration, we plot the corresponding photobleaching and photoproduct profiles for $[\text{S}_0]_0$ equal to 17 and 170 μM in Figures 4.6 and 4.7, respectively. When the initial sensitizer concentration is reduced to 17 μM (Figure 4.6), sensitizer triplet reactions contribute more significantly to the bleaching process, and the bleaching is more rapid at lower oxygen concentration. As shown in Figure 4.6b, however, significantly more photoproduct is still produced in well-oxygenated tissue than in poorly oxygenated tissue. In the case of the higher initial sensitizer concentration of 170 μM , the photobleaching is dominated by $^1\text{O}_2$ reactions and exhibits the oxygen-dependence expected of $^1\text{O}_2$ -mediated bleaching, as shown in Figure 4.7a, with more rapid bleaching at higher oxygen concentration. At this high sensitizer concentration, the majority of the drug molecules are bleached by $^1\text{O}_2$ -reactions, even in poorly-oxygenated tissue, as indicated by the photoproduct accumulation plotted in Figure 4.7b.

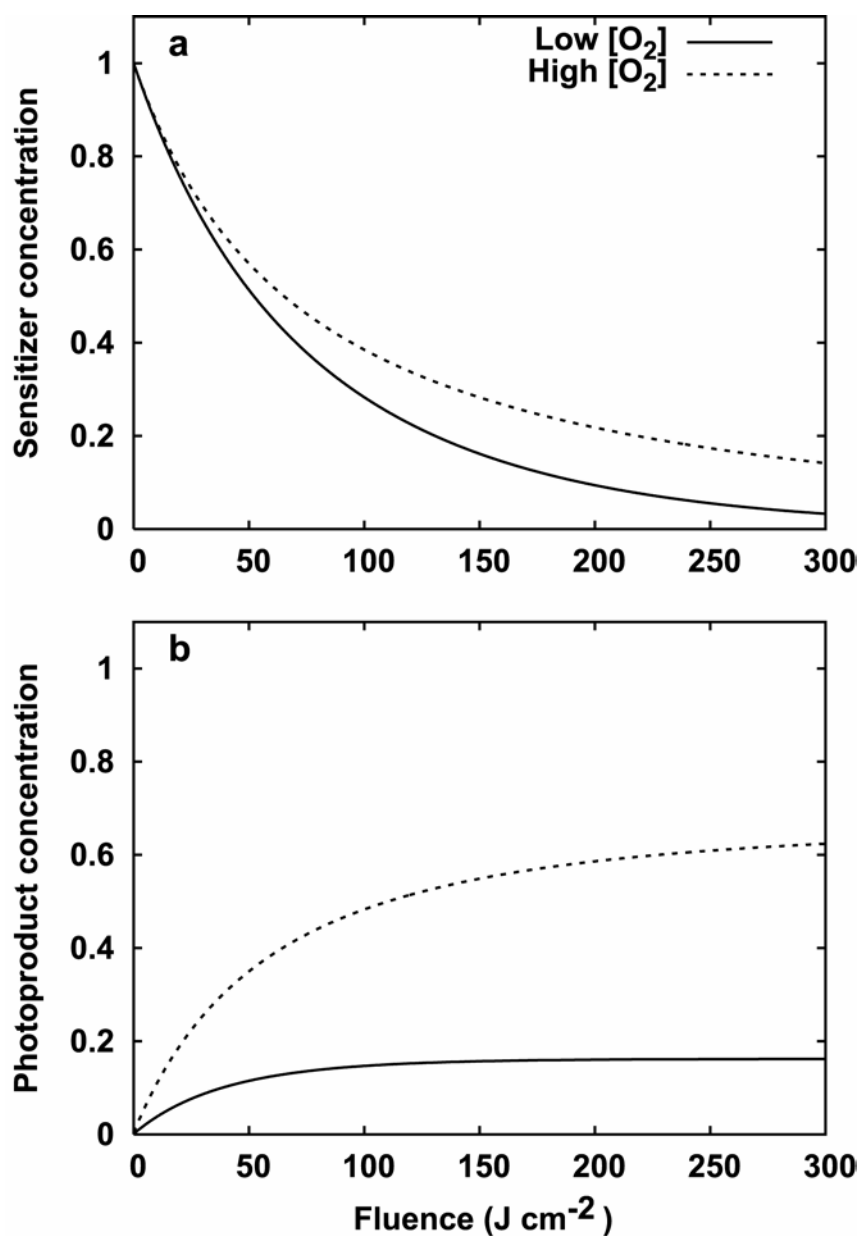


Figure 4.6. Concentrations of (a) ground state sensitizer and (b) photoproduct predicted by kinetic equations for mixed-mechanism bleaching in the case of constant oxygen for well (- - -) and poorly (—) oxygenated tissue based on a sensitizer concentration of 17 μM . Reproduced from Finlay (18).

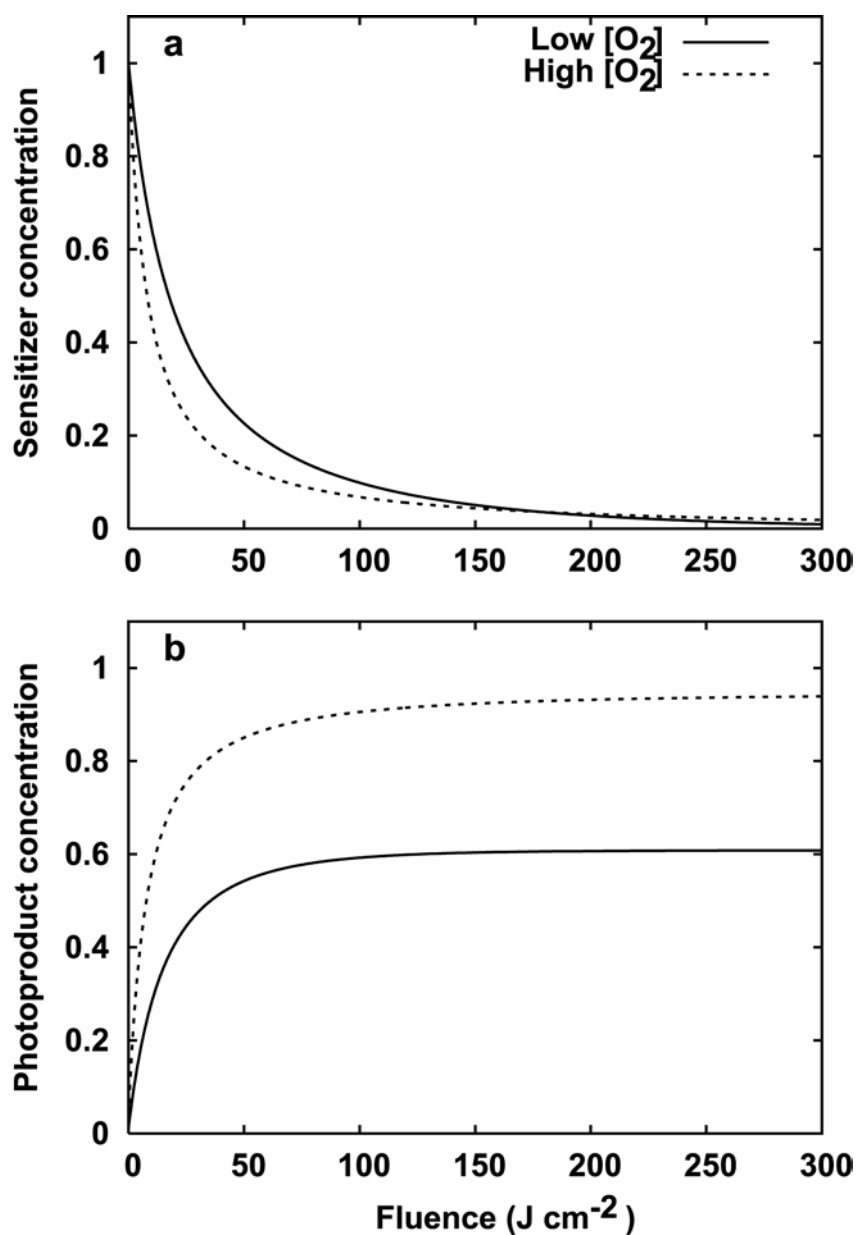


Figure 4.7. Concentrations of (a) ground state sensitizer and (b) photoproduct predicted by kinetic equations for mixed-mechanism bleaching in the case of constant oxygen for well (- - -) and poorly (—) oxygenated tissue based on a sensitizer concentration of $170 \mu\text{M}$. Reproduced from Finlay (18).

4.4.2 Fluorescence photobleaching and photoproduct formation in multicell tumor spheroids

To investigate the predictions of the SSTB model, we irradiated spheroids incubated with three different concentrations of Photofrin. Figure 4.8 shows representative spectra obtained from a spheroid peripheral region pre- and post-Photofrin-PDT. The post-irradiation spectra were obtained after the spheroid was subjected to fluences of 5 and 20 J cm⁻². An irradiance of 200 mW cm⁻² was used so as to drive steep spatial oxygen gradients in the spheroid. The Photofrin emission with a peak at 634 nm is greatly reduced relative to its pre-irradiation value, concomitant with sensitizer bleaching. Further, we observe the appearance of a rather featureless region between 650 and 680 nm in the PDT-treated spectra. This region includes a contribution from the photoproduct emission with a peak at around 663 nm, which is masked by the fact that it coincides with a valley in the emission of Photofrin. However, the SVD fitting algorithm can separate this component even though it is not directly apparent to the eye. Figure 4.9 shows SVD analysis of (a) pre-irradiation and (b) post-5 J cm⁻² treatment spheroid fluorescence spectra. The SVD algorithm identifies the contributions from Photofrin, photoproduct and autofluorescence as indicated in the Figure.

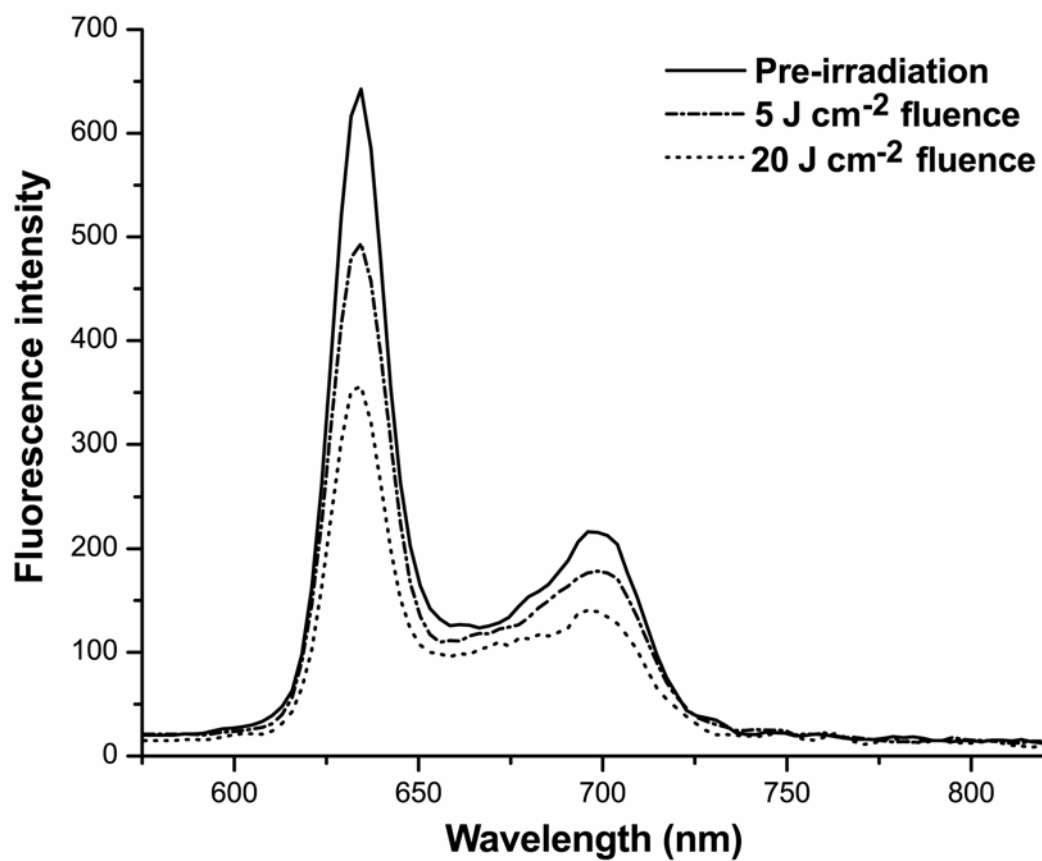


Figure 4.8. A series of fluorescence emission spectra obtained from the peripheral region of a spheroid sensitized with $30 \mu\text{g mL}^{-1}$ Photofrin during irradiation with 514 nm light administered at 200 mW cm^{-2} .

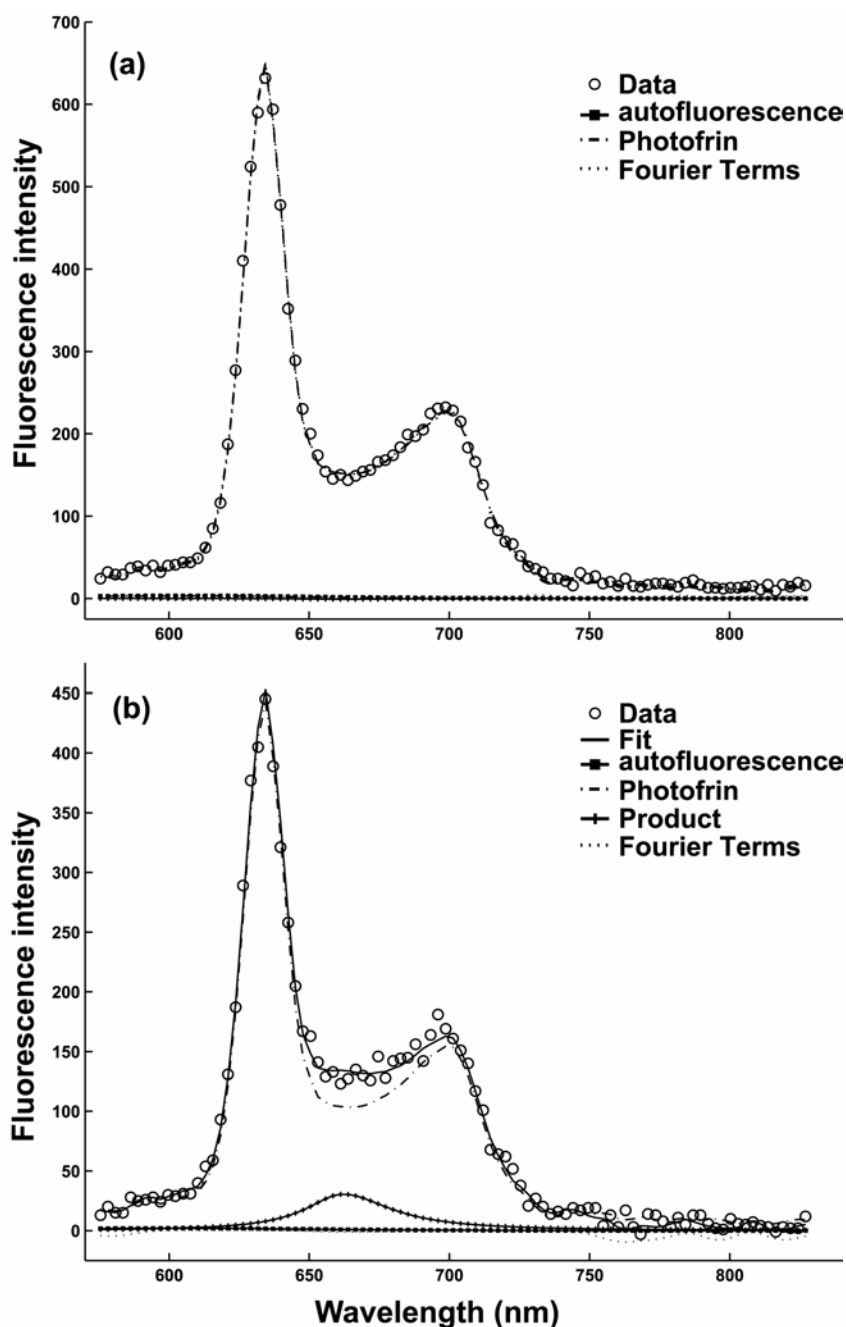


Figure 4.9. SVD analysis of typical (a) pre- and (b) post-irradiation fluorescence spectra obtained from spheroids. The spheroids were subjected to 5 J cm^{-2} of Photofrin-PDT at 200 mW cm^{-2} irradiance. The Photofrin basis spectrum accounts for the pre-irradiation fluorescence data in (a), while the analysis successfully picks out the photoproduct fluorescence component in (b) with a peak around 663 nm, and discerns its contribution from that of Photofrin.

Figure 4.10 plots the changes in Photofrin intensity and photoproduct formation measured from the interior and peripheral regions of spheroids as functions of irradiation fluence. These spheroids were sensitized with $30 \mu\text{g mL}^{-1}$ Photofrin 24 hours prior to PDT. The data points and error bars represent averages and standard deviations, respectively, from a group of 10 experiments. The Photofrin amplitudes are normalized to their initial pre-irradiation amplitude before averaging. At this relatively high concentration the bleaching of Photofrin is more rapid in the peripheral regions of the spheroid where oxygen is most available, consistent with a predominantly $^1\text{O}_2$ -mediated bleaching mechanism. The photoproduct amplitudes in Figure 4.10b are normalized to the corresponding pre-irradiation Photofrin amplitude prior to averaging. We observe that photoproduct accumulation is higher in the peripheral compared to the interior spheroid regions.

Figure 4.11 shows the Photofrin and photoproduct amplitude changes as functions of fluence when spheroids sensitized with $10 \mu\text{g mL}^{-1}$ Photofrin, an intermediate incubation concentration, were subjected to PDT. In this case, the Photofrin bleaching rates in the interior and the periphery are similar, even though the photoproduct accumulation is significantly higher in the spheroid periphery. The bleaching trend is reversed in the case where spheroids sensitized with a concentration of $2.5 \mu\text{g mL}^{-1}$ Photofrin were subjected to PDT (Figure 4.12a). In this case, we observe slightly faster bleaching in the spheroid interior

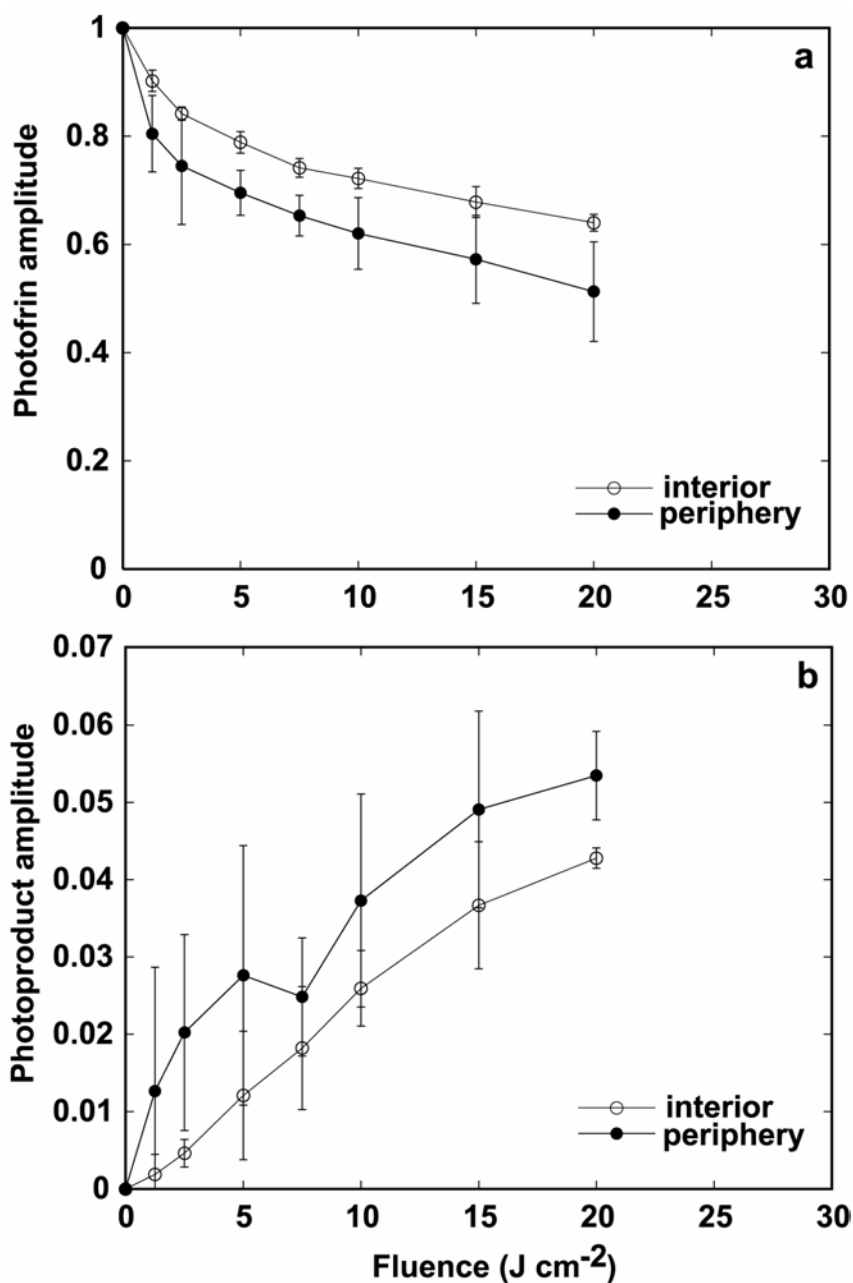


Figure 4.10. (a) Mean Photofrin amplitude as a function of PDT treatment fluence obtained from the interior and peripheral regions of spheroids sensitized with $30 \mu\text{g mL}^{-1}$ Photofrin. Data are normalized to initial pre-irradiation value before averaging. (b) Photoproduct amplitude as a function of fluence. Photoproduct amplitudes are normalized to pre-irradiation Photofrin amplitude before averaging.

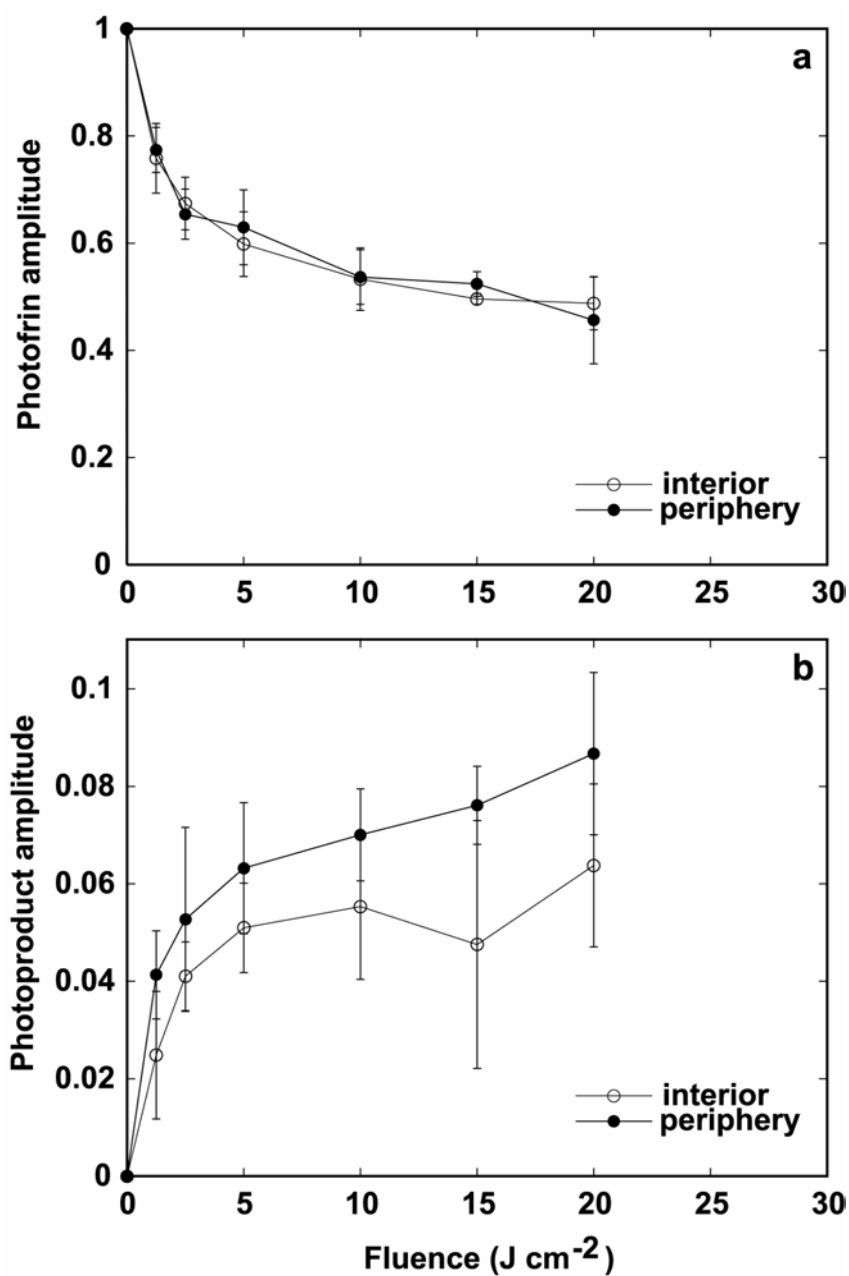


Figure 4.11. Mean (a) Photofrin and (b) photoproduct amplitude as a function of PDT treatment fluence obtained from the interior and peripheral regions of spheroids sensitized with $10 \mu\text{g mL}^{-1}$ Photofrin. Data points were calculated as described in the legend of Figure 4.10.

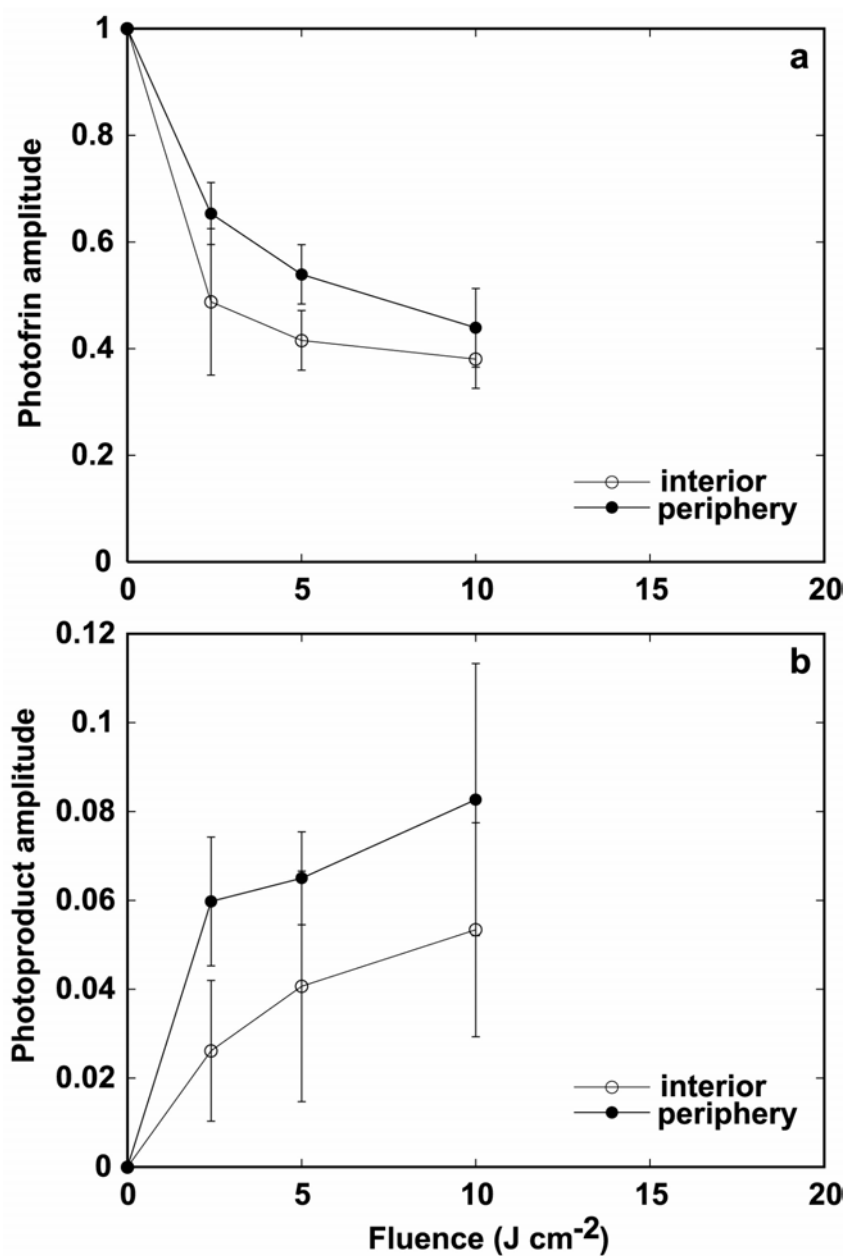


Figure 4.12. Mean (a) Photofrin and (b) photoproduct amplitude as a function of PDT treatment fluence obtained from the interior and peripheral regions of spheroids sensitized with $2.5 \mu\text{g mL}^{-1}$ Photofrin. Data points were calculated as described in the legend of Figure 4.10.

compared to the periphery, consistent with a bleaching process dominated by a sensitizer triplet-mediated mechanism. However, similar to the pattern observed for the high and intermediate concentrations, the photoproduct accumulation is significantly greater in the spheroid periphery (Figure 4.12b). The consistent pattern of greater product accumulation in the periphery for all three cases explored in these spheroid experiments indicates that irrespective of the dominant bleaching mechanism, the photoproduct formation is driven *via* reactions between $^1\text{O}_2$ and Photofrin molecules. Using confocal fluorescence spectroscopy measurements, we thus show that the kinetics of Photofrin photobleaching and photoproduct accumulation in spheroids sensitized with high, intermediate and low initial sensitizer concentrations are remarkably consistent with predictions of the SSTB model for these three concentration regimes.

As mentioned earlier, Georgakoudi *et al.* (12) reported a Photofrin bleaching mechanism consistent with a purely $^1\text{O}_2$ -mediated process using analysis of oxygen concentration changes measured in spheroids subjected to PDT. The spheroid incubation concentration of $10\ \mu\text{g mL}^{-1}$ in that study was identical to that at which we observe evidence of equal contribution from both $^1\text{O}_2$ - and sensitizer triplet-mediated bleaching reactions to Photofrin bleaching (Fig. 4.11a). The fact that Georgakoudi *et al.* did not detect the triplet bleaching mechanism in their experiments is likely due to the analysis used in that work. The authors analyzed the electrode data using either a pure $^1\text{O}_2$ - or a

fluence-dependent simple exponential bleaching process but did not consider a pure sensitizer triplet-mediated or a simultaneous mixed bleaching mechanism. In an attempt to resolve this disagreement between the direct observations of fluorescence and the previous analysis of microelectrode experiments, we decided to re-analyze the microelectrode data obtained by Georgakoudi *et al.* using a purely sensitizer triplet-mediated bleaching process. The analysis was performed using a model of oxygen diffusion with consumption that incorporated the effects of sensitizer bleaching due to reactions of excited sensitizer triplet molecules with cellular substrates. The details of the model and the fitting procedure were similar to that described in section 2.2 of chapter 2, with the rate of photochemical oxygen consumption, $\Gamma_{PDT}(r,t)$, in this case given by

$$\Gamma_{PDT}(r,t) = \Gamma_0 \left(\frac{[{}^3O_2](r,t)}{[{}^3O_2](r,t) + k_p / k_{ot}} \right) \exp \left\{ - \frac{\sigma_{SO} \Phi_t}{h\nu} \left(\frac{k_{ta}[A] / k_{ot}}{k_p / k_{ot} + [{}^3O_2](r,t)} \right) D \right\}, \quad (24)$$

where Γ_0 is the initial maximum 3O_2 consumption rate and D is the fluence. This mathematical description of the sensitizer triplet bleaching reactions was suggested by Michael Patterson (32).

A representative trace of time-dependent 3O_2 concentrations observed at the edge of a $10 \mu\text{g mL}^{-1}$ Photofrin-sensitized spheroid undergoing PDT at an irradiance of 50 mW cm^{-2} and analyzed using a purely 1O_2 -mediated and a purely sensitizer triplet-mediated bleaching mechanism is shown in Figure 4.13. While

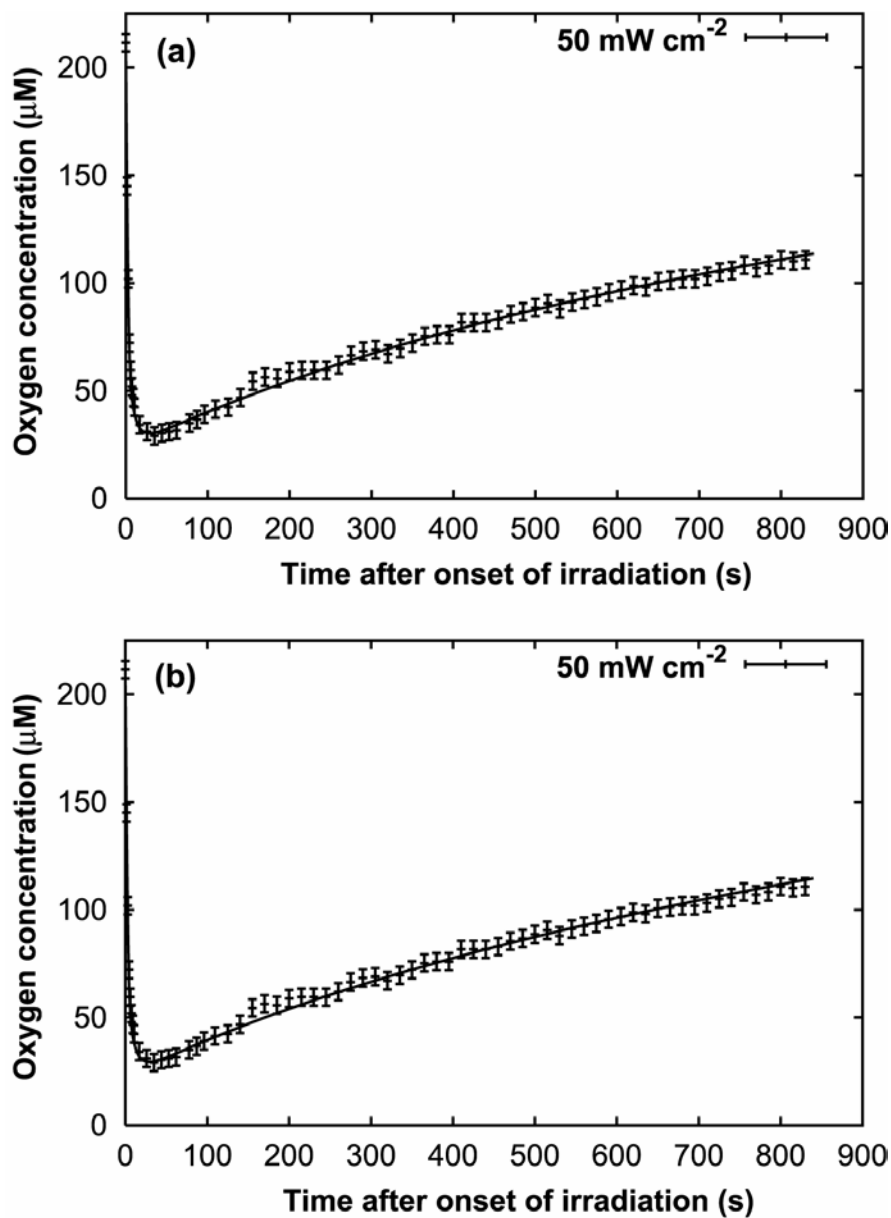


Figure 4.13. Time-dependent $^3\text{O}_2$ concentration changes recorded using a microelectrode placed at the edge of a $10 \mu\text{g mL}^{-1}$ Photofrin-sensitized spheroid during PDT. The solid line is the best fit to the data assuming (a) a $^1\text{O}_2$ bleaching model or (b) a sensitizer triplet-mediated bleaching described by eqn. 24. Error bars represent estimates of the uncertainty in the $^3\text{O}_2$ electrode measurements.

the $^1\text{O}_2$ -mediated fit was in excellent agreement with the experimental data (Fig. 4.13a), the sensitizer triplet-mediated fit also captured all of the essential features of the $^3\text{O}_2$ distribution (Fig. 4.13b). This result indicates that, rather than being in contradiction with the fluorescence measurements, a more complete analysis of the electrode data suggests that both $^1\text{O}_2$ - and sensitizer triplet-reactions contribute to Photofrin bleaching for an incubation concentration of $10 \mu\text{g mL}^{-1}$.

4.5 Discussion

The SSTB model examines the irreversible photobleaching of a sensitizer mediated by simultaneous $^1\text{O}_2$ - and sensitizer triplet-mediated reactions and predicts that the relative contributions of these two photobleaching mechanisms are dependent on the initial drug concentration. In order to test the predictions of this new theory of PDT-induced photobleaching we performed measurements in an experimental system where a range of low to high initial sensitizer concentrations can be readily obtained. In this respect, spheroids provide an ideal tumor model in which the sensitizer concentrations can be varied by controlling the incubation drug concentration. Further, as described in chapter 3, spheroids exhibit PDT-induced gradients in oxygen that allow us to clearly identify the existence of candidate bleaching mechanisms by measuring the loss of sensitizer fluorescence in their interior and peripheral regions. Fluorescence

spectroscopy performed in confocal optical sections of intact spheroids allows us to acquire emission spectra from carefully selected interior and peripheral regions.

In the case of spheroids exposed to the highest Photofrin incubation concentration of $30 \mu\text{g mL}^{-1}$, corresponding to a Photofrin concentration within the spheroid of $\sim 510 \mu\text{M}$, we observed that with increasing PDT fluences a relatively greater number of sensitizer molecules are irreversibly bleached in the well oxygenated periphery (Figure 4.10). As the peripheral regions are closest to the oxygen-rich medium, these results indicate that under these experimental conditions the initial sensitizer concentration is sufficiently high that $^1\text{O}_2$ molecules can readily react with drug molecules and thus, Photofrin bleaching is dominated by the $^1\text{O}_2$ -mediated process. The findings are in good qualitative agreement with the predictions of the mixed-mechanism bleaching theory for the highest modeled initial concentration of $170 \mu\text{M}$, where more rapid bleaching under well vs. poorly oxygenated conditions is predicted (Figure 4.7). When the spheroid incubation concentration is reduced to $10 \mu\text{g mL}^{-1}$, we observe that photobleaching rates in the periphery and the interior are nearly matched (Figure 4.11), consistent with the patterns of bleaching predicted by the theoretical model for an intermediate sensitizer concentration of $34 \mu\text{M}$ (Figure 4.5). These results suggest that at these intermediate initial Photofrin concentrations, both $^1\text{O}_2$ - and sensitizer triplet-mediated bleaching play an equally important role. Finally, for

the lowest incubation concentration of $2.5 \mu\text{g mL}^{-1}$, we observe a reversal in the bleaching pattern with increased loss of fluorescence in the interior vs. peripheral spheroid regions (Figure 4.12). These findings are in agreement with the theoretical predictions for a sensitizer concentration of $17 \mu\text{M}$ (Figure 4.6) with more rapid bleaching in poorly vs. well oxygenated conditions. In the poorly oxygenated interior spheroid regions, sensitizer triplet molecules are less likely to be quenched by molecular oxygen and therefore significant sensitizer triplet concentrations will accumulate. These spheroid results thus confirm that for this low initial Photofrin concentration, the probability of reactions between $^1\text{O}_2$ and sensitizer molecules is reduced, and reactions between sensitizer triplet molecules and cellular substrates dominate the bleaching process, resulting in more rapid sensitizer photodegradation in the spheroid interior.

For all three incubation concentrations we observe that as the treatment fluence increases, a greater concentration of photoproduct is accumulated near the spheroid periphery. As the periphery is closest to the medium and thus has the most oxygen available to it, these results indicate that the photoproducts are formed due to reactions with $^1\text{O}_2$, consistent with the findings of Konig *et al.* (19) and with our SSTB model.

Although the kinetics of Photofrin bleaching and photoproduct accumulation obtained from the fluorescence measurements in spheroids for the three concentration regimes are in agreement with the general predictions of the

SSTB model, there are consistent discrepancies in the sensitizer concentrations at which the important trends are observed. As indicated in table 4.3, we find that the phenomena defining the three concentration regimes are observed in SSTB model simulations at Photofrin concentrations that are consistently ~ 2.5 - to 5 -fold lower than they are observed experimentally. As mentioned earlier, the choice of an intermediate sensitizer concentration of $34 \mu\text{M}$ for the SSTB model simulations originated from an estimate of the Photofrin concentration in the skin of rats in our *in vivo* experiments, which was based on values reported in the literature (28). Therefore, some of the discrepancy may be due to errors in estimating Photofrin concentrations *in vivo* (28) and in spheroids (11). Other factors that could also contribute to this modest difference are uncertainty associated with numerical values assigned to the variables in the SSTB model and the fact that Photofrin's distribution in spheroids is nonuniform, as illustrated in Figure 2.3 of chapter 2, while the SSTB model assumes a homogeneous medium with uniform distributions of oxygen and sensitizer. We considered the possibility that the nonuniformity of Photofrin distribution in spheroids may be significant enough to create conditions that suggest the existence of different initial concentration regimes in the interior and peripheral spheroid regions for a given Photofrin incubation concentration. However, Photofrin concentration estimates in $20 \mu\text{m}$ -thick radial bins in the peripheral and interior regions of the

Table 4.3

Initial sensitizer concentration regime	Photofrin incubation concentration in spheroids	Estimated concentration of Photofrin in spheroids	Sensitizer concentration in the SSTB model
HIGH	30 $\mu\text{g mL}^{-1}$	510 μM	170 μM
INTERMEDIATE	10 $\mu\text{g mL}^{-1}$	170 μM	34 μM *
LOW	2.5 $\mu\text{g mL}^{-1}$	42.5 μM	17 μM

* The estimated concentration of Photofrin in skin at which an irradiance independent bleaching behavior was observed *in vivo*.

Table 4.3. Photofrin concentrations corresponding to the high, intermediate and low regimes at which experimentally observed bleaching patterns are in agreement with the general predictions of the SSTB model.

spheroid indicated that the gradient was not steep enough to support that possibility (data not shown).

For the case of spheroids sensitized with $10 \mu\text{g mL}^{-1}$ Photofrin, we addressed the apparently contradictory results between the previously performed analysis of electrode measurements, which indicated that Photofrin bleaching is predominantly mediated by $^1\text{O}_2$ -reactions (12), and the fluorescence measurements reported here (Fig. 4.11b), which strongly suggest the presence of both $^1\text{O}_2$ - and sensitizer triplet-mediated reactions in the bleaching process. A re-analysis of the electrode data confirmed that this indirect measure of Photofrin bleaching is also consistent with a sensitizer-triplet mediated mechanism and thereby reconciled the two experimental measurements.

In conclusion, the results presented in this chapter illustrate that the apparently conflicting observations regarding the Photofrin photobleaching mechanism made previously in tumor spheroids (12) and in rat skin *in vivo* (18) can be successfully reconciled within the context of a theory which incorporates two simultaneous bleaching mechanisms. We demonstrate the remarkable ability of spatially- and spectrally-resolved fluorescence measurements in confocal optical sections of intact spheroids to investigate complicated sensitizer photobleaching patterns, such as those caused by the presence of more than one bleaching mechanism. Finally, the consequences of bleaching *via* multiple simultaneous mechanisms for the clinical implementation of a fluorescence-

based dosimetry during PDT warrant some attention. Our results motivate careful attention to the local concentration of sensitizer and to the details of a sensitizer's bleaching mechanism in the formulation of dosimetry and treatment protocols, and demonstrate that for the case of Photofrin-PDT, photoproduct accumulation is a better predictor of dose deposition.

REFERENCES

1. Dougherty, T. J., C. J. Gomer, B. W. Henderson, G. Jori, D. Kessel, M. Korbelik, J. Moan, and Q. Peng (1998) Photodynamic therapy. *J. Natl. Cancer Inst.* **90**: 889-905.
2. Gibson, S. L., K. R. VanDerMeid, R. S. Murant, R. F. Raubertas, and R. Hilf (1990) Effects of various photoradiation regimens on the antitumor efficacy of photodynamic therapy for R3230AC mammary carcinomas. *Cancer Res.* **50**: 7236-7241.
3. Foster, T. H., R. S. Murant, R. G. Bryant, R. S. Knox, S. L. Gibson, and R. Hilf (1991) Oxygen consumption and diffusion effects in photodynamic therapy. *Radiat. Res.* **126**: 296-303.
4. Gibson, S. L., T. H. Foster, R. H. Feins, R. F. Raubertas, M. A. Fallon, and R. Hilf (1994) Effects of photodynamic therapy on xenografts of human mesothelioma and rat mammary carcinoma in nude mice. *Br. J. Cancer* **69**: 473-481.
5. Feins, R. H., R. Hilf, H. Ross, and S. L. Gibson (1990) Photodynamic therapy for human malignant mesothelioma in the nude mouse. *J. Surg. Res.* **49**: 311-314.
6. Sitnik, T. M. and B. W. Henderson (1998) The effect of fluence rate on tumor and normal tissue responses to photodynamic therapy. *Photochem. Photobiol.* **67**: 462-466.
7. Henderson, B. W., T. M. Busch, L. A. Vaughan, N. P. Frawley, D. Babich, T. A. Sosa, J. D. Zollo, A. S. Dee, M. T. Cooper, D. A. Bellnier, W. R. Greco, and A. R. Oseroff (2000) Photofrin photodynamic therapy can significantly deplete or preserve oxygenation in human basal cell carcinomas during treatment, depending on fluence rate. *Cancer Res.* **60**: 525-529.
8. Tromberg, B. J., A. Orenstein, S. Kimel, S. J. Barker, J. Hyatt, J. S. Nelson, and M. W. Berns (1990) In vivo tumor oxygen tension measurements for

- the evaluation of the efficiency of photodynamic therapy. *Photochem. Photobiol.* **52**: 375-385.
9. Sitnik, T. M., J. A. Hampton, and B. W. Henderson (1998) Reduction of tumour oxygenation during and after photodynamic therapy in vivo: effects of fluence rate. *Br. J. Cancer* **77**: 1386-1394.
 10. Foster, T. H., D. F. Hartley, M. G. Nichols, and R. Hilf (1993) Fluence rate effects in photodynamic therapy of multicell tumor spheroids. *Cancer Res.* **53**: 1249-1254.
 11. Nichols, M. G. and T. H. Foster (1994) Oxygen diffusion and reaction-kinetics in the photodynamic therapy of multicell tumor spheroids. *Phys. Med. Biol.* **39**: 2161-2181.
 12. Georgakoudi, I., M. G. Nichols, and T. H. Foster (1997) The mechanism of Photofrin photobleaching and its consequences for photodynamic dosimetry. *Photochem. Photobiol.* **65**: 135-144.
 13. Mang, T. S., T. J. Dougherty, W. R. Potter, D. G. Boyle, S. Somer, and J. Moan (1987) Photobleaching of porphyrins used in photodynamic therapy and implications for therapy. *Photochem. Photobiol.* **45**: 501-506.
 14. Moan, J. (1986) Effect of bleaching of porphyrin sensitizers during photodynamic therapy. *Cancer Lett.* **33**: 45-53.
 15. Potter, W. R., T. S. Mang, and T. J. Dougherty (1987) The theory of photodynamic therapy dosimetry: consequences of photo-destruction of sensitizer. *Photochem. Photobiol.* **46**: 97-101.
 16. Boyle, D. G. and W. R. Potter (1987) Photobleaching of photofrin II as a means of eliminating skin photosensitivity. *Photochem. Photobiol.* **46**: 997-1001.
 17. Spikes, J. D. (1992) Quantum yields and kinetics of the photobleaching of hematoporphyrin, Photofrin II, tetra(4-sulfonatophenyl)-porphine and uroporphyrin. *Photochem. Photobiol.* **55**: 797-808.

18. Finlay, J. C. (2003) *Reflectance and fluorescence spectroscopies in photodynamic therapy*. Ph.D. thesis. University of Rochester, Rochester, NY.
19. König, K., H. Wabnitz, and W. Dietel (1990) Variation in the fluorescence decay properties of haematoporphyrin derivative during its conversion to photoproducts. *J. Photochem. Photobiol. B* **8**: 103-111.
20. Georgakoudi, I. and T. H. Foster (1998) Singlet oxygen- versus nonsinglet oxygen-mediated mechanisms of sensitizer photobleaching and their effects on photodynamic dosimetry. *Photochem. Photobiol.* **67**: 612-625.
21. Moan, J. and K. Berg (1991) The photodegradation of porphyrins in cells can be used to estimate the lifetime of singlet oxygen. *Photochem. Photobiol.* **53**: 549-553.
22. Moan, J. and D. Kessel (1988) Photoproducts formed from Photofrin II in cells. *J. Photochem. Photobiol. B* **1**: 429-436.
23. Bigelow, C. E., C. J. Harkrider, D. L. Conover, T. H. Foster, I. Georgakoudi, S. Mitra, M. G. Nichols, and M. Rajadhyaksha (2001) Retrofitted confocal laser scanner for a commercial inverted fluorescence microscope. *Rev. Sci. Instr.* **72**: 3407-3410.
24. Bigelow, C. E., D. L. Conover, and T. H. Foster (2003) Confocal fluorescence spectroscopy and anisotropy imaging system. *Opt. Lett.* **28**: 695-697.
25. Press, W. H., S. A. Teukolsky, W. T. Vetterling, and B. P. Flannery (1992) *Numerical Recipes in C: The Art of Scientific Computing*. Cambridge University Press, New York.
26. Finlay, J. C., D. L. Conover, E. L. Hull, and T. H. Foster (2001) Porphyrin bleaching and PDT-induced spectral changes are irradiance dependent in ALA-sensitized normal rat skin in vivo. *Photochem. Photobiol.* **73**: 54-63.

27. Finlay, J. C., S. Mitra, and T. H. Foster (2002) In vivo mTHPC photobleaching in normal rat skin exhibits unique irradiance-dependent features. *Photochem. Photobiol.* **75**: 282-288.
28. Windahl, T., Q. Peng, J. Moan, S. Hellsten, B. Axelsson, and L. Lofgren (1993) Uptake and distribution of intravenously or intravesically administered photosensitizers in the rat. *Cancer Lett.* **75**: 65-70.
29. Boag, J. W. (1969) Oxygen diffusion and oxygen depletion problems in radiobiology. In *Current Topics in Radiation Research*. North-Holland, Amsterdam/London. p 141-195.
30. Jacques, S. L. (1992) Simple optical theory for light dosimetry during PDT. *Proc. SPIE* **1645**: 155-165.
31. Star, W. M. (1989) Comparing the P3-approximation with diffusion theory and with Monte Carlo calculations of light propagation in a slab geometry. *SPIE Institute Series* **IS5**: 46-54.
32. Patterson, M. S. (1998) Personal communication.

Chapter 5: Increased oxygenation improves light penetration at 630 and 650 nm in murine tumors *in vivo*

5.1 Introduction

Photodynamic therapy (PDT) shares with ionizing radiation therapy a keen interest in tumor oxygenation. Several studies have reported that the administration of carbogen, a mixture of 95% oxygen and 5% carbon dioxide, increases tumor oxygenation and enhances tumor response to radiotherapy (1-3). These findings and an appreciation of the profound oxygen dependence of PDT have motivated the investigation of the possibility that carbogen inhalation may

enhance PDT treatment efficacy. Improved tumor response to PDT *in vivo* with carbogen breathing has been reported by Schouwink *et al.* (4) and by Chen *et al.* (5). While oxygen is of course necessary for the photochemical formation of singlet oxygen ($^1\text{O}_2$) and the consequent PDT-induced damage, other potential benefits of improved tumor oxygenation have not been explored, such as the possible effects of oxygen-dependent tissue optical properties on red light propagation in tissue.

The absorption coefficient of tissue is dominated by hemoglobin at visible wavelengths and by hemoglobin and water in the deep red and near infrared (NIR). A pronounced “valley” exists between the visible absorption bands of hemoglobin and the NIR bands of water. This region of relatively low absorption between approximately 600 – 900 nm has been referred to as the “therapeutic window”, as light at these wavelengths can penetrate on the order of centimeters into tissue. Wavelengths beyond 600 nm are typically used for exciting photochemistry of commonly used PDT sensitizers such as Photofrin, δ -aminolevulinic acid (ALA)-induced protoporphyrin IX (PpIX) and meso-tetra hydroxyphenyl chlorin (mTHPC), among others. As shown in Figure 5.1, the absorption spectrum of hemoglobin is of course strongly oxygen dependent. In particular, the absorbance of deoxyhemoglobin is significantly greater than that of oxyhemoglobin in the wavelength range between 600 – 700 nm, and it

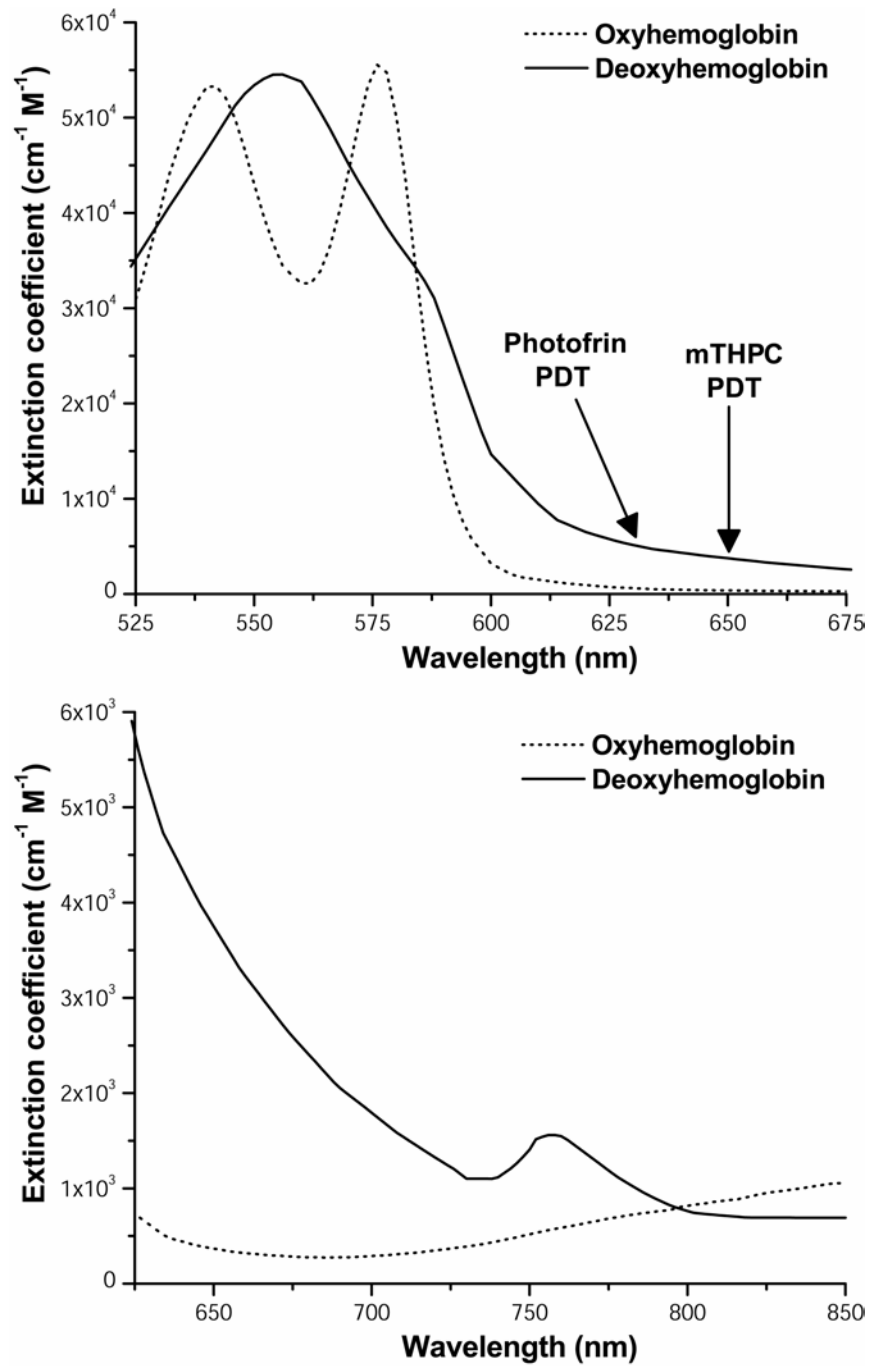


Figure 5.1. Absorption spectra of oxy- and deoxyhemoglobin. In clinical applications, Photofrin and mTHPC-PDT are typically performed at wavelengths of 630 and 650 nm, respectively.

remains greater until the isosbestic point near 800 nm. With this in mind, we explored the relationship between tumor oxygenation and the optical properties at two representative PDT treatment wavelengths, 630 and 650 nm, anticipating that a shift toward increased hemoglobin-oxygen saturation would reduce attenuation of the treatment beam and thus allow effective treatment of deeper lying tissue. We evaluated the hypothesis that oxygen-preserving or enhancing strategies would increase the penetration of PDT treatment beams at these wavelengths. We tested this hypothesis with experiments performed in tissue-simulating liquid phantoms containing intact human red blood cells and in a murine tumor model *in vivo* by measuring the fluence rates at these two wavelengths over a range of oxygenation conditions. Measurements in phantoms demonstrated that the fluence rate at depth in a surface-irradiated, air-saturated sample was enhanced by an order of magnitude relative to a completely deoxygenated phantom. Results obtained from experiments *in vivo*, where changes in transmission through 1-cm-thick subcutaneous murine tumors were measured at 630 and 650 nm, illustrated that the improved oxygenation induced by carbogen breathing resulted in a 40 - 50% average increase in transmission over the initial baseline values.

Using the fluence rate measurements at 630 and 650 nm in the phantoms, we extend the comparison of photodynamic efficacy between Photofrin and mTHPC, presented earlier in chapter 2, to a more complete *in vivo* situation. In

this chapter, we perform PDT dose calculations at the two wavelengths similar to the ones described in chapter 2, but here incorporate the effects of attenuation of PDT treatment beams due to hemoglobin absorption. Our calculations indicate that by accounting for changes in tissue optical properties under different oxygenation conditions a significant further enhancement in the photodynamic efficacy of mTHPC *vs.* Photofrin, over the approximately 175-fold reported in chapter 2, is obtained.

5.2 Materials and Experimental Methods

5.2.1 Erythrocyte phantom preparation

Tissue-simulating phantoms were made from a mixture of 1:10 parts 10% Liposyn II[®] (Abbott Labs, North Chicago, IL) in buffered Hanks' Balanced Salt Solution (HBSS). The 0.9% lipid content of this emulsion produced a scattering coefficient of 1 mm^{-1} at 630 nm, which is similar to that of tissue (6). Buffered HBSS was prepared by adding 50 mM phosphate and adjusting the pH to 7.4 at 37°C . The buffered HBSS had a phosphate concentration equivalent to standard phosphate buffered saline (PBS) and included glucose and potassium in concentrations similar to those encountered by human erythrocytes *in vivo*.

Intact human erythrocytes were prepared from whole blood drawn from healthy, non-smoking volunteers. The blood was drawn into glass tubes

pre-filled with sodium heparin to prevent clotting and was then transferred into centrifuge tubes and mixed with buffered HBSS in approximately equal volume. The samples were then centrifuged at 2500 rpm for 5 minutes. The supernatant, including a surface layer of non-erythrocyte constituents, was decanted by aspiration. Once a clear supernatant was obtained after repeated decantations, the supernatant was aspirated, and the remaining erythrocyte pellet was refrigerated until further use.

As hemoglobin-oxygen dissociation kinetics are temperature dependent, it was important to maintain the phantoms at an approximately constant temperature (7). This was accomplished using the thermal controller of a heated stirplate (Corning Model 460), which continuously monitored the temperature of the phantom *via* a thermometer accessory. To verify the stirplate's thermal control, the temperature was also monitored using an electronic thermometer. The maximum variation in temperature throughout the course of each experiment was less than 1⁰C. The phantoms were continuously stirred to prevent settling of the constituents and to preserve an optically homogeneous sample.

The oxygen partial pressure in the phantom was continuously monitored by an oxygen-sensitive microelectrode (Microelectrodes Inc., Londonderry, NH). At the beginning of an experiment prior to the addition of erythrocytes, a two-point calibration at air-saturated and at zero oxygen tension was performed for the electrode. The phantom was deoxygenated with Na₂S₂O₄ (sodium dithionite).

Assuming a linear response between the two calibration points, the calibration allowed the conversion of the measured electrode current to oxygen tension. The calibration procedure was repeated after the end of an experiment to control for any drift in the electrode reading. The outputs of the oxygen electrode and the electronic thermometer were recorded at 10 Hz by a computer equipped with a 12-bit data acquisition board (Iotech, Cleveland, OH, USA).

To begin an experiment the red blood cells were removed from the refrigerator, warmed, and then added to the phantom at an approximately physiological concentration of 1.6% to simulate hemoglobin absorption in tissue. This red cell fraction is based on a blood volume of 4.0% and a hematocrit of 40%. The phantoms were deoxygenated by addition of approximately 1 cc of dry baker's yeast, allowing the phantom to gradually deoxygenate over a period of 20 – 30 minutes.

5.2.2 Hemoglobin-oxygen dissociation curve: The Hill curve

The fractional occupancy of the oxygen-binding sites in hemoglobin is defined by the saturation, SO_2 , given by

$$SO_2 = \frac{[HbO_2]}{[HbO_2] + [Hb]}, \quad (1)$$

where $[Hb]$ and $[HbO_2]$ are concentrations of deoxy- and oxyhemoglobin,

respectively. A plot of SO_2 versus pO_2 , the partial pressure of oxygen, is the oxygen dissociation curve, which was shown to be sigmoidal in shape by Archibald Hill in 1913. It is hence referred to as the Hill curve. The Hill curve is defined by the expression,

$$SO_2 = \frac{(pO_2)^n}{(pO_2)^n + (p_{50})^n} , \quad (2)$$

where p_{50} is the partial pressure of oxygen at which half of the hemoglobin binding sites are bound to oxygen, and n is the Hill coefficient, which is a measure of the cooperativity of binding. Typical values of p_{50} and n are 26 torr and 2.8, respectively (8).

5.2.3 Measurements in tissue-simulating erythrocyte phantoms

Fluence rate measurements in the phantoms were performed using an optical fiber terminated with a spherical diffusing tip. The fiber was fixed on a translation device, which allowed measurement of the fluence rates at different depths from the top, illuminated surface of the liquid phantom. The surface was irradiated with either 630 or 650 nm light from an argon-ion laser pumped tunable dye laser (Coherent model 599, Santa Clara, CA, USA). The laser light was coupled into an optical fiber that was terminated with a gradient index (GRIN) lens (Rawson Optics Inc., Brentwood, CA, USA), which was positioned

above the surface of the phantom to illuminate an area of approximately 2 cm diameter.

The light detected by the spherical diffuser was recorded by a power meter (Newport Corporation, Irvine, CA, USA) and digitized by the 12-bit data acquisition board before storage. The fluence rate was measured at 0.5 cm increments from the phantom surface to a depth of 2 cm. The initial measurements at both 630 and 650 nm were made in a scattering phantom devoid of any erythrocytes. Erythrocytes were then added to the phantom and similar recordings were performed at both wavelengths. Once the measurements were completed in the air-saturated phantom ($SO_2 = 1.0$), the spherical diffuser probe was placed at a depth of 1 cm from the surface, and the laser wavelength was set to either 630 or 650 nm. Yeast was then added in order to slowly deoxygenate the phantom. This allowed a continuous recording of the fluence rate as the oxygenation status of the phantom gradually changed from being fully oxygenated to completely deoxygenated. The oxygen tension in the phantom was recorded simultaneously by the oxygen-sensitive microelectrode. Once the phantom was fully deoxygenated ($SO_2 = 0.0$), a fluence rate measurement *vs.* depth was performed again at both 630 and 650 nm. For every phantom experiment, the laser power exiting the irradiating fiber was carefully measured before and after each set of recordings to ensure constant incident power.

5.2.4 Measurements *in vivo*

Mouse mammary carcinoma EMT6 cells were grown in culture media under 5% CO₂ at 37⁰ C. While still subconfluent, the cells were detached from the substrate using trypsin, washed once in serum-containing Eagle's Basal Medium (BME) and washed twice in HBSS to remove any remaining culture media and trypsin. Cells were centrifuged at 1200 rpm for 5 min between washings. The concentration of viable cells was assessed with a Trypan blue exclusion assay. The cells were then resuspended in HBSS and stored on ice until used. Tumors were initiated in the subcutaneous space on the upper back of female BALB/c mice by injection of a 0.1 mL bolus of HBSS containing 5 x 10⁵ EMT6 cells. Tumors were allowed to grow to a diameter of approximately 1 cm, which required 12 to 16 days. After a tumor had grown to the desired size, the mouse was initially anesthetized with approximately 60 mg kg⁻¹ ketamine hydrochloride (Bedford Laboratories, Bedford, OH, USA) and 6 mg kg⁻¹ xylazine (The Butler Company, Columbus, OH, USA). Hair removal from the skin surface over the tumor was then accomplished by shaving with an electric shear followed by application of the hair removal lotion Nair (Carter-Wallace Inc., NY, USA) and subsequent rinsing with distilled water. To restrain the animal for the duration of the experiment, sodium pentobarbital (The Butler Company, Columbus, OH, USA) was injected at a dose of 65 mg kg⁻¹. To prevent movement, the mouse was also mechanically restrained with tape. Once the animal was completely

anesthetized, a 13-gauge bone biopsy needle (Cook Incorporated, Bloomington, IN) was used to make a small incision (approx. 5 mm) in the skin at the base of the tumor. A 2.5-cm-long cylindrical diffusing tip fiber with an outside diameter of 800 μm (Cardiofocus, Norton, MA) was then advanced through the hollow biopsy needle and placed beneath the tumor. The tumor area was then irradiated with either 630 or 650 nm light from the argon-ion laser pumped tunable dye laser. The laser light was coupled into a GRIN-lens-terminated optical fiber positioned to illuminate an area covering the tumor surface. The cylindrical diffuser measured the initial fluence rate at 630 and 650 nm as the mouse breathed room air. With the baseline values established for a particular mouse, carbogen was administered through a nose cone at a flow rate of 3 liters min^{-1} , and the fluence rate was measured at both wavelengths at the identical location. Once the measurement was approximately constant, the carbogen administration was terminated, the animal was again allowed to breathe room air, and the fluence rate was again recorded. Finally, as the last phase of the experiment, the animal inhaled nitrogen in order to render the tumor hypoxic, and measurements were repeated again at the identical position.

5.2.5 Efficacy comparison between mTHPC- and Photofrin-PDT

The comparison between the photodynamic potency of mTHPC *vs.* Photofrin was evaluated using methods described in detail in section 2.2.6 of chapter 2. In

this chapter, we examine the influence and contribution of tissue optical properties towards the clinical phototoxicity of the two sensitizers. The simulations of $^1\text{O}_2$ dose deposition are performed using values of the initial maximum rate of photochemical oxygen consumption, Γ_0 , for mTHPC and Photofrin, modified to incorporate the effect of the experimentally measured changes in fluence rate in the erythrocyte phantoms for a range of oxygenation status at different depths.

5.3 Results and analysis

5.3.1 Erythrocyte phantom experiments

Measurements in erythrocyte phantoms were performed to examine the effects of oxygen tension on red light propagation at different depths in a tissue-simulating medium. Figure 5.2 compares the fluence rates measured at 630 and 650 nm at depths of 0.5 - 2 cm in well-oxygenated vs. completely deoxygenated phantoms. The data points at each depth are normalized to the values recorded at the corresponding depth in a phantom consisting of only the lipid emulsion and devoid of any erythrocytes. The results demonstrate that at both of these PDT treatment wavelengths, the fluence rate at all depths is significantly enhanced under conditions where the phantom is well oxygenated. The 650 nm fluence rates in the oxygenated phantom were approximately 3- and 8-fold higher than those in a hypoxic phantom at depths of 0.5 and 1 cm, respectively. At 630 nm,

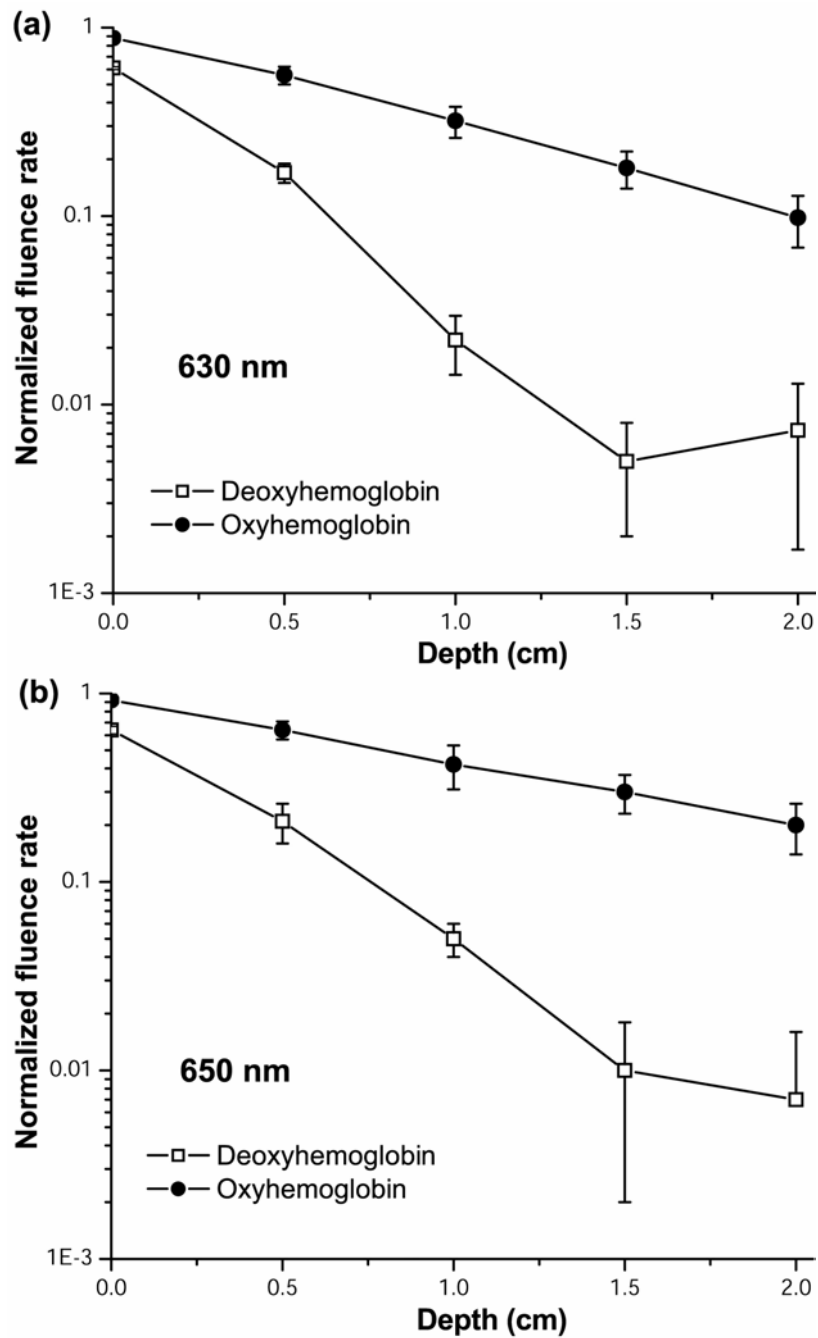


Figure 5.2. Fluence rate vs. depth in a well-oxygenated (●) and completely deoxygenated (□) homogeneous tissue-simulating liquid phantom measured during surface irradiation at (a) 630 nm and (b) 650 nm. The data points and the error bars represent means and standard deviations from a set of 6 experiments at each wavelength.

the corresponding oxygen-dependent enhancements in fluence rate at the same two depths were approximately 3.3- and 15-fold. The more significant gain in PDT treatment beam fluence rate at these depths at 630 nm is consistent with the hemoglobin absorption spectra shown in Figure 5.1. Further, at each depth the normalized fluence rate measured at 630 nm in a well-oxygenated phantom was significantly greater than that at 650 nm in a hypoxic phantom. For example, at a depth of 0.5 cm, the normalized fluence rate at 630 nm in a phantom containing oxyhemoglobin (Figure 5.2a) was about 2.5-fold higher than that measured at 650 nm in a deoxyhemoglobin phantom (Figure 5.2b). Again, this is consistent with the lower absorbance of oxyhemoglobin at 630 nm vs. that of deoxyhemoglobin at 650 nm.

The plots in Figure 5.2 demonstrate changes in fluence rate with depth at two extreme hemoglobin saturations. In order to examine the changes in fluence rate for a continuously changing oxygenation, the spherical diffuser probe was placed at a depth of 1 cm from the irradiated surface of the phantom, and measurements were recorded as the phantom was slowly deoxygenated. Figure 5.3 illustrates a representative measurement made in a phantom during 650 nm illumination. The dashed line in the plot corresponds to a Hill curve defined by equation (2), where typical values for n of 2.8 and p_{50} of 26 torr were chosen for the calculation. The solid line in the Figure shows the decrease in fluence rate

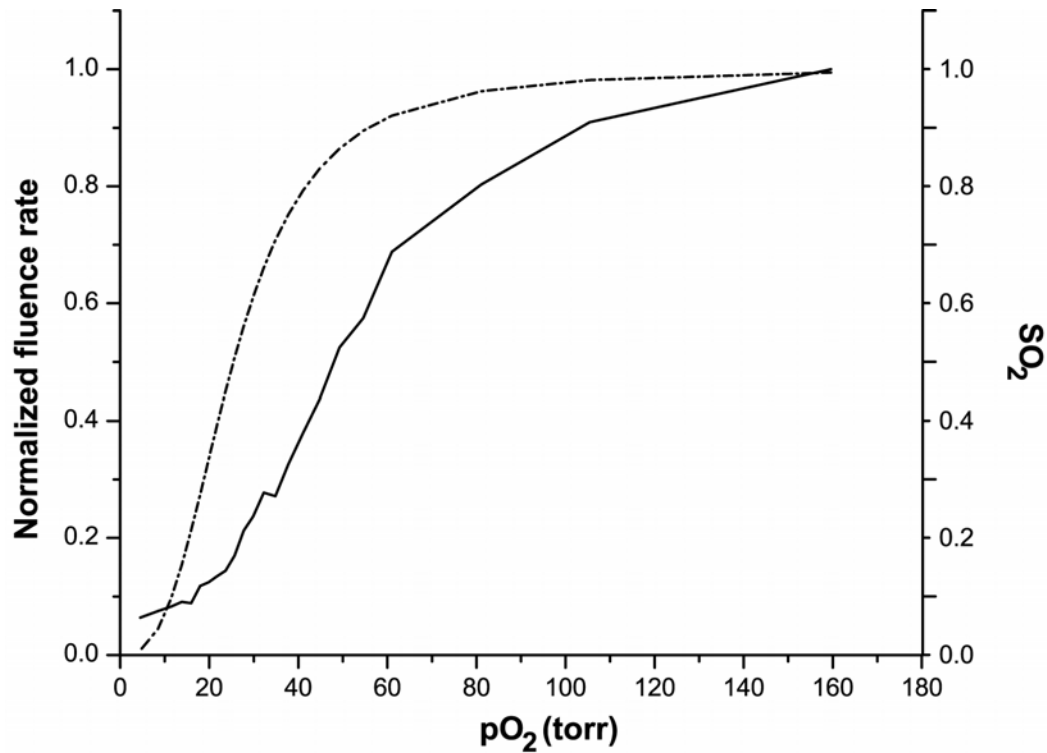


Figure 5.3. Hemoglobin-oxygen saturation (SO_2) and 650 nm fluence rate measured in a homogeneous erythrocyte-containing phantom as a function of oxygen partial pressure (pO_2). The dashed line represents a calculated hemoglobin-oxygen dissociation (Hill) curve assuming an n of 2.8 and a p_{50} of 26 torr. The solid line is the normalized 650 nm fluence rate measured at a depth of 1 cm inside the phantom.

measured by the optical probe as the oxygen tension in the phantom was gradually reduced through yeast metabolism.

Figure 5.4 summarizes the fluence rate at 630 nm measured by the spherical probe placed at a 1 cm depth in the erythrocyte phantom as a function of (a) oxygen tension and (b) hemoglobin-oxygen saturation. As demonstrated in both plots, the fluence rate falls appreciably as the oxygen tension and hemoglobin saturation decrease in the phantom. The drastic dependence of the optical properties on oxygenation is emphasized in Figure 5.4b, where a reduction from 1.0 to 0.95 in SO_2 results in an approximately 50% loss in fluence rate at this wavelength. At $SO_2 = 0.5$, the fluence rate drops to only 10% of that measured at $SO_2 = 1.0$. As shown in Figure 5.5, a similar pattern is observed for experiments performed with 650 nm light, where a 50% loss in fluence rate at 1 cm accompanies a reduction in SO_2 from 1.0 to 0.9. These results indicate the tremendous importance of well-oxygenated tissue in order to deliver PDT treatment light effectively at depth.

5.3.2 *In vivo* experiments

Measurements of fluence rate at the base of a subcutaneous EMT6 tumor were performed under a variety of breathing conditions to investigate the effects of

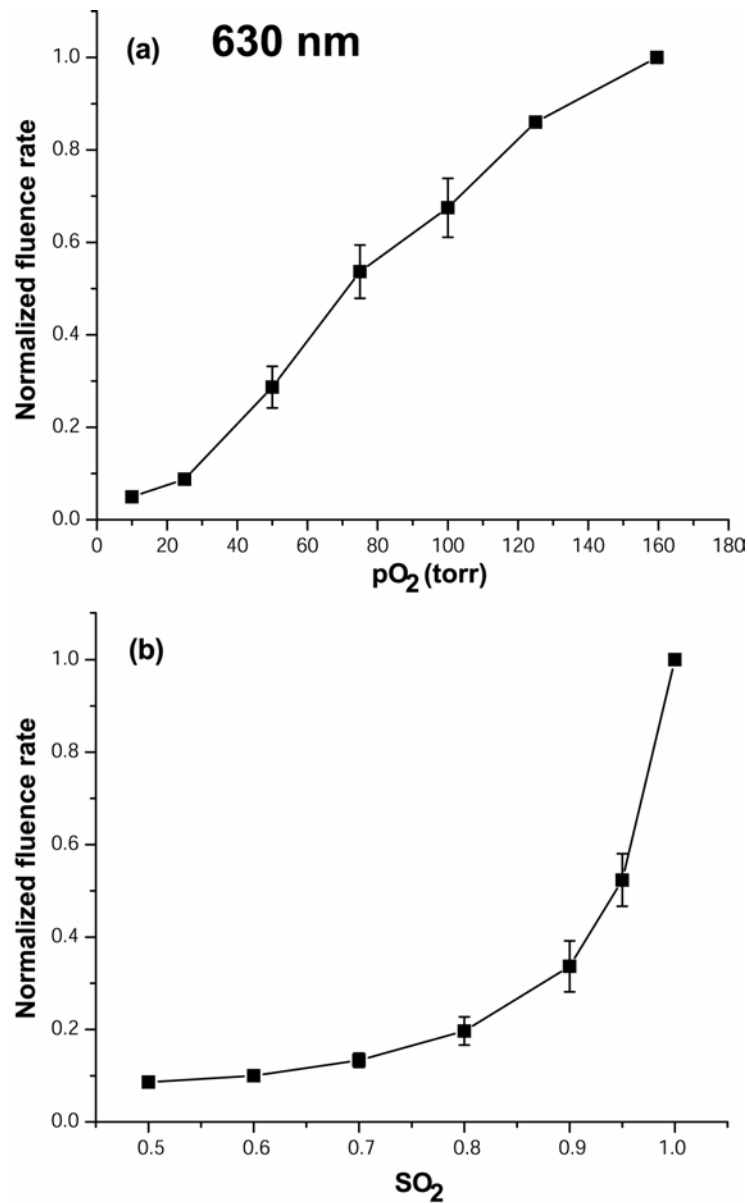


Figure 5.4. 630 nm fluence rate vs. (a) oxygen partial pressure (pO_2) and (b) hemoglobin-oxygen saturation (SO_2) measured in an erythrocyte-containing tissue-simulating phantom during deoxygenation. The saturations were calculated from measurements of the pO_2 using the Hill equation and assigning values of 2.8 and 26 torr to n and p_{50} , respectively. Data points represent means from 3 experiments with the spherical probe positioned at a 1 cm depth from the irradiated surface of the phantom. The fluence rates in each experiment were normalized to their initial values in an air-saturated phantom.

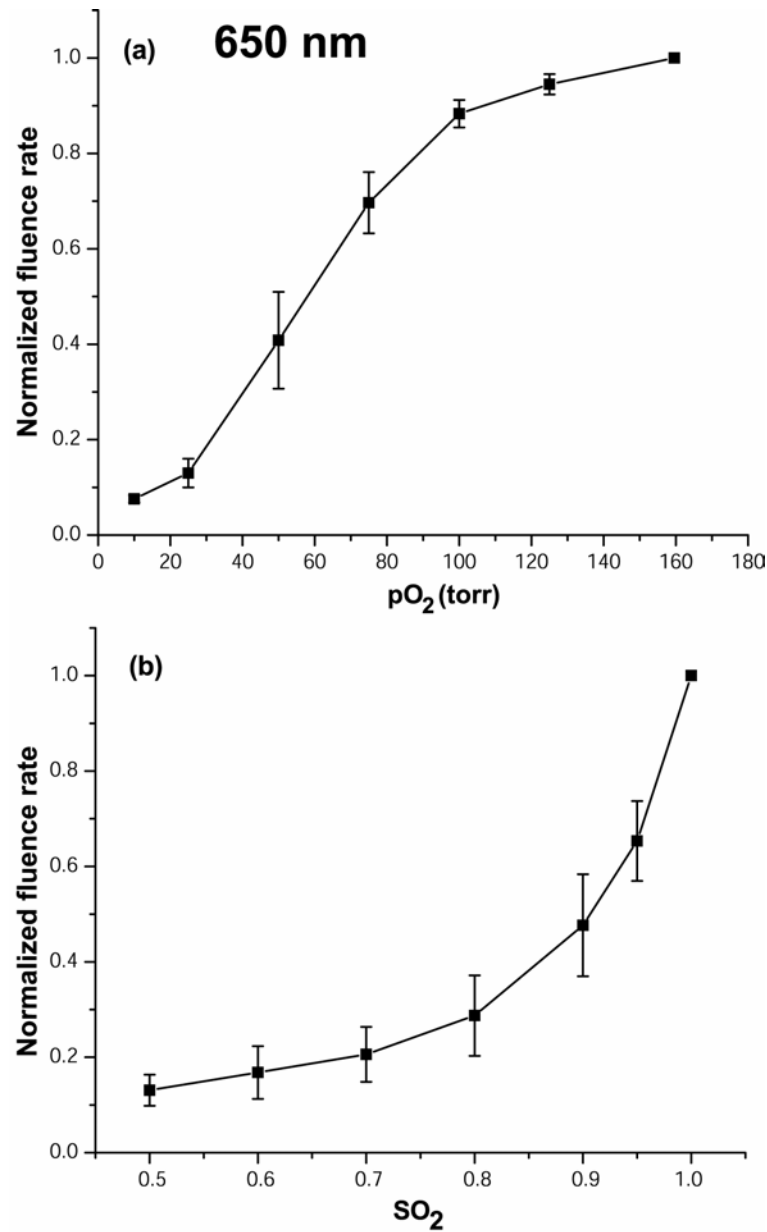


Figure 5.5. 650 nm fluence rate vs. (a) oxygen tension (pO_2) and (b) hemoglobin-oxygen saturation (SO_2) measured in an erythrocyte phantom during deoxygenation. Data points represent means from 3 experiments with the spherical probe positioned at 1 cm depth from the irradiated surface of the phantom. The fluence rates in each experiment were normalized to their initial values in an air-saturated phantom.

oxygen tension on PDT treatment beam transmission at 630 and 650 nm *in vivo*. Figure 5.6 illustrates a representative progression of light transmission changes recorded continuously by a cylindrical diffuser probe positioned beneath a 1-cm-thick tumor irradiated at 630 nm while the mouse breathed room air, carbogen, or nitrogen. The changes are plotted relative to an initial baseline value, which was assigned an arbitrary value of 100. An increase in light transmission by as much as 65% was obtained by enhancing tumor oxygenation with carbogen inhalation. Once the carbogen administration was stopped, the transmission decreased but remained higher than the initial baseline value obtained under identical room air breathing conditions. Finally, when the animal was subjected to nitrogen inhalation, the intensity dropped steeply and equilibrated to a level significantly below its initial value, consistent with the tumor being rendered severely hypoxic and thus presenting increased light attenuation from deoxyhemoglobin.

Figure 5.7 summarizes the relative changes in fluence rate at 630 and 650 nm measured *in vivo* as described above. The plots report the average relative changes in fluence rates recorded from three mice during the different breathing conditions with each tumor serving as its own control. This was important as each tumor was expected to have a different initial hemoglobin saturation and thus a different initial transmission value. The results indicate that the average fluence rate at both wavelengths increased by 40% or more in

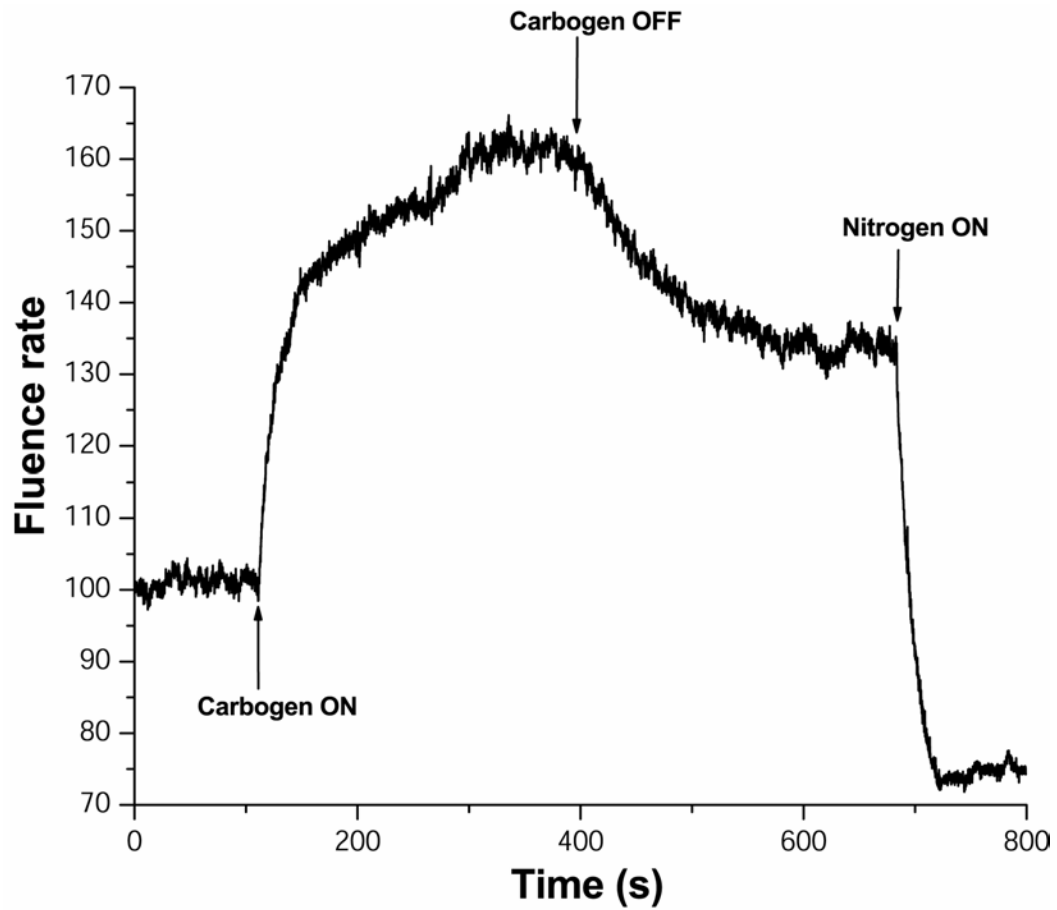


Figure 5.6. 630 nm fluence rate changes recorded continuously at the base of a 1-cm-thick subcutaneous EMT6 tumor while the mouse was subjected to a variety of breathing conditions. The initial baseline transmission was assigned an arbitrary value of 100.

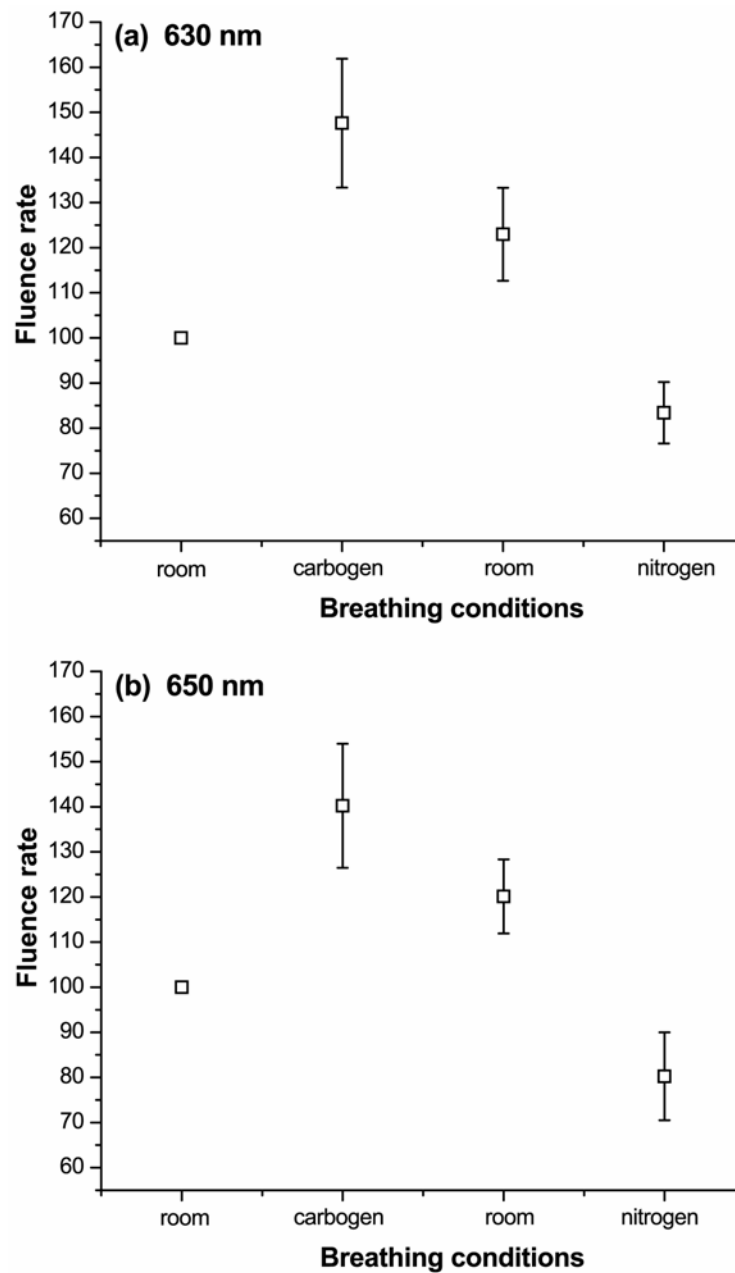


Figure 5.7. Average changes in fluence rate under different breathing conditions measured in 3 animals at 630 and 650 nm. The fluence rates were measured using a cylindrical diffusing fiber positioned at the base of 1-cm-thick EMT6 tumors grown subcutaneously in female BALB/c mice as the tumor was irradiated from the surface.

response to carbogen breathing relative to the initial values. As mentioned previously, we observed that when carbogen breathing was ceased and the animal resumed inhalation of room air, the transmission decreased and equilibrated to a value about 20% higher than its initial level. This pattern was reproducible for each of the intensity measurements performed in all three of the tumors studied. Finally, as expected we found that as the animal inhaled nitrogen the average transmission dropped to nearly 20% below its initial value as the tumor became hypoxic and the hemoglobin was completely deoxygenated, consistent with the individual transmission profile illustrated in Figure 5.6. This confirmed that the tumors initially contained partially saturated hemoglobin.

5.3.3 Potency of mTHPC vs. Photofrin: Influence of tissue optical properties

In chapter 2, an irradiance of 7.5 and 70 mW cm⁻² was chosen for performing PDT dose calculations for mTHPC and Photofrin, respectively, without invoking effects of tissue optical properties. Now in order to incorporate the influence of hemoglobin absorption of red light based on the fluence rate measurements performed in the erythrocyte phantoms, the treatment irradiance and consequently Γ_0 used for simulating the ¹O₂ dose distribution had to be modified

Table 5.1

Depth (cm)	Hemoglobin- oxygen saturation (SO₂)	Normalized 630 nm fluence rate	Normalized 650 nm fluence rate
0	1.0	0.88	0.92
0.5	1.0	0.56	0.64
1	1.0	0.32	0.42
1	0.95	0.14	0.25
1	0.90	0.09	0.17
1	0.75	0.043	0.09
1	0.50	0.023	0.047
1	0.25	0.016	0.033
1	0.10	0.013	0.028

Table 5.1. Average normalized fluence rate at 630 and 650 nm measured at three depths of 0, 0.5 and 1 cm inside an erythrocyte phantom for a range of hemoglobin-oxygen saturations from 1.0 to 0.1. The values of fluence rate are reproduced from the data sets used for plotting Figures 5.2, 5.4 and 5.5.

accordingly. For example, in a phantom consisting of fully saturated hemoglobin, the average fluence rate at the surface dropped to 0.92 and 0.88 of their initial values at 650 and 630 nm, respectively (Table 5.1 and Figure 5.2). Thus, the irradiance values used for the dose simulations were reduced to 6.9 mW cm^{-2} ($7.5 \text{ mW cm}^{-2} \times 0.92$) at 650 nm and 61.6 mW cm^{-2} ($70 \text{ mW cm}^{-2} \times 0.88 = 61.6 \text{ mW cm}^{-2}$) at 630 nm. Using these values and re-computing the $^1\text{O}_2$ dose distributions as described in section 2.2.6 yielded a Photofrin-PDT dose of 22.2 mM and an mTHPC-PDT dose of 123.1 mM. This corresponds to a 5.5-fold increased $^1\text{O}_2$ dose deposition for mTHPC-PDT in comparison to Photofrin-PDT. Table 5.2 lists the Photofrin- and mTHPC-PDT doses computed by taking into account the measured fluence rates at depths of 0, 0.5 and 1 cm in a fully oxygenated erythrocyte phantom. As indicated in chapter 2, a 33.3-fold lower incubation dose of mTHPC in comparison to Photofrin had been used to perform the experiments in spheroids which allowed us to extract the photophysical parameters required to perform the $^1\text{O}_2$ dose simulations. Thus by computing the product of the $^1\text{O}_2$ dose deposition at the three depths and the 33.3-fold difference in incubation concentration, an enhanced photodynamic efficacy of about 185- to 265-fold with mTHPC vs. Photofrin was obtained (Figure 5.8). $^1\text{O}_2$ doses for Photofrin- and mTHPC-PDT were also calculated for a range of hemoglobin-saturations at a depth of 1 cm based on the corresponding fluence

Table 5.2

Depth (cm)	$^1\text{O}_2$ dose (mM) Photofrin-PDT	$^1\text{O}_2$ dose (mM) mTHPC-PDT
0	22.2	123.1
0.5	15.1	97
1	9	71.3

Table 5.2. $^1\text{O}_2$ doses for Photofrin and mTHPC calculated at three depths using irradiances which incorporated the effects of light attenuation based on 630 and 650 nm fluence rate measurements in erythrocyte phantoms consisting of fully-saturated hemoglobin, *i.e.* $\text{SO}_2 = 1.0$.

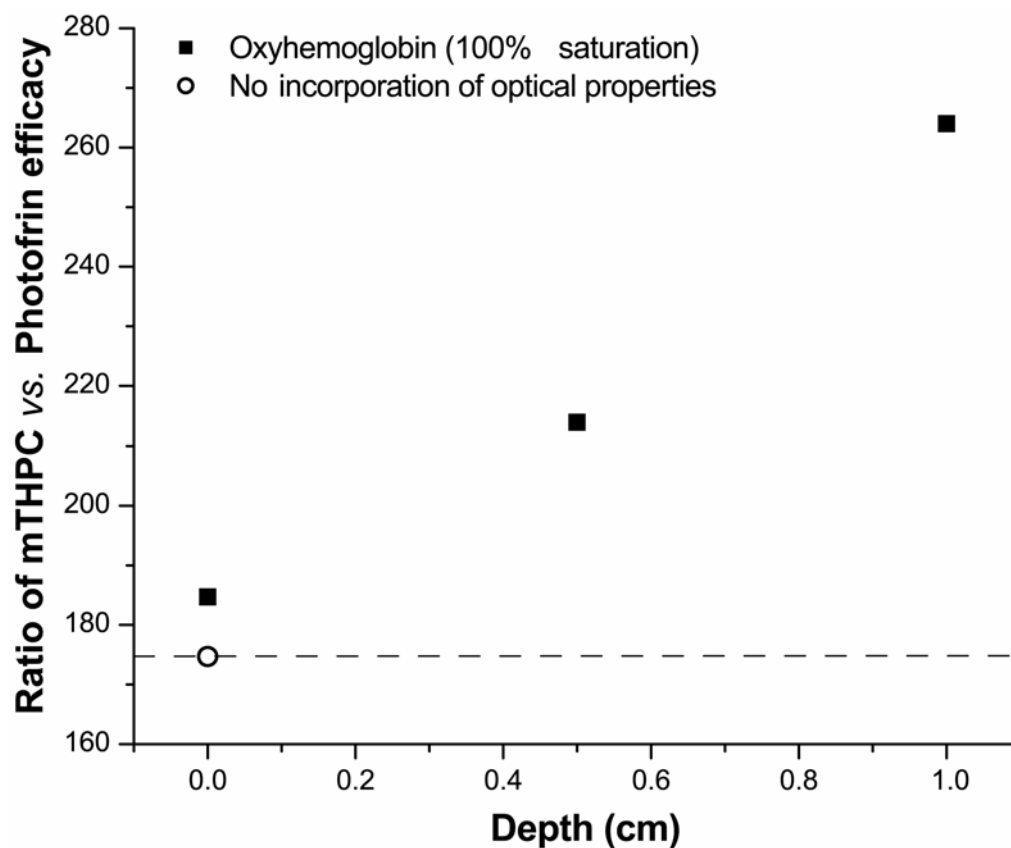


Figure 5.8. Plot of the ratio of mTHPC vs. Photofrin efficacy at depths of 0, 0.5 and 1 cm. The efficacy factor is calculated from the $^1\text{O}_2$ dose depositions for the two sensitizers taking into account the difference in their respective incubation concentrations used in the spheroid microelectrode experiments from which the photophysical parameters used in the dose simulations were extracted.

rate measurements at 630 and 650 nm (Figures 5.4 and 5.5). Although the $^1\text{O}_2$ dose generated by both sensitizers is reduced with decreasing hemoglobin-saturation (Table 5.3), a significant increase in the ratio of mTHPC- vs. Photofrin-PDT dose was obtained when SO_2 changed from 1.0 to 0.75. Taking into account the difference in incubation concentrations, the dose calculations translated into a 440-fold improved efficacy factor for mTHPC vs. Photofrin at $\text{SO}_2 = 0.9$. The efficacy factor jumped to approximately 590-fold when SO_2 was reduced to 0.75 (Figure 5.9) and remained fairly constant for saturations lower than that.

5.4 Discussion and Conclusions

5.4.1 Influence of improved oxygenation on PDT treatment fluence rate

It is now established that tumors *in vivo* can be driven to hypoxia by PDT-induced photochemical oxygen consumption (9, 10) and/or if the supply of oxygen is compromised by PDT damage to the tumor microvasculature (11, 12). Further, it has been extensively documented that many tumors are chronically and/or transiently hypoxic (13, 14). Direct evidence of hypoxia in human cancers has been shown convincingly by several studies (15-17).

Table 5.3

SO₂	¹O₂ dose (mM) Photofrin-PDT	¹O₂ dose (mM) mTHPC-PDT
1.0	9	71.3
0.95	4	46.7
0.9	2.5	33.1
0.75	1	17.7
0.5	0.45	8.1
0.25	0.25	4.7
0.1	0.2	3.8

Table 5.3. ¹O₂ doses computed from simulated dose plots for Photofrin- and mTHPC-PDT performed at a depth of 1 cm in a tissue volume for a range of SO₂ from 1.0 (fully saturated) to 0.1. The input values of 630 and 650 nm irradiance used in the dose simulations for Photofrin- and mTHPC-PDT, respectively, were modified according to the normalized fluence rates measured in the erythrocyte phantoms at a 1 cm depth, as reported in Table 5.1.

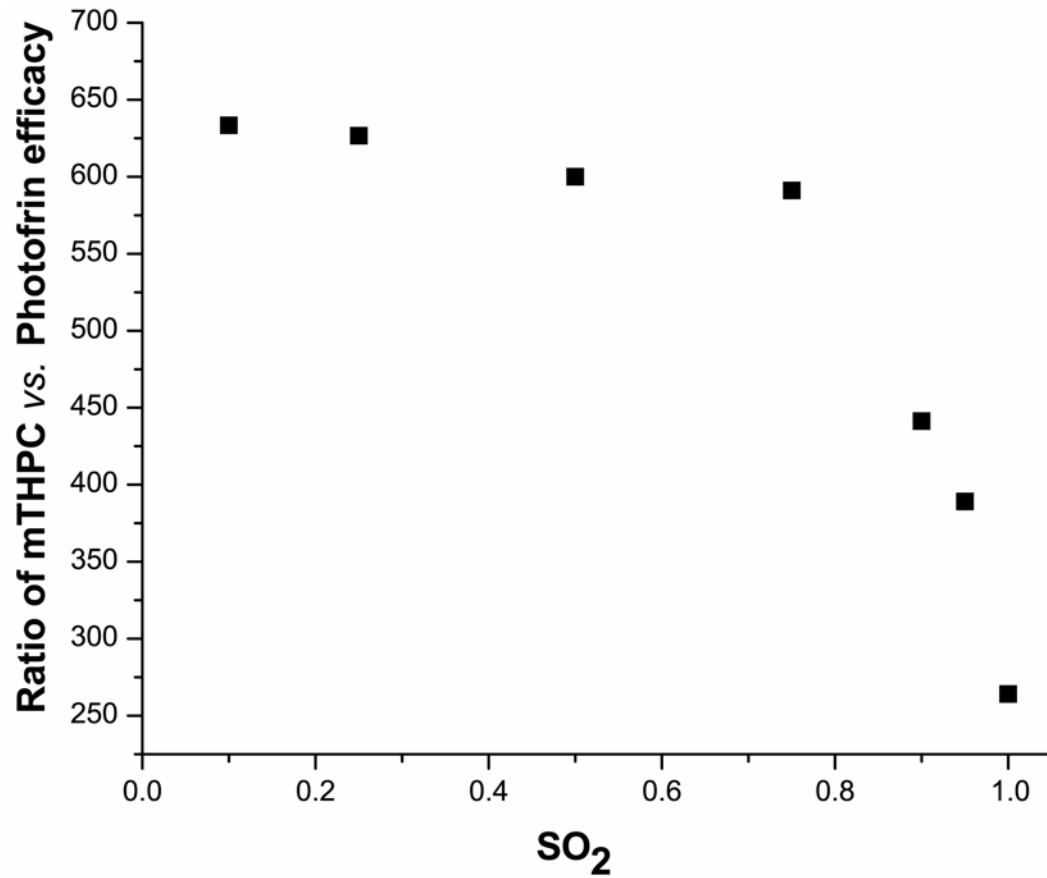


Figure 5.9. Ratio of PDT efficacy for mTHPC vs. Photofrin, assuming PDT treatment at a depth of 1 cm inside a tissue volume for a range of SO_2 from 1.0 to 0.1.

Because molecular oxygen plays an essential role in the PDT-induced photochemical reactions that result in biological damage, several investigators have considered methods aimed at enhancing the levels of oxygen in the target tissue during PDT. These include the use of lower irradiances, which cause a reduced rate of photochemical oxygen depletion in the tissue (18), light fractionation schemes which would allow for oxygen transport into the treated volume during brief interruptions in irradiation (19), and tumor oxygen modifiers such as carbogen (4, 5). All of these studies explored the possibility of improving PDT efficacy by enhancing or maintaining the oxygen tension in the treated tissues in order to increase the efficiency of $^1\text{O}_2$ generation. With respect to the use of oxygen modifiers like carbogen, an extensive study by Chen *et al.* (5) in which animals bearing severely hypoxic tumors ($p\text{O}_2 < 10$ mmHg) were subjected to Photofrin-PDT in combination with either hyperbaric or normobaric oxygen is of particular relevance, as both hyperoxygenation protocols demonstrated improved tumor response.

No previous studies, however, have investigated the potential benefits that improved tissue oxygenation offers as a consequence of oxygen-dependent tissue optical properties. In this report, we show through measurements performed in tissue-simulating phantoms and *in vivo* that enhanced oxygenation results in a significant increase in the penetration of PDT treatment beams at 630 and 650 nm wavelengths. The experiments in strongly scattering, erythrocyte-

containing phantoms allowed us to evaluate the effects of oxygen on the fluence rate over a range of clinically relevant depths and a wide range of oxygen partial pressures. Several important results were obtained through these measurements. First, PDT treatment beam fluence rates can be enhanced several-fold at significant depths in well-oxygenated *vs.* hypoxic tissues (Figure 5.2). For example, at a depth of 2 cm we observed that, although the fluence rates in a well-oxygenated phantom had decreased to approximately 10% and 20% of their incident values at 630 and 650 nm, respectively, these fluence rates were 10 - 30 times higher than in a deoxygenated phantom. A related feature of the data in Figure 5.2 is that, at both wavelengths, the fluence rates at depths of 1.5 - 2 cm in the well-oxygenated phantom are comparable to or exceed those at 0.5 cm in the deoxygenated case. This suggests that PDT may be used to treat even 2-cm-thick-tumors effectively with 630 and 650 nm light, provided the oxygenation status of the tumor is sufficiently high.

Yet another related finding to emerge from the phantom studies was that at each depth, the 630 nm fluence rate in a well-oxygenated phantom was higher than the corresponding 650 nm fluence rate in a hypoxic phantom. A major effort in the field of PDT has been the development of photosensitizers with strong absorption at longer wavelengths, such as mTHPC, benzaporphyrin derivative (BPD), and Lutetium texaphyrin (Lutex), among several others (20). One of the motivations behind this development is that longer-wavelength-

absorbing sensitizers would take advantage of the reduced absorption of hemoglobin and enable the treatment of thicker tumors. The experimental observations from the phantom experiments reported here indicate that increased depths of light penetration sought through these new sensitizers can be efficiently achieved even at 630 nm with carbogen-enhanced hemoglobin oxygen saturation. This observation makes it clear that, while at a given level of tissue oxygenation, irradiating with longer wavelengths will increase the depth of penetration of PDT treatment beams, significant benefits at a given wavelength can be attained by ensuring the highest possible level of oxygenation in the target tissue. The oxy- and deoxyhemoglobin absorption spectra of Figure 5.1 show that the benefits of increased oxygenation on light propagation persist out to 690 and 730 nm, where BPD and Lutex have absorption maxima, although the effects here are not as great as they are in the 630 – 650 nm range.

Finally, the erythrocyte phantom experiments showed that even a modest reduction in hemoglobin oxygen saturation results in appreciable reduction in treatment beam fluence rate at both 630 and 650 nm. This dependence on SO_2 is most pronounced at the highest saturations. Thus, significant gains in light penetration can be achieved by increasing SO_2 to the maximum possible extent, and in particular to levels well above that required to support efficient 1O_2 formation.

The measurements performed in tissue-simulating phantoms demonstrated that a shift towards increased hemoglobin oxygen saturation could reduce attenuation of PDT treatment beams significantly and allowed determination of the maximum effect achievable *in vivo*. However, hemoglobin in tumors *in vivo* is expected to have some fractional saturation, so the effects on light transmission derived from influencing the saturation either upwards *via* carbogen breathing or downwards were likely to be less dramatic than the maximum effect observed in response to the most extreme oxygen conditions in the phantoms. Nevertheless, as demonstrated in the 630 nm transmission data of Figure 5.6 and the summary results of Figure 5.7, an average of 40 - 50% increase in PDT treatment beam transmission was obtained with carbogen breathing. These remarkable increases validate the hypothesis that oxygen-enhancing strategies improve the transmission of PDT treatment beams. Interestingly, following a cessation in carbogen breathing the transmission decreased gradually but stabilized at a level higher than the initial baseline value.

Near-infrared reflectance spectroscopy studies by Hull *et al.* (21) and by Liu *et al.* (22) examined carbogen-induced changes in hemoglobin oxygen saturation *in vivo* in several subcutaneous rat tumor models. More recently, Finlay and Foster (23) performed similar reflectance spectroscopy studies in the BALB/c mouse EMT6 model that we have used here. Each of these reports described changes in the tumor absorption spectra reconstructed from reflectance

measurements consistent with a shift toward an increased SO_2 with carbogen inhalation. These changes in saturation were accompanied by little or no change in tumor blood volume. Interestingly, with the cessation of carbogen breathing, spectroscopy showed that the SO_2 declined only gradually and remained significantly above initial baseline levels for hundreds of seconds. This finding supports our observation that, when carbogen inhalation was stopped and the mice resumed room air breathing, the red light transmission through the EMT6 tumors equilibrated at levels consistently higher than their pre-carbogen values. We noted that with nitrogen asphyxiation the 630 and 650 nm transmission dropped steeply as the tumor was rendered hypoxic. This is also in agreement with the spectroscopy studies of Finlay and Foster (23), who observed that the SO_2 in EMT6 tumors fell to zero with nitrogen breathing. Thus, on the basis of these spectroscopic results we can conclude that the changes in light transmission through the 1-cm-thick subcutaneous EMT6 tumors in response to carbogen and nitrogen inhalation are unequivocally due to corresponding changes in hemoglobin saturation.

Our data may contribute to an interpretation of results reported by Curnow *et al.* (24, 25), in which ALA-PDT was performed on normal rat colon. Those authors observed that fractionated irradiation caused necrotic areas three times larger than those observed in response to the same incident fluence administered using continuous irradiation. Although fractionated light doses

would be expected to improve the oxygen availability within the treated volume (19), an oxygen diffusion-with-reaction model does not predict the appearance of an increased lesion size. Rather, these results are more likely a consequence of oxygen-dependent tissue absorption, such that under improved oxygenation status the treatment light penetrates more deeply and has increased lateral distribution, thereby increasing the area of necrosis. In contrast, a study by Chen *et al.* (26) examined the effects of irradiance in Photofrin-PDT of normal rat brain and found that lowering the irradiance from 200 to 10 mW cm⁻² produced no significant increase in the depth of PDT-induced lesions. It is possible that that photochemical oxygen consumption was not high enough in this case to influence the optical properties.

In conclusion, the data reported here establish that schemes to increase oxygenation may allow effective PDT treatment of thicker tumors at 630 and 650 nm by taking advantage of the oxygen-dependent absorption of hemoglobin, which is the predominant tissue absorber at visible and NIR wavelengths. These results may have important clinical implications.

5.4.2 Effects of hemoglobin absorption on photodynamic efficacy of mTHPC vs. Photofrin

The ¹O₂ dose calculations presented in chapter 2 allowed us to account for an approximately 175-fold enhanced photodynamic potency for mTHPC compared

to that of Photofrin. In this chapter we extended our study into the efficacy of the two sensitizers by examining the effects of hemoglobin absorption on PDT treatment fluence rate. The investigation was based on our measurements of fluence rate changes with depth in erythrocyte phantoms for a range of hemoglobin-oxygen saturations. Accounting for tissue optical properties in our potency comparison between the two sensitizers allowed us to examine a more realistic *in vivo* condition. We report findings which show that while the potency of mTHPC can be about 185-fold higher than Photofrin in the case of treatment of superficial lesions in the presence of fully oxygenated hemoglobin, the factor increases rapidly to 214- and 265-fold when the target tissue volume is 0.5 and 1 cm, below the irradiated surface, respectively (Figure 5.8). As mentioned earlier, hemoglobin in tumors *in vivo* is expected to have some fractional saturation. Therefore, we evaluated the photodynamic potency of mTHPC *vs.* Photofrin in treating a 1-cm-deep tissue volume for a range of hemoglobin-oxygen saturations, based on the 630 and 650 nm fluence rate measurements performed in phantoms (Figure 5.4 and 5.5). We obtained an efficacy factor with mTHPC which was about 390-fold higher than that of Photofrin at $SO_2 = 0.95$, and this factor increased to nearly 590-fold for an $SO_2 = 0.75$. These findings are consistent with the observation that for a given level of tissue oxygenation, mTHPC-PDT treatment beams at 650 nm will have better light transmission than Photofrin-PDT treatment beams at 630 nm due to the reduced absorption by

hemoglobin at 650 vs. 630 nm (Figure 5.1). Interestingly, as illustrated in Figure 5.9, for saturations lower than $SO_2 = 0.75$ no further appreciable enhancement in the ratio of efficacy of mTHPC-PDT vs. Photofrin-PDT is observed, in fact the ratio seems to reach a plateau. As shown in Figure 5.10, this can be explained by the observation that the ratio of 650 vs. 630 nm normalized fluence rates for the different saturations, calculated from the data shown in Table 5.1, have a similar pattern with an increasing ratio for SO_2 of 1.0 to 0.75 and a plateau for lower saturations. This pattern suggests something about the shape of the hemoglobin-absorption spectrum for intermediate saturations between SO_2 of 1.0 and 0. While Figure 5.1 clearly illustrates that the difference in hemoglobin extinction at 630 vs. 650 nm increases as the oxygenation status changes from fully oxygenated to completely deoxygenated, it is not however evident how the gradient in extinction at the two wavelengths changes for intermediate saturations. The calculations presented in Figure 5.10 may indicate that the difference in extinction coefficient between 630 and 650 nm changes rapidly as SO_2 drops from 1.0 to 0.75 and remains fairly unchanged for lower saturations.

In conclusion, incorporating the influence of depth- and oxygen-dependent light attenuation in tissue has allowed us to successfully account for efficacy factors of mTHPC vs. Photofrin well beyond the 175-fold computed in chapter 2 on the basis of photophysical parameters and drug retention and binding properties.

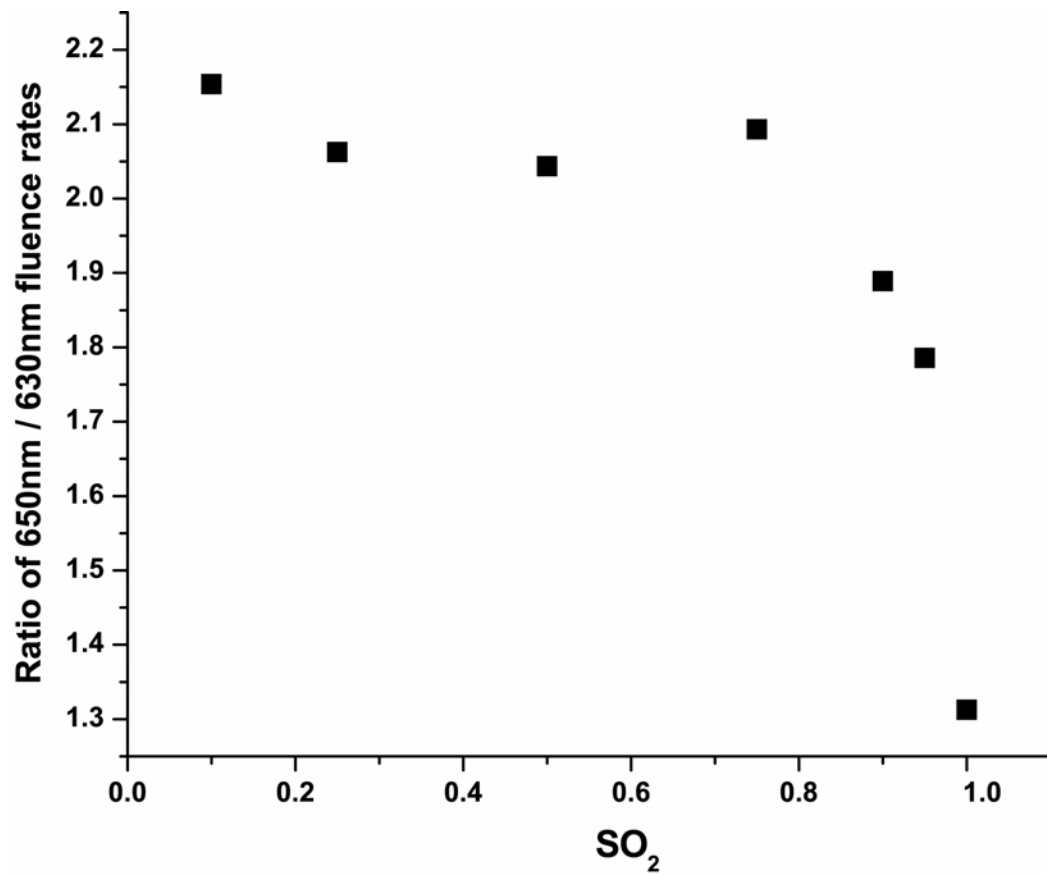


Figure 5.10. Ratio of normalized fluence rates at 650 vs. 630 nm measured in erythrocyte phantoms at a depth of 1 cm for a range of SO₂ from 1.0 to 0.1. The ratios are calculated from the fluence rates presented in table 5.1.

REFERENCES

1. Wouters, B. G., S. A. Weppeler, M. Koritzinsky, W. Landuyt, S. Nuyts, J. Theys, R. K. Chiu, and P. Lambin. (2002) Hypoxia as a target for combined modality treatments. *Eur. J. Cancer* **38**:240-257.
2. Powell, M. E., D. R. Collingridge, M. I. Saunders, P. J. Hoskin, S. A. Hill, and D. J. Chaplin. (1999) Improvement in human tumour oxygenation with carbogen of varying carbon dioxide concentrations. *Radiother. Oncol.* **50**:167-171.
3. Hoskin, P. J., M. I. Saunders, H. Phillips, H. Cladd, M. E. Powell, K. Goodchild, M. R. Stratford, and A. Rojas. (1997) Carbogen and nicotinamide in the treatment of bladder cancer with radical radiotherapy. *Br. J. Cancer* **76**:260-263.
4. Schouwink, H., M. Ruevekamp, H. Oppelaar, R. van Veen, P. Baas, and F. A. Stewart. (2001) Photodynamic therapy for malignant mesothelioma: preclinical studies for optimization of treatment protocols. *Photochem. Photobiol.* **73**:410-417.
5. Chen, Q., Z. Huang, H. Chen, H. Shapiro, J. Beckers, and F. W. Hetzel. (2002) Improvement of tumor response by manipulation of tumor oxygenation during photodynamic therapy. *Photochem. Photobiol.* **76**:197-203.
6. Hull, E. L., and T. H. Foster. (2001) Cytochrome spectroscopy in scattering suspensions containing mitochondria and red blood cells. *Appl. Spect.* **55**: 149-154.
7. Zwart, A., G. Kwant, B. Oeseburg, and W. G. Zijlstra. (1984) Human whole-blood oxygen affinity: effect of temperature. *J Appl. Physiol.* **57**:429-434.
8. Stryer, L. (1988) *Biochemistry*. W. H. Freeman and Company, New York. p.155

9. Busch, T. M., S. M. Hahn, S. M. Evans, and C. J. Koch. (2000) Depletion of tumor oxygenation during photodynamic therapy: detection by the hypoxia marker EF3 [2-(2-nitroimidazol-1[H]-yl)-N-(3,3,3-trifluoropropyl)acetamide]. *Cancer Res.* **60**:2636-2642.
10. Busch, T. M., E. P. Wileyto, M. J. Emanuele, F. Del Piero, L. Marconato, E. Glatstein, and C. J. Koch (2002) Photodynamic therapy creates fluence rate-dependent gradients in the intratumoral spatial distribution of oxygen. *Cancer Res.* **62**:7273-7279.
11. Henderson, B. W., S. M. Waldow, T. S. Mang, W. R. Potter, P. B. Malone, and T. J. Dougherty. (1985) Tumor destruction and kinetics of tumor cell death in two experimental mouse tumors following photodynamic therapy. *Cancer Res.* **45**:572-576.
12. Henderson, B. W. and V. H. Fingar. (1987) Relationship of tumor hypoxia and response to photodynamic treatment in an experimental mouse tumor. *Cancer Res.* **47**:3110-3114.
13. Durand, R. E. and N. E. LePard. (1995) Contribution of transient blood flow to tumour hypoxia in mice. *Acta. Oncol.* **34**:317-323.
14. Coleman, C. N. (1988) Hypoxia in tumors: a paradigm for the approach to biochemical and physiologic heterogeneity. *J. Natl. Cancer Inst.* **80**:310-715.
15. Vaupel, P., K. Schlenger, C. Knoop, and M. Hockel. (1991) Oxygenation of human tumors: evaluation of tissue oxygen distribution in breast cancers by computerized O₂ tension measurements. *Cancer Res.* **51**:3316-3322.
16. Brizel, D. M., G. L. Rosner, L. R. Prosnitz, and M. W. Dewhirst. (1995) Patterns and variability of tumor oxygenation in human soft tissue sarcomas, cervical carcinomas, and lymph node metastases. *Int. J. Radiat. Oncol. Biol. Phys.* **32**:1121-1125.
17. Evans, S. M., S. M. Hahn, D. P. Magarelli, P. J. Zhang, W. T. Jenkins, D. L. Fraker, R. A. Hsi, W. G. McKenna, and C. J. Koch (2001) Hypoxia in

- human intraperitoneal and extremity sarcomas. *Int. J. Radiat. Oncol. Biol. Phys.* **49**:587-9615.
18. Gibson, S. L., K. R. VanDerMeid, R. S. Murant, R. F. Raubertas, and R. Hilf. (1990) Effects of various photoradiation regimens on the antitumor efficacy of photodynamic therapy for R3230AC mammary carcinomas. *Cancer Res.* **50**:7236-7241.
 19. Foster, T. H., R. S. Murant, R. G. Bryant, R. S. Knox, S. L. Gibson, and R. Hilf. (1991) Oxygen consumption and diffusion effects in photodynamic therapy. *Radiat. Res.* **126**:296-303.
 20. Dougherty, T. J., C. J. Gomer, B. W. Henderson, G. Jori, D. Kessel, M. Korbek, J. Moan, and Q. Peng (1998) Photodynamic therapy. *J. Natl. Cancer Inst.* **90**:889-90515.
 21. Hull, E. L., D. L. Conover, and T. H. Foster. (1999) Carbogen-induced changes in rat mammary tumour oxygenation reported by near infrared spectroscopy. *Br. J. Cancer* **79**:1709-1716.
 22. Liu, H. L., Y. L. Song, K. L. Worden, X. Jiang, A. Constantinescu, and R.P.Mason. (2000) Noninvasive investigation of blood oxygenation dynamics of tumors by near-infrared spectroscopy. *Appl. Opt.* **39**:5231-5243.
 23. Finlay, J. C. and T. H. Foster (2004) Hemoglobin oxygen saturations in phantoms and in vivo from measurements of steady state diffuse reflectance at a single, short source-detector separation. *Med. Phys.* Submitted.
 24. Curnow, A., J. C. Haller, and S. G. Bown. (2000) Oxygen monitoring during 5-aminolaevulinic acid induced photodynamic therapy in normal rat colon. Comparison of continuous and fractionated light regimes. *J. Photochem. Photobiol. B* **58**:149-155.
 25. Curnow, A., B. W. McIlroy, M. J. Postle-Hacon, A. J. MacRobert, and S.G.Bown. (1999) Light dose fractionation to enhance photodynamic

therapy using 5-aminolevulinic acid in the normal rat colon. *Photochem. Photobiol.* **69**:71-76.

26. Chen, Q., M. Chopp, M. O. Dereski, B. C. Wilson, M. S. Patterson, A. Schreiber, and F. W. Hetzel. (1992) The effect of light fluence rate in photodynamic therapy of normal rat brain. *Radiat. Res.* **132**:120-123.

Chapter 6: Fluorescent reporter proteins as biomolecular markers in PDT

6.1 Introduction

In addition to evaluating new sensitizers such as mTHPC (meso-tetra hydroxyphenyl chlorin) and investigating their photophysical properties in terms of optimizing therapy, numerous studies have been performed to identify the subcellular targets of PDT and examine site-specific responses to the therapy (1-4). These efforts have successfully identified mitochondria, lysosomes and/or various cytoplasmic membranes as among the primary targets of PDT-mediated

damage, depending on the particular photosensitizer (5). Besides activating several signal transduction pathways such as protein kinase cascades, cytokine expression (6), expression of early response genes (7), and glucose regulated proteins (GRPs) (8), PDT also induces expression of heat shock proteins (HSPs) (9-16) as a result of cellular oxidative stress.

The heat shock protein 70 (HSP70) family has been the most widely studied of all the heat shock proteins and belongs to a large family of protein chaperones. In addition to assisting in refolding and unfolding of proteins in cells (17,18), HSP70s are also involved in many other cellular activities including reorganization of cytoskeletal components, translation initiation, nuclear protein import and export, ribosome assembly, chromatin structure and DNA synthesis. They are not only constitutively and ubiquitously expressed but are also inducible in response to a variety of stressful conditions and are thus commonly referred to in the literature as stress proteins (19).

Figure 6.1 illustrates the various stages in regulation of heat shock response. In the unstressed cell, heat shock transcription factor (HSF) is maintained in a monomeric, non-DNA binding form through its interactions with HSP70. Upon heat shock or other forms of stress, HSF assembles into a trimer and binds to specific sequence elements in heat shock gene promoters called heat shock elements (HSE) and becomes phosphorylated. Transcriptional activation

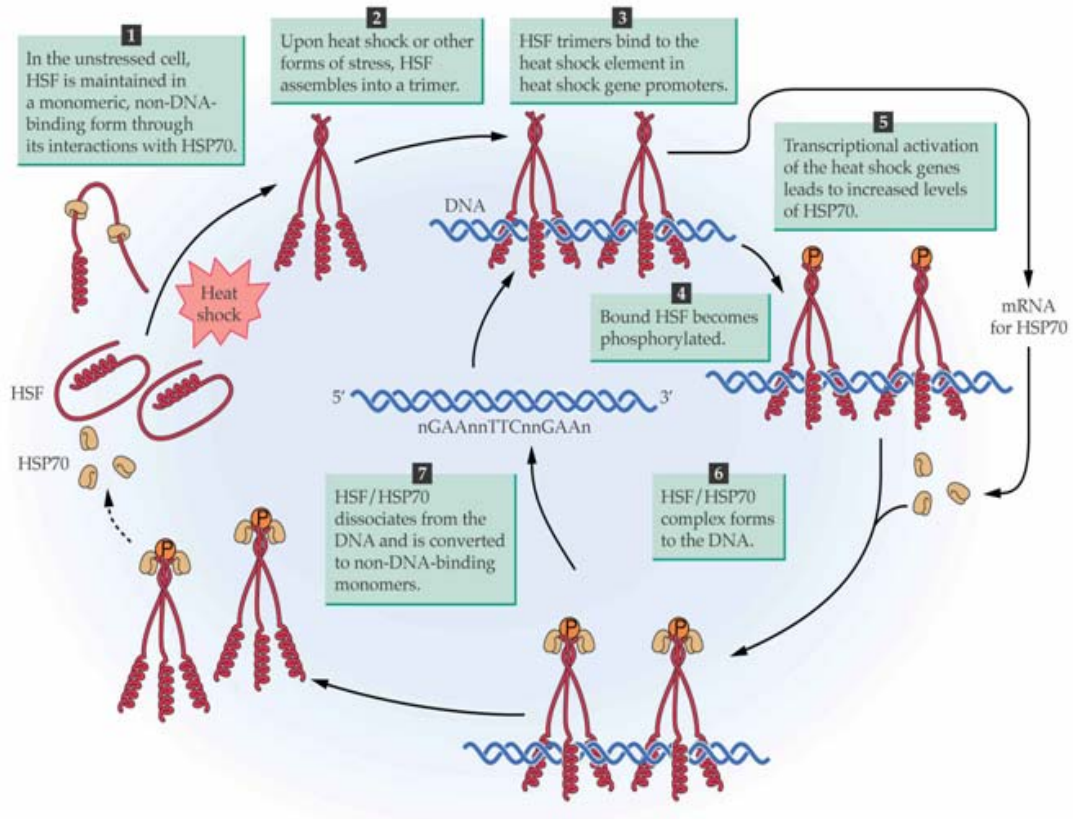


Figure 6.1. A model of HSF regulation.

of the heat shock genes leads to increased levels of HSP70.

In addition to induction by hyperthermia, as illustrated in Figure 6.2, HSPs are also activated by a wide range of physical, chemical and biological agents such as anticancer drugs, transition heavy metals, amino acid analogues, etc. (19, 20). Among the several stress proteins, the HSP70 family is the most abundant and conserved and has been frequently proposed as a potential biomarker of cellular toxicity (21, 22).

Using the chlorin-based photosensitizer mTHPC, we examined the PDT-stress-mediated activation of HSP70 and its relation to cellular toxicity in a mouse tumor cell line transfected with a plasmid consisting of the gene for a green fluorescent protein (GFP) under the control of an *hsp70* promoter. This allowed us to study the mTHPC-PDT-mediated inducible expression of GFP in living specimens *in vitro* and *in vivo* using fluorescence imaging. A primary goal of this work was to assess the range of PDT treatment conditions that would enable the use of mTHPC-PDT as a photophysical switch to activate one specific and widely applicable reporter gene. Our results demonstrated that *hsp70*-driven GFP expression is induced at a cellular level not only by mTHPC-PDT but also by mTHPC sensitization alone. We also noninvasively imaged GFP in a subcutaneous HSP70-GFP/EMT6 tumor *in vivo* and found increased GFP expression in response to mTHPC-PDT.

These preliminary results established the feasibility of using this general

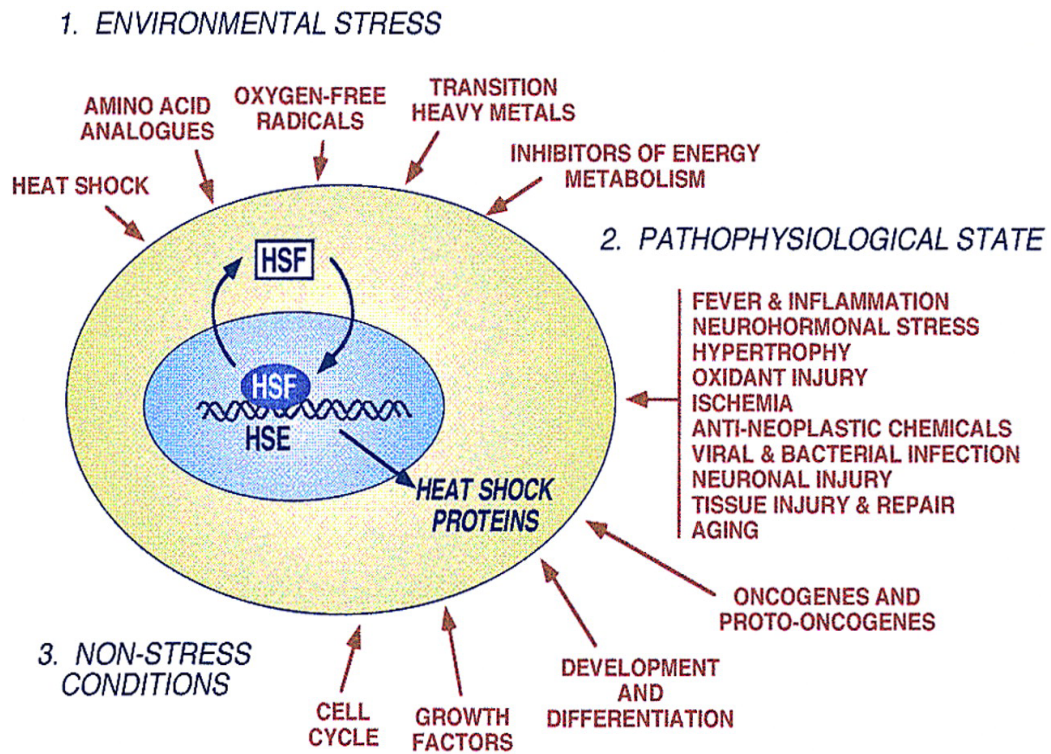


Figure 6.2. Heat shock proteins are expressed in response to a range of diverse stress and non-stress conditions. Reproduced with permission from Morimoto, R.I. (1998) *Genes & Development* **12**:3788–3796

strategy to image molecular responses to PDT in animal models. Finally, with respect to possible clinical relevance, the results suggested that optimal HSP70 accumulation occurs in response to sub-lethal PDT doses. Given the recent interest in the use of HSP70 vaccines to elicit tumor-specific immune responses in patients (23-25), it is possible that a low, sub-curative dose of PDT at the primary tumor site could be used to enhance therapies designed to recruit a systemic immune response.

6.2 Experimental Methods

6.2.1 Chemicals

The photosensitizer mTHPC was obtained from Biolitec Pharma Ltd (Edinburgh, U.K.). The stock solution was prepared by dissolving the drug in a solvent mixture of 30% polyethylene glycol 400, 20% ethanol and 50% water according to the manufacturer's recommendations. Fetal calf serum (FCS) was purchased from Atlanta Biologicals (Atlanta, GA, USA). Hanks' balanced salt solution (HBSS), Lipofectin Reagent and G-418 were purchased from GIBCO (Grand Island, NY, USA). Unless otherwise noted, all other chemicals and reagents were obtained from Sigma Chemical (St. Louis, MO, USA).

6.2.2 Establishing a transfected cell line

We established a mouse mammary EMT6 cell line stably transfected with the

plasmid pR70/GFP. The plasmid construct, providing inducible expression of GFP under the control of a rat hsp70 promoter fragment (approx. 950 bp), was kindly provided by Zdzislaw Krawczyk (Maria Sklodowska Memorial Institute, Glwice, Poland) (26). This reporter plasmid was transfected into EMT6 cells using Lipofectin Reagent. To select stably transfected clones, cells were grown in Basal Eagle Medium (BME) supplemented with 10% FCS containing the antibiotic G-418 at a concentration of $400 \mu\text{g mL}^{-1}$. The pR70/GFP plasmid contains the SV40 promoter driving expression of the neo gene that confers resistance to G-418, allowing for selection of the transfected cells. G-418-resistant clones were then expanded and tested for GFP expression using heat (42°C for 1 hour) as a positive inducible treatment. A single clone exhibiting high heat-induced expression and low basal levels of GFP fluorescence was selected for subsequent studies, and the cells derived from this clone are referred to as HSP70-GFP/EMT6 cells (Figure 6.3).

6.2.3 Cell monolayer imaging

HSP70-GFP/EMT6 cells were grown as monolayers on coverslips placed in Petri dishes containing BME supplemented with 10% FCS and G-418. The cells were then incubated for 24 h with a range of mTHPC concentrations ($0.25 - 7 \mu\text{g mL}^{-1}$) at 37°C . Following incubation, the media containing the sensitizer

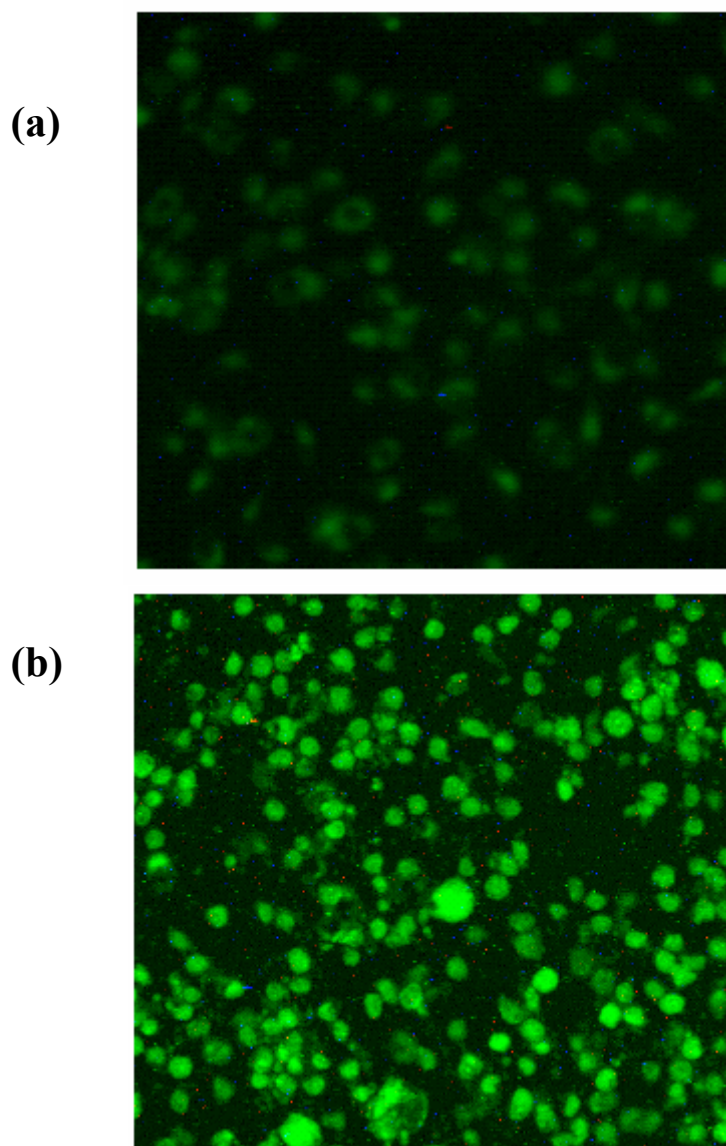


Figure 6.3. (a) GFP fluorescence image of a selected clone under control conditions. (b) GFP fluorescence image of the same clone exposed to heat at 42⁰ C for 1 h and imaged 7 h later.

was removed and replaced with fresh media. PDT irradiation was performed on cell monolayers sensitized with $0.5 \mu\text{g mL}^{-1}$ mTHPC using 650 nm light from an argon-ion laser pumped tunable dye laser (model 599, Coherent, Santa Clara, CA, USA). An irradiance of 5 mW cm^{-2} was used to deliver treatment fluences ranging from $0.025 - 0.75 \text{ J cm}^{-2}$. To compare PDT activation of the hsp70 promoter with that induced by heat, the HSP70-GFP/EMT6 cells were subjected to 42°C for 1 h, consistent with Wycsocka and Krawczyk (26). Immediately after PDT or heat treatment, the coverslips were returned to the incubator for 7 hours to allow sufficient time for GFP synthesis. The choice of a 7 h time point was based on the previous reports of Curry and Levy (10) and of Gomer *et al.* (12). Cells that were exposed only to drug sensitization or to heat or that were used as controls were treated identically (including the medium change) with the exception of irradiation. The control, mTHPC-, heat-, and PDT-treated cells were taken out of the incubator and washed with HBSS. The coverslips were then inverted and placed on a microscope slide and imaged using an Olympus Model BX40F microscope. Images were acquired with a 20X objective (NA 0.5) and digitized using an 8-bit Sony DXC9000 3CCD camera (Sony, Tokyo, Japan). Image acquisition was controlled using Image-Pro software (Version 4.0, Media Cybernetics, Silver Spring, MD, USA). Unless otherwise mentioned all fluorescence images were captured with a 0.3 s acquisition time. For GFP imaging, a GFP bandpass filter cube was used (Endow GFP Bandpass; Chroma

Technology Corporation, Brattleboro, VT), which consisted of an exciter (450 - 490 nm), a 495 nm long pass dichroic and a 500 - 550 nm emitter. A typical EGFP absorption and emission spectrum is shown in Figure 6.4. For each fluorescence image, a corresponding bright field image of the same field of view (FOV) was also acquired. To enable a direct comparison between GFP fluorescence and cell viability in the same field of cells, the drug- or PDT-treated cell samples were immersed in 20% trypan blue for 2 minutes and then washed with HBSS prior to imaging. Trypan blue stained cells with compromised membranes blue, while the viable cells excluded the dye. To account for day to day variations in background GFP expression in control cells, cover slips containing control cells were processed in parallel with every experimental group. Throughout, fluorescence from treated cells was normalized to the parallel control samples.

6.2.4 Image analysis

The digitized images were analyzed using ImageJ (NIH, URL: <http://rsb.info.nih.gov/ij/>) and MATLAB (The MathWorks Inc., Natick, MA). Quantifying the extent and heterogeneity of GFP expression in these samples required various image processing and analysis steps. In order to calculate the area occupied by cells, the contrast in the bright field images was enhanced using the background subtraction tool in ImageJ. This enhancement allowed the

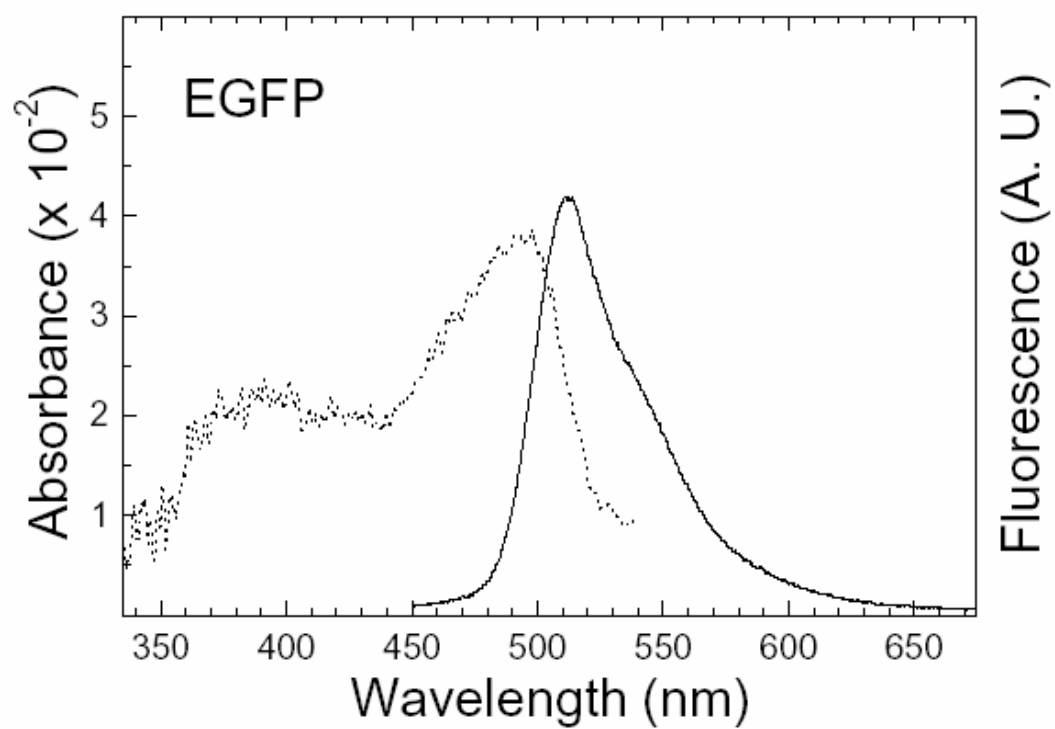


Figure 6.4. Absorption (dotted line) and emission (solid line) spectra of EGFP.

ImageJ thresholding tool to successfully select and calculate all the pixels corresponding to cells in the FOV. The fluorescence images, which were initially saved as 8-bit RGB images, were converted to 8-bit grayscale images with GFP information in the green channel. The pixels with GFP signal were easily selected using the thresholding tool. To calculate GFP intensity, the signals from all of the GFP-positive pixels in an image were summed and then divided by the total number of pixels containing cells as calculated from the corresponding bright field image. This allowed us to quantify the GFP intensity as a function of the total cell area independent of whether or not all of the cells exhibited GFP fluorescence. The analysis also enabled us to estimate the fraction of cells expressing GFP above a threshold. To generate whole-field histograms of GFP intensity, we used MATLAB to superimpose the bright field image of a FOV onto its corresponding GFP fluorescence image. This was done in order to ensure that the fluorescence histograms took into account only those pixels corresponding to regions occupied by cells and ignored artifacts. Cell viability was quantified by counting the total number of pixels that were stained blue in a bright field image and dividing it by the total number of pixels occupied by cells in the same field. The blue-stained pixels offered an image contrast that allowed them to be cleanly selected by the thresholding tool.

6.2.5 *In vivo* treatment and microscopy of HSP70-GFP/EMT6 tumors

We wanted to evaluate the ability of the hsp70 promoter to drive GFP expression in response to PDT-mediated oxidative stress *in vivo* and monitor the same noninvasively. Towards that end, 2 female BALB/c mice were injected subcutaneously in the nape of their necks with 10^6 HSP70-GFP/EMT6 cells. The mice were used for experiments when the tumor diameter had reached approximately 1 cm. Hair removal from the skin surface over the tumor was accomplished by shaving with an electric shear followed by application of the hair removal lotion Nair (Carter-Wallace Inc., NY, USA) and subsequent rinsing with distilled water. One of the mice was used as a control while the other was subjected to PDT. 36 hours prior to PDT, the mouse to be treated was anesthetized with approximately 60 mg kg^{-1} ketamine hydrochloride (Bedford Laboratories, Bedford, OH, USA) and 6 mg kg^{-1} xylazine (The Butler Company, Columbus, OH, USA). mTHPC was administered at a dose of 0.2 mg kg^{-1} body weight by tail vein injection. The mouse was then kept in dark conditions with access to food and water until the start of irradiation. Immediately before PDT, the sensitized mouse was anesthetized with sodium pentobarbital (Butler Company) at a dose of 65 mg kg^{-1} , which was sufficient to chemically restrain her for the duration of irradiation. To prevent movement during irradiation, the mouse was also mechanically restrained with tape. The tumor area was irradiated with 1 J cm^{-2} 650 nm light from the argon-ion laser pumped tunable

dye laser. The laser light was coupled into an optical fiber that was terminated with a gradient index lens (General Fiber Optics, Fairfield, NJ, USA), which was positioned to give a treatment area of about 1 cm diameter and an incident irradiance of 5 mW cm^{-2} . Six hours post-PDT, the treated mouse and the control mouse were again anesthetized with 65 mg kg^{-1} sodium pentobarbital to immobilize them during imaging. Imaging was performed through the shaved skin over the tumor using a Nikon fluorescence stereomicroscope (model SMZ-1500) equipped with a 100 W mercury lamp. Selective excitation of GFP and its fluorescence collection was performed using a GFP band-pass filter cube (Endow GFP Bandpass, Chroma). High-resolution images of 1390×1040 pixels were captured and digitized by a Photometrics 12-bit monochrome cooled charge-coupled-device (CCD) camera (CoolSNAPHQ-M; Roper Scientific, Inc, Trenton, NJ).

6.3 Results and analysis

6.3.1 Cell monolayer experiments

The panel of bright field and their corresponding fluorescence images in Figure 6.5 illustrates the expression of GFP in the HSP70-GFP/EMT6 cells under various conditions. As illustrated in the top panel of images in Figure 6.5 ((-) Light), we found that as the drug concentration was increased from $0.5 \mu\text{g mL}^{-1}$

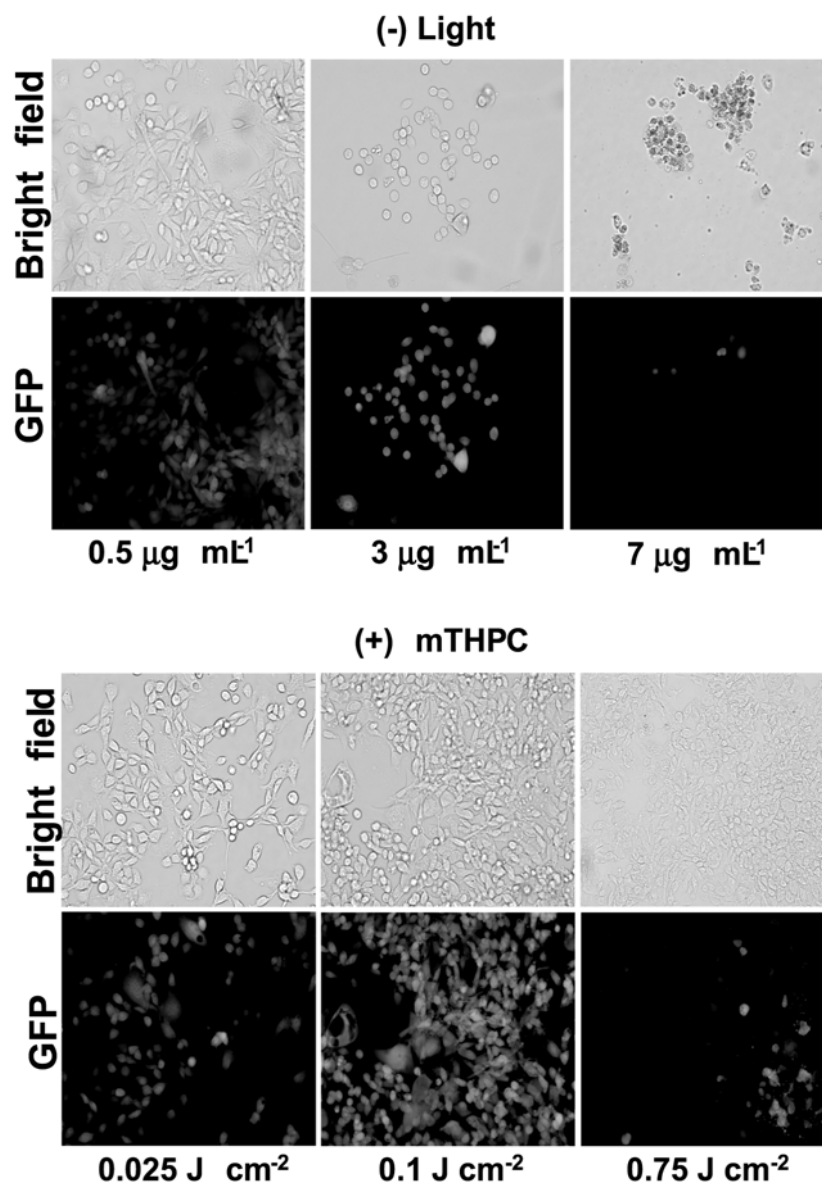


Figure 6.5. Top panel (-) Light: Bright field and GFP fluorescence images of HSP70-GFP/EMT6 cells incubated with various mTHPC concentrations as described in the text. Bottom panel (+) mTHPC: cells sensitized with $0.5 \mu\text{g mL}^{-1}$ mTHPC and irradiated with fluences of 0.025 J cm^{-2} , 0.1 J cm^{-2} , and 0.75 J cm^{-2} . Images were acquired 7 h post-irradiation.

to $3 \mu\text{g mL}^{-1}$ there was an enhancement in the GFP signal intensity and also in the fraction of cells expressing GFP. However, as the drug concentration was increased beyond $3 \mu\text{g mL}^{-1}$, the cells progressively lost their ability to express GFP. An incubation with $7 \mu\text{g mL}^{-1}$ mTHPC greatly diminished the induced GFP signal. We also observed a change in cell morphology in the bright field images of Figure 6.5 (top panel) as the mTHPC concentrations were increased. A similar pattern of GFP induction was observed in the lower panel of images in Figure 6.5 (+ mTHPC), wherein with increasing PDT treatment fluences of 0.025 J cm^{-2} - 0.1 J cm^{-2} there was a progressive increase in GFP signal, which then diminished significantly in response to a higher fluence of 0.75 J cm^{-2} . Although not illustrated, we note that there was a low background level of GFP in the control (- drug, - light) cells, consistent with constitutive expression of HSP70.

Figure 6.6a summarizes the extent of GFP expression in response to a range of mTHPC drug concentrations from $0.25 \mu\text{g mL}^{-1}$ - $7 \mu\text{g mL}^{-1}$. The GFP intensities are normalized to the control value obtained from analysis of cells subjected to neither mTHPC nor light. GFP signal initially increased with increasing mTHPC doses and then decreased. The maximal induction of GFP in these cells was about 5-fold relative to the control levels and was obtained at a concentration of $3 \mu\text{g mL}^{-1}$ mTHPC. Figure 6.6b shows the fraction of cells expressing GFP over the same range of drug incubation concentrations. The

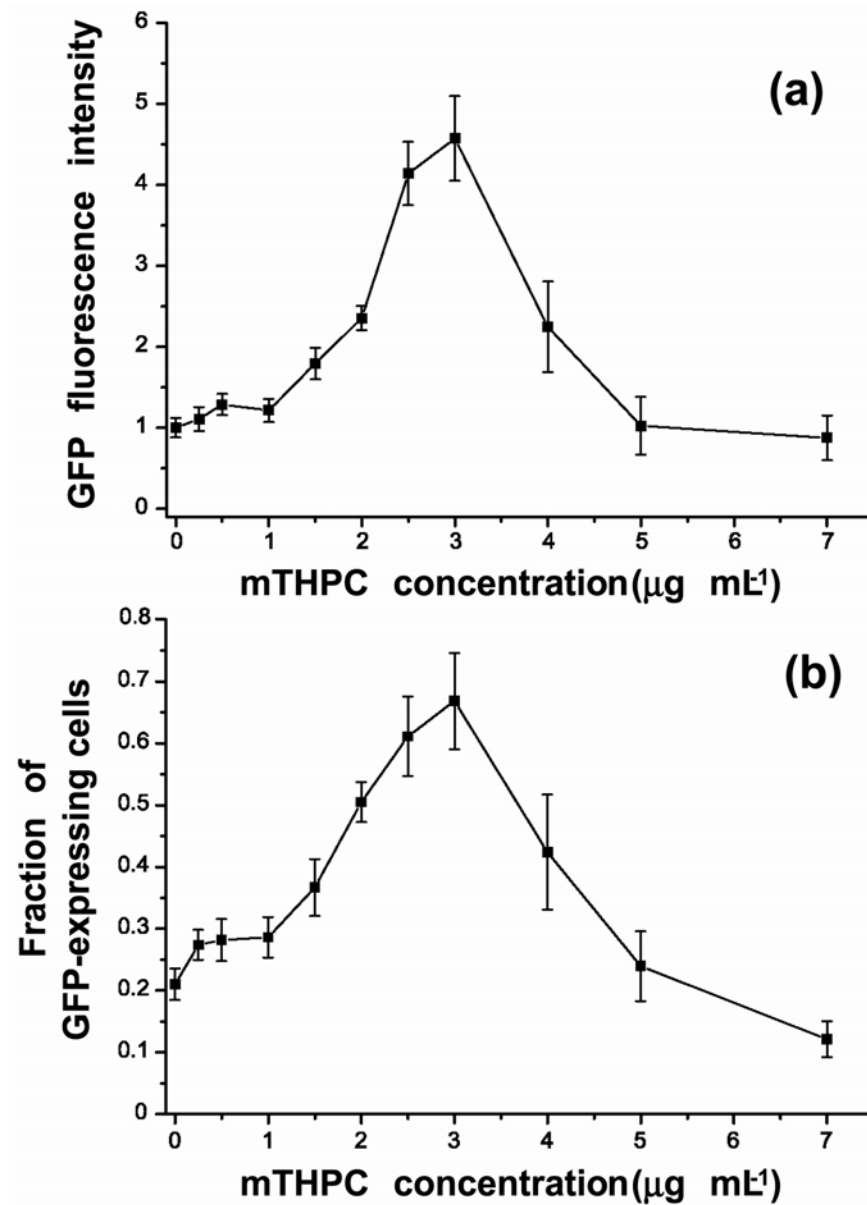


Figure 6.6 (a) Mean GFP fluorescence intensity vs. mTHPC incubation concentration. The intensities are normalized to those measured in untreated controls. (b) The fraction of cells expressing GFP for the same range of mTHPC concentrations. Data were averaged from at least ten separate fields of view. Error bars represent standard error of the mean (SEM).

maximum fraction of GFP expressing cells was also obtained at an mTHPC incubation concentration of $3 \mu\text{g mL}^{-1}$, with levels progressively falling in response to higher drug doses. A similar pattern in both the normalized GFP signal intensity and the fraction of cells expressing GFP was observed in the case where the $0.5 \mu\text{g mL}^{-1}$ mTHPC-sensitized cells were irradiated with a range of fluences from 0.025 J cm^{-2} to 0.75 J cm^{-2} (Figure 6.7). Again the maximal induction in GFP was approximately 5-fold relative to the control levels and was obtained after a treatment fluence of 0.1 J cm^{-2} (Figure 6.7a). At fluences higher than 0.1 J cm^{-2} the cells showed reduced GFP intensity, and a smaller fraction of cells expressed GFP (Figure 6.7b). When the cells were treated with light alone and no drug (*i.e.*, (-) mTHPC), the GFP expression was similar to control levels. We note also that no increase in either GFP levels or toxicity was observed when cells were exposed to the mTHPC solvent at solvent concentrations corresponding to those used for 3 and $7 \mu\text{g mL}^{-1}$ mTHPC incubations. Heat treatment (42°C for 1 h) induced GFP levels similar to that maximally induced (*i.e.* ~ 5 -fold greater than control) by mTHPC alone or by PDT. These results indicate that either mTHPC incubation alone or mTHPC-PDT-mediated stress can maximally activate a transgene under the control of an hsp promoter.

In Figure 6.8, histograms of GFP fluorescence intensity obtained from pixels occupied by cells in an imaged field indicate that, as the mTHPC or PDT doses are increased, the distribution of counts changes appreciably over the 8-bit

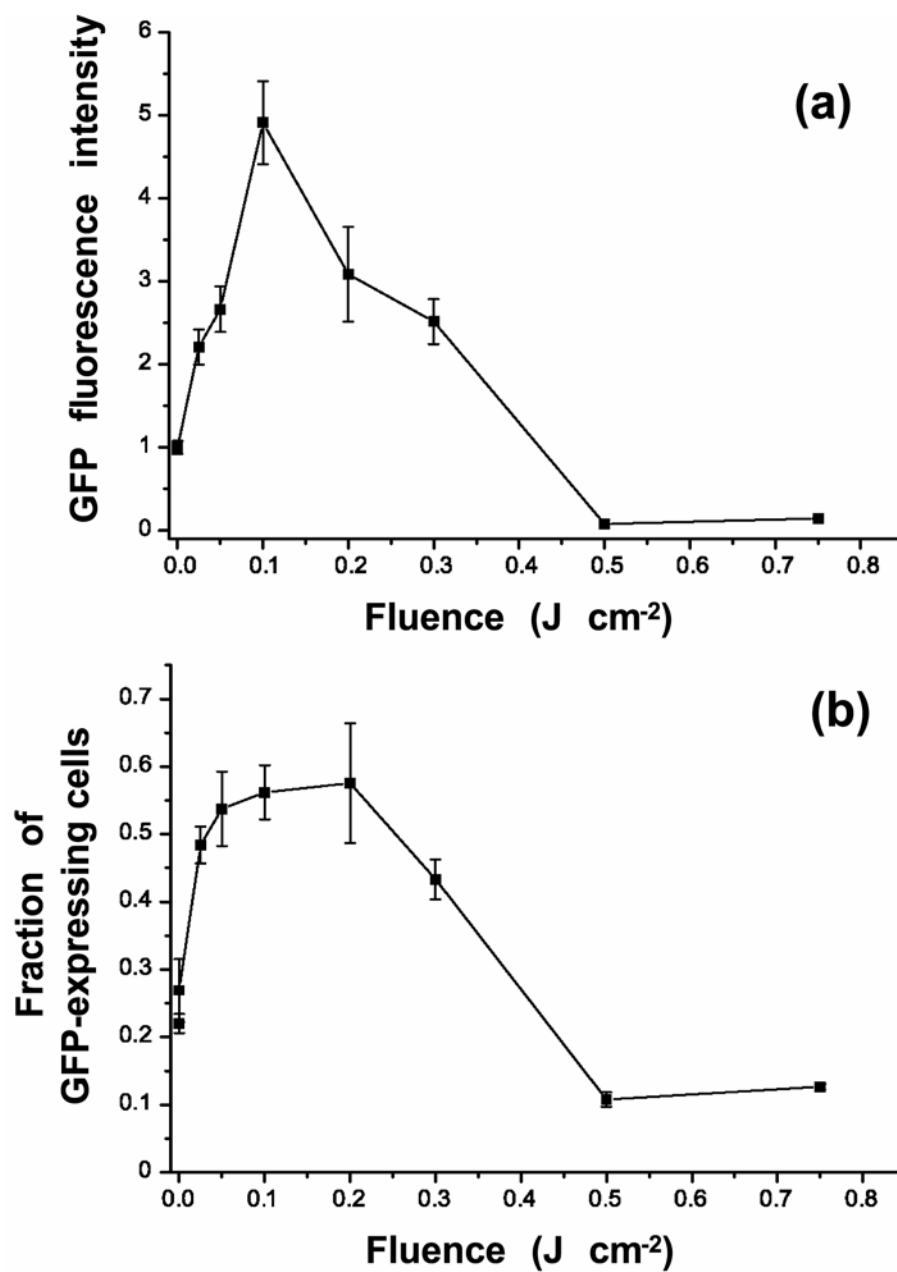


Figure 6.7. (a) Normalized GFP fluorescence intensity vs. PDT treatment fluence in cells sensitized with $0.5 \mu\text{g mL}^{-1}$ mTHPC for 24 h. (b) The fraction of cells expressing GFP for the same range of treatment fluences. Data were averaged from at least ten separate fields of view. Error bars represent SEM.

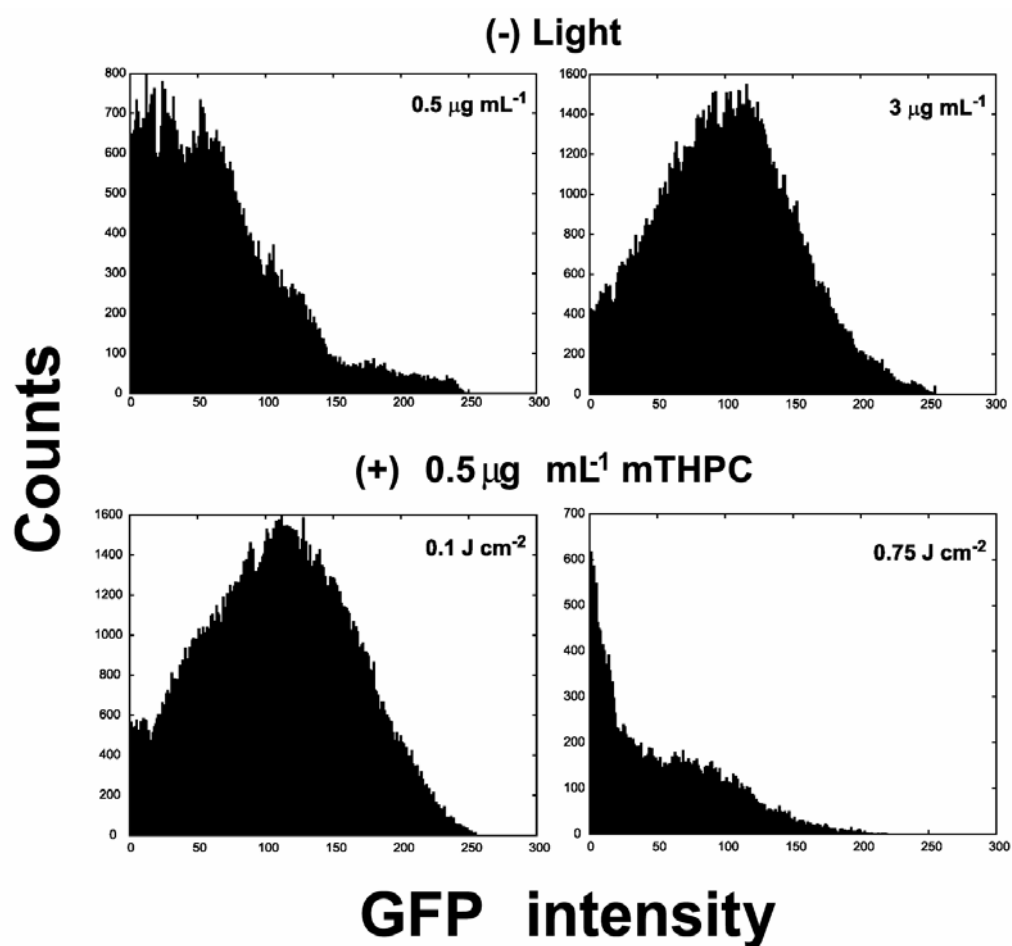


Figure 6.8. Histograms of GFP fluorescence intensity in HSP70-GFP/EMT6 cells subjected to mTHPC incubation with 0.5 $\mu\text{g mL}^{-1}$ (-) light, 3 $\mu\text{g mL}^{-1}$ mTHPC (-) light, 0.5 $\mu\text{g mL}^{-1}$ mTHPC (+) 0.1 J cm^{-2} , and 0.5 $\mu\text{g mL}^{-1}$ mTHPC (+) 0.75 J cm^{-2} .

dynamic range. Compared to the $0.5 \mu\text{g mL}^{-1}$ mTHPC, (-) light case, the count distributions for a drug dose of $3 \mu\text{g mL}^{-1}$ ((-) light) and for a PDT dose of $0.5 \mu\text{g mL}^{-1}$ mTHPC and a fluence of 0.1 J cm^{-2} are not only broader but also exhibit more pixels with higher intensity values. However, as the fluence is increased to 0.75 J cm^{-2} the distribution becomes narrower with increased counts in the lower intensity pixel ranges, consistent with decreased GFP levels as shown in Figure 6.7. In order to determine whether these pixel intensity distributions were the result of intracellular heterogeneity or differences in the extent of induction among cells, we also analyzed intracellular distributions in individual cells. The representative histograms in Figure 6.9 were obtained from regions of interest corresponding to two different cells in a field of cells that had been PDT treated with $0.5 \mu\text{g mL}^{-1}$ mTHPC and a fluence of 0.1 J cm^{-2} . The distribution of pixel counts in both of these intra-cellular histograms are relatively narrow and clearly do not account for the broader distribution observed in Fig 6.8 for the same treatment condition. Thus, the panels of histograms in Figures 6.8 and 6.9 establish that while there is a spatial heterogeneity in HSP70-GFP expression at an intracellular level and among cells, the heterogeneity among similarly treated cells is greater than the heterogeneity within any individual cell. From the whole-field histograms of GFP pixel brightness, we calculated the pixel counts with intensity values greater than 100 as a fraction of the total population of fluorescent pixels in a FOV for three

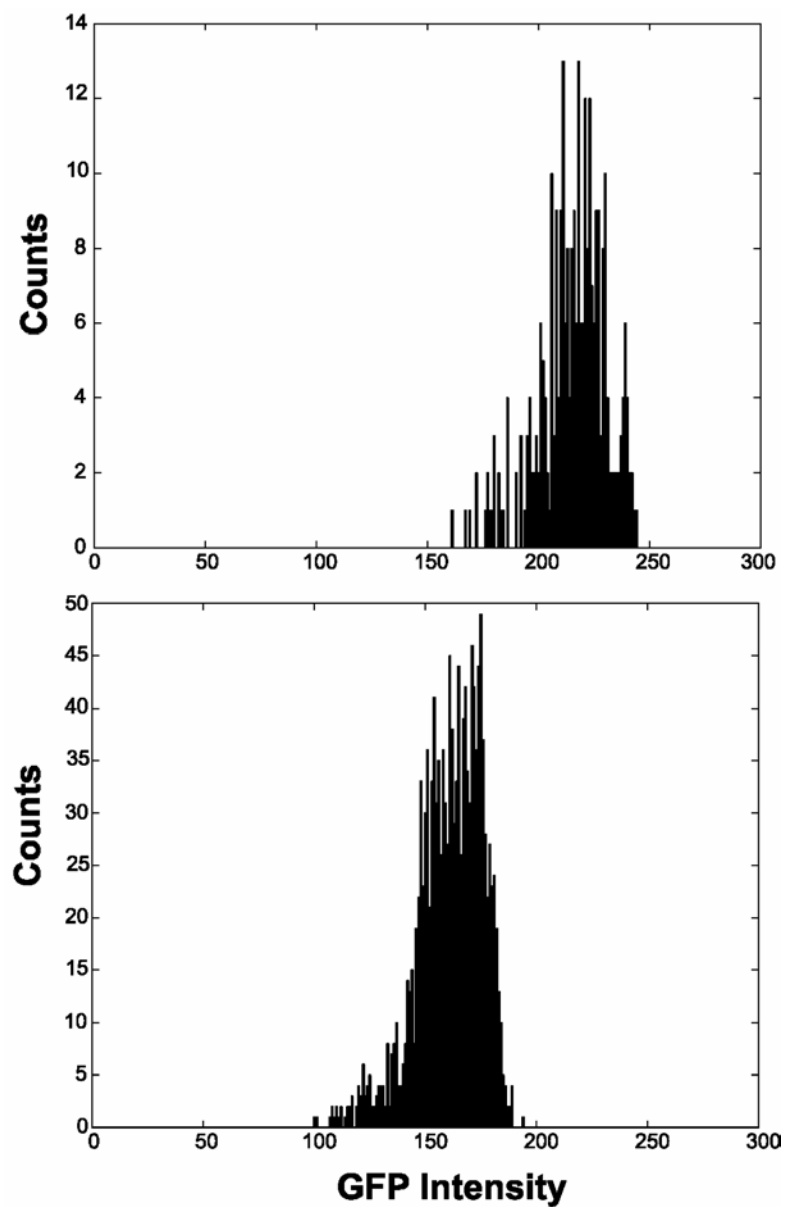


Figure 6.9. Histograms of intracellular GFP intensity in cells treated with $0.5 \mu\text{g mL}^{-1}$ mTHPC and a fluence of 0.1 J cm^{-2} . Histograms were generated from regions of interest superimposed on cells expressing GFP fluorescence.

mTHPC-sensitized and mTHPC-PDT-treated cases. These results are collected in Table 6.1. We observed that as the mTHPC dose or the fluence was increased to $3 \mu\text{g mL}^{-1}$ or 0.1 J cm^{-2} , respectively, there was a significant increase in the percentage of GFP-positive pixels expressing intensities higher than 100. The percentage is considerably lower for cells that were treated with either low mTHPC concentration ($0.5 \mu\text{g mL}^{-1}$) or fluence (0.025 J cm^{-2}). Low pixel count fractions were also obtained for cells treated with either high drug dose ($7 \mu\text{g mL}^{-1}$) or PDT (0.75 J cm^{-2}). These results demonstrate that the initial enhancement followed by the decrease in GFP signal intensities (Figures 6.6a, 6.7a) in response to mTHPC concentrations or mTHPC-PDT is a function of both the number of pixels occupied by cells expressing GFP and their corresponding intensities.

In order to investigate possible reasons for the loss in GFP fluorescence at the higher mTHPC and PDT doses, we assessed cell viability as measured by trypan blue exclusion. The bright field images in Figure 6.10 illustrate the trypan-blue-stained cells under various treatment conditions. The non-viable cells are stained blue, and as is evident, the fraction of non-viable cells increases with increasing mTHPC concentration and PDT dose. Counts are calculated relative to the total number of GFP fluorescent pixels in an imaged field. The GFP fluorescence images corresponding to their respective bright field images show that cells which have been stained blue do not fluoresce, indicating that

Table 6.1

Treatment Conditions	Mean percentage of pixel counts with GFP intensity > 100	Standard Deviation
0.5 $\mu\text{g mL}^{-1}$ mTHPC (n = 4)	19	8.9
3 $\mu\text{g mL}^{-1}$ mTHPC (n = 3)	46.1	14
7 $\mu\text{g mL}^{-1}$ mTHPC (n = 3)	15.8	2.6
0.025 J cm^{-2} mTHPC-PDT (n = 4)	29.1	4.5
0.1 J cm^{-2} mTHPC-PDT (n = 5)	50.4	3.5
0.75 J cm^{-2} mTHPC-PDT (n = 3)	15.2	11.6

Table 6.1. The percentage of GFP-positive pixels with intensities greater than 100 are evaluated from imaged fields exposed to the indicated treatment conditions. Counts are calculated relative to the total number of GFP fluorescent pixels in an imaged field.

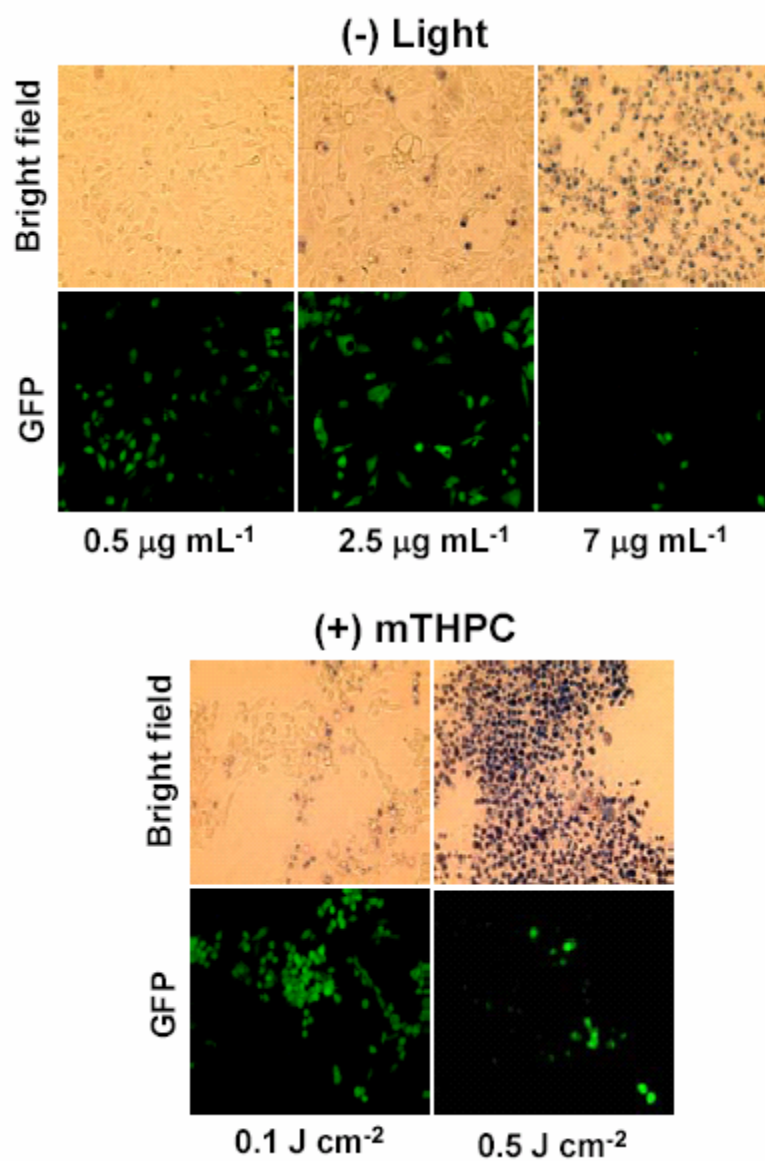


Figure 6.10. Bright field and the corresponding GFP fluorescence images of HSP70-GFP/EMT6 cells assayed for viability with trypan blue. Viable cells exclude trypan blue while nonviable cells are stained blue in the bright field images. Top panel, (-) light: cells were sensitized with 0.5 $\mu\text{g mL}^{-1}$, 2.5 $\mu\text{g mL}^{-1}$ and 7 $\mu\text{g mL}^{-1}$ mTHPC for 24 h. Bottom panel, (+) mTHPC: cells were sensitized with 0.5 $\mu\text{g mL}^{-1}$ mTHPC and irradiated with fluences of 0.1 J cm^{-2} and 0.5 J cm^{-2} .

non-viable cells do not express GFP. In Figure 6.11, the cell viability is plotted as a function of mTHPC incubation concentration (-) light or PDT dose. An mTHPC exposure of $7 \mu\text{g mL}^{-1}$ results in an approximate 70% loss of cell viability (Figure 6.11a), while a PDT fluence of 0.5 J cm^{-2} results in cell viability of less than 20% (Figure 6.11b). These results confirm that loss of GFP expression in cells with increased drug or light doses is a result of non-viable cells which have lost their ability to synthesize GFP.

6.3.2 *In vivo* experiments

Results of pilot experiments designed to demonstrate feasibility of using these cells to report PDT-induced HSP expression *in vivo* are presented in Figure 6.12, where fluorescence images of HSP70-GFP/EMT6 tumors grown in mice and imaged using the stereo microscope are shown. The two images are unscaled and were generated from unprocessed pixel intensity data. A comparison between the control tumor (Figure 6.12a) and the PDT-treated tumor (Figure 6.12b) illustrates that PDT-mediated oxidative stress induced enhanced GFP expression in the mouse tumor *in vivo*. A clear heterogeneity of GFP expression in the image of the treated tumor is observed, with the brightest pixels in the image corresponding to the area illuminated directly by the treatment beam. The levels of GFP expression in the regions outside of the irradiated field were

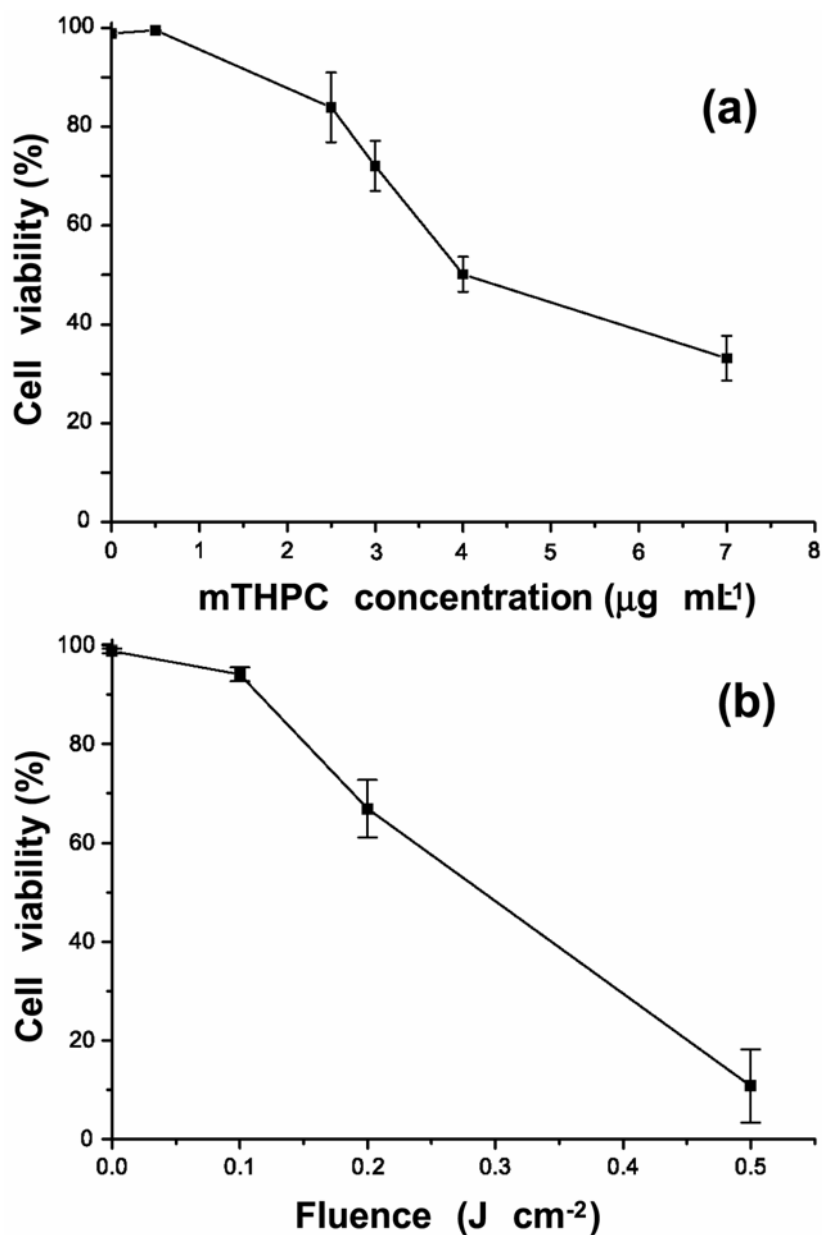


Figure 6.11. (a) Cell viability vs. drug concentration as quantified using the trypan blue assay. The control viability case corresponds to (-) mTHPC (-) light controls. (b) Cell viability vs. fluence. The control viability (0.0 J cm^{-2}) case corresponds to cells incubated with $0.5 \mu\text{g mL}^{-1}$ mTHPC but not exposed to light. Viabilities are calculated from analysis of at least 3 fields of view. Error bars are SEM.

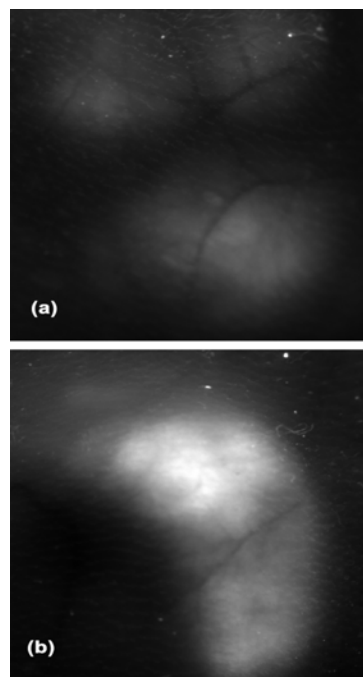


Figure 6.12. Grayscale GFP fluorescence images of HSP70-GFP/EMT6 tumors grown subcutaneously in BALB/c mice and imaged through the skin *in vivo*. (a) Image of a control tumor in an untreated mouse, (-) mTHPC (-) light, and (b) image of a tumor sensitized with a tail vein injection of 0.2 mg kg^{-1} mTHPC 24 h prior to irradiation with 1 J cm^{-2} 650 nm light at an irradiance of 5 mW cm^{-2} . The image was acquired 6 h after PDT.

comparable to the levels induced in the control tumor. This leads to the conclusion that the injected drug concentration of 0.2 mg kg^{-1} mTHPC used for sensitization induced minimal GFP expression in the tumor.

6.4 Discussion

A gel electrophoresis study by Mang and Dougherty (9) on populations of EMT6 cells was the first to show that dihematoporphyrin ether-PDT-mediated oxidative stress resulted in enhanced expression of HSPs. Curry and Levy (10) reported increased induction of HSP47, HSP70, HSP90 and HSP110 following benzoporphyrin derivative, monoacid ring A (BPD)-PDT *in vitro*. Using two-dimensional gel electrophoresis of excised tumor cells subjected to BPD-PDT *in vivo*, these authors observed the induction of the same set of stress proteins except HSP47. Gomer *et al.* (11) examined the transcription and translation of oxidative stress genes in response to PDT and found that Photofrin incubation, Photofrin-PDT and Rose Bengal-PDT caused increased HSP34 (heme oxygenase) mRNA production and heme oxygenase synthesis. In a subsequent study, Gomer *et al.* (12) showed that PDT performed on RIF-1 cells *in vitro* using either a chlorin (mono-L-aspartyl chlorin e6 (Npe6))- or a purpurin (tin etio-purpurin (SnET2))-based sensitizer enhanced HSF binding activity and HSP70 mRNA and protein production. They also observed that dark incubation of cells with SnET2 resulted in increased specific HSF binding. Identical *in vitro*

photosensitization conditions with Photofrin activated minimal HSF binding and no HSP70 induction. However, reverse transcriptase PCR analysis of RIF-1 tumors *in vivo* demonstrated that PDT with all three sensitizers, NPe6, SnET2 and Photofrin, induced enhanced HSP70 mRNA transcription. Luna *et al.* (13) used an hsp70 promoter to drive the expression of reporter genes such as CAT (chloramphenicol acetyl transferase) and β -gal (β -galactidose) after Npe6-PDT and observed increased levels of expressed genes post-PDT. They also observed that both Npe6- and Photofrin-PDT induced hsp70-promoter-driven β -gal expression in RIF tumors *in vivo*, although Photofrin-PDT was unable to elicit any significant response in RIF cells *in vitro*. In the same study, the authors reported Npe6-PDT-activated inducible expression of therapeutically relevant human genes p53 and TNF- α in SKOV cells transfected with vector constructs containing either p53 or TNF- α under the control of an hsp70 promoter. Hanlon *et al.* (16) used flow cytometry to analyze the induction of HSP60 expression in two different cell lines using a fluorescent antibody targeted to HSP60 and found enhanced stress protein levels induced not only by Photofrin-PDT but also by Photofrin incubation alone.

A primary goal of our study was to investigate a range of conditions under which mTHPC-PDT could function as a photophysical switch for controlling the expression of a particular reporter gene. Our method involved using an inducible promoter for PDT-mediated activation of hsp70 gene

expression. We hypothesized that the *hsp70* promoter could be exploited for coupling the oxidative effects of PDT to the inducible expression of a fluorescent reporter protein such as GFP, thereby enabling the study of HSP70 expression in response to PDT in individual, intact cells in culture and in the intact animal *in vivo*.

We observed that there was a variable basal expression of GFP in the transfected EMT6 cells, which is likely attributed to non-environmental stress factors such as the cell cycle (19). Increased levels of GFP were observed following incubation of cells with mTHPC-sensitization alone. The GFP expression showed an mTHPC dose-dependent response with an initial gradual increase to maximally induced levels and then a drop to basal levels or lower with further increase in mTHPC concentrations. The mTHPC-induced stress response was not totally unexpected as prior studies have shown that Photofrin incubation induced expression of HSP60 in RIF and HT29 cells (16) and of HSP34 (heme oxygenase) in V79 cells (11). As noted above, Gomer *et al.* (12) reported increased HSF binding in response to SnET2 incubation, although minimal HSF binding and no HSP70 induction was observed following Photofrin incubation. These varied results reported in the literature in addition to our finding thus indicate that stress responses to drug incubation are specific and strongly sensitizer dependent.

For PDT experiments, an mTHPC dose of $0.5 \mu\text{g mL}^{-1}$ was chosen

because this incubation concentration induced minimal GFP expression over the basal level. This allowed us to study the extent of HSP70 induction with increasing light fluences. An important advantage of sensitizing cells with a low drug dose is that this not only exposes them to negligible dark stress / toxicity levels but also does not "prime" them for light treatment by initiating any kind of tolerance mechanism. Patterns of GFP intensity in response to increasing mTHPC-sensitized PDT were similar to those observed with mTHPC incubation in the absence of irradiation. We observed a fluence-dependent increase in GFP fluorescence intensity until maximal levels were induced at a fluence of 0.1 J cm^{-2} and a rapid fall off at higher fluences. With both increasing mTHPC incubation concentrations and mTHPC-PDT doses, the overall dose dependence of GFP fluorescence intensity (Fig. 6.6a and 6.7a) was similar to that reported by the fraction of cells expressing GFP in a treated field (Fig. 6.6b and 6.7b).

To verify that the variations in GFP signal intensity were not due simply to corresponding variations in the fraction of expressing cells but also to changes in pixel intensities, we analyzed the GFP intensity histograms for various treatment cases. As summarized in Table 6.1, the conditions of mTHPC incubation ($3 \mu\text{g mL}^{-1}$) or PDT fluence (0.1 J cm^{-2}) that invoked optimal GFP signal intensity also induced a significant increase in the percentage of the highest intensity GFP-positive pixels compared to the other treatment cases. We thus conclude that the calculated GFP intensities in Figures 6.6a and 6.7a report

both the individual pixel intensities and the fraction of GFP-expressing pixels. Further, we noted that the analysis of histograms of GFP intensity obtained from whole-field and intra-cellular regions demonstrated that the heterogeneity in fluorescence within any one cell was narrower than the heterogeneity among cells.

In order to test the hypothesis that the observed decrease in GFP expression with increasing mTHPC concentrations or PDT fluences was due to loss in cell viability we performed a trypan blue dye exclusion assay on the treated cells. As illustrated in the bright field images of Figure 6.10 and the summary plots of Figure 6.11, the cell viability dropped significantly with mTHPC or PDT doses higher than those which activated maximal GFP induction. At a PDT fluence of 0.1 J cm^{-2} approximately 90% of the cells were viable, indicating that sublethal PDT-doses resulted in maximal hsp70-activated GFP expression. In contrast, an mTHPC incubation with $7 \mu\text{g mL}^{-1}$ or a fluence of 0.5 J cm^{-2} resulted in 30% or fewer viable cells. These findings demonstrate that the reduced cell viability is responsible for the reduction in GFP intensity with increasing mTHPC or PDT doses. Our results are in qualitative agreement with a report by Luna *et al.* (13), in which the authors examined the Npe6-PDT-mediated expression of the CAT reporter gene under the control of an hsp70 promoter in RIF cells and observed that the CAT expression initially increased with increasing PDT doses and then decreased. They attributed the decrease in

CAT expression to a greater percentage of cells being killed by the treatment, although viability was not measured directly. The dark toxicity observed in our studies with mTHPC sensitization alone is consistent with prior findings of Stephanie Coutier (27), whose experiments were performed on 500- μm diameter Colo26 spheroids. She found that sensitization with $10\ \mu\text{g mL}^{-1}$ mTHPC in the absence of irradiation resulted in approximately 50% cell survival.

To establish “proof of principle” that our cell monolayer findings could be translated into the *in vivo* situation, we needed to assess whether the transfected EMT6 cells could be grown successfully as a subcutaneous tumor and if the hsp70 promoter could drive the expression of GFP in response to PDT *in vivo*. The latter was not obvious given the oxygen requirement for the synthesis of GFP and the possible presence of pre-existing and PDT-induced hypoxia in the tumor. We observed that PDT treatment of an HSP70-GFP/EMT6 tumor *in vivo* indeed did result in unambiguous enhanced expression of GFP fluorescence as compared to the control, non-sensitized tumor. In our fluorescence images, we observed that both in the control as well as the treated tumor there was a heterogeneous distribution of GFP expression levels. In the image of the treated tumor in Figure 6.12, the region where the GFP expression is highest is that corresponding to the PDT irradiation spot. The adjacent areas were illuminated only minimally by scattered light or not at all. Areas of the treated tumor other than the irradiated spot show levels of expression comparable to control levels,

thus indicating that an mTHPC dose of 0.2 mg kg^{-1} caused little or no HSP70-induced GFP expression. Although the *in vivo* findings presented here represent only an initial feasibility study, they confirm that PDT-mediated oxidative stress results in HSP70-induced GFP expression and illustrate the potential for using GFP as a fluorescent reporter for molecular responses to PDT *in vivo*. To the best of our knowledge this result represents the first report of PDT-induced gene expression optically imaged in a live animal model.

Our studies with GFP as a fluorescent reporter coupled to an inducible hsp70 promoter provide us with a model system which can be used to investigate several potentially interesting research problems in PDT and in cancer research more broadly. The system described here provides a useful means to monitor noninvasively the therapy-induced expression in a living specimen and to evaluate both spatial heterogeneity and the time course of induction with each tumor serving as its own internal control. Cell monolayer experiments with fluorescent reporters permit the study of inducible expression on per cell basis, while biochemical assays or measurements involving CAT or β -gal as reporter genes provide complementary information from whole populations of cells.

With respect to potential clinical relevance, the results from both the *in vitro* and the pilot *in vivo* experiments, where sublethal doses of PDT stimulated optimal induction of HSP70, can be exploited in a strategy in which low dose PDT is administered with the intent to prime a tumor-specific immune response,

as suggested by several published reports indicating that HSPs may play a pivotal role in antitumor immunity *in vivo* by activating dendritic cells, antigen presentation, and enhancing host cell infiltration (23-25). Even in situations where PDT is intended to be curative, however, the low photodynamic doses that induce significant HSP70 accumulation may be present at the periphery of the treated target volume and may contribute to an immune response through this mechanism.

6.5 Future Direction

We are currently in the process of extending the work reported here to related studies using multicell tumor spheroids grown from the HSP70-GFP/EMT6 cells. These experiments will evaluate spatial non-uniformity of HSP70 induction in a model system that includes heterogeneity in cell proliferative status, photosensitizer concentration and in oxygen and will provide an opportunity to extend methods used for determining photodynamic thresholds for clonogenic cell death to the determinations of corresponding thresholds for gene induction. The hypothesis motivating these studies is that the PDT-induced activation of HSP70 will exhibit a threshold in $^1\text{O}_2$ and that this threshold can be determined by relating the spatial distribution of photochemical oxygen consumption, *i.e.* the PDT dose, in spheroids to that of the GFP fluorescence. Unlike the determination of clonogenic threshold, which requires dissociation of spheroids

following PDT treatment, these experiments will exploit our ability to perform simultaneous two-color laser scanning confocal imaging.

To perform two color confocal imaging, the confocal setup shown in chapter 3 is slightly modified. The modified setup includes an additional imaging detection channel using a second photomultiplier tube (PMT) detector as shown in Figure 6.13. 488 nm light from the argon-ion laser will be used to excite both GFP and mTHPC fluorescence from the spheroid confocal sections. The excited fluorescence will be deflected from the dichroic mirror DM1 (488 DMXPX, Chroma technology corporation, Brattelboro, VT) and then passed through a longpass filter (HQ500LP, Chroma) to further minimize any excitation light in the detection path. For the purposes of two-color imaging, the mTHPC and GFP fluorescent photons after passing through the confocal pinhole are separated by another dichroic DM2 (560 DCXR, Chroma) placed in front of the two PMT detectors. A bandpass filter (HQ515/30, Chroma) is placed before PMT₂ and a long pass cutoff filter RG645 (Schott Glass Technologies, Duryea, PA) before PMT₁. This allows the simultaneous collection of GFP fluorescence by PMT₂ and that of mTHPC sensitizer fluorescence by PMT₁. This experimental setup allows us to examine GFP expression levels in intact PDT-treated spheroids and correlate the spatial distribution of GFP with sensitizer photobleaching and PDT dose deposition. Finally, these fluorescent reporter protein systems can also be used to design studies, both in spheroids and in

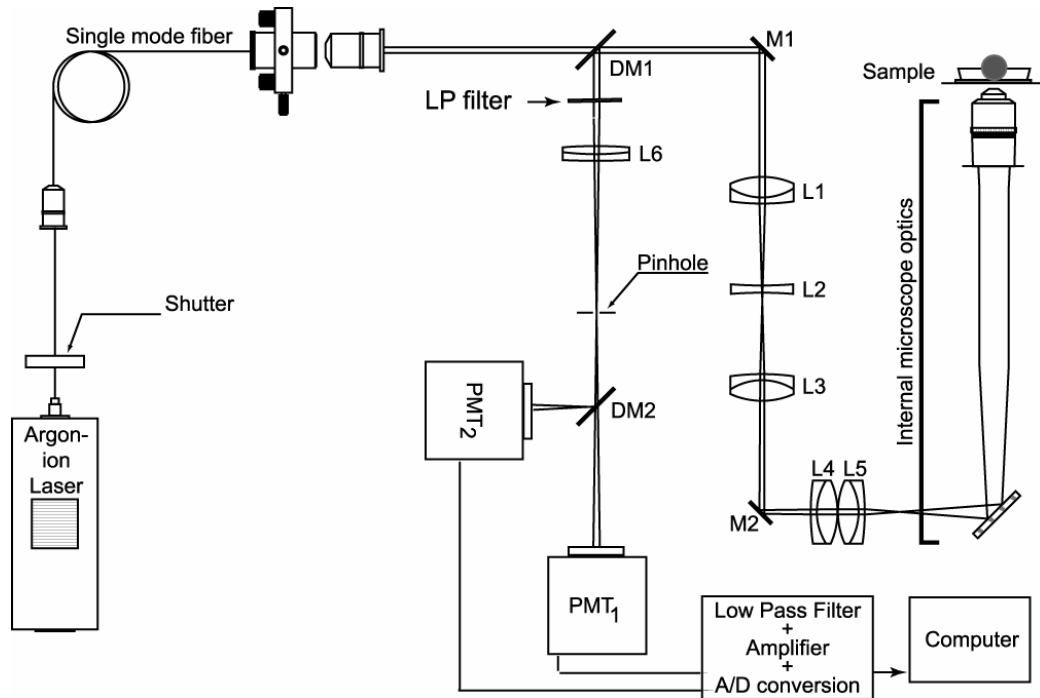


Figure 6.13. Basic confocal microscope setup for simultaneous two-color imaging of GFP and mTHPC fluorescence in spheroids. The dichroic mirror DM1 separates the GFP and mTHPC fluorescence from the backscattered 488 nm excitation light. The dichroic DM2 splits the fluorescence signal, with PMT₂ collecting the GFP fluorescence and PMT₁ detecting the mTHPC fluorescence photons.

rodent tumors grown *in vivo*, to investigate the effects of other PDT-induced effects such as that of hypoxia.

REFERENCES

1. Dougherty, T. J. (2002) An update on photodynamic therapy applications. *J. Clin. Laser Med. Surg.* **20**, 3-7.
2. Ackroyd, R., C. Kelty, N. Brown, and M. Reed (2001) The history of photodetection and photodynamic therapy. *Photochem. Photobiol.* **74**, 656-669.
3. Oleinick, N. L., R. L. Morris, and I. Belichenko (2002) The role of apoptosis in response to photodynamic therapy: what, where, why, and how. *Photochem. Photobiol. Sci.* **1**, 1-21.
4. Vrouenraets, M. B., G. W. Visser, G. B. Snow, and G. A. van Dongen (2003) Basic principles, applications in oncology and improved selectivity of photodynamic therapy. *Anticancer Res.* **23**, 505-522.
5. Oleinick, N. L. and H. H. Evans (1998) The photobiology of photodynamic therapy: cellular targets and mechanisms. *Radiat. Res.* **150**, 146-156.
6. Moor, A. C. (2000) Signaling pathways in cell death and survival after photodynamic therapy. *J. Photochem. Photobiol. B* **57**, 1-13.
7. Luna, M. C., S. Wong, and C. J. Gomer (1994) Photodynamic therapy mediated induction of early response genes. *Cancer Res.* **54**, 1374-1380.
8. Gomer, C. J., A. Ferrario, N. Rucker, S. Wong, and A. S. Lee (1991) Glucose regulated protein induction and cellular resistance to oxidative stress mediated by porphyrin photosensitization. *Cancer Res.* **51**, 6574-6579.
9. Mang, T. S. and T. J. Dougherty (1985) Time and sequence dependent influence of in vitro photodynamic therapy (PDT) survival by hyperthermia. *Photochem. Photobiol.* **42**, 533-540.

10. Curry, P. M. and J. G. Levy (1993) Stress protein expression in murine tumor cells following photodynamic therapy with benzoporphyrin derivative. *Photochem. Photobiol.* **58**, 374-379.
11. Gomer, C. J., M. Luna, A. Ferrario, and N. Rucker (1991) Increased transcription and translation of heme oxygenase in Chinese hamster fibroblasts following photodynamic stress or Photofrin II incubation. *Photochem. Photobiol.* **53**, 275-279.
12. Gomer, C. J., S. W. Ryter, A. Ferrario, N. Rucker, S. Wong, and A. M. Fisher (1996) Photodynamic therapy-mediated oxidative stress can induce expression of heat shock proteins. *Cancer Res.* **56**, 2355-2360.
13. Luna, M. C., A. Ferrario, S. Wong, A. M. Fisher, and C. J. Gomer (2000) Photodynamic therapy-mediated oxidative stress as a molecular switch for the temporal expression of genes ligated to the human heat shock promoter. *Cancer Res.* **60**, 1637-1644.
14. Verrico, A. K. and J. V. Moore (1997) Expression of the collagen-related heat shock protein HSP47 in fibroblasts treated with hyperthermia or photodynamic therapy. *Br. J. Cancer* **76**, 719-724.
15. Verrico, A. K., A. K. Haylett, and J. V. Moore (2001) In vivo expression of the collagen-related heat shock protein HSP47, following hyperthermia or photodynamic therapy. *Lasers Med. Sci.* **16**, 192-198.
16. Hanlon, J. G., K. Adams, A. J. Rainbow, R. S. Gupta, and G. Singh (2001) Induction of Hsp60 by Photofrin-mediated photodynamic therapy. *J. Photochem. Photobiol. B* **64**, 55-61.
17. Morimoto, R. I. (1993) Cells in stress: transcriptional activation of heat shock genes. *Science* **259**, 1409-1410.
18. Morimoto, R. I. and M. G. Santoro (1998) Stress-inducible responses and heat shock proteins: new pharmacologic targets for cytoprotection. *Nat. Biotechnol.* **16**, 833-838.

19. Morimoto, R. I. (1998) Regulation of the heat shock transcriptional response: cross talk between a family of heat shock factors, molecular chaperones, and negative regulators. *Genes Dev.* **12**, 3788-3796.
20. Ait-Aissa, S., J. Porcher, C. Kretz-Remy, G. Velarde, A. Arrigo, and C. Lambre (1999) Induction of the hsp70 gene promoter by various anticancer drugs. *Toxicol. in vitro* **13**, 651-655.
21. Fischbach, M., E. Sabbioni, and P. Bromley (1993) Induction of the human growth hormone gene placed under human hsp70 promoter control in mouse cells: a quantitative indicator of metal toxicity. *Cell Biol. Toxicol.* **9**, 177-188.
22. Blechinger, S. R., J. T. Warren, Jr., J. Y. Kuwada, and P. H. Krone (2002) Developmental toxicology of cadmium in living embryos of a stable transgenic zebrafish line. *Environ. Health Perspect.* **110**, 1041-1046.
23. Liu, B., A. M. DeFilippo, and Z. Li (2002) Overcoming immune tolerance to cancer by heat shock protein vaccines. *Mol. Cancer Ther.* **1**, 1147-1151.
24. Srivastava, P. K. and R. J. Amato (2001) Heat shock proteins: the 'Swiss Army Knife' vaccines against cancers and infectious agents. *Vaccine* **19**, 2590-2597.
25. Srivastava, P. K., A. Menoret, S. Basu, R. J. Binder, and K. L. McQuade (1998) Heat shock proteins come of age: primitive functions acquire new roles in an adaptive world. *Immunity* **8**, 657-665
26. Wysocka, A. and Z. Krawczyk (2000) Green fluorescent protein as a marker for monitoring activity of stress-inducible hsp70 rat gene promoter. *Mol. Cell Biochem.* **215**, 153-156.
27. Coutier, Stephanie. (2001) Ph.D. Thesis. Unité de recherche en Thérapie Photodynamique, Centre Alexis Vautrin. Vandoeuvre-les-Nancy Cedex, France.

Appendix I: Spheroid Culture

EMT6 mouse mammary carcinoma cells are maintained as a monolayer culture in a complete medium consisting of Cellgro[®]-Basal Eagle medium (BME; Mediatech, Herndon, VA) and 10% fetal calf serum (FCS; Hyclone, South Logan, UT) supplemented with penicillin-streptomycin and fungizone. The cultures are incubated at 37° C in a humidified 5% CO₂ atmosphere.

The EMT6 spheroids are initiated by plating approximately 5×10^6 cells onto a 100-mm suspension culture plastic dish containing 15 mL of the culture medium. After 3-4 days, the cells form small aggregates which are then collected and seeded into a 500-mL glass spinner flask (Bellco Glass Inc., Vineland, NJ) containing 300 mL BME with 10% FCS. The spinner flasks are kept inside an incubator with humidified 5% CO₂-95% air atmosphere and placed on a magnetic spinner plate operating approximately at 100 rpm. Spheroid culture medium is changed every 2-3 days by allowing spheroids to settle to the bottom of the flask, carefully aspirating 200 mL of the spent medium, and replacing it with an identical volume of fresh medium. After about 4-5 days the spheroids reach approximately 250 μm in diameter and become 500 μm in

diameter in 10-12 days. The smaller sized spheroids are appropriate for confocal imaging experiments while the larger sized spheroids are suitable for electrode experiments.

Once the spheroids have reached the desired size, they are removed from the spinner flask and placed in a 100 mm suspension or non-tissue culture petri dish containing medium, sensitized with a photosensitizer, and placed in the dark at 37° C in a humidified 5% CO₂-95% air atmosphere for the incubation period before PDT irradiation.

Appendix II: Preparation of spheroid frozen sections

Approximately 100 EMT6 spheroids (500 μm diameter) were picked from a spinner flask and placed in a non-tissue culture dish containing Eagle's basal medium (BME) with 10% fetal calf serum. The photosensitizer was added to the medium and the dish was then put inside an incubator at 37⁰ C in a humidified 5% CO₂-95% air atmosphere for the incubation period, usually 24 hours for both mTHPC and Photofrin. Following incubation, the spheroids were transferred to a 15 mL centrifuge tube, centrifuged and washed three times with Hanks' balanced salt solution (HBSS, Gibco-BRL). Once the spheroids settled at the bottom of the tube, the HBSS was carefully aspirated using a pasteur pipette. A small amount of aqueous embedding media (Tissue-Tek OCT compound, Sakura Finetek USA Inc., Torrance, CA) was placed at the bottom of a 10 mm x 5 mm cryomold (Sakura Finetek USA Inc.) and allowed to freeze at -23⁰ C. The spheroids were then picked from the centrifuge tube and placed on top of the frozen OCT. More OCT was then added to the cryomold so that the spheroids were completely covered, and the block was frozen solid at -23⁰ C. The frozen

block was then mounted onto a cryostat and 15- μm -thick spheroid sections were placed onto microscope slides for fluorescence imaging.

Appendix III: A procedure for determining sensitizer concentration in spheroids

30 spheroids (500 μm diameter) are sensitized with a prescribed incubation concentration. After the incubation period, the spheroids, along with the media, are placed in a 15 mL centrifuge tube and centrifuged for 5 minutes. After centrifugation, the medium above the spheroid pellet is aspirated, and fresh HBSS is added to it. The centrifugation and the washing of the spheroid pellet with HBSS is repeated several times. The HBSS is then carefully aspirated, and 1.5 mL of 10% trypsin with phenol red (Invitrogen, Carlsbad, CA) is added. The sample is gently vortexed and agitated for 3 - 5 minutes. The trypsin results in the dissociation of the spheroids into cells. 0.5 mL of scintigest is added to the sample to dissolve the cells. The result is a 2 mL solution of 25% scintigest consisting of the drug extracted from the 30 spheroids. We measure the fluorescence or absorption spectrum of the sample. The sensitizer concentration is then calculated using a calibration curve generated from the fluorescence or absorption of known sensitizer concentrations in the same solvent of 25% scintigest.